UNIVERSIDADE FEDERAL DE UBERLÂNDIA

INSTITUTO DE QUÍMICA

Programa de Pós-Graduação em Química

Laboratório de Fotoquímica e Ciência dos Materiais (LAFOT-CM)

LUCAS LEÃO NASCIMENTO

Development and Optoelectronic Characterization of Photoactive Materials for Photo(electro)reforming of Industrial Waste Streams and Low Carbon Hydrogen Evolution

Uberlândia - MG

2025

LUCAS LEÃO NASCIMENTO

Development and Optoelectronic Characterization of Photoactive Materials for Photo(electro)reforming of Industrial Waste Streams and Low Carbon Hydrogen Evolution

Tese apresentada ao Programa de Pós-Graduação em Química da Universidade Federal de Uberlândia, como requisito para obtenção do título de Doutor em Química.

Orientador: Prof. Dr. Antonio Otavio de Toledo Patrocinio

Uberlândia - MG

2025

Ficha Catalográfica Online do Sistema de Bibliotecas da UFU
com dados informados pelo(a) próprio(a) autor(a).

N244 Nascimento, Lucas Leão, 1994-
2025 Development and Optoelectronic Characterization of Photoactive Materials for Photo(electro)reforming of Industrial Waste Streams and Low Carbon Hydrogen Evolution [recurso eletrônico] / Lucas Leão Nascimento. - 2025.

Orientador: Antonio Otavio de Toledo Patrocinio.
Tese (Doutorado) - Universidade Federal de Uberlândia, Pós-graduação em Química.
Modo de acesso: Internet.
DOI http://doi.org/10.14393/ufu.te.2025.471
Inclui bibliografia.

1. Química. I. Patrocinio, Antonio Otavio de Toledo,1983-, (Orient.). II. Universidade Federal de Uberlândia. Pós-graduação em Química. III. Título.

CDU: 54

Bibliotecários responsáveis pela estrutura de acordo com o AACR2:
Gizele Cristine Nunes do Couto - CRB6/2091
Nelson Marcos Ferreira - CRB6/3074

UNIVERSIDADE FEDERAL DE UBERLÂNDIA
Coordenação do Programa de Pós-Graduação em Química
Av. João Naves de Ávila, 2121, Bloco 5I - Bairro Santa Mônica, Uberlândia-MG, CEP 38400-902
Telefone: (34) 3239-4385 - www.cpgquimica.iq.ufu.br - cpgquimica@ufu.br

ATA

Programa de Pós-Graduação em:	Química				
Defesa de:	Tese de Doutorado Acadêmico, 172, PPGQUI				
Data:	Vinte e cinco de julho de dois mil e vinte e cinco	Hora de início:	14h	Hora de encerramento:	18:15
Matrícula do Discente:	12123QMI004				
Nome do Discente:	Lucas Leão Nascimento				
Título do Trabalho:	“Development and Optoelectronic Characterization of Photoactive Materials for Photo(electro)reforming of Industrial Waste Streams and Low Carbon Hydrogen Evolution”				
Área de concentração:	Química				
Linha de pesquisa:	Ciência dos Materiais: Química do Estado Sólido				
Projeto de Pesquisa de vinculação:	“Síntese e caracterização de óxidos semicondutores nanoestruturados com aplicação voltada ao tratamento fotocatalítico de efluentes e águas residuárias, conversão de energia solar, células fotoeletroquímicas, fotossíntese artificial e outras aplicações”				
ODS 7	ODS 7 - Energia limpa e acessível: garantir acesso à energia barata, confiável, sustentável e renovável para todos.				

Reuniu-se, por webconferência, no link: https://meet.google.com/jve-farx-nvc, a Banca Examinadora, designada pelo Colegiado do Programa de Pós-graduação em Química, assim composta: Professores Doutores: **Carla Eponina Hori,** da Universidade Federal de Uberlândia -FEQ; **Christian Gonçalves Alonso**, da Universidade Federal de Goiás-UFG; **Flavio Leandro de Souza**, da Universidade Federal do ABC-UFABC; **Luciana Almeida da Silva**, da Universidade Federal da Bahia-UFBA; e **Antonio Otavio de Toledo Patrocinio**, orientador(a) do(a) candidato(a).

Iniciando os trabalhos o presidente da mesa, **Dr. Antonio Otavio de Toledo Patrocinio**, apresentou a Comissão Examinadora e o(a) candidato(a), agradeceu a presença do público, e concedeu ao(à) Discente a palavra para a exposição do seu trabalho. A duração da apresentação do(a) Discente e o tempo de arguição e resposta foram conforme as normas do Programa.

A seguir o senhor(a) presidente concedeu a palavra, pela ordem sucessivamente, aos(às) examinadores(as), que passaram a arguir o(a) candidato(a). Ultimada a arguição, que se desenvolveu dentro dos termos regimentais, a Banca, em sessão secreta, atribuiu o resultado final, considerando o(a) candidato(a):

Aprovado.

Esta defesa faz parte dos requisitos necessários à obtenção do título de Doutor.

O competente diploma será expedido após cumprimento dos demais requisitos, conforme as normas do Programa, a legislação pertinente e a regulamentação interna da UFU.

Documento assinado eletronicamente por **Antonio Otavio de Toledo Patrocínio**, **Professor(a) do Magistério Superior**, em 25/07/2025, às 18:22, conforme horário oficial de Brasília, com fundamento no art. 6º, § 1º, do Decreto nº 8.539, de 8 de outubro de 2015.

Documento assinado eletronicamente por **Carla Eponina Hori**, **Professor(a) do Magistério Superior**, em 25/07/2025, às 18:24, conforme horário oficial de Brasília, com fundamento no art. 6º, § 1º, do Decreto nº 8.539, de 8 de outubro de 2015.

Documento assinado eletronicamente por **Flavio Leandro de Souza**, **Usuário Externo**, em 25/07/2025, às 18:24, conforme horário oficial de Brasília, com fundamento no art. 6º, § 1º, do Decreto nº 8.539, de 8 de outubro de 2015.

Documento assinado eletronicamente por **Christian Gonçalves Alonso**, **Usuário Externo**, em 25/07/2025, às 18:25, conforme horário oficial de Brasília, com fundamento no art. 6º, § 1º, do Decreto nº 8.539, de 8 de outubro de 2015.

Documento assinado eletronicamente por **Luciana Almeida da Silva**, **Usuário Externo**, em 25/07/2025, às 18:26, conforme horário oficial de Brasília, com fundamento no art. 6º, § 1º, do Decreto nº 8.539, de 8 de outubro de 2015.

A autenticidade deste documento pode ser conferida no site https://www.sei.ufu.br/sei/controlador_externo.php?acao=documento_conferir&id_orgao_acesso_externo=0, informando o código verificador **6355477** e o código CRC **35ADF0A1**.

Referência: Processo nº 23117.033949/2025-41 SEI nº 6355477

À Deus, nosso pai criador.
Aos meus pais, Stela e Luiz, por serem o pilar primordial da minha formação.
À minha noiva Mariana, a luz da minha vida, pelo amor e dedicação.
Ao meu sogro, Eli, pelo apoio e companheirismo.
Ao meu orientador Antonio Otavio, por ter sido a inspiração que me fez chegar até aqui.

Agradecimentos

Agradeço primeiramente a Deus por ter me dado forças para alcançar essa conquista.

Agradeço profundamente aos meus pais, Maria Stela Leão e Luiz Mário do Nascimento, que me proporcionaram um lar com amor e apoio, constituindo a base que possibilitou a realização deste doutorado. Vocês sempre apoiaram a minha carreira e se sacrificaram ao máximo para que eu pudesse chegar até aqui.

À minha noiva Mariana, pelo amor, paciência e dedicação incondicionais durante todo esse período. Você foi a luz que iluminou o meu caminho e me guiou ao longo de toda essa jornada.

Ao meu orientador e amigo, Prof. Dr. Antonio Otavio, cuja orientação, incentivo e paixão pela ciência foram minha maior inspiração. Você me acolheu desde o começo da minha graduação, e desde então construímos uma relação de admiração e amizade. Sou muito grato por todos os ensinamentos que você me passou ao longo destes anos, eu não poderia ter pedido por um orientador melhor.

Sou grato também pelas amizades construídas ao longo dessa jornada, em especial à Ju, Rafael, Leandro, Gonçalves, Sinval e Léo, cuja convivência tornou esta experiência mais leve e gratificante.

Aos meus familiares, Marlen, Wilson, Fernando, Júnior, Cris, Sophie e Leonardo, por todo carinho e atenção dedicados a mim. O apoio e afeto de vocês foi essencial durante o período que eu passei no Reino Unido.

Aos colegas de laboratório, pelo ambiente de trabalho colaborativo e harmonioso que compartilhamos.

Ao Prof. Dr. Alex Cowan por ter me recebido sob sua orientação na University of Liverpool durante o meu estágio sanduíche. Aos meus colegas de laboratório durante esse período, especialmente, Alicia, Adrian, Chao, Nathaniel, Cathy, Hamsaem, Owen e Khadija. Aprendi muito com vocês e sou grato por ter compartilhado tantas experiências com pessoas de culturas diferentes.

Ao Prof. Dr. Thomas Bein e Dra. Jenny Schneider, da Ludwig-Maximilians-Universität München, pela parceria e por terem me recebido de braços abertos na Alemanha. Ao Shuo pela ajuda e convivência amistosa durante o período na Alemanha. Um agradecimento especial à Klaudija pela parceria e amizade que

desenvolvemos ao longo dessa colaboração. Aprendi muito com você e espero poder te encontrar novamente.

Às todas as parcerias científicas que foram essenciais para o desenvolvimento deste trabalho. Sou grato ao professor Klaus pelas análises de EPR, ao professor Teodorico pelos cálculos computacionais. Um agradecimento especial para o professor Osmando pelo apoio e pelas discussões científicas que enriqueceram este trabalho.

Ao Programa de Pós-Graduação em Química da Universidade Federal de Uberlândia (PPGQUI-UFU), pelo suporte acadêmico e institucional oferecido ao longo de toda a minha formação acadêmica. Ao Magayver pelas análises de MEV e RMN. Ao Guilherme do INFIS-UFU pelas análises de espectroscopia Raman.

À CAPES, ao CNPq, ao CEHTES (FAPEG) e à FAPEMIG pelo apoio financeiro. Ao programa CAPES-Print (88887.892434/2023-00) pelo financiamento do período sanduíche no Reino Unido. À fundação Alexander von Humboldt-Stiftung pelo financiamento da visita na Alemanha.

RESUMO

Este trabalho tem como foco o desenvolvimento e a caracterização de novos materiais fotocatalíticos e fotoanodos capazes de absorver luz visível para promover a foto(eletro)reforma de substratos orgânicos, especialmente de derivados de biomassa, com o objetivo de produzir hidrogênio de baixo carbono e produtos de oxidação de alto valor agregado. Estratégias sintéticas hidrotérmicas e solvotérmicas foram empregadas para introduzir vacâncias de oxigênio e dopantes em óxidos semicondutores de bandgap elevado, como Bi_2WO_6, Nb_2O_5 e TiO_2, aumentando a absorção de luz visível. Além disso, oxinitreto de titânio e nióbio (NbTiON) e *Covalent Organic Frameworks* (COFs) foram sintetizados como fotocatalisadores alternativos com propriedades optoeletrônicas modulares. Os materiais obtidos foram caracterizados por diferentes técnicas a fim de elucidar a morfologia, propriedades optoeletrônicas e a dinâmica dos portadores de carga. Os fotocatalisadores mais promissores foram imobilizados na forma de filmes para a fabricação de fotoanodos, os quais foram avaliados sob irradiação solar simulada (AM 1.5G, 100 mW cm^{-2}) e luz visível (λ > 420 nm, 100 mW cm^{-2}) em células fotoeletroquímicas (PECs) contendo glicerol ou flegmaça. PECs com fotoanodos de $BiVO_4$ dopados com 5% m/m de Nb^{5+} converteram 91,4% do glicerol com 88,9% de seletividade para formação de ácido fórmico após 5 horas de irradiação de luz solar simulada, alcançando uma velocidade de evolução de H_2 (HER) de 4,2 µmol H_2 cm^{-2} h^{-1} (84% maior do que o obtido com o $BiVO_4$ não modificado). Ademais, a inserção de vacâncias de oxigênio foi empregada para melhorar o desempenho de fotoanodos à base de Bi_2WO_6 frente à conversão do glicerol bruto, elevando a conversão de 17,0% para 24,5%. Concomitantemente, a HER aumentou de 32 para 63 µmol h^{-1} cm^{-2}. Explorando novos materiais, as propriedades de COFs baseados em tiofeno foram moduladas por meio da conversão da ligação imina em amida, resultando em um aumento de 300% na HER. Esses resultados destacam os benefícios da inserção de defeitos estruturais, dopagem e rotas sintéticas alternativas na modulação das propriedades optoeletrônicas e catalíticas de semicondutores. De forma geral, este trabalho avança no design de materiais e fotoeletrodos eficientes, estáveis e abundantes para a valorização de biomassa e produção de hidrogênio impulsionadas pela energia solar.

Palavras-chaves: fotorreforma, fotocatálise, PEC, hidrogênio, COF, glicerol, flegmaça, conversão de energia, defeitos estruturais, valorização de biomassa

ABSTRACT

This work focuses on the development and characterization of novel photocatalytic materials and photoanodes capable of harvesting visible light to promote the photo(electro)reforming of organic substrates, especially real industrial biomass-derived waste streams, aiming at the production of low-carbon hydrogen and value-added oxidation products. Hydrothermal and solvothermal synthetic strategies were employed to introduce oxygen vacancies and dopant species into wide-bandgap semiconductor oxides such as Bi_2WO_6, Nb_2O_5, and TiO_2, effectively narrowing their band gaps and enhancing visible light absorption. Additionally, oxynitride materials (NbTiON) and covalent organic frameworks (COFs) were synthesized as alternative photocatalysts with tunable optoelectronic properties. The obtained materials were comprehensively characterized by different techniques to elucidate their morphology, optoelectronic properties, and charge carrier dynamics. The most promising photocatalysts were immobilized as thin films to fabricate photoanodes, which were evaluated under simulated solar (AM 1.5G, 100 mW cm^{-2}) and visible irradiation ($\lambda >$ 420 nm, 100 mW cm^{-2}) in photoelectrochemical cells (PECs) containing glycerol or flegmass as sacrificial agents. PECs with $BiVO_4$ photoanodes doped with 5 wt.% Nb have converted 91.4% of glycerol with 88.9% selectivity toward formic acid formation after 5 hours of simulated sunlight illumination, achieving a H_2 evolution rate (HER) of 4.2 μmol H_2 cm^{-2} h^{-1}. This value is 84% higher than that of unmodified $BiVO_4$. Additionally, oxygen vacancies engineering was employed to improve the photoelectrocatalytic performance of Bi_2WO_6-based photoanodes towards crude glycerol conversion, from 17.0% for the pristine oxide to 24.5%. Concomitantly, HER was enhanced from 32 to 63 μmol h^{-1} cm^{-2}. Looking at new materials for photoreforming, the properties of thiophene-based COFs were modulated through linkage conversion from imine to amide resulting in a 300% increase in the photocatalytic HER compared to its imine form. These findings highlight the synergistic benefits of defect engineering, doping, and alternative synthetic pathways in tailoring the optoelectronic and catalytic properties of semiconductors. Overall, this work advances the design of efficient, stable, and abundant photoelectrodes for solar-driven biomass valorization and hydrogen production.

Keywords: photoreforming, photocatalysis, PEC, hydrogen, COF, glycerol, flegmass, energy conversion, defect engineering, biomass valorization

ABBREVIATIONS AND SYMBOLS

PEC	Photoelectrochemical Cell
HER	Hydrogen Evolution Reaction
OER	Oxygen Evolution Reaction
COF	Covalent Organic Framework
DRS	Diffuse Reflectance Spectroscopy
PXRD	Powder X-Ray Diffraction
SEM	Scanning Electron Microscopy
TEM	Transmission Electron Microscopy
XPS	X-ray Photoelectron Spectroscopy
EIS	Electrochemical Impedance Spectroscopy
LSV	Linear Sweep Voltammetry
PL	Photoluminescence
UV-Vis	Ultraviolet-Visible Spectroscopy
BET	Brunauer-Emmett-Teller (surface area analysis)
AM 1.5G	Air Mass 1.5 Global (standard solar spectrum)
RHE	Reversible Hydrogen Electrode
SHE	Standard Hydrogen Electrode
P25	Commercial TiO_2 photocatalyst (Degussa P25)
VB	Valence Band
CB	Conduction Band
DOS	Density of States
BZ	Brillouin Zone
GGA-PBE	Generalized Gradient Approximation - Perdew-Burke-Ernzerhof
DFT	Density Functional Theory
U	Hubbard Correction Parameter
QD	Quantum Dot
IPA	Isopropyl Alcohol

PA	Analytical Grade
FTO	Fluorine-doped Tin Oxide
CBED	Convergent Beam Electron Diffraction
E	Energy (eV)
E_g	Band Gap Energy
Φ	Photon Flux
hv	Photon Energy
λ	Wavelength (nm)
ΔG^0	Standard Gibbs Free Energy
k	Rate Constant
Rct	Charge Transfer Resistance
Rs	Series Resistance
Cdl	Double Layer Capacitance
V	Potential
F	Faraday Constant (96,485 $C \cdot mol^{-1}$)
e^-	Electron
h^+	Hole
μ	Charge carrier mobility
τ	Carrier lifetime
α	Absorption coefficient

LIST OF FIGURES

LIST OF TABLES

Table of Contents

1. Introduction and Objectives

1.1. Outlook

Climate change induced by anthropologic activities is a central issue in modern society, driving the search for new industrial processes able to provide energy and chemicals in a sustainable way (AHMED, MAHMOUD; DINCER, 2019). One possibility would be the development of materials and processes capable of using solar light as primary energy source to promote the conversion of Earth-abundant low energy substances or existing industrial residues into fuels and/or high-value chemicals. Such processes can effectively contribute to lowering carbon emissions and for the so-called circular economy (NASCIMENTO, LUCAS LEÃO et al., 2024). In solar-driven fuel production, sunlight is employed to promote the conversion of low-energy content and abundant species into fuels. Among the possible substrates that can be applied in the artificial photosynthetic systems, CO_2 and H_2O would be the ideal candidates as in the natural photosynthesis; however, both CO_2 reduction and water oxidation reactions are kinetically challenging multielectron processes and, so far, the proposed catalytic systems have not yet reached the performance and stability levels that would allow practical application. Alternatively, raw sustainable materials and residues can be photocatalytically converted into valuable compounds of industrial interest in a process that combines the necessary treatment of waste streams with the production of green hydrogen and/or chemicals that can be used as feedstocks.

The photoconversion of non-edible biomass derivatives, in which part of the harvested solar energy is stored as chemical bonds, calls special attention as a suitable and renewable pathway to obtain valuable green products (WU, X. et al., 2020). Initially, photocatalytic systems for biomass processing were focused on the mineralization of organic matter as an alternative advanced oxidation process for environmental remediation. In the last decades, however, more elaborated photo(electro)chemical systems based on nanostructured semiconductors have been reported with focus on biomass valorization, i.e., the selective photoconversion of the different residues and derivatives into carbon-based chemicals of industrial interest. Concomitantly, green hydrogen can be produced under anaerobic conditions, offering a new pathway for production of this important energy vector.

Investigations on the selective transformation of a variety of biomass derivatives have been carried out in recent decades which include polyols, sugars and carbohydrates along with lignocellulose-derived compounds. The studies also involve

the use of biomass byproducts and residues from well-stablished industries such as those from the biodiesel and sugarcane processing plants. In the first case, crude glycerol is the main byproduct, while vinasse is the main waste in the sugarcane processing. Considerable advances have been reported in terms of materials design with the preparation of more efficient nanostructured photocatalysts (KAUSHIK et al., 2022). Mechanistic studies have also been carried out in order to exert control on the product selectivity (BUZZETTI; CRISENZA; MELCHIORRE, 2019; NGUYEN, C. C. et al., 2021). The broader perspective is to combine such findings with device engineering aiming at large scale applications.

1.2. Photoreforming of biomass derivatives mediated by semiconductor oxides

Early reports of photoreforming of biomass derivatives back to 80s, when Kawai and Sakata employed $RuO_2/TiO_2/Pt$ composites to produce H_2 from carbohydrate aqueous alkaline solutions. Saccharose, starch and cellulose were evaluated and the photocatalyst was able to fully oxidize the substrates to CO_2, while H_2 evolved from the Pt surface. As stated by Kuehnel and Reisner (KUEHNEL; REISNER, 2018) solar reforming of glucose-derived biomass is an energy neutral process (E^0 ~0.001 V *vs* RHE, equation 1), hereby, photons are only needed to drive the kinetics and overcome activation barriers. Thus, in theory, these species as well as most polyols found on different biomass sources can undergo oxidation by low energy photons, making them suitable electron donors for most photocatalytic systems. Moreover, the thermodynamic energy to drive biomass oxidation is considerably lower than that for water splitting (Equation 2) (SIMÕES; BARANTON; COUTANCEAU, 2012).

$$(C_6H_{12}O_6)_n + 6nH_2O \xrightarrow{h\nu} 6nCO_2 + 12nH_2 \quad E^0 \cong 0.001 \text{ V } \textit{vs} \text{ RHE} \quad \text{(Equation 1)}$$

$$H_2O \xrightarrow{h\nu} \tfrac{1}{2}\, O_2 + 1H_2 \quad E^0 = 1.23 \text{ V } \textit{vs} \text{ RHE} \quad \text{(Equation 2)}$$

The photoreforming reaction promoted by heterogeneous photocatalysts takes place under anaerobic conditions. Incident light is absorbed by a semiconductor material to yield electron-hole pairs. The photogenerated holes (h^+) on the catalyst surface are used to oxidize the organic compounds while free electrons (e^-) eventually reduce protons to H_2 (HERRMANN, 2005; RAVELLI et al., 2009; JUNG et al., 2016).

The H_2 evolution rates under photoreforming conditions are typically much higher than those obtained by the water splitting reaction (Equation 2) because the photogenerated holes can be efficiently consumed by the organic substrates and, therefore, the competitive electron recombination process is effectively suppressed (PANAGIOTOPOULOU; KARAMEROU; KONDARIDES, 2013; JUNG et al., 2016; NIE et al., 2018).

In the last decade, focus is given to photocatalytic systems that are active under visible light and allow for selective oxidation of the organic substrates aiming at concomitant production of H_2 and valuable chemicals as illustrated in Figure 1. In biomass-derived photoreforming, photons are used to drive the redox reactions, producing molecules with lower energy content, while storing the exceeding energy as green H_2. In that way, it is possible to obtain multiple valuable products within an energetic neutral and sustainable process. Furthermore, looking at the so-call biorefinery concept, attempts have been made to use residues from industries of different sectors as sacrificial agents for H_2 production (ESSIE et al., 2023). This approach pushes towards harnessing the full energy potential of renewable resources, contributing to the development of a sustainable and circular economy.

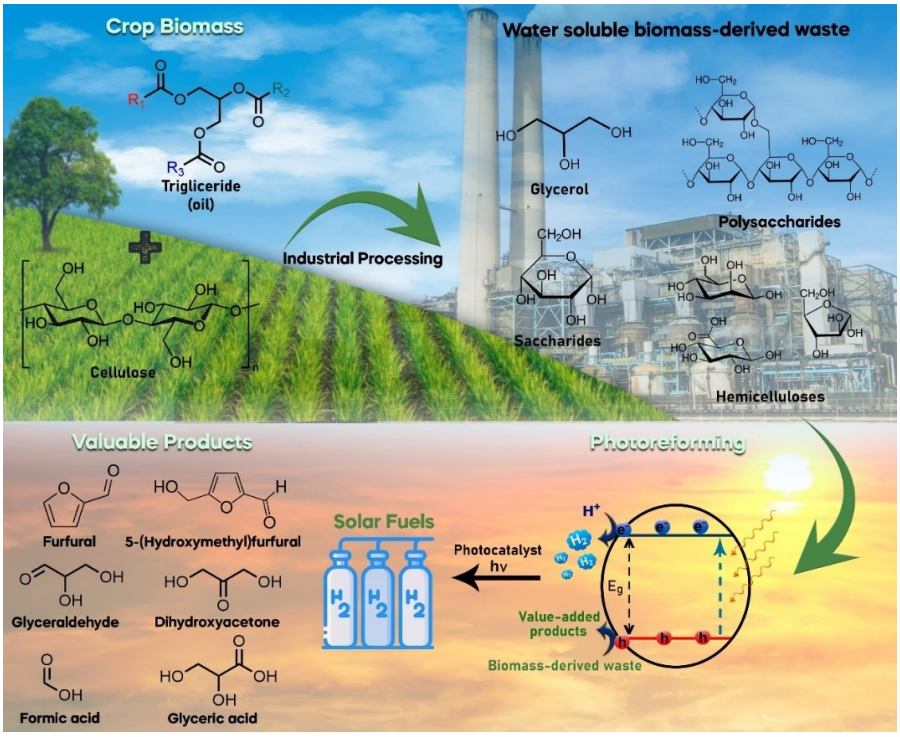

Figure 1. Scheme illustrating the photoreforming of biomass-derived compounds by heterogeneous photocatalysts.

Typically, photoreforming systems are evaluated through key Figures of merit such as photonic efficiency, ξ, Faradaic Efficiency, FE, H_2 evolution rate and product selectivity. The photonic efficiency gives the percentage of irradiated photons that were effectively used to drive the desired reaction and it is calculated as the ratio between the conversion rate, r, and the incident photon flux, I, Equation 3, corrected by the number of electrons involved in the photochemical process, z (in the H_2 evolution, z = 2). When the incident radiation is monochromatic, quantum yield can be used instead. If the photon flux is not determined, hydrogen evolution is simply normalized by the weight of the photocatalyst and the irradiation time. For photoelectrochemical systems, Faradaic Efficiency can be used. This parameter takes into consideration the total charge that passed through a given electrochemical circuit and can be used to describe the selectivity of a photoelectrochemical process, both in the anode and in the cathode. It is defined as shown in Equation 4, in which n is the measured amount of product, F is the Faraday constant and Q is the charge that flowed through the system, Q. The resulting organic products of the process are also evaluated through the carbon-based selectivity, which corresponds to the moles of initial carbon that were converted into a specific product.

$$\boldsymbol{\varepsilon} = \frac{\boldsymbol{zr}}{\boldsymbol{I}} \qquad \text{(Equation 3)}$$

$$\boldsymbol{FE} = \frac{\boldsymbol{znF}}{\boldsymbol{Q}} \qquad \text{(Equation 4)}$$

Looking at the existing biomass-based industrial processes, potential substrates for photoreforming can be identified. Byproducts from wood and crop processing (especially cereal crops and sugarcane) as well as those from the paper & cellulose industry offer a significant volume of organic matter that can be conveniently explored for H_2 evolution. Besides the recalcitrant lignocellulosic compounds, these processes also generate different water-soluble waste streams, formed mostly by mono, oligo or polysaccharides and organic acids (FLÓREZ PARDO; LÓPEZ GALÁN; LOZANO RAMÍREZ, 2018; YAO et al., 2020; NAVAKOTESWARA RAO et al., 2021; PLUCINSKI; LYU; SCHMIDT, 2021). Particularly, glucose has been employed in proof-of-concept studies (IERVOLINO et al., 2016; MADRIZ et al., 2020; NWOSU et al., 2022).

Another byproduct of interest is glycerol from biodiesel production (NAVARRO et al., 2009; DODEKATOS; SCHÜNEMANN; TÜYSÜZ, 2018; CHECA et al., 2020). Although purified glycerol is highly used in the cosmetics and food industry, the current

glycerol availability greatly surpasses its global demand due to the growing production of biodiesel (CHOL et al., 2018; ZIYAI et al., 2019; AUGUSTIN et al., 2022). After refining and distillation processes, the triol is commercialized as glycerine, a colourless, odourless, biodegradable, hygroscopic and non-toxic viscous liquid at room temperature (CHOL et al., 2018). In most cases, the processing and refining costs of crude glycerol is higher than its selling price, which may hinder the sustainability of the whole production chain. In the recent years, glycerol has been by far the most studied biomass-derived sacrificial agent for photocatalytic valorization and green H_2 production, given its chemical properties and availability. Therefore, its oxidation reaction will be used here as a model to introduce the most important aspects of biomass photoreforming.

Glycerol is a highly functionalized molecule with three hydroxyl groups. The variety of value-added products that can be obtained through glycerol oxidation ranges from acrylic, glyceric, lactic and formic acid, as well as dihydroxyacetone or 1,2-propanediol, **Figure 2** (CARGNELLO et al., 2011; DODEKATOS; SCHÜNEMANN; TÜYSÜZ, 2018). The glycerol conversion process leads to molecules with high O/C ratios that are up to two orders of magnitude more valuable than the glycerol itself (LUO et al., 2022).

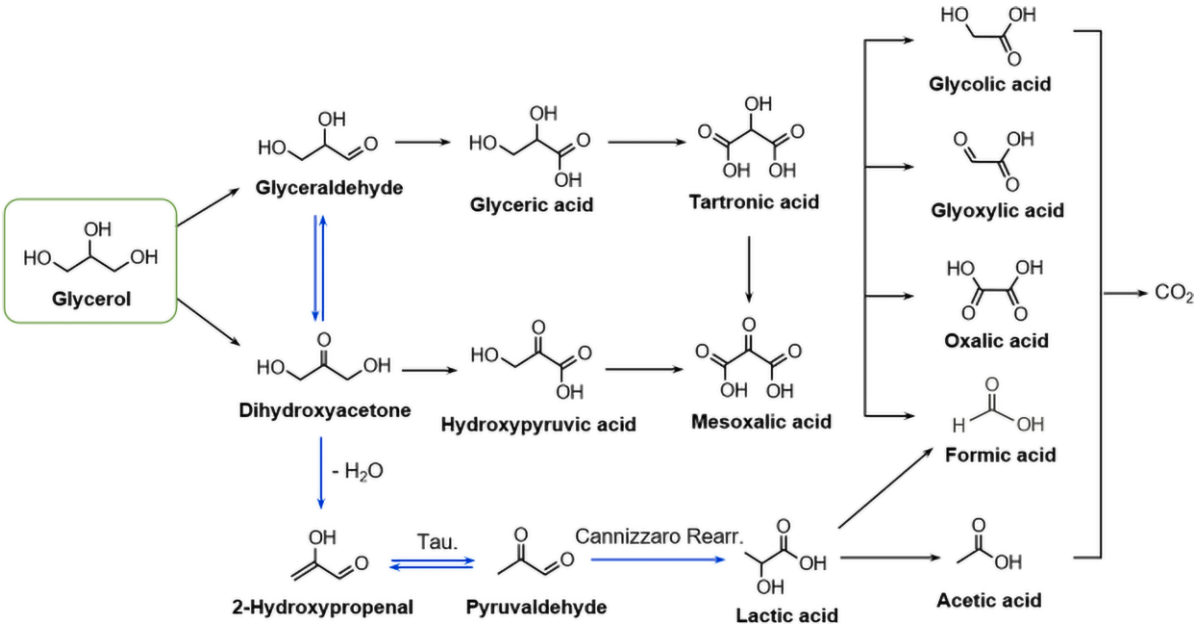

Figure 2. Reaction schematic of possible products from glycerol oxidation. Adapted from (HU et al., 2023).

Intensive research is being conducted to find means for glycerol valorization, which includes thermal (HE, S. et al., 2018; BATISTA et al., 2019; SHAHIRAH et al., 2019), electro (KWON et al., 2012; AHMAD, M. S. et al., 2021; HE, Z. et al., 2021; KIM, D. et al., 2023) and photocatalytic routes (JUNG et al., 2016; HUANG; VO; CHIANG, 2019; LIU, D. et al., 2019). Amid glycerol transformation processes, the aerobic heterogeneous thermocatalytic oxidation can efficiently convert glycerol into several important derivatives such as aldehydes, ketones and carboxylic acids (HE, Z. et al., 2021). However, this process is associated with poor selectivity, as the mechanism generally involves highly reactive radicals derived from O_2 (ZHONG, W. et al., 2022). This limitation could compromise real applicability as product separation is costly and hard to achieve.

Different from thermal processes, in photocatalysis the selective oxidation of glycerol depends on the band structure of the photocatalyst and its surface properties. H_2 evolution typically occurs from a metallic co-catalyst. TiO_2 was naturally the first material to be applied in such reactions. Litchin *et al.* (LICHTIN; DONG; VIJAYAKUMAR, 1992) first reported photoinduced mineralization of aqueous glycerol promoted by Degussa P25 TiO_2. Later, Kondarides et al. (KONDARIDES et al., 2008) described the complete mineralization of glycerol to H_2 and CO_2 over Pt(0.5 wt%)-TiO_2 under anaerobic conditions and UV irradiation. In these studies, no focus was given to the oxidation products. As TiO_2 can efficiently promote the formation of high reactive hydroxyl radicals, poor selectivity, or even full mineralization of the triol is typically observed.

Yu and coworkers (YU et al., 2021) have compared the activity of pure TiO_2 and pure WO_3 for selective glycerol photooxidation. Although TiO_2 reached a considerably higher glycerol conversion (97%) compared to the 44% conversion showed by WO_3, the selectivity for C3 oxidation products was remarkably lower, reaching only 5% for glyceraldehyde against 29% reached by WO_3. The lower selectivity for TiO_2 was explained by the further photooxidation of glycerol oxidation products, leading to full mineralization, while the higher glyceraldehyde selectivity of WO_3 was linked to its surface acidity which facilitates the desorption of glyceraldehyde, avoiding its further photooxidation.

Maurino *et al.* (MAURINO et al., 2008) showed that the selectivity of the pristine Degussa P25 TiO_2 photocatalyst could be increased by submitting it to a fluorination process. The as modified photocatalyst was able to partially oxidize glycerol to

dihydroxyacetone and glyceraldehyde. Moreover, Augugliaro and co-workers (AUGUGLIARO et al., 2010) have evaluated various commercial and synthesized TiO_2 nanoparticles with different phase compositions against aqueous glycerol selective photooxidation, and found low selectivity for all investigated oxidation products, except CO_2. As shown in

Table 1, few examples in the literature employing TiO_2-based systems quantify the oxidation products. In few cases, when typically, a composite is employed, some details can be found.

Table 1. Results of different photocatalyst towards glycerol photoreforming.

Photocat.	Irradiation conditions	[Glycerol] mol L^{-1}	Overall conversion	H_2 evolution rate / mmol g^{-1} h^{-1}	Main Products (Selectivity)	Ref.
TiO_2	LED lamp 41.5 mW cm^{-2}	2.72 (Crude glycerol)	-	3.2	-	(RUMAYOR et al., 2022)
TiO_2	300 W Xe arc 350 mW cm^{-2} under argon	1.36	-	0.72	-	(CAI et al., 2018)
TiO_2	UV-A 18W lamp 5.60 mW cm^{-2}	1.10×10^{-3}	97%	-	Glyceraldehyde (5%)	(YU et al., 2021)
TiO_2/Pt (0.5% wt.)	75 W Xe arc under argon	0.68	-	6.0	-	(BEDNARCZYK; STELMACHOWSKI; GMUREK, 2019)
TiO_2/Pt (0.5% wt.)	450 W Xe arc under argon	7.38×10^{-3}	-	0.15	-	(DASKALAKI; KONDARIDES, 2009)
TiO_2/Pt (1.5% wt.)	125 W Hg lamp (λ > 320 nm) under argon	1.36	.	15	H_2 and CO_2 (100%)	(LÓPEZ-TENLLADO et al., 2017)
TiO_2/Pt (1% wt.)	30W LED light source (λ = 380 nm) under argon	0.06	18%	1.4	Glyceraldehyde (28%), lactic acid (34%) and glycolic aldehyde (38%)	(KOZLOVA et al., 2021)
TiO_2/Pt (1% wt.)/Cu^{2+}-Doped (2% wt.)	450 W Hg lamp 278 mW cm^{-2} (λ > 350nm) under argon	1.36	-	3.3	-	(PAI et al., 2016)

TiO_2/Cu–Pt (0.08 mol%)	522 mW cm^{-2} under argon	1.36	-	2.6	-	(JUNG et al., 2016)
TiO_2/rGO (3% wt.)/Pt (3.8% wt.)	450 W Hg lamp and LED 230 W	0.14 (Crude glycerol)	-	71 (glycerin) 13 (crude glycerol)	CO_2 (3.41%) CO (14.28%) CH_4 (0.89%) C_2H_6 (0.15%) H_2 (81.27%)	(RIBAO et al., 2019)
TiO_2/CuO_x (1% wt.)	30W LED ($\lambda \cong$ 380 nm) Under argon	0.06	9%	0.55	Glyceraldehyde (24%) lactic acid (23%) glycolaldehyde (32%), ethyleneglycol (21%)	(KOZLOVA et al., 2021)
TiO_2 /Cu^{2+} Nanodot-Doped (1% wt.)	300 W Xe arc 100 mW cm^{-2} (λ > 350nm) under argon	0.68	-	0.17	-	(ZHANG, M. et al., 2016)
TiO_2/Cu_2O (2% wt.)	400W metal halide lamp under argon	0.68	-	0.07	-	(SEGOVIA-GUZMÁN et al., 2020)
TiO_2-/N/Cu (0.025 mol%)	Hg lamp 450 W under argon	1.36	-	1.62	-	(TAYLOR; MEHTA; SAMOKHVALOV, 2014)
TiO_2/Ag_2O	300 W Xe arc 120 mW cm^{-2} (λ > 350nm) under argon	0.95	-	0.18	-	(YANG, Z. et al., 2020)
TiO_2/Au (1.5% wt.)	UV lamp 6.5 mW cm^{-2} ($\lambda \cong$ 365nm) under nitrogen	1.36	-	32	-	(DEAS et al., 2020)
TiO_2/N/Co (0.025 mol%)	Hg lamp 450 W under argon	1.36	-	0.31	-	(TAYLOR; MEHTA; SAMOKHVALOV, 2014)
TiO_2-/N/Cr (0.025 mol%)	Hg lamp 450 W under argon	1.36	-	0.12	-	(TAYLOR; MEHTA; SAMOKHVALOV, 2014)
TiO_2/N/Ni (0.025 mol%)	Hg lamp 450 W under argon	1.36	-	0.51	-	(TAYLOR; MEHTA; SAMOKHVALOV, 2014)
TiO_2/Mesoporous	UV lamp 116 mW cm^{-2} under argon	1.36	-	5.8	-	(ESCAMILLA et

Carbon (40% wt.)						al., 2020)
TiO_2/Rh (1% wt.)	300 W Xe arc 350 W m^{-2} under argon	2.00×10^{-4}	33%	1.3	Formate (61%) dihydroxyacetone (26%) Glyceraldehyde (13%)	(SANWALD et al., 2016)
Bi_2WO_6 /Pt (1% wt.)	300 W Xe arc 120 mW cm^{-2} (λ > 380nm) under argon	0.68	80%	0.72	formate (99%)	(MARINHO et al., 2022b)
Bi_2WO_6/Pt (1% wt.)	150 W Xe arc 110 mW cm^{-2} (λ > 320 nm)	0.275	-	-	dihydroxyacetone (-)	(DITTMER et al., 2016)
Bi_2WO_6/MoOx/Pt	150 W Xe arc 110 mW cm^{-2} (λ > 320 nm)	0.275	-	-	dihydroxyacetone (-)	(DITTMER et al., 2016)
BiTiO /Pt (0.2% wt.)	125 W UV lamp ($\lambda \cong$ 360 nm) under argon	5.00×10^{-3}	-	0.08	dihydroxyacetone (50%) Glyceraldehyde (1.2%)	(MUSSO et al., 2023)
Bi_2WO_6/SiO_2 (10% wt.)	300 W Xe arc (λ > 420nm) under oxygen	0.066 mol L^{-1}	40%	-	dihydroxyacetone 94% Glyceraldehyde 6%	(ZHANG, Y. et al., 2014)
WO_3	UV-A 18W lamp 5.60 mW cm^{-2}	1.10×10^{-3}	44%	-	Glyceraldehyde (29%)	(YU et al., 2021)
i_2WO_6 ($AgNO_3$ scavenger for photogenerated electrons)	300 W Xe arc (λ > 420nm) under oxygen	0.066	90%	-	dihydroxyacetone (93%) Glyceraldehyde (7%)	(ZHANG, Y. et al., 2013)
ε-Fe_2O_3	150 W Xe arc 180 mW cm^{-2} λ > 300nm	1.0	-	24	1,3-dihydroxypropanone (-), Hydroxyacetaldehyde (-), hydroxy-2-propanone (-), ethanol (-) and dimethyl-1,4-dioxane (-)	(CARRARO et al., 2014)

Kozlova *et al.* (KOZLOVA et al., 2021) performed a comparison between Pt/TiO_2 and CuO_x/TiO_2 photocatalysts in terms of activity towards hydrogen production from aqueous glycerol solutions under UV illumination. The Pt/TiO_2 photocatalyst has shown greater activity and stability compared to the CuO_x/TiO_2 counterpart. The initial hydrogen evolution rate for Pt/TiO_2 was 2.5 times higher than that observed for the CuO_x/TiO_2 photocatalyst. However, the use of CuO_x/TiO_2 as photocatalyst allowed the obtention of a wider variety of products, which includes glyceraldehyde, lactic acid and

glycolaldehyde. Notably, ethyleneglycol was not detected as a product of glycerol photoreforming in the presence of Pt/TiO_2, but its formation occurred with the use of copper oxide as co-catalyst. The authors discuss that the deactivation of the CuO_x/TiO_2 might be a result of reduction of Cu^{2+} ions to Cu^{1+}. In fact, this would explain the proportionally higher formation of C2 products, as the parallel reduction process within the Cu sites would partially increase the TiO_2 oxidizing strength. Thus, CuO_x/TiO_2 showed efficacy for glycerol oxidation, but the copper co-catalyst was not effective for hydrogen production.

Another aspect to be considered in the glycerol photoreforming is the substrate purity. Ribao and co-workers (RIBAO et al., 2019) have compared the use of crude and synthetic glycerol (glycerin) as sacrificial agents for H_2 production over TiO_2 loaded with rGO and Pt^0. They found that not only the experimental conditions and catalyst composition have direct impact on the H_2 production, but also the degree of impurities in crude glycerol. Under optimum conditions, a H_2 evolution rate of 70.8 mmol h^{-1} g^{-1} was achieved using pure glycerin as electron donor against only 12.7 mmol h^{-1} g^{-1} for crude glycerol. The authors suggest that this could be explained by the presence of impurities competing for adsorption on photocatalyst surface and by the greater turbidity of crude glycerol suspensions, which partially blocks light absorption by the photocatalyst.

Despite being the most studied photocatalyst, TiO_2 offers low selectivity towards oxidation products and a tendency for full mineralization of glycerol and other organic substrates, which is justified by the formation of highly reactive oxygen radicals in aqueous media. In this scenario, different semiconductors with more positive valence band energies and with visible light activity have been studied. Ternary bismuth oxides call particular attention due to their crystalline and electronic structures. For example, Bismuth tungstate (Bi_2WO_6), is a *n*-type semiconductor with Aurivillius structure (MARINHO et al., 2015; ALFAIFI; TAHIR; WIJAYANTHA, 2019) and a narrower band gap (2.70–3.0 eV) (DAS et al., 2021). It is pointed as a promising material for the selective photoreforming of glycerol, due to its ability to promote hole transfer directly to glycerol without the formation of non-selective $^{\bullet}OH$ radicals (SUN et al., 2014; MARINHO et al., 2022b).

Zhang and co-workers (ZHANG, Y. et al., 2013) were the first to report the use of Bi_2WO_6 prepared by hydrothermal treatment as a selective photocatalyst for

dihydroxyacetone formation from glycerol under visible light irradiation. Dihydroxyacetone was generally formed in good yields (80 to 90%) after 5 h of irradiation. The influence of the hydrothermal conditions on the photocatalytic activity of Bi_2WO_6 was initially reported by Zhang and Zhu (ZHANG, C.; ZHU, 2005), employing Bi_2WO_6 nanoplates obtained in different temperatures and reaction times. The different samples were evaluated against rhodamine-B degradation, and it was concluded that larger particles grew at the cost of the smaller ones during the reaction due to the solubility difference between them, as predicted by the Gibbs-Thomson law. Later, Chunxiao Xu and collaborators (JIANG, W. et al., 2019), conducted a thorough mechanistic investigation on the Bi_2WO_6 hydrothermal growth, in which they observed the formation of self-assembled stacked plates, resulting in multi-layered disks. They concluded that the crystal growth process of primary nanoparticles occurs simultaneously with oriented assembly of the as-forming square nanoplates into a 3D disk. The square nanoplates tend to assemble on a multilayer disk preferentially oriented along the (0 0 1) direction, increasing in crystallinity and crystallite size as a function of the reaction time.

Later, our research group (MARINHO et al., 2022a) investigated the influence of pH of the hydrothermal treatment on the performance of Bi_2WO_6 as photocatalyst in the glycerol photoreforming. Samples prepared in an acid medium (pH = 0 and 2) exhibit smaller and less crystalline particles, while those obtained at higher pHs are characterized by a more crystalline orthorhombic structure. At highly alkaline reaction medium (pH > 13), the formation of a cubic non-stoichiometric crystalline phase is observed and identified as $Bi_{3.84}W_{0.16}O_{6.24}$. In-depth structural information was obtained through Rietveld refinement of the XRD data.

The Bi_2WO_6 sample prepared at pH = 0 exhibited the highest photonic efficiency for H_2 evolution from glycerol aqueous solutions (ξ = 1.4 ± 0.1%) among the samples investigated, showing 99% C-based selectivity for formic acid and 80% of total glycerol conversion. Such performance is followed by the $Bi_{3.84}W_{0.16}O_{6.24}$ sample which also exhibited good results with ξ = 1.2 ± 0.1% for H_2 evolution, 87% of selectivity for formic acid production and 63% of total glycerol conversion. The results indicate that the selectivity of Bi_2WO_6 in glycerol photoreforming is very dependent on its structural/morphologic parameters. The presence of oxygen vacancies in the samples prepared in acidic conditions as well as the Bi(III)-rich phase obtained at pH = 13 favor

the strong adsorption of glycerol and the first reaction intermediates, increasing both the overall glycerol conversion and the selectivity for C1 products.

Dittmer and et al. (DITTMER et al., 2016) have modified Bi_2WO_6 with MoO_x, deposited via chemical vapor deposition and investigated the photocatalytic activity of these materials for oxygen evolution and selective glycerol oxidation to dihydroxyacetone. The authors could show that for both pristine and MoO_x-modified Bi_2WO_6, the covering with Pt^0 greatly improved dihydroxyacetone yield. The authors concluded that MoO_x modification is beneficial for the photochemical process as it promotes more efficient charge separation following band gap excitation.

Another oxide employed in glycerol photoreforming is Fe_2O_3, which is characterized by an improved visible light absorption. Carraro and co-workers (CARRARO et al., 2014) investigated two iron (III) oxide polymorphs, β and ε-Fe_2O_3, which have shown good activity towards light-driven H_2 production from glycerol aqueous solutions (1 mol L^{-1}). For ε-Fe_2O_3 and β-Fe_2O_3, H_2 production rates equivalent to 24.5 and 8.9 mmol h^{-1} g^{-1} were obtained, with significantly higher performances compared to the commonly used α-Fe_2O_3. The major oxidation products of glycerol were 1,3-dihydroxypropanone, hydroxyacetaldehyde, 1-hydroxy-2-propanone, ethanol and dimethyl-1,4-dioxane. These promising results evidence that H_2 evolution can be efficiently induced even by low-energy photons, as the reported band gap of Fe_2O_3-based materials lies within 2.2–2.4 eV.

In glycerol photoreforming, the adsorption/desorption mechanisms are determinant for the improvement of both the conversion efficiency and product selectivity. The strong adsorption of reaction intermediates on Bi_2WO_6 surface led to nearly 100% of selectivity to formic acid. This condition is found on more acidic media that favor the adsorption when compared to more alkaline conditions (MARINHO et al., 2022a; NASCIMENTO, LUCAS L. et al., 2022). Sanwald et. al,. (SANWALD et al., 2016) found that, when using TiO_2 as photocatalyst, formaldehyde was the main C1 glycerol oxidation product instead of formic acid due to its comparatively low adsorption constant on TiO_2. As a result, most of the formic acid produced would get mineralized into CO_2 and H_2. The authors proposed that glycerol photoreforming occurs mainly through two different pathways on oxide surfaces: direct oxidative C-C cleavage of glycerol yielding glycolaldehyde and formaldehyde (pathway A, **Figure 3**), which is the preferred pathway for the aerobic glycerol conversion; and the formation of carbonyl groups as a result of a single-step 2 electron oxidation of a glycerol

hydroxyl group to yield glyceraldehyde or dihydroxyacetone (pathway B). The glyceraldehyde can be further converted into formic acid and glycolaldehyde, while dihydroxyacetone results in the formation of formaldehyde as the main final product. In aerobic conditions, these pathways are minoritarian due to the regioselectivity of the hydroxyl groups. On top of that, it is hard to achieve high selectivity towards dihydroxyacetone and glyceraldehyde formation, the most valuable glycerol products, even at anaerobic conditions due to the tendency to produce C-C cleavage products from the subsequent direct hole transfer at the photocatalyst surface. Moreover, light-driven dehydration of glycerol (pathway C) is a possible side reaction.

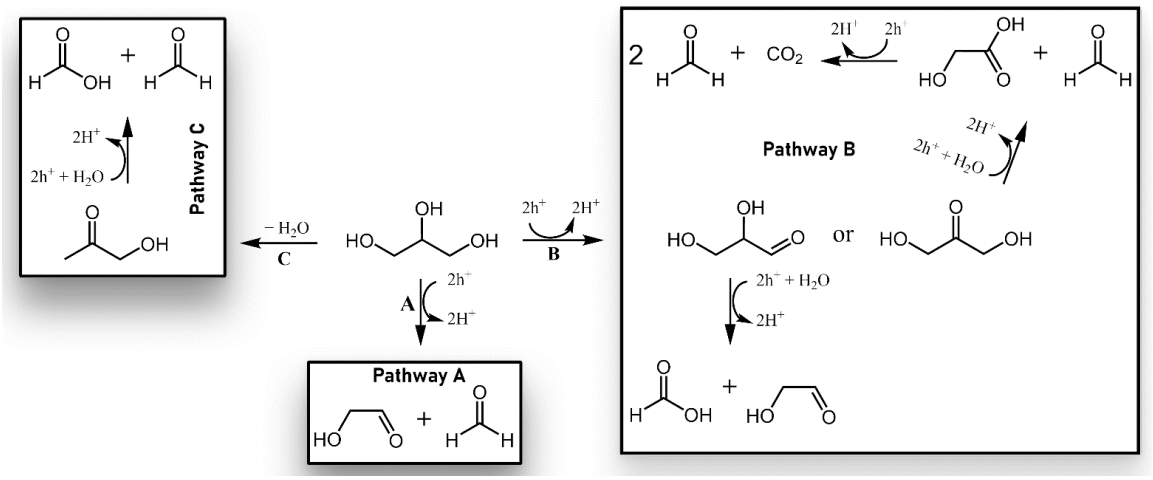

Figure 3. Possible reaction pathways for photoreforming of glycerol: direct oxidative C–C-cleavage to form glycolaldehyde and formaldehyde (A) occurs primarily over formation of carbonyl groups to produce glyceraldehyde or dihydroxyacetone (B). Light-driven dehydration to hydroxyacetone (C) constitutes a side reaction. Adapted from (SANWALD et al., 2016).

Other substrates despite glycerol have also been employed on photoreforming studies. For saccharides and polysaccharides, TiO_2 is still the most investigated oxide and therefore, few information on the oxidation products is found in the literature. Nevertheless, enhanced H_2 evolution rates have been reported, Table 2. Lervolino and co-workers (IERVOLINO et al., 2016) reported a facile calcination method to obtain TiO_2 anatase modified with fluorine and covered with 0.5 wt% Pt^0 resulting in a material referred as Pt-F-TiO_2. The photocatalyst was able to remove 74% glucose in an aqueous suspension (1.5 mg_{cat} mL^{-1}) with significant H_2 production after just 3 hours of UV irradiation. The glucose degradation was mainly attributed to hydroxyl

radical formation from water at the Pt-F-TiO_2 surface. As a result, only H_2 and CO_2 were detected as reaction products and, intriguingly, by varying the pH of the suspension, a higher H_2 production rate was obtained at the pH where glucose degradation was lower (pH=6), which indicates that glucose is not being fully mineralized as suggested by the authors.

Table 2 Key examples of photoreforming of biomass-derived (poly)saccharides.

Photocatalyst	**Irradiation conditions**	**Suspension composition**	**H_2 evolution rate / μmol g^{-1} h^{-1}**	**Ref**
TiO_2/Pt-F	10W UV-LED	Aqueous glucose at pH = 2	2500	(IERVOLINO et al., 2016)
TiO_2/Pd	400W Xe arc	Different saccharides aqueous suspensions	900	(KENNEDY et al., 2018)
TiO_2/Pt	Natural sunlight	Water cellulose suspension	58.93	(SPELTINI et al., 2014)
TiO_2/Pt	Natural sunlight	Water rice husk suspension	28.57	(SPELTINI et al., 2014)
TiO_2/Pt	300W Xe arc 1.3×10^{-6} Einsteins s^{-1}	Different saccharides aqueous suspensions	502.5	(KONDARIDES; PATSOURA; VERYKIOS, 2010)
Bi_2WO_6 /Pt	300 W Xe arc 100 mW cm^{-2} (AM 1.5 G)	Aqueous glucose	45000	(MADRIZ et al., 2020)
Cu_2O	300 W Xe arc (λ > 420nm)	Aqueous glucose	19	(ZHANG, L. et al., 2014)
Cu_2O/Cu- palygorskite	300 W Xe arc 100 mW cm^{-2} (AM 1.5 G)	Aqueous cellulose	32000	(ZHONG, M. et al., 2022)
CdS/Au (nanorods)	300 W Xe arc (λ > 400nm)	Aqueous glucose	90	(WANG, X. et al., 2020)
Fe_2O_3	300 W Xe arc 100 mW cm^{-2} (AM 1.5G)	LPMO enzyme-catalyzed cellulose oxidative degradation in water	–	(WANG, D. et al., 2022)

Similarly, Kennedy et. al. (KENNEDY et al., 2018) reported the complete dehydrogenation and decarbonylation of a series of sugars and polyols using Pd-loaded TiO_2 P25 (0.5 wt%). The authors correlate the H_2 production with the number of hydroxyl groups available at each studied polyol, which follows a linear increasing trend, however, the number of hydroxyl groups had no effect at the H_2 production from sugars. These results further corroborate that hydrogen production from polysaccharides photoreforming is limited by kinetics rather than by thermodynamics.

In biomass photoreforming, light is not necessarily directly stored as H_2 but it drives the kinetics of degradation and, consequently, the conversion of the energy content within the biomass-derived compound into H_2. Moreover, it is essential to build photocatalytic materials that able to harvest visible light to enable the practical solar-driven biomass reforming. However, there are still fewer studies showing promising results using photocatalysts with the band gap energy in the visible region. Zhang et al. (ZHANG, L. et al., 2014) described the photocatalytic reforming of glucose under visible light over Cu_2O, reaching 113 μmol g^{-1} H_2 production over 6 hours of reaction ($\lambda > 420$ nm). These results are encouraging, especially if the low surface area of the Cu_2O photocatalyst (< 8 m^2 g^{-1}) and the visible-only irradiation is taken into consideration. Moreover, Chen's group reported visible-light photocatalytic H_2 evolution from aqueous glucose on Au/CdS nanorods with simultaneous Au^{3+} self-reduction (WANG, X. et al., 2020). Only H_2 and CO_2 were detected as glucose reforming products and continuous H_2 production is reported for up to 17 hours. Moreover, the authors found that the Au loading was key for the H_2 evolution.

So far, during the last few years, great advances have been achieved in the preparation of photocatalysts, starting with TiO_2 up to ternary bismuth oxides, with new insights on structure-activity relationship being obtained. This is essential for further development of better photocatalysts and optimization of the experimental parameters for improved activity/selectivity control. It can be concluded that the development of advanced materials is not the only bottleneck holding the practical glycerol and (poly)saccharides photoreforming. The optimization of the physicochemical parameters, elucidation and modulation of adsorption/desorption equilibria, the amount and composition of the impurities that might be present in suspension, as well as a deeper kinetic understanding of the process are essential to guide future research on biomass valorization. Clearly, the use of different semiconductors, especially,

ternary oxides has contributed to the increase of the oxidation product selectivity, despite the hydrogen evolution rates were not as high as those observed for TiO_2-based systems under similar reaction conditions. In fact, although heterogeneous photocatalysis can be efficiently used for biomass reforming, it offers sluggish conversion kinetics when compared to other catalytic approaches.

The electrochemical approach, for example, has been described as an alternative for selective glycerol oxidation with concomitant H_2 generation at relevant rates since 80s (HORANYI; RIZMAYER, 1983; KAHYAOGLU; BEDEN; LAMY, 1984; KIMURA et al., 1993). Typically, Au or Pt-based electrodes are employed as anodes. A relevant work by Kim et al. (KIM, H. J. et al., 2017) have reported a detailed techno-economical study of glycerol oxidation into glyceraldehyde, glyceric acid, and hydroxypyruvic acid employing metallic Pt/C electrodes. Overall, favorable kinetics at moderate potentials are observed; however, the use of precious metals still hinds the large-scale application of such systems.

To overcome the kinetic limitation offered by photocatalysis while taking advantage of the improved conversion rates of the electrocatalysis, photoelectrochemical oxidation of abundant organics or biomass feedstocks (e.g. glycerol) has been intensively studied as an emerging field with enormous potential for the sustainable production of hydrogen and value-added chemicals (WU, Y.-H. et al., 2021; BHATTACHARJEE et al., 2022). The use of abundant semiconductor electrodes in photoelectrochemical devices along with suitable organic substrates as electron donors allows for reducing considerably the system overpotentials, paving the way towards solar driven fuel production (WU, Y.-H. et al., 2021). In a standard PEC system, Figure 4, photoexcitation of the photoanode yields electron/hole pairs at the electrode surface, so organic species at the electrolyte can react with the holes at the semiconductor/electrolyte interface, while electrons are directed through the external circuit to the counterelectrode, where it can promptly react with H^+ yielding H_2. In this way, the main bottleneck of photocatalysis, i.e., the rapid recombination of charge carriers, is mitigated by a small external bias, which provides the driving force to separate the charge carriers, assuring that the desired reactions can occur efficiently by drastically increasing the hole consumption rate at the photocatalyst surface. In fact, many works have reported that electron recombination can be fully suppressed by the use of biomass-derived molecules, such as glycerol and glucose, as sacrificial agents (HUANG; VO; CHIANG, 2019; MADRIZ et al., 2020).

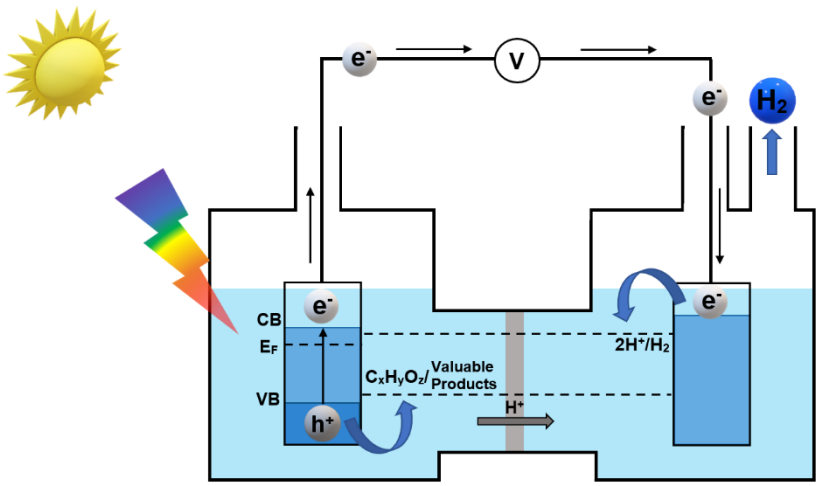

Figure 4. Working principle of a photoelectrochemical cell (PEC) for biomass reforming.

$BiVO_4$ has been largely investigated in PECs for water splitting (FANG; LIU; HAN, 2020; CHEN, D. et al., 2022; QI et al., 2022; KE et al., 2023) and it is also a very promising material for selective glycerol photoreforming. The ternary oxide has a band gap of ~2.4 eV and therefore exhibits visible light photoactivity, which makes its theoretical Solar-to-Hydrogen efficiency (STH) far superior than semiconductor oxides active only in the UV (KIM, J. H. et al., 2019). However, $BiVO_4$ is highly susceptible to photocorrosion, with dissolution of Bi^{3+} and VO_4^{3-} from the crystal lattice under illumination (KE et al., 2023). This limits the stability of PECs for water splitting but is less pronounced on photoelectroreforming as the applied potentials are much smaller.

Liu and coworkers (LIU, D. et al., 2019) have reported the selective conversion of glycerol to dihydroxyacetone and formic acid by photoanodes composed by $BiVO_4$ nanoarrays. The influence of the pH and the applied bias on product selectivity have been investigated. In acidic conditions (pH =2) and relative high potentials (0.6 to 1.2 V vs. RHE), selectivity towards dihydroxyacetone (DHA) is greatly improved as glycerol adsorption is stronger at lower pHs. On the other hand, at lower potentials and in neutral to alkaline pH range, the formation of formic acid is favoured. The reaction mechanism of glycerol oxidation by $BiVO_4$ photoanodes was also studied using an isotope labelled electrolyte (10% $H_2{}^{18}O$). The ^{18}O from the electrolyte was found in both dihydroxyacetone and glyceraldehyde during the product analysis, indicating that the adsorbed glycerol undergoes one electron oxidation by the photogenerated holes followed by a reaction with water and subsequent dehydration,

Figure 5. ESR studies did not find any hydroxyl radicals from water in the presence of glycerol, further corroborating with the proposed reaction between glycerol and holes, which is essential for good product selectivity. Representative examples for photoelectrochemical reforming of glycerol are summarized in Table 3.

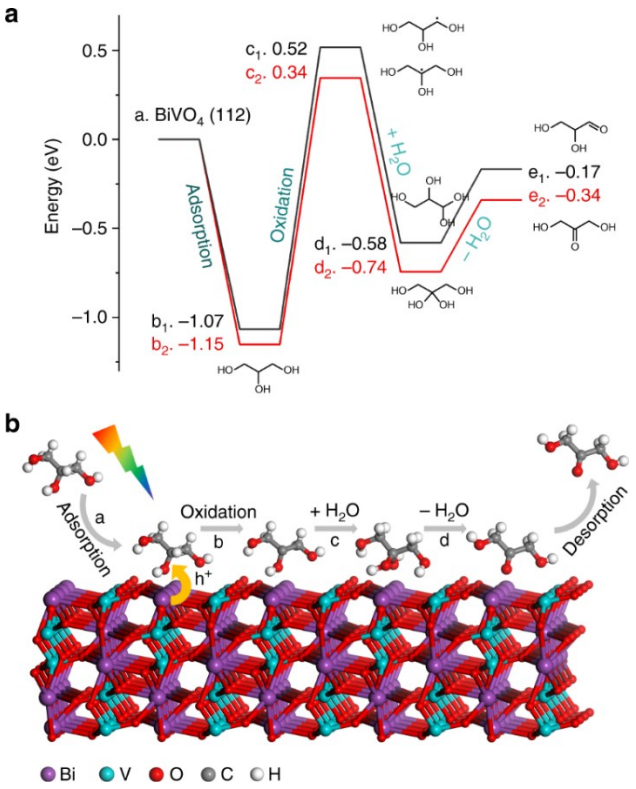

Figure 5. Glycerol photoelectroreforming mechanism on $BiVO_4$ photoanodes. **a** Energy profile of glycerol oxidation on $BiVO_4$ surface. 1 (black) and 2 (red) stand for reactions that take place at the terminal and middle carbon, respectively. **b** Schematic illustration showing glycerol oxidation to dihydroxyacetone on $BiVO_4$ surface. Adapted from (LIU, D. et al., 2019).

Wu and co-workers (WU, Y.-H. et al., 2021) have developed tungsten-doped bismuth vanadate (W:$BiVO_4$) electrodes combined with an atomic-layer-deposited nickel (oxy)hydroxide $NiO_x(OH)_y$ co-catalyst, as a photoanode material for the photoelectrochemical oxidation of glycerol. They have found that the insertion of $NiO_x(OH)_y$ improved the photocurrent density. The addition of glycerol also enhanced the photocurrent and hole injection efficiency, evidencing the faster kinetics of glycerol oxidation with respect to the oxygen evolution reaction from water. Glyceraldehyde, dihydroxyacetone and glycolaldehyde were the primary oxidation products found

during the long-term photoelectrochemical studies. Moreover, it was verified that the nickel co-catalyst gradually dissolves in alkaline electrolyte, causing a continuous drop in the photocurrent. However, in acidic pH, the current increases despite the dissolution of the co-catalyst layer. The authors have attributed this behaviour to a positive effect on the reaction kinetics due to the acidification of the medium, which contradicts the conclusions taken by Liu et al. (LIU, D. et al., 2019). Additionally, the authors also found that, at lower pHs and applied potentials, the selectivity for formic acid was favoured, while DHA production was boosted at higher applied potentials and higher pHs.

Table 3 Photoelectrochemical reforming of glycerol.

Material	Irradiation conditions	Electrolyte composition	Applied Bias	Main Products (Selectivity)	H_2 evolution rate	Ref.
$BiVO_4$	300 W Xe arc 100 mW cm^{-2} (AM 1.5G)	0.1 mol L^{-1} glycerol in 0.5 mol L^{-1} Na_2SO_4 (pH = 2)	0.6 V vs RHE	DHA (51%)	-	(LIU, D. et al., 2019)
Bi_2WO_6	300 W Xe arc 120 mW cm^{-2} (λ > 380 nm)	1.26 mol L^{-1} glycerol in 0.1 mol L^{-1} K_2SO_4 (pH = 8)	1.3 V vs RHE	Formate (88%)	110 mmol h^{-1} m^{-2}	(NASCIMENTO, LUCAS L. et al., 2022)
W:$BiVO_4$/ $NiO_x(OH)_y$	300 W Xe arc 100 mW cm^{-2} (AM 1.5G)	0.1 mol L^{-1} glycerol in 0.5 mol L^{-1} Na_2SO_4	1.2 V vs RHE	Formate (~50%) DHA (20%)	-	(WU, Y.-H. et al., 2021)
Mo/$BiVO_4$	300 W Xe arc 100 mW cm^{-2} (AM 1.5G)	10% glycerol in 0.1 mol L^{-1} phosphate buffer (pH = 7)	1.2 V vs RHE	–-	0.431 mmol L^{-1} h^{-1} (STH 5.5%)	(BORA et al., 2022)
Fe_2O_3	300 W Xe arc 100 mW cm^{-2} (AM 1.5G)	0.1 mol L^{-1} glycerol in 0.1 mol L^{-1} KOH (pH = 13)	1.0 V vs RHE	Glycerate (-) lactate (-) formate (-) glycolate (-)	-	(PERINI et al., 2021)
WO_3	UV lamp 41 mW cm^{-2}	0.1 mol L^{-1} glycerol	1.2 V vs Pt/C	GAD (26%), DHA (12%) formate (2%)	44.0 mmol h^{-1} m^{-2}	(YU et al., 2023)

GAD: glyceraldehyde; DHA: dihydroxyacetone; RHE: reversible hydrogen electrode; STH: solar-to-hydrogen efficiency.

More recently, our group have reported the application of Bi_2WO_6 photoanodes for the selective conversion of aqueous glycerin (NASCIMENTO, LUCAS L. et al., 2022). The photoelectrochemical behavior was investigated as a function of the electrolyte pH. At pH 6, H_2 production rate was 19.6 μmol cm^{-2} h^{-1} with formic acid as main oxidation product (41% selectivity). In acid media, this selectivity increases to 88%, similarly to that reported by Wu (WU, Y.-H. et al., 2021), but the photocurrent decreases by 50%. In alkaline electrolyte, glycerol oxidation is facilitated and photocurrents up to 0.80 mA cm^{-2} are reached at the cost of poor product selectivity. Furthermore, EIS studies showed that the addition of glycerol greatly reduces charge transfer resistance at the photocatalyst/electrolyte interface, especially in alkaline media. The low selectivity observed in alkaline media was attributed to poor glycerol adsorption on the Bi_2WO_6 surface, while at acidic pH glycerol is strongly adsorbed, suffering multiple oxidation steps, hindering the photocurrent but greatly increasing product selectivity towards formic acid.

Yu et al. (YU et al., 2023) reported a 2-eletrode flow-through PEC device for simultaneous H_2 production and glycerol conversion into C3 products at near-neutral pH. Carbon cloth-supported Pt and WO_3 were used as the counter/reference electrode and photoanode, respectively. The photoanode was front-side illuminated through a quartz window by UV light irradiation at 41 mW cm^{-2}. The PEC device was kept at 60 ºC and the influence of external bias on the oxidation products was investigated. Similar glycerol conversions of 4.2 to 4.7% were reached under applied potential ranging from 0.3 V to 1.2 V, after 6 hours of experiment. However, the selectivity of glyceraldehyde (GAD) and dihydroxyacetone production increased from 15.2% at 0.3 V to 38.3% at 1.2 V. Formic acid production was also significantly increased at 1.2 V. Despite the relative low glycerol conversion (< 5%), good selectivity for C3 products and H_2 evolution was achieved under optimum conditions, with 26% of glyceraldehyde selectivity, 12% of dihydroxyacetone selectivity and a H_2 evolution of 44.0 mmol m^{-2} h^{-1}.

1.3. Novel materials for photocatalysis

While inorganic semicondutors (metal oxides, chalcogenides, II-Vs) are the largely employed materials in photo(electro)catalysis, many advancements have been made for the development of innovative materials for photocatalysis. One promising approach that can be employed is the introduction of oxygen vacancies and other structural defects into existing semiconducting materials through specific synthetic routes. Significant advances have been made in this area in recent years. Huo and collaborators have shown that the absorption spectrum of Bi_2WO_6 can be easily shifted into the visible range by inducing oxygen vacancies in the material's structure (HUO et al., 2019). Oxygen vacancies create intermediate states that act as electron traps, increasing the charge carrier lifetime and reducing the band gap energy of the resulting material. This can be achieved by manipulating the conditions of hydrothermal or solvothermal synthesis. When using solvents with lower oxygen availability, such as ethylene glycol, and milder synthesis temperatures, the material grows with a slower oxygen transfer rate into the crystal lattice. As a result, a material with oxygen vacancies and unique photophysical, morphological, and structural properties is obtained (CHEN, H. et al., 2019; HUO et al., 2019; WANG, T. et al., 2021).

An alternative strategy involves doping the material of interest, which leads to modifications in its structural properties and shifts in the conduction and/or valence band energies. Doping can be p-type, when an electron-deficient species is introduced into the material, or n-type, involving the incorporation of an electron-rich species into the crystal lattice. In both cases, doping creates intermediate energy levels (midgap states) within the valence band (p-type) or conduction band (n-type) of the photocatalyst, which can trap photogenerated charges and reduce the band gap energy of the material. Therefore, it is possible to tailor the properties of the material based on the type of dopant introduced, or even by varying the dopant content.

A class of materials that has recently attracted attention and employs both of the aforementioned synthetic strategies is that of oxynitrides (NISHIMURA et al., 2010; BRANCHO et al., 2017). These compounds are known for a larger unit cell volume and improved conductivity compared to conventional oxides. The synthesis of oxynitrides generally starts with the formation of the corresponding nitride, which can then be partially oxidized, via calcination, for example, to produce the desired metal oxynitride. The nitride synthesis step is the most challenging one, as it typically

involves high pressures of N_2, N_2/H_2, or even NH_3, in temperatures between 400 and 1000 °C. The result is a substitution of oxygen by nitrogen in the crystal lattice, which usually requires the addition of a second metal to stabilize the material's charge, yielding a compound similar to those of ternary oxides, often adopting a perovskite-type structure. Alternative nitrogen sources have been successfully employed to simplify the nitride synthesis step. Brancho and co-workers have reported the synthesis of titanium and niobium oxynitrides using urea as a nitrogen source, resulting in materials with visible light absorption and promising photocatalytic properties (BRANCHO et al., 2017).

Another promising category of compounds are the Covalent Organic Frameworks (COFs) as they have garnered significant attention as promising photocatalysts, in special for H_2 evolution, owing to their crystalline porous structure, high chemical stability, and virtually limitless tunability in terms of both structure and optoelectronic properties (CARMO et al., 2023) (CÔTÉ et al., 2005; CARMO et al., 2023). In 2014, B. Lotsch et al. reported the first water-stable hydrazine-based COF for the hydrogen evolution reaction (HER), achieving a reaction rate of 1979.0 μmol g^{-1} h^{-1} (STEGBAUER; SCHWINGHAMMER; LOTSCH, 2014). Subsequent studies have focused on the molecular engineering of COFs to enhance their photocatalytic H_2 evolution efficiency by optimizing light-harvesting capabilities, charge-carrier separation, thermodynamic driving force, water dispersibility, and photostability (LI, X. et al., 2018; STEGBAUER et al., 2018; ZHANG, G. et al., 2018; GHOSH, S. et al., 2020; SONG et al., 2021; KARAK; DEY; BANERJEE, 2022; SHI et al., 2022; XIAO, Y. et al., 2024).

Likewise, many synthetic strategies can be employed to improve COFs photoactivity. Linkage chemistry has proven to be an effective tool for tailoring the physicochemical properties of COFs for photocatalytic applications. Liu et al. demonstrated that fully π-conjugated sp^2 carbon linkages not only broaden the visible-light absorption of COFs but also enhance charge transfer and separation efficiency, compared to imine linkages (LI, Z. et al., 2023). Recently, Thomas et al. showed that protonation of a series of imine-linked donor-acceptor COFs enhances photocatalytic H_2 evolution performance, which was attributed to improved light absorption, charge carrier separation efficiency, and hydrophilicity of the COFs upon protonation (YANG, J. et al., 2021). In a further study, Pan and co-workers investigated the effect of linkage isomerism on photocatalytic hydrogen evolution

(ZHANG, M. et al., 2023). While the influence of linkages on optoelectronic properties has been widely explored, leveraging COF linkage chemistry to modulate interfacial chemical and electrostatic interactions between COFs and reactants for improved photocatalytic H_2 evolution has yet to be reported.

Typical reactants in the photocatalytic H_2 evolution reaction include charged precursors for co-catalyst deposition, such as H_2PtCl_6, and sacrificial electron donors, which often also serve as proton sources (WANG, Y. et al., 2019; COSTANTINO; KAMAT, 2022). Tuning the surface charge to promote the preferential adsorption of specific compounds at the photocatalyst surface, thereby controlling the photocatalytic reaction mechanism, is a well-established strategy in traditional inorganic photocatalysis (HOFFMANN et al., 1995). This method relies on modulating the electrostatic interactions between the adsorbate and the adsorbent, either by altering the chemical environment or by tailoring the surface charge of the photocatalyst. However, systematic studies on this approach applied to COFs remain rare.

Overall, the development of novel photocatalytic materials has witnessed remarkable progress in recent years, driven by the pursuit of efficient, sustainable strategies for solar-driven chemical transformations. From engineering oxygen vacancies and doping semiconductors to designing oxynitrides and covalent organic frameworks with tailored optoelectronic and surface properties, researchers have expanded the landscape of photocatalysts far beyond conventional oxide materials. Continued efforts in integrating synthetic innovation with fundamental mechanistic understanding are expected to unlock further breakthroughs, enabling practical solar-fuel technologies.

In this thesis, we have explored different strategies and materials for low carbon hydrogen production through reforming reaction of organic substrates. In the second chapter, the engineering of oxygen vacancies in Bi_2WO_6 nanoparticles is exploited aiming at photoelectrochemical reforming of biomass-derivatives. In the third chapter, Nb(V) doping of $BiVO_4$ is proposed as an effective strategy to improve both the photoelectrochemical performance and stability of photoanodes for glycerol reforming. In the fourth and fifth chapters, novel photocatalysts for H_2 evolution are introduced based on COFs (chapter 4) and Ni^{2+}-doped oxides and oxynitrides (chapter 5).

1.4. Main Objective

The main objective of this work was to develop state-of-the-art visible light active photocatalysts and photoanodes for the photo(electro)reforming of organic substrates for low carbon H_2 production. For that, different strategies were explored using ternary oxides, oxynitrides and covalent organic frameworks as well as standard sacrificial electron donors and real industrial waste streams. Each system was deeply investigated employing structural and optoelectronic techniques aiming at the rationalization of the photo(electro)chemical properties.

2. Unveiling The Role of Oxygen Vacancies in the Charge Dynamics of Bi_2WO_6-Based Photoanodes for Photoelectrochemical Glycerol Reforming

In a previous study we have evaluated the influence of pH variation during the hydrothermal treatment on the performance of Bi_2WO_6 as photocatalyst in the glycerol photoreforming (NASCIMENTO, LUCAS L. et al., 2022). It was found that the material obtained in pH = 0 had the best performance, both in terms of glycerol conversion and hydrogen evolution, which was attributed to a balance between crystallinity and structural defects like oxygen vacancies. Then photoanodes were made using the best performing material (pH 0), which again displayed excellent performance for the selective photoelectroreforming of glycerol to formic acid and concomitant hydrogen evolution (NASCIMENTO, LUCAS L. et al., 2022). However, the main drawback of Bi_2WO_6 is that its light absorption is limited to the UV region.

Based on the forementioned results, Bi_2WO_6 with engineered oxygen vacancies were prepared aiming at enhancing the photoactivity of the material and shifting the absorption spectrum to the visible region, thus enhancing the sunlight absorption capabilities of the material. Oxygen deficient Bi_2WO_6 ($BiWO_{vac}$) was obtained through a simple solvothermal synthesis. This strategy revolves around replacing water with ethylene glycol to reduce the oxygen availability in the reaction media, so the oxygen transfer kinects to the lattice of the material is severely slowed, resulting in oxygen vacancy rich samples.

2.1. Specific Objectives

The specific objectives for the work showed this chapter were:

- Synthetize Bi_2WO_6 with induced engineered oxygen vacancies
- Perform simulations to pinpoint the optimal sites for the oxygen vacancies
- Investigate the effect of oxygen vacancies on the charge dynamics of Bi_2WO_6 photoanodes in glycerol phoelectroreforming by performing *in situ operando* TA studies in the ps-ns and us-s timescale
- Test the performance of the $BiWO_{(vac)}$ photoanodes compares to Bi_2WO_6 for the photoelectroreforming of glycerol

2.2. Methodology

All chemicals were bought from Aldrich. The Bi_2WO_6 powder samples were synthesized by an ease hydrothermal method as described elsewhere (MARINHO et al., 2022a). In summary, $Bi(NO_3)_3{\cdot}5H_2O$ and $Na_2WO_4{\cdot}2H_2O$ precursors were dissolved in nitric acid (1.0 mol L^{-1}) and water, respectively, under constant stirring. The resulting mixture (pH = 0) was transferred to a teflon vessel which was inserted in a stainless steel autoclave and kept at 200 °C for 3 h. The oxygen vacancy induced samples $BiWO_{(vac)}$ were obtained with a solvothermal synthesis, as previously described.(WANG, T. et al., 2021) Briefly, $Bi(NO_3)_3{\cdot}5H_2O$ and $Na_2WO_4{\cdot}2H_2O$ precursors were dissolved in ethyleneglycol and kept at 200 ºC for 24 hours. After cooling at room temperature, the powder samples were washed and subsequently dried at 80 °C.

The Bi_2WO_6-based photoanodes were deposited on clean FTO substrates using the screen-printing method. The paste for screen printing was prepared following the methodology previously described elsewhere (GÜNNEMANN et al., 2019). In summary, 3 g of photocatalyst powder were meticulously ground within a mortar that contained 15 mL of ethanol, 2.5 mL of water, and 0.5 mL of acetic acid, subsequently transferring the resultant mixture to a round-bottom flask with the subsequent incorporation of 50 mL of ethanol, 10 g of terpineol, and 15 g of a 10% wt/v ethyl cellulose solution in ethanol. The composite was subjected to sonication and stirring until the components were thoroughly homogenized. Ultimately, the solvent was eliminated utilizing a rotary evaporator. The resultant pristine Bi_2WO_6 films underwent annealing at 500 ºC for a duration of 30 minutes and the $BiWO_{(Vac)}$ films were annealed at 300 ºC using a 10 ºC min ramp.

X-ray diffraction analysis (XRD) was executed utilizing an XRD600 powder diffractometer (Shimadzu) functioning at 40 kV and 30 mA with Cu Kα radiation as the excitation source. Raman spectroscopy was carried out on a LabRAM HR Evolution spectrometer (Horiba). X-ray photoelectron spectroscopy (XPS) measurements were conducted using a Thermo Scientific model K-Alpha spectrometer, which is equipped with an Al Kα X-ray source. All spectra underwent calibration against the C 1s peak, considering a standard binding energy of 284.6 eV. The morphologies of the films were assessed through Scanning Electron Microscopy (SEM) employing a TESCAN Vega3 microscope. Diffuse Reflectance Spectra (DRS) were collected using a UV 2600

spectrophotometer (Shimadzu) that is equipped with an integrating sphere. The transmittance values were converted to absorption equivalent values using the Kulbelka-munk function.(PATTERSON; SHELDEN; STOCKTON, 1977; YANG, L.; KRUSE, 2004) The electrochemical characterization was accomplished on an Autolab PGSTAT204 (Metrohm) potentiostat/galvanostat containing a FRA32M module for Electrochemical Impedance Spectroscopy (EIS) measurements. A 300 W Xe arc lamp (Oriel) equipped with an AM 1.5G filter was used as light source, whose intensity was estimated using a power meter 1916-R (Newport) with an optical sensor 818-UV/DB.

The oxygen vacancies in Bi_2WO_6 were investigated through first-principles calculations using the Quantum ESPRESSO software package (AHMAD, H. et al., 2021; HOSSAIN et al., 2023). The orthorhombic unit cell of Bi_2WO_6, consisting of 36 atoms, 8 bismuth (Bi), 4 tungsten (W), and 24 oxygen (O) atoms was used as the structural model. A plane-wave basis set was employed with an energy cutoff of 380 eV to expand the electronic wavefunctions. Brillouin zone sampling was performed using a 6 × 6 × 2 Monkhorst-Pack k-point mesh. The generalized gradient approximation (GGA) with the Perdew-Burke-Ernzerhof (PBE) exchange-correlation functional was used to describe electron interactions. Additionally, Hubbard U corrections (GGA+U) were applied to the W 5d and O 2p orbitals to account for the on-site Coulomb interactions and improve the description of electron localization around the vacancy sites.

A custom-made PTFE photoelectrochemical cell with H geometry was used for the (photo)electrochemical assays, **Figure 6**. The electrolyte was 0.1 M K_2SO_4 with added crude glycerol. A platinum coil was used as counter electrode and Ag/AgCl with 3M NaCl as reference. The backside illumination was done through a 3.8 cm^2 quartz rounded window.

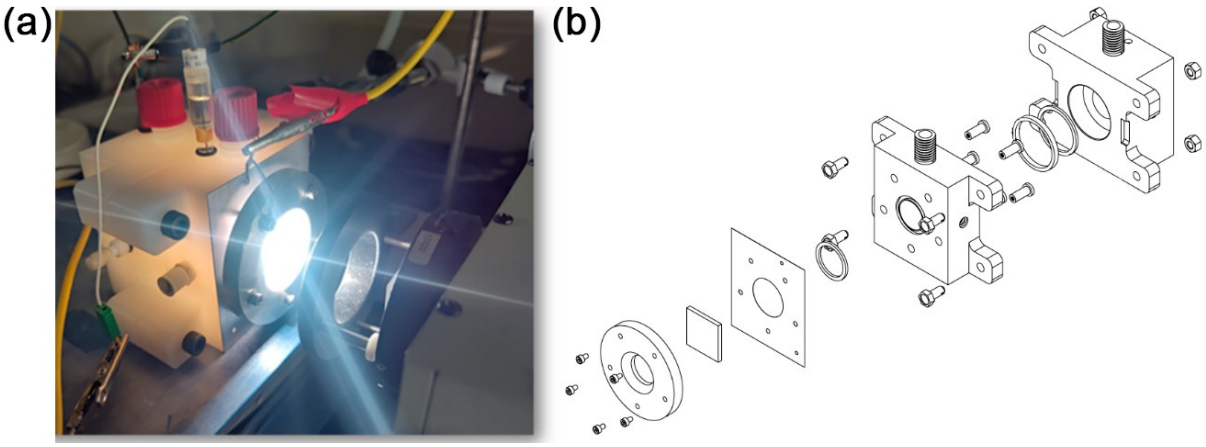

Figure 6. (a) Photoelectrochemical cell used in the photoelectrochemical experiments reported in this work and (b) scheme representing the components of the photoelectrochemical cell.

The final composition of the anolyte was characterized by High-Performance Liquid Chromatography (HPLC) analysis. HPLC analysis was performed on a Waters e2695 system equipped with a DAD-RID detector and using a Aminex HPX-87H column (300 × 7.8 mm, 5 µm) in isocratic conditions. The mobile phase was a mixture of MeCN:H2O 35:65 (30 min) and H2SO4 (0.005 mol L^{-1}). A flow rate 0.6 mL/min was employed and the signals were detected at 254 nm. Quantification was made by calibration curves, obtained through the analysis of mixtures of chemical standards in known concentrations. All samples were filtered using PES 0.22 µm syringe filters. The gas products were identified and quantified in a Clarus 580 (Perkin Elmer) GC-TCD equipped with a molecular sieve and a porapak N packed column. Calibration curves, obtained by injecting known quantities of analytical grade H_2, were used to quantify the green H2 produced during the photoreforming assays.

Ultra fast TA spectra (ps–ns timescale) were collected on a Harpia TA spectrometer (Light Conversion) in an experimental configuration reported previously.(LI, X. et al., 2023) Briefly, the pump light was generated using a Pharos-SP-10W (Light Conversion; ~170 fs, 10 kHz, 1030 nm) coupled to an OPA (Light Conversion, Orpheus). The white-light probe beam was achieved by focusing a portion of the Pharos-SP-10W 1030 nm output onto a sapphire crystal within the Harpia spectrometer. Samples were excited with a 355 nm pump light with a power of 200 mW (5 KHz). The pump beam (~0.6 mm diameter) and the probe beam (~0.4 mm diameter) were overlapped on the sample position. Data were initially collected using

the Harpia TA spectrometer and analysed using Carpetview software (Light Conversion). A quartz cuvette with a 2 cm path length, sealed with a rubber septa cap and degassed by Ar bubbling for 20 min prior to the measurements was used as sample holder.

The μs–s timescale TA measurements were performed using the third harmonic (355 nm) output of a Nd:YAG laser (Continuum, Surelite I-10, 532 nm, 6 ns pulse width) and excitation (0.275 mJ cm^{-2} at 0.33 Hz). The laser output was transmitted to the sample via a liquid light guide. A 100 W tungsten lamp coupled with a monochromator (OBB Corp., typically set to 4 nm resolution) was used as the probe light. The change of optical density (ΔOD) of the sample was calculated through measuring the transmitted light using a Si Photodiode and a homemade amplification system coupled to both an oscilloscope (Textronix TDS 220) and data acquisition card (DAQ card, National Instruments NI-6221). The oscilloscope data were for the study at the μs timescale while the DAQ card covered milliseconds to seconds. The data were averaged over 600 laser shots per wavelength to improve the signal to noise ratio. A 10 W 365 nm LED was used to illuminate the samples during the *operando in situ* experiments.

.

2.3. Results and Discussion

Oxygen deficient Bi_2WO_6 ($BiWO_{vac}$) was obtained through a simple solvothermal synthesis. This strategy revolves around replacing water with ethylene glycol to reduce the oxygen availability in the reaction media, so the oxygen transfer kinects to the lattice of the material is severely slowed, resulting in oxygen vacancy rich samples.

Structural characterization was conducted to assess whether the solvothermal introduction of oxygen vacancies influenced the phase composition of Bi_2WO_6. X-ray diffraction (XRD) patterns, Figure 7a, confirm that the oxygen-vacancy-rich sample retained the orthorhombic structure characteristic of Bi_2WO_6. However, a noticeable decrease in crystallinity was observed, which is evidenced by the broadening of the diffraction peaks with the full width at half maximum (FWHM) of the main diffraction peak varying from 0.38° to 0.82°. Raman spectroscopy, Figure 7b, further supports these findings, displaying the characteristic vibrational modes of orthorhombic Bi_2WO_6 in both samples (MARINHO et al., 2022a). The $BiWO_{(vac)}$ sample exhibits reduced short-range ordering, consistent with the expected structural disorder induced by oxygen vacancies, as previously reported by Wang et al. (WANG, T. et al., 2021). The peaks at 830 and 795 cm^{-1} correspond to the symmetric and antisymmetric stretching vibrations (A_1g modes) of the O–W–O bonds, respectively. The peak at 710 cm^{-1}, assigned to the asymmetric stretching mode (Eu) of the WO_6 chain bridges, is almost completely suppressed in the $BiWO_{(vac)}$ sample, indicating significant oxygen deficiency within the lattice. Additionally, the band at 306 cm^{-1}, associated with the translational motion (E_g mode) of Bi^{3+} and WO_6^{6-} units, and the peak at 152 cm^{-1}, corresponding to external lattice vibrations (A_1g mode) of the WO_6 octahedra, have reduced intensities in the oxygen-deficient sample.

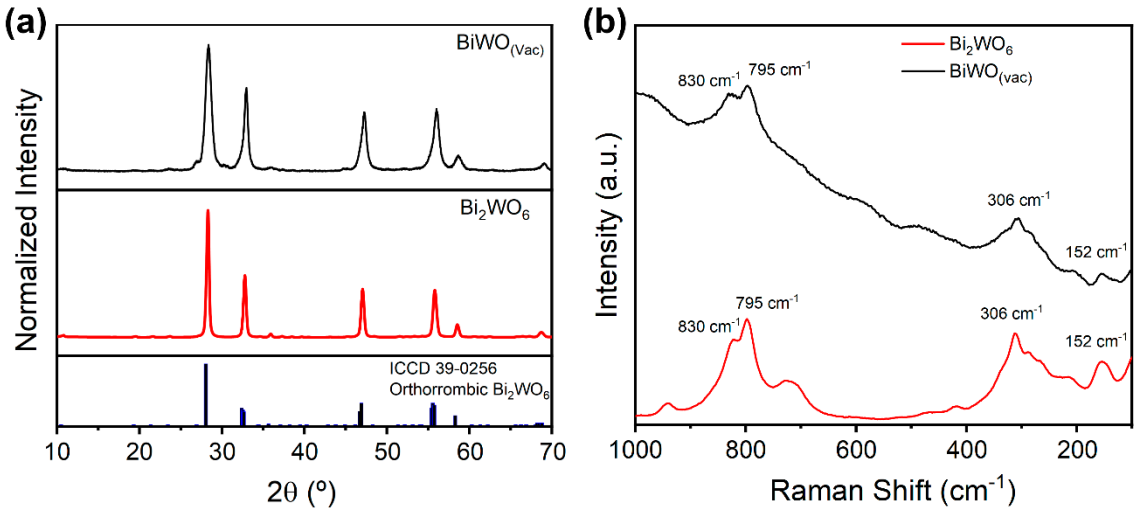

Figure 7. (a) XRD patterns and (b) Raman spectra of Bi_2WO_6 (red) and $BiWO_{(vac)}$ (black) powders.

X-ray photoelectron spectroscopy (XPS) was used to investigate the superficial composition of the synthesized materials. No significant impurities can be observed in the XPS survey spectra of both samples, Figure A1. Unlike Bi_2WO_6, the oxygen-vacancy-rich sample $BiWO_{(vac)}$ exhibited different oxidation states for tungsten and bismuth: W(V, VI) and Bi(III, III – x), Figure 8a,b. This is attributed to the oxygen deficiency, where the oxidation state of cations adjusts to compensate for the charge imbalance caused by the lack of O^{-2} anions. Additionally, both samples display two distinct oxygen peaks, Figure 8c. The major peak at 532 eV corresponds to lattice oxygen (O^{2-}), while the peak at higher binding energy is associated with adsorbed oxygen species, an indicative of the presence of structural defects and/or adsorbed water (HUO et al., 2019; SACHA et al., 2019; WANG, T. et al., 2021).

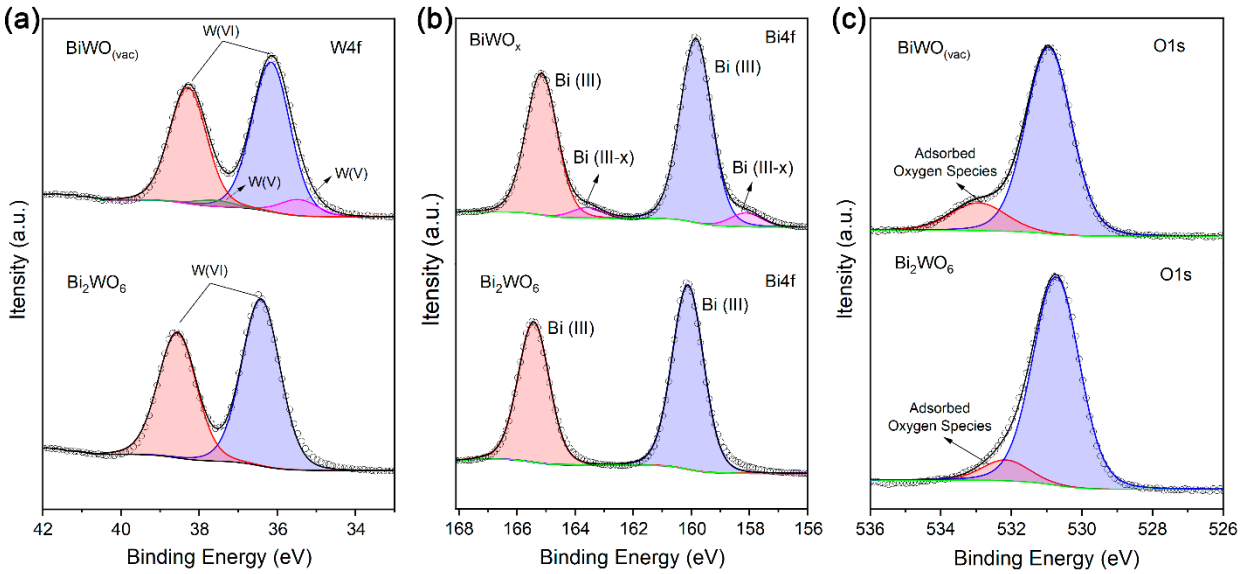

Figure 8. High-resolution XPS spectra of (a) W4f, (b) Bi4f and (c) O1s for the synthetized samples.

The effect of oxygen vacancies on the optical absorption properties of Bi_2WO_6 was investigated using diffuse reflectance spectroscopy (DRS), Figure 9. The hydrothermally synthesized pristine Bi_2WO_6 exhibited an absorption edge at approximately 400 nm, corresponding to a wide optical band gap of 2.85 eV. In contrast, $BiWO_{(vac)}$ displayed an extended absorption tail reaching up to 450 nm, with a reduced optical band gap energy of 2.65 eV. This narrowing of the band gap is attributed to the formation of defect states below the conduction band, induced by oxygen vacancies (WANG, T. et al., 2021). To further elucidate this behavior, density functional theory (DFT) calculations were performed using the Quantum ESPRESSO suite. Among the proposed structures for $BiWO_{(vac)}$, Figure 9b, those with the lowest calculated total energies, in which oxygen atoms are removed from positions 1 or 2, exhibited theoretical band gap values of 2.619 eV, Figure 9d, in good agreement with the experimental results. These findings suggest that oxygen removal at positions 1 and 2 is energetically more favorable, supporting their identification as the most probable sites for vacancy formation in $BiWO_{(vac)}$. The DFT-calculated parameters are summarized in Table 4.

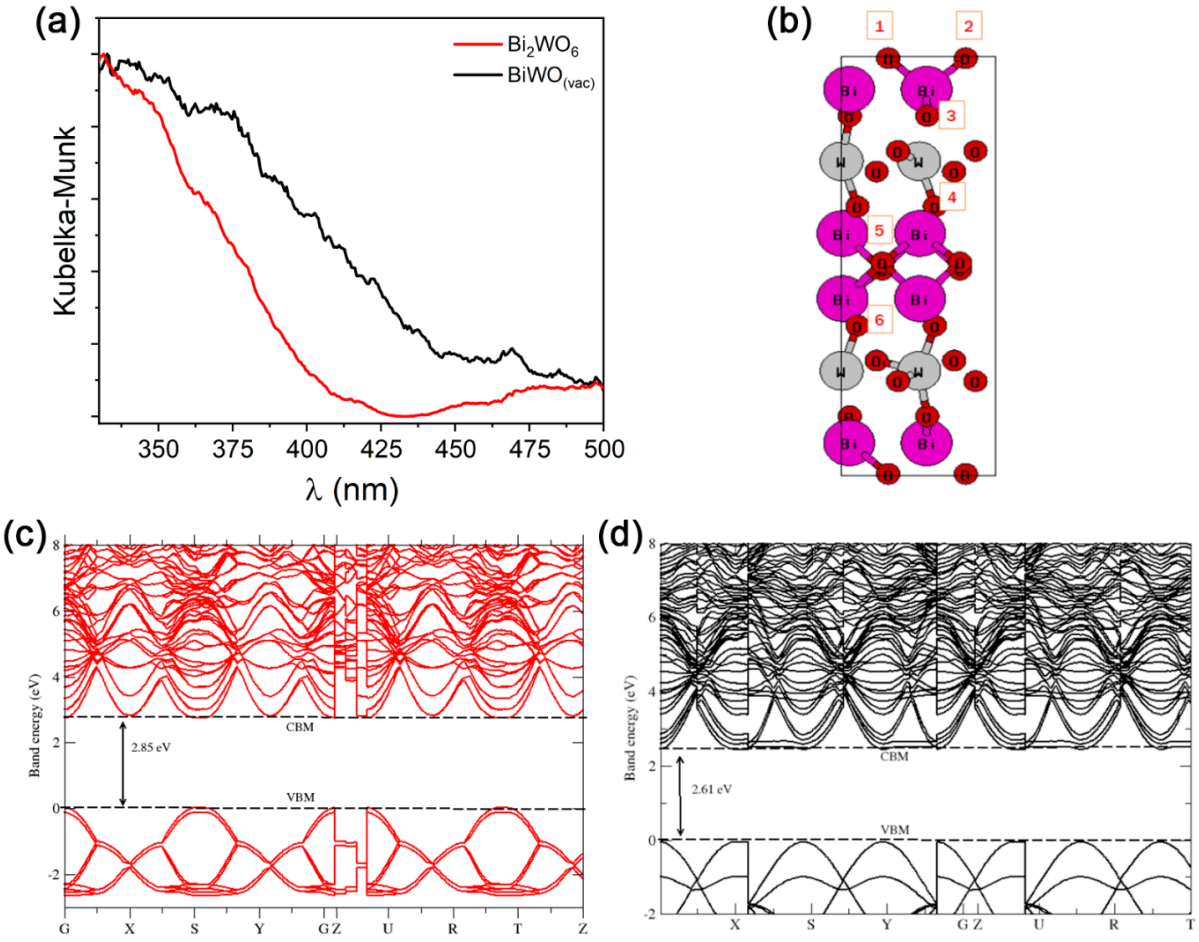

Figure 9. UV-Vis spectra of the Bi_2WO_6 (red) and $BiWO_{(vac)}$ (black) powder samples. (b) Unit cell model highlighting and numbering the potential oxygen vacancy sites in $BiWO_{(vac)}$. (c) DFT-calculated band structure of pristine Bi_2WO_6 and (d) DFT-calculated band structure of $BiWO_{(vac)}$ with the oxygen atom removed from position 1, corresponding to the lowest-total energy configuration.

Table 4. Calculated total energies and band gap energies of the proposed $BiWO_{(vac)}$ unit cells according to the position of the removed oxygen atom.

$BiWO_{(vac)}$	Energy (Ry)	Band Gap (eV)
P1	-2645.8960	2.6195
P2	-2645.8960	2.6180
P3	-2645.8688	2.1560
P4	-2645.8502	1.5925
P5	-2645.8527	1.6980
P6	-2645.8712	1.9920

The $BiWO_{(vac)}$ powders were then deposited on clean FTO glass substrates and tested as photoanodes in a photoelectrochemical cell for glycerol photoelectroreforming. Light chopped linear sweep voltammetry (LSV) under visible light (λ > 400 nm, 100 mw cm^{-2}) and in crude glycerol electrolyte, Figure 10a, were conducted on the photoanodes in order to verify if their photoresponse was broadened by the oxygen vacancies. The $Bi_2WO_{6(vac)}$ showed prompt photoresponse as the light was turned on, unlike hydrothermal Bi_2WO_6 which barely shows any photoresponse in this condition, corroborating that the oxygen vacancies broadened the light absorption of the material. However, photocurrents were very low even in the oxygen vacancy material, suggesting that most of its photoactivity still depends on UV excitation. When simulated sunlight (100 mW cm^{-2}, AM 1.5G), containing ~9% of photons on UV region, was used instead, both materials showed a significant increase in photocurrent, Figure 10b, with $BiWO_{(vac)}$ still achieving higher photocurrents than Bi_2WO_6. Notably, Bi_2WO_6 films displayed a characteristic signature of severe charge recombination: a sharp rise in photocurrent upon illumination followed by a gradual decay to a steady-state plateau. In contrast, this recombination behavior in BiWO(vac) was only observed at lower applied biases and was completely mitigated at potentials above 0.5 V vs Ag/AgCl, indicating significantly improved charge transfer kinetics.

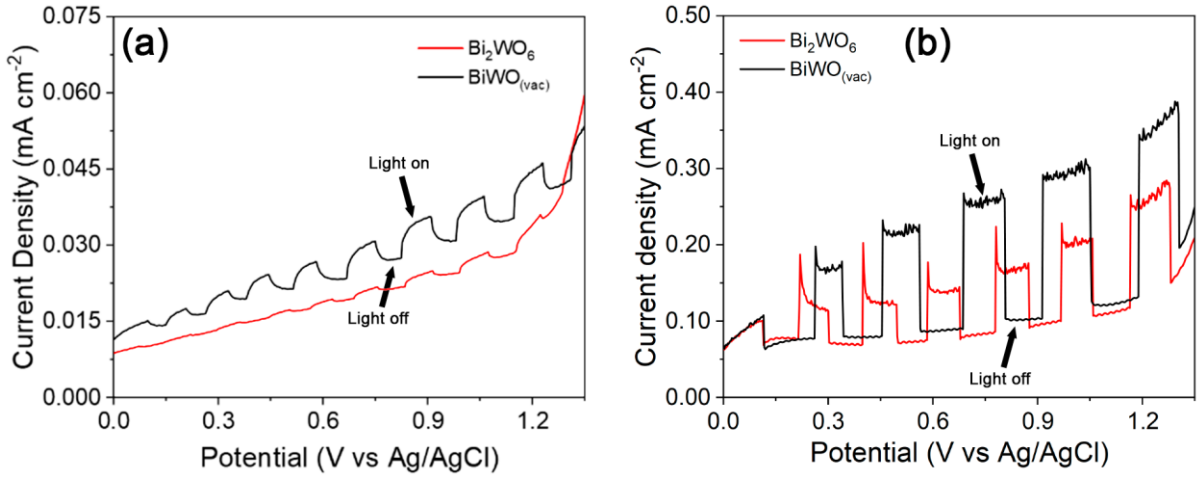

Figure 10. Light-chopped linear sweep voltammetry using (a) visible light only (λ > 400 nm, 100 mW cm^{-2}) and (b) simulated sunlight (AM 1.5G, 100 mW cm^{-2}). Electrolyte: Crude glycerol 10% v/v in 0.1M K_2SO_4.

$BiWO_{(vac)}$ was subsequently tested for long-term photoelectroreforming of crude glycerol, the raw byproduct obtained from a biodiesel production plant, following simple filtration to remove solid impurities. The $BiWO_{(vac)}$ photoanodes exhibit good stability during long-term experiments, Figure 11a, exhibiting only a 25% decrease in photocurrent over 5 hours of continuous operation. Additionally, glycerol photoreforming resulted in a hydrogen evolution rate of 63 µmol cm^{-2} h^{-1}, Figure 11b, with a Faradaic efficiency (FE) of 91%. Glycerol conversion was monitored via HPLC analysis, revealing that $BiWO_{(vac)}$ photoanodes achieved 24.5% glycerol consumption at pH = 6 with 85% selectivity toward formic acid production, comparatively, pristine Bi_2WO_6 photoanodes yielded 32 µmol cm^{-2} h^{-1} H_2 with 95% of FE and 17% glycerol conversion with 64% of formic acid production selectivity, Figure A2.

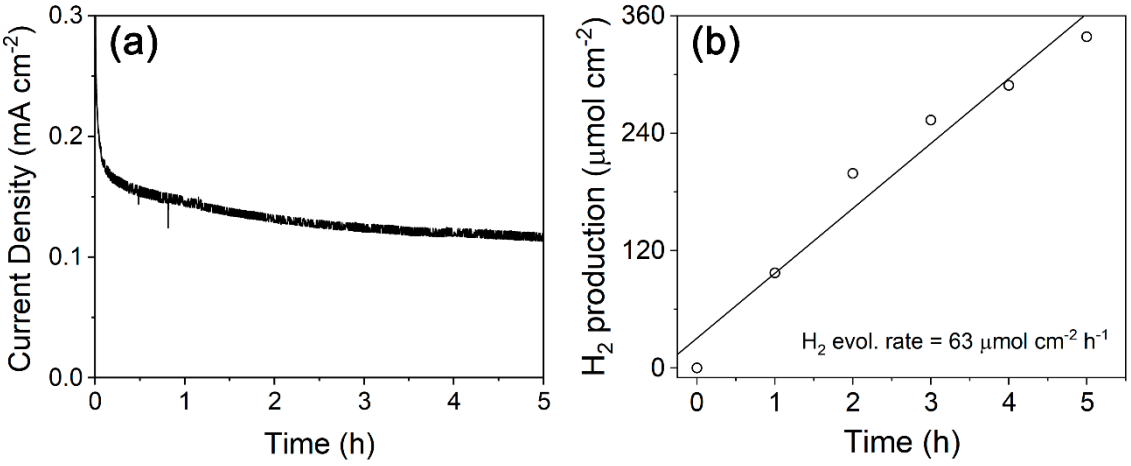

Figure 11. Chronoamperometry of $BiWO_{(vac)}$ in crude glycerol 10% v/v in K_2SO_4 under 0.8 V vs Ag/AgCl and AM 1.5G, 100 mW cm^{-2} and (b) H_2 evolution from the chronoamperometric experiment.

The photoelectrochemical results were rationalized with EIS analysis, Figure 12. Data collected at different applied potentials under illumination and under the dark can be fitted using an equivalent circuit based on the charge-carrier trapping mechanism, Figure 12b,d *inset* (LIU, D. et al., 2019; NASCIMENTO, LUCAS L. et al., 2022). The equivalent circuit consists of a space-charge capacitance element, C_{sc}, a surface state capacitance, CPE_{ST}, while R_s is the electrolyte resistance, R_{Tp} is the resistance ascribed from the charge transport within the bulk of the material, and R_{ct} is the charge transfer resistance at the interface photoanode/electrolyte. The photoelectrochemical parameters obtained from the EIS data fitting are summarized

in Table A1. A comparison between the R_{CT} and R_{Tp} values in the dark and under illumination is shown in Figure 13.

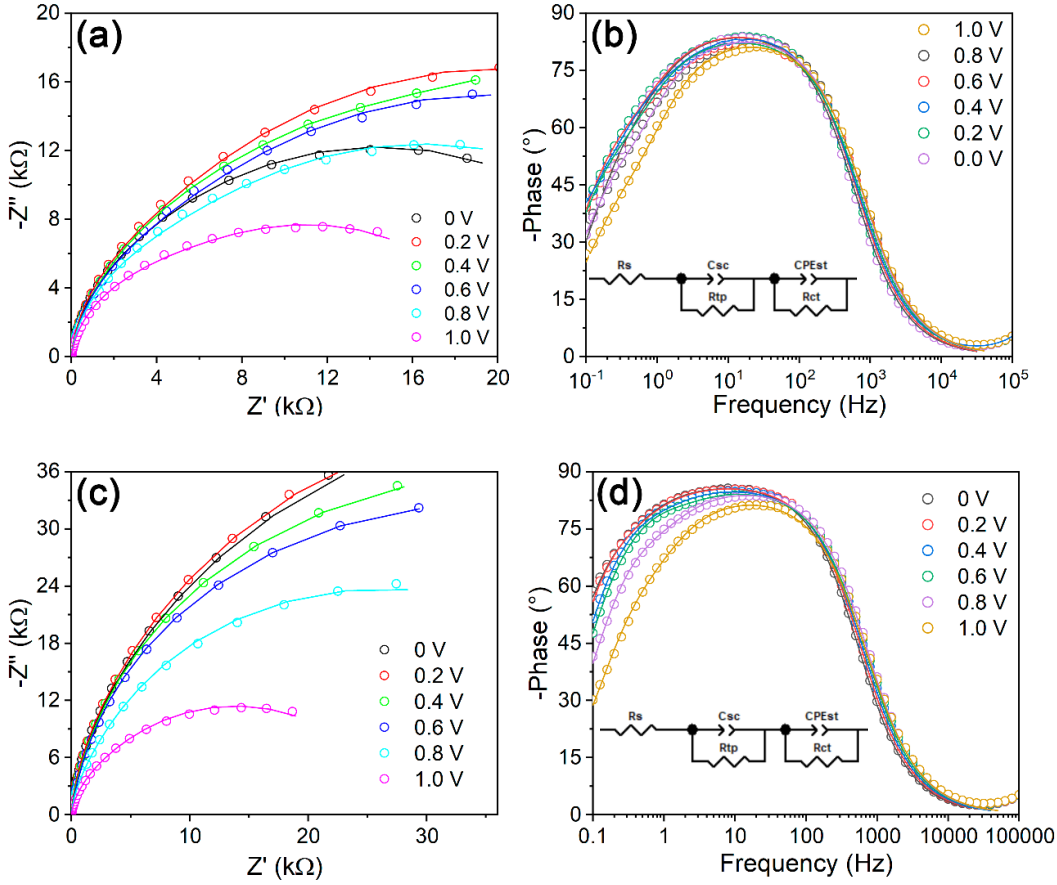

Figure 12. (a,b) EIS Nyquist and Bode plot of $BiWO_{(vac)}$ in dark and (b) EIS Nyquist and Bode plot of $BiWO_{(vac)}$ taken in illuminated conditions (AM 1.5G, 100 mW cm^{-2}).

Upon illumination, a substantial reduction in R_{CT} was observed at all potentials, highlighting the activation of photogenerated carriers and improved interfacial kinetics. For instance, at 1.0 V vs Ag/AgCl, R_{CT} decreased from 23.5 kΩ (dark) to 14.0 kΩ (light), consistent with the photoinduced generation of additional charge carriers. In comparison, pristine Bi_2WO_6 exhibited an R_{CT} of 23.2 kΩ under the same conditions, Figure A3, which is approximately 65% higher than that of $BiWO_{(vac)}$, highlighting the beneficial role of oxygen vacancies in lowering charge transfer resistance and improving photoelectrochemical performance. Similarly, under illumination, R_{CT} values consistently decreased with increasing bias, reaching a minimum at 1.0 V. In contrast, R_{Tp} behavior under illumination showed a distinct trend. While R_{Tp} values under dark conditions were generally low, under illumination they increased, remaining relatively

stable around 5~6 kΩ across the analyzed potential range. This behavior suggests that under operational (light) conditions, electron trapping becomes a more pronounced limiting factor compared to dark conditions, potentially due to a higher density of populated states. Moreover, these results suggest that the density and nature of the surface states responsible for trapping are largely intrinsic to the $BiWO_{(vac)}$ material and not significantly affected by external field strengths within the tested range.

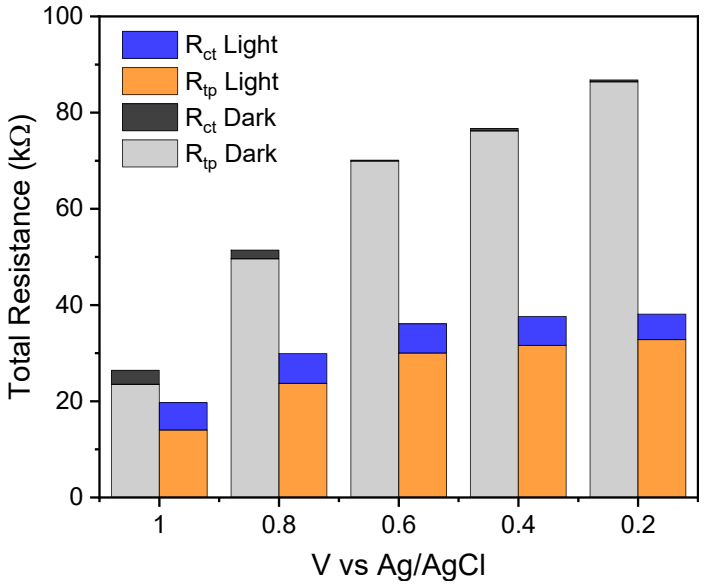

Figure 13. Rct and R_{Tp} components extracted from the EIS circuit under dark and irradiation conditions (AM 1.5G, 100 mW cm^{-2}) at different applied potentials.

Under dark conditions, R_{ct} values were significantly higher than that attributed to R_{Tp} at all applied potentials, indicating that in the absence of illumination, the overall kinetics are dominated by sluggish interfacial charge transfer rather than by charge trapping phenomena. As the applied bias increased from 0.2 V to 1.0 V vs Ag/AgCl, R_{CT} decreased from 86.4 kΩ to 23.5 kΩ, reflecting the enhanced band bending and facilitated charge transfer at more anodic potentials.

Overall, these results indicate that while illumination significantly enhances charge transfer across the interface (R_{CT}), charge recombination within the bulk of the semiconductor layer, expressed by the transport resistance (R_{Tp}), becomes a more prominent recombination pathway under light conditions. The oxygen vacancies also resulted in a reduction in R_{CT} in comparison to the pristine Bi_2WO_6. These findings are consistent with the presence of oxygen vacancies, which introduce mid-gap states

facilitating light absorption and charge transfer but can also act as trapping sites for photoexcited electrons.

To gain further insight into the photophysical behavior of Bi_2WO_6-based materials in the absence of an interfacial hole scavenging, ultrafast TAS experiments were performed under an inert argon atmosphere, Figure 14. This approach isolates the intrinsic charge carrier dynamics without the influence of electrolyte oxidation processes. As shown in Figure 14a, the pristine Bi_2WO_6 sample exhibits moderate ΔmOD signals across the 600–1250 nm range, with the signal onset occurring within a few picoseconds and remaining relatively stable over the 1 ns timescale. The spectral evolution, Figure 14c, reveals a gradual red-shift and broadening of the absorption band with increasing delay, consistent with free carrier absorption from electrons accumulating in the conduction band (CB) and/or shallow trap states (BARROSO et al., 2013; KAHRAMAN et al., 2019; MOSS et al., 2020).

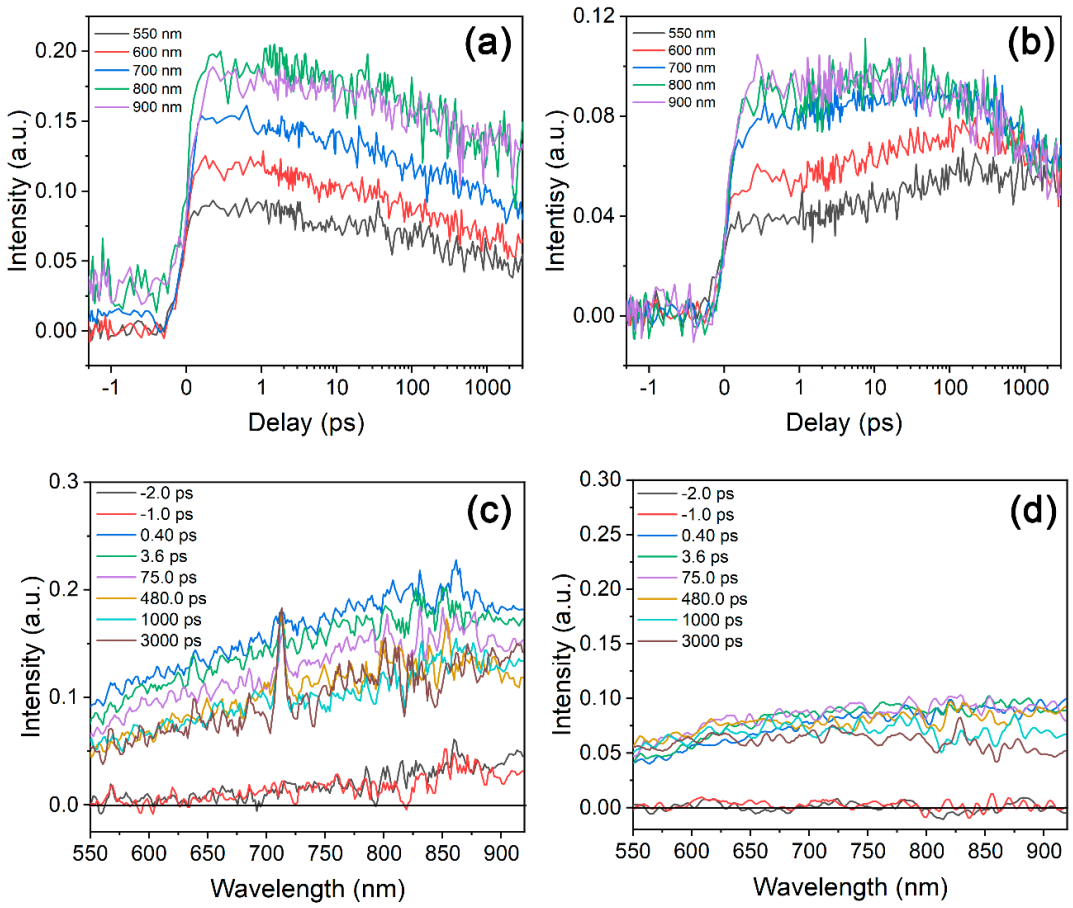

Figure 14. Ultrafast transient absorption decay dynamics of Bi_2WO_6-based photoanodes under argon atmosphere following 355 nm band gap excitation. (a) Kinetic traces of Bi_2WO_6 and (b) BiWO(vac) at selected probe wavelengths. (c)

Spectral evolution of Bi_2WO_6 and (d) BiWO(vac) at representative pump-probe delay times.

In contrast, $BiWO_{(vac)}$ displays a rising ΔmOD signals for the first ~100 ps after excitation, Figure 14b, particularly in the 700–1100 nm region, indicating significant trapping of photogenerated electrons for a prolonged period post-excitation. The spectral evolution, Figure 14d, shows a broadened and red-shifted absorption consistent with transitions involving vacancy-induced midgap states (GRIGIONI et al., 2017). The early-time intensity and persistence of the signals suggest that these vacancies function as shallow electron traps, temporarily storing photogenerated charges and delaying recombination. Notably, the $BiWO_{(vac)}$ sample also shows a delayed spectral stabilization relative to the pristine material, suggesting slower electron relaxation and potential involvement of localized states in the process (NAM et al., 2019).

Ultra-fast transient studies were also performed in operando conditions (with an applied positive bias and under CW illumination from a LED) with both glycerol and plain K_2SO_4 electrolyte. Pristine Bi_2WO_6 in plain electrolyte at 0.8 V, Figure 15a, exhibits a broad and gradually increasing ΔmOD signal with wavelength, also consistent with free electron absorption in the CB. Upon introduction of glycerol, Figure 15b, a marked enhancement in signal intensity and persistence is observed across the spectrum, indicating more efficient charge separation and stabilization due to hole scavenging. In contrast, $BiWO_{(vac)}$, Figure 15c, shows lower initial signals in plain electrolyte at 0.8 V, suggesting rapid recombination via trap states introduced by oxygen vacancies. However, in the presence of glycerol, Figure 15d, a strong enhancement in ΔmOD is again observed, with particularly long-lived signals at 700–1100 nm, showing that oxygen vacancies facilitate shallow electron trapping and promote improved charge retention in the presence of glycerol as sacrificial electron donor.

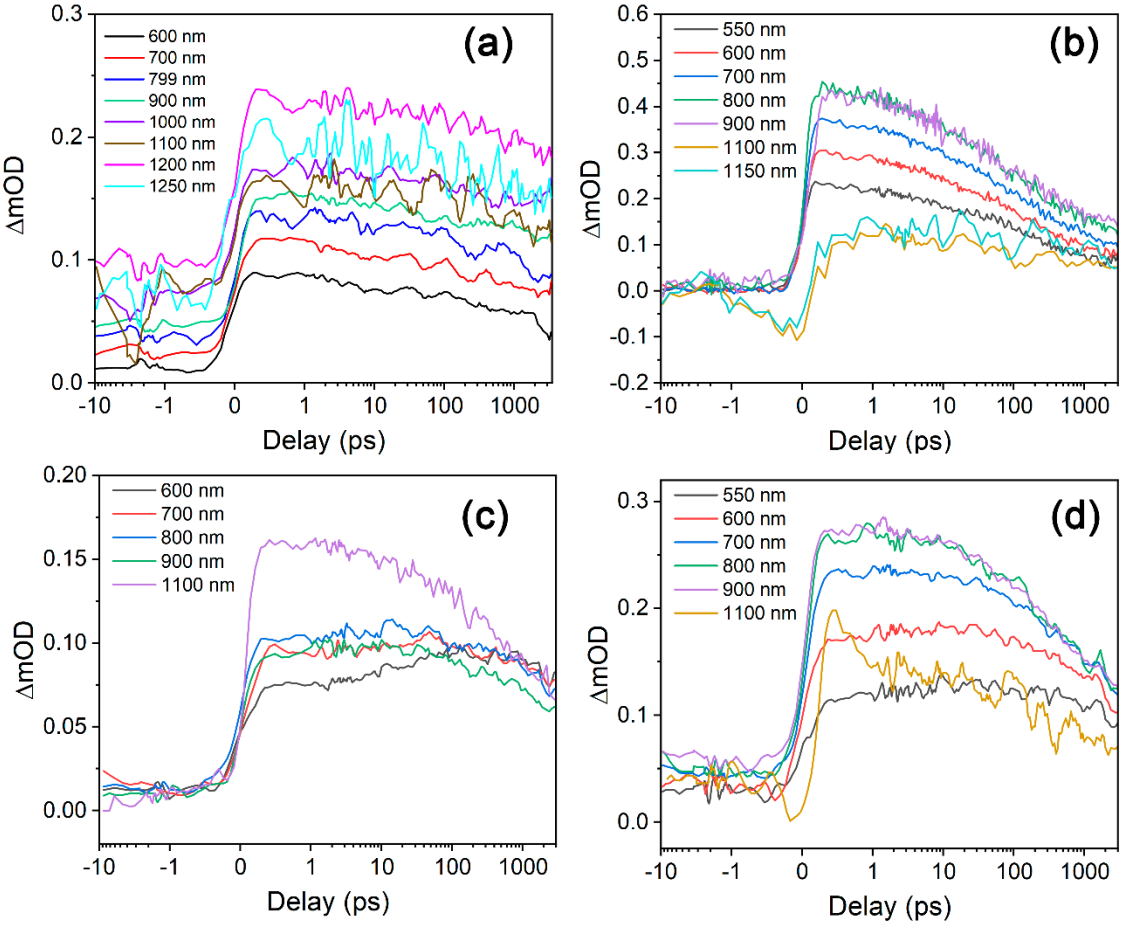

Figure 15. Ultra-fast transient absorption decay dynamics as a function of the probed wavelength and electrolyte composition of Bi_2WO_6-based photoanodes, after bandgap excitation with 355 nm laser light (a) Bi_2WO_6 photoanodes under 0.8 V vs Ag/AgCl in plain electrolyte 0.1M K_2SO_4 and (b) 5% v/v glycerol in 0.1M K_2SO_4. (c) $BiWO_{(vac)}$ photoanodes under 0.8 V vs Ag/AgCl in plain electrolyte 0.1M K_2SO_4 and (d) 5% v/v glycerol in 0.1M K_2SO_4.

The charge transfer dynamics was also investigated μs to s timescales under *operando* conditions to probe the role of oxygen vacancies. The transient kinetic traces, Figure 16, reveal an increasing signal intensity with longer probe wavelengths, consistent with the absorption response of free carrier absorption as previously observed in the ultrafast TAS experiments (WILSON et al., 2023). In pristine Bi_2WO_6, the transient absorptions at open-circuit potential shows fast decay components with modest signal intensities, indicating rapid recombination of photogenerated carriers. Under an applied bias of 0.8 V vs Ag/AgCl (operando conditions), a significant increase in the absorption signal is observed, particularly in the 600–900 nm range.

This enhancement is attributed to improved charge separation and extraction driven by external bias, leading to an increased population of long-lived electrons.

In contrast, the $BiWO_{(vac)}$ samples, Figure 16c,d, show distinct behavior. At OCP, $BiWO_{(vac)}$ displays lower ΔmOD signals compared to pristine Bi_2WO_6, suggesting faster carrier recombination or a lower free carrier population due to trap-assisted recombination at oxygen vacancy sites. However, under an applied bias of 0.8 V, $BiWO_{(vac)}$ exhibits intense and long-lived transient signals indicating significant photogenerated carrier accumulation. This further corroborates the hypothesis that oxygen vacancies act as shallow electron traps, prolonging carrier lifetimes. Furthermore, faster electron extraction kinetics are observed for $BiWO_{(vac)}$ films in the 1–10 ms lifetime range due to improved charge transport. To validate these observations, power-law decay fitting (MOSS et al., 2020; LI, C. et al., 2021; NANDAL et al., 2021) was used to analyse the decay of the transient absorption signal at 900 nm (assigned to trapped electrons) at 0.8 V for both materials (Figure A4). Pristine Bi_2WO_6 yielded a decay exponent (α) of 0.19 ± 0.01, while $BiWO_{(vac)}$ exhibited a significantly higher value of 1.53 ± 0.01. These results point to sluggish, probably anisotropic-limited electron transport in Bi_2WO_6 (MOSS et al., 2020), whereas $BiWO_{(vac)}$ exhibits faster decay dynamics, likely associated with enhanced charge separation and mobility. This suggests that oxygen vacancies also contribute to improved electronic conductivity in the material.

Transient photocurrent (TPC) measurements were performed by coupling the potentiostat with an oscilloscope, enabling the capture of the temporal profile of the photoresponse of $BiWO_{(vac)}$ photoanodes under pulsed illumination. As shown in **Error! Reference source not found.**, the TPC traces exhibit a photocurrent rise followed by a decay, with a distinctive feature across microsecond to second timescales. The time-resolved data reveal a pronounced current peak within the 1–10 ms window, closely matching the carrier dynamics observed in the TA experiments. This correlation confirms that the long-lived carriers observed spectroscopically also manifest as sustained photocurrent signals, which are characteristic of charge transport processes across the photoelectrode. The ms-range decay is thus attributed to the slow diffusion and drift of photogenerated electrons within the $BiWO_{(vac)}$ film with prolonged lifetimes.

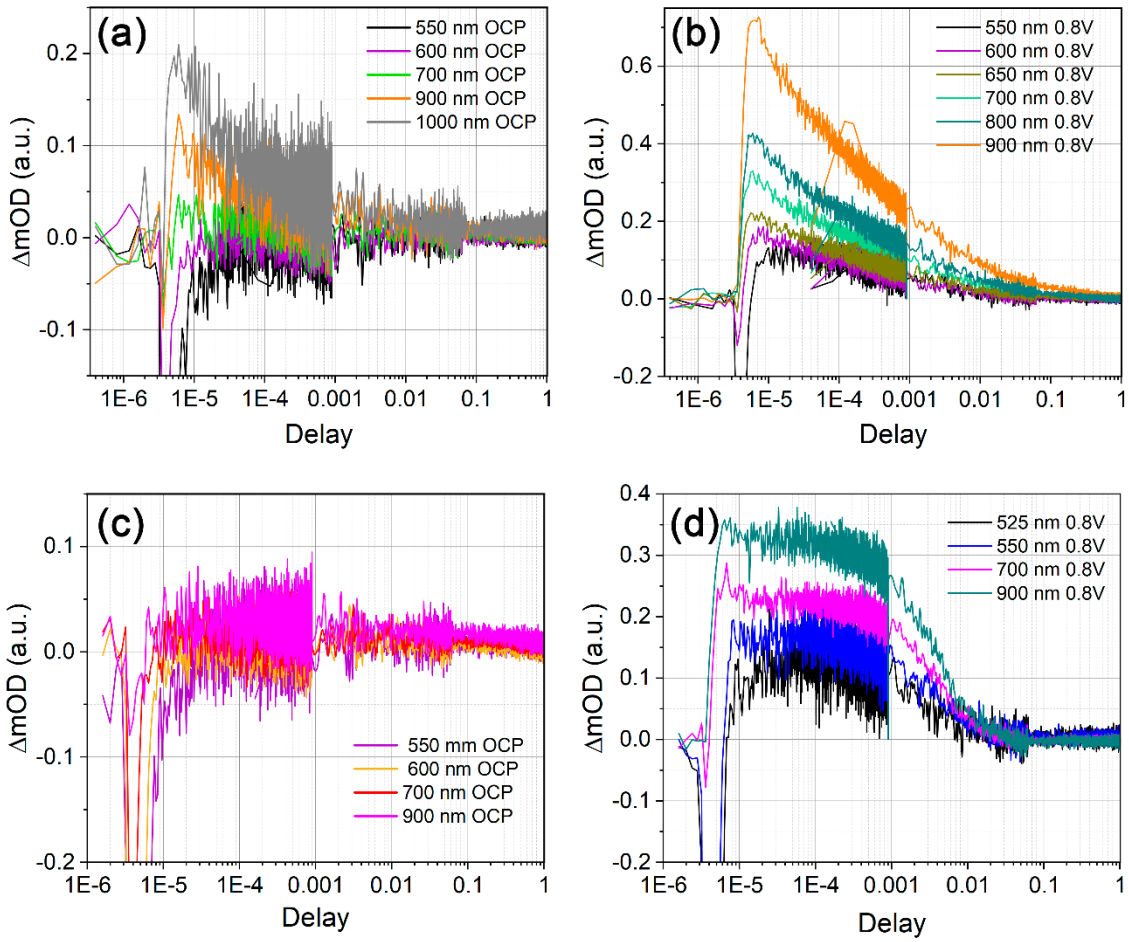

Figure 16. Transient absorption decay dynamics as a function of the probed wavelength and applied bias of Bi_2WO_6-based photoanodes in glycerol electrolyte, after bandgap excitation with 355 nm laser light and frontside illumination with a white led. (a,b) Bi_2WO_6 photoanodes under OCP and 0.8 V vs Ag/AgCl, (c,d) $BiWO_{(vac)}$ photoanodes under 0.8 V vs Ag/AgCl and OCP. Transient absorption decay dynamics as a function of the probed wavelength and applied bias of Bi2WO6-based photoanodes in glycerol electrolyte, after bandgap excitation with 355 nm laser light and frontside illumination with a white led. (a,b) Bi2WO6 photoanodes under OCP and 0.8 V vs Ag/AgCl, (c,d) BiWO(vac) photoanodes under 0.8 V vs Ag/AgCl and OCP.

Overall, these results highlight the beneficial role of oxygen vacancies in promoting charge separation, extending carrier lifetimes, and improving the photoelectrochemical performance of Bi_2WO_6-based photoanodes for photo-assisted reactions.

2.4. Conclusions

In this study, Bi_2WO_6 with induced oxygen vacancies was successfully synthesized via a facile solvothermal method and evaluated for the photoelectrochemical reforming of crude glycerol waste derived from biodiesel production. Structural analyses confirmed that oxygen vacancies were effectively introduced without altering the crystalline phase, though they induced noticeable changes in crystallinity and short-range arrangement. Optical characterization revealed a redshift in the absorption edge and a narrowed band gap for $BiWO_{(vac)}$, supported by DFT calculations, confirming the formation of intermediate states associated with oxygen vacancies. The $BiWO_{(vac)}$ photoanodes showed excellent results for crude glycerol photoreforming, which resulted in a hydrogen evolution rate of 63 μmol cm^{-2} h^{-1} with a faradaic efficiency of 91%, two times bigger than pristine Bi_2WO_6. Glycerol conversion was found to be 24.5% at pH = 6 with 85% selectivity toward formic acid production.

Transient absorption spectroscopy under *operando* conditions demonstrated that oxygen vacancies significantly enhance charge carrier dynamics, acting as shallow traps that prolong electron lifetimes and improving the material's conductivity. Electrochemical impedance measurements further corroborated the improved conductivity and reduced charge-transfer resistance in the oxygen-deficient samples. These synergistic effects translated into enhanced photoelectrochemical performance for glycerol reforming. Altogether, this work highlights the strategic role of oxygen vacancies in modulating the optoelectronic properties of Bi_2WO_6, offering a promising avenue for developing efficient photoanodes for solar-driven valorization of industrial waste streams.

3. Photoelectroreforming Of Industrial Waste Streams Using Nb-Doped $BiVO_4$ Photoanodes for Sustainable Hydrogen Production

Photoelectroreforming is a promising approach that combines cost-effective and abundant photocatalysts with the enhanced kinetics offered by electrocatalysis. Among photoanode materials, $BiVO_4$ stands out due to its favorable light absorption properties, relatively high photocurrent, and near-optimal theoretical Solar-to-Hydrogen (STH) efficiency (KIM, J. H. et al., 2019). However, $BiVO_4$ is highly susceptible to photocorrosion and exhibits short-lived carriers, resulting in sluggish kinetics and lack of long-term stability (CHEN, D. et al., 2022). Many approaches have been studied to address this phenomenon. Ke and co-workers reported that surface doping of $BiVO_4$ photoanodes with Mo^{5+} or W^{5+} significantly increased photocurrent and stability for water oxidation (KE et al., 2023). Liang and co-authors decorated $BiVO_4$ surface with MoOx nanoparticles, increasing the conversion of poly(ethylene-terephthalate) into formate, acetate, and H_2, which the authors attributed to improved charge transfer within the materials (LIANG et al., 2024). Kalanur and Seo reported Nb(V)-doped $BiVO_4$ photoanodes with enhanced water splitting performance when compared to pristine $BiVO_4$. The doping with Nb(V) increased the carrier density in the bulk of $BiVO_4$, improved the charge separation, charge transfer, diffusion, and decreased the charge transfer resistance at the photoanode/electrolyte interface (KALANUR; SEO, 2022). So far, such strategies have been poorly explored on photoelectroreforming, especially those employing real biomass-derived residues.

Herein, for the first time, a photoelectrochemical cell assembled with Nb(V)-doped $BiVO_4$ (Nb:$BiVO_4$) was applied for the photoreforming of crude glycerol and flegmass residues, collected from a biodiesel plant and a sugarcane processing refinery, respectively. The morphological and the electronic properties of the photoanode were evaluated as a function of dopant concentration following by photoelectrochemical assays employing real residues for hydrogen production and biomass valorization.

3.1. Specific Objectives

The specific objectives for the work showed this chapter were:

- Synthetize Nb-doped $BiVO_4$ samples with different Nb^{5+} content
- Characterize the doped samples and study their influence on the optoelectronic properties of $BiVO_4$
- Test the performance of the Nb-doped samples against the photoelectroreforming of real industrial wastes and compare the results with that of pristine $BiVO_4$
- Access the mechanisms involved in the glycerol photoelectroreforming on $BiVO_4$-based photoanodes using EPR in situ studies

3.2. Methodology

All chemicals were used as received and bought from Aldrich in analytical or HPLC grade. Nanocrystalline $BiVO_4$ and Nb:$BiVO_4$ were prepared by adding 5 mmol of $Bi(NO_3)_3$ in 10 mL of 4M HNO_3 solution, 5 mmol of NH_4VO_4 in 10 mL of 2M NaOH and 2 mL of H_2O_2 30%. After complete dissolution of the precursors, the V^{5+} solution was added on the Bi^{3+} solution dropwise, under vigorous stirring. The resulting mixture was neutralized using a 2M NaOH solution. Following, the mixture was transferred to a PTFE vessel, which was then inserted in a sealed hydrothermal reactor and submitted to hydrothermal treatment under 200 ºC (180 psi) for 4h. The Nb:$BiVO_4$ samples were obtained by adding niobium(V) ammonium oxalate to the precursor's solution, yielding 1 and 5% w/w of Nb content in the resulting materials. The obtained powders were washed with deionized water, ethanol and dried at 80 ºC.

The $BiVO_4$-based photoanodes were deposited on clean FTO substrates using the screen printing method (HEDAYAT; DU; ILKHANI, 2017). The paste for screen printing was prepared following the methodology previously described elsewhere (GÜNNEMANN et al., 2019). Briefly, 3 g of the photocatalyst powder were thoroughly grinded in a mortar containing 15 mL of ethanol, 2.5 mL of water and 0.5 mL of acetic acid, and then transferred to a round flask with the further addition of 50 mL of ethanol, 10 g of terpineol and 15 g of a 10% wt. ethyl cellulose solution in ethanol. The mixture was sonicated and stirred until the material was completely dispersed. Finally, the

solvent was removed with a rotary evaporator. The obtained films were annealed at 500 ºC for 30 min to remove organic impurities and increase their mechanical stability.

X-ray diffraction analysis (XRD) was performed with an XRD600 powder diffractometer (Shimadzu) operating at 40 kV and 30 mA employing Cu Kα radiation. Raman spectroscopy was conducted in a LabRAM HR Evolution spectrometer (Horiba). X-ray photoelectron (XPS) spectroscopic measurements were obtained in a Thermo Scientific model K-Alpha spectrometer, equipped with Al Kα x-ray source. All spectra were corrected using the C 1s with the binding energy at 284.6 eV. Transmission Electronic Microscopy was conducted on a JEOL JEM 2100 High Resolution Transmission Electron Microscope operated at 200 kV and equipped with an Oxford Instruments X-Max 80T Energy Dispersive Spectrometer (EDS) system. Carbon support film coated copper TEM grids (200 mesh) were used to support the samples. HRTEM images were taken by Gatan Model 794 Slow Scan CCD Camera.

Film morphologies were evaluated by Scanning Electron Microscopy (SEM) using a TESCAN Vega3 microscope. Diffuse Reflectance Spectra (DRS) were obtained in a UV 2600 spectrophotometer (Shimadzu) equipped with an integrating sphere. The electrochemical characterization was carried on an Autolab PGSTAT204 (Metrohm) potentiostat/galvanostat equipped with an Electrochemical Impedance Spectroscopy (EIS) FRA32M module. The irradiation source was a 300 W Xe arc lamp (Oriel) equipped with an AM 1.5G filter, the light intensity was measured by a power meter 1916-R (Newport) connected to an optical sensor 818-UV/DB.

A PTFE customized H-shaped photoelectrochemical cell was used for all (photo)electrochemical experiments, **Figure 6**. The catholyte chamber was filled with 0.1 M K_2SO_4 electrolyte and the anolyte chamber with glycerol 10% v/v in 0.1 M K_2SO_4 or bare flegmass with added 0.1 M K_2SO_4. Platinum was used as counter electrode and Ag/AgCl as reference. A Nafion® proton selective membrane was placed between the anolyte and catholyte chambers. The backside illumination was done through a 3.8 cm^2 quartz circular window placed at the front of the anolyte chamber.

The final composition of the anolyte was characterized by Chemical Oxygen Demand (COD) and the oxidation products identified and quantified by High-Performance Liquid Chromatography (HPLC) analysis. HPLC analysis was performed on a Waters e2695 system equipped with a DAD-RID detector and using a

Aminex HPX-87H column (300 × 7.8 mm, 5 μm) in isocratic conditions. The mobile phase was a mixture of MeCN:H_2O 35:65 (30 min) and H_2SO_4 (0.005 mol L^{-1}). A flow rate 0.6 mL/min was employed and the signals were detected at 254 nm. Quantification was made by calibration curves, obtained through the analysis of mixtures of chemical standards in known concentrations. All samples were filtered using PES 0.22 μm syringe filters. The gas products were identified and quantified in a Clarus 580 (Perkin Elmer) GC-TCD equipped with a molecular sieve and a porapak N packed column. Calibration curves, obtained by injecting known quantities of analytical grade H_2, were used to quantify the green H_2 produced during the photoreforming assays.

Electron paramagnetic resonance (EPR) spectroscopy was conducted on solid photocatalyst powders to examine residual paramagnetic defects. EPR, combined with the spin trapping method, was utilized to explore the reaction mechanisms involved in the photocatalytic tests. For this purpose, the spin traps *5,5-Dimethyl-1-pyrroline N-oxide* (DMPO) and *N-tert-butyl-α-phenylnitrone* (PBN) were dissolved in distilled water and water/methanol mixture, respectively, with each solution containing 10% of analytical glycerol. Different photocatalysts were then added to these solutions under magnetic stirring, and the samples were illuminated with a white LED lamp (16 mW cm^{-2}). At different time intervals, aliquots were taken, and EPR spectra were recorded. A similar procedure was performed using solutions without glycerol for comparison. Additionally, spin-trapping experiments were conducted using different $BiVO_4$ photoanodes paired with a Pt cathode under an applied bias and white light illumination. All EPR spectra were acquired using a Magnettech MiniScope MS 400 (Germany) at room temperature.

3.3. Results and Discussion

The pursue for efficient visible-light-active photocatalyst materials has drawn significant attention in the last decades (AHMED, MAHMOUD; DINCER, 2019; KIM, J. H. et al., 2019). In this context, $BiVO_4$ is highlighted the most promising material due to its broad light absorption across the UV-Vis spectrum, good balance between bang gap energy and recombination kinetics and favourable surface properties for the photoelectroreforming of biomass-derived molecules (LIU, D. et al., 2019; LI, T. et al., 2020; WU, Y.-H. et al., 2021). Additionally, $BiVO_4$ is the single photocatalyst with the

highest maximum theoretical Solar-to-Hydrogen efficiency (STH), highlighting its great light harvesting capabilities. However, it suffers from poor long-term performance due to the photocorrosion phenomena, in which VO^{4-} ions are released from the lattice (KE et al., 2023). Thus, $BiVO_4$ was doped with Nb^{5+}, as Nb^{+5} can easily replace V^{5+} atoms due to the similarity of the ionic radius of both cations, creating beneficial defects for photoelectrocatalytic applications, as reported by Kalanur and co-workers (KALANUR; SEO, 2022).

$BiVO_4$ samples dopped with different Nb^{5+} content were synthetized through an hydrothermal route. The goal was to fabricate photoanodes with optimal sunlight harvesting while maintaining the selective glycerol photoreforming displayed by the Bi_2WO_6-based photoanodes. The synthetized materials were analysed through XRD and Raman spectroscopy to elucidate its structural properties, Figure 17. The diffractograms of all samples were mainly indexed to the monoclinic phase with some tetragonal contribution, especially for the pure $BiVO_4$. The preferred orientation for all samples was the (1 1 2) plane at 28.97º with major contributions from the (0 0 4) crystalline plane at 34.55º, consistent with monoclinic $BiVO_4$ (OBREGÓN; CABALLERO; COLÓN, 2012; LOPES et al., 2016; DABODIYA; SELVARASU; MURUGAN, 2019). Moreover, the diffraction peaks shift to slightly lower angles as the Nb^{5+} content increases, indicating an expansion of the lattice parameters due to lattice distortion caused by Nb^{5+} insertion. This effect is attributed to the larger radius of Nb^{5+} (0.69 Å) (ZHANG, Y. et al., 2022) when compared to V^{5+} (0.50 Å), indicating the Nb^{5+} incorporation into the $BiVO_4$ lattice by replacing V^{5+} sites (YANG, X. et al., 2025). Raman spectra also show peaks characteristics to the monoclinic phase, particularly the signal at 830 cm^{-1} assigned to the asymmetric stretching of the tetrahedral V-O bonds. Bands around 320 and 367 cm^{-1} were attributed to asymmetric and symmetric deformation modes of the VO_4 tetrahedron. Additionally, the $BiVO_4$ sample also shows a less intense stretching peak at 248 cm^{-1} relative to the Bi-O symmetric vibration of the tetragonal phase. These bands are broadened as Nb content increases, with a pronounced effect on the bands associated with deformations in the VO_4^{3-} tetrahedra. This change indicates loss of the short-range arrangement due to Nb^{5+} doping at V^{5+} sites. Additionally, the slight shift of Raman features toward lower wavenumbers suggests changes in the short-range symmetry of the VO_4^{3-} tetrahedra, (DABODIYA; SELVARASU; MURUGAN, 2019; DABODIYA et al., 2024) further supporting the

hypothesis that Nb^{5+} doping occurs at V^{5+} sites. Additional characterizations were carried out for the 5% Nb:$BiVO_4$ sample and compared to the pristine $BiVO_4$.

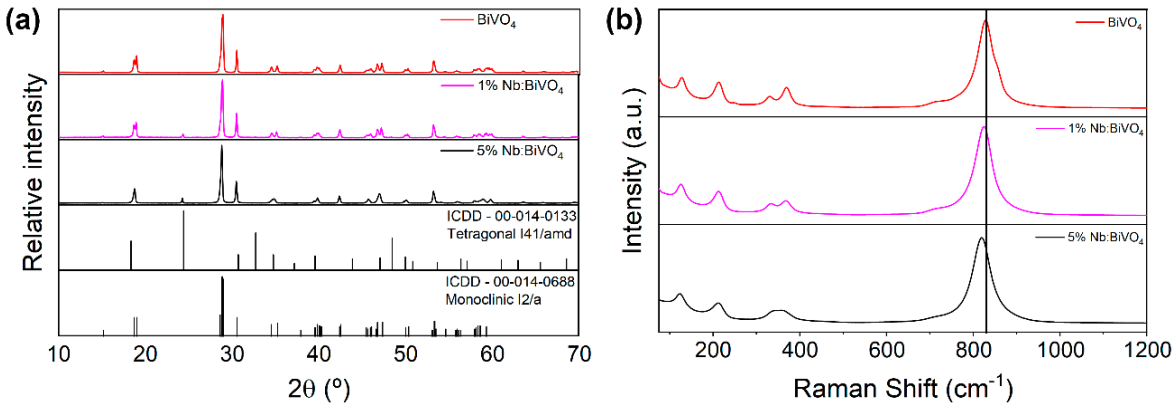

Figure 17. XRD and Raman of pristine $BiVO_4$ and Nb:$BiVO_4$ samples

X-ray photoelectron spectroscopy (XPS) was performed to analyze the surface composition and electronic properties of the different $BiVO_4$ samples Figure 18a shows the XPS survey spectra of all synthesized materials, indicating no significant contamination. The high-resolution XPS spectra in Figure 18b shows two distinct oxygen peaks for both the pristine and the 5% Nb doped $BiVO_4$ samples. The peak at lower binding energy corresponds to lattice oxygen (O_{lig}), while the less intense peak at higher binding energy is attributed to oxygen-adsorbed species and can be correlated to oxygen vacancies (O_{vac}) in the $BiVO_4$ surface (WANG, T. et al., 2021; XIAO, D. et al., 2024). The relative intensity of the oxygen vacancy peak is twice as high in the 5% Nb:$BiVO_4$ sample compared to $BiVO_4$, suggesting an increased concentration of oxygen vacancies due to niobium doping. In the spectral region of Nb 3d peak, Figure 18c, the expected doublet for Nb^{5+} species is observed, further confirming the presence of Nb(V) at the surface of 5% Nb:$BiVO_4$ (ZUBAIR et al., 2019; QARAAH et al., 2020; KALANUR; SEO, 2022). Elementary quantification of the surface reveals a niobium content of 5.1 ± 0.1% wt.% for the 5% Nb:$BiVO_4$ sample, while the vanadium content decreased by 4.9 ± 0.1% relative to the pristine sample, Table B1, corroborating the hypothesis that Nb^{5+} replaces V^{5+} in the lattice (KE et al., 2023).

EPR spectra measured at room temperature with microwave frequency of about 9.43 GHz of the different solid-state powders are shown in Figure 18d. The spectra show a broad paramagnetic resonance line (line with about 75(5) mT) with a

g factor of about 2.05 (5), typical of paramagnetic salts of transition metal ions (Nb^{4+}, V^{4+}) or a paramagnetic niobium oxygen vacancy complex. The highest EPR signal intensity is observed for the $BiVO_4$ sample doped with 5% of niobium, followed by the sample with 1% of Nb doping. The pristine sample does not show this broad paramagnetic signal. The results suggest that part of the Nb doped into the $BiVO_4$ samples is incorporated in the samples as Nb^{4+}, which is paramagnetic with spin S = ½ compared with Nb^{5+} that is diamagnetic. In a first look, this result is contradictory to the XPS analysis, in which only Nb^{5+} signals were clearly observed, but this is actually explained by the sensitivity of each technique. By comparing the EPR signal intensity with that of an anhydrous $CuSO_4$ standard powder sample, the concentration of the broad EPR signal in the 5% Nb:$BiVO_4$ sample is estimated to be approximately 10^{15} cm^{-3}. Assuming that Nb^{4+} is principally incorporated at the surface, maybe complexed with oxygen vacancies, the concentration of these defects in the surface region would be about 3 orders higher. This concentration is still below the detection limit for XPS spectroscopy, explaining missing Nb^{4+} transitions in the XPS spectra. One can conclude then, that the increased oxygen vacancy concentration on the Nb:$BiVO_4$ samples can be associated to the formation of Nb^{4+} species.

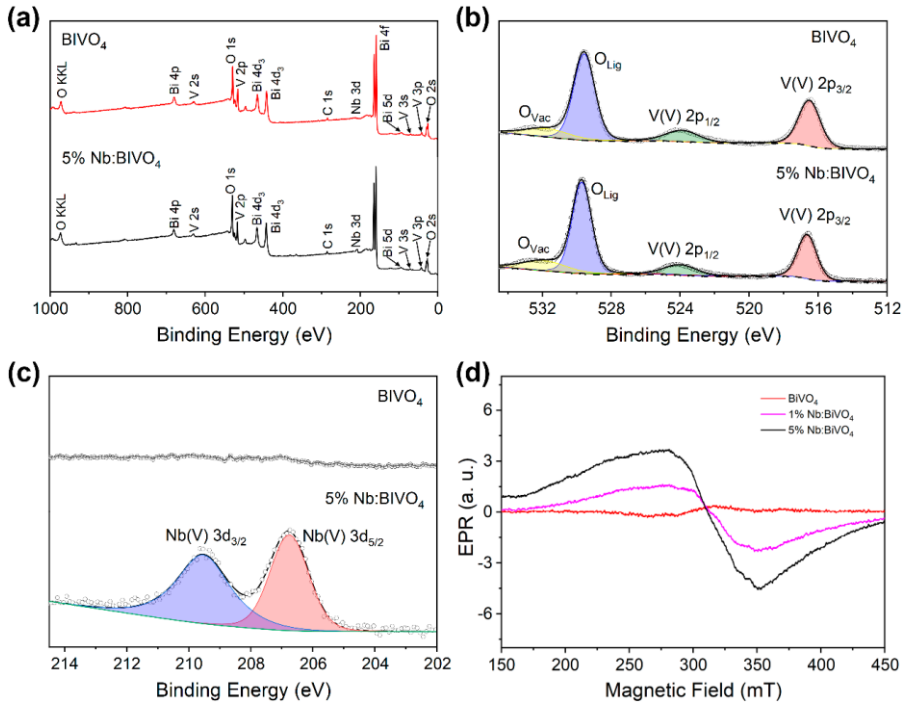

Figure 18. (a) Survey spectra of $BiVO_4$ and 5% Nb:$BiVO_4$, (b) high-resolution XPS spectra of V 2p and O 1s, (c) Nb 3d and (d) EPR spectra of the solid-state powder $BiVO_4$-based catalysts.

High-Resolution Transmission Electron Microscopy (HRMET) images, Figure 19a-d, show both $BiVO_4$ and 5% Nb:$BiVO_4$ samples with interplanar spaces of 0.31 nm attributed to the (112) plane of monoclinic $BiVO_4$, in good agreement with the XRD spectra in which high relative intensities for (112) lattice plane are observed for all samples.(PINGMUANG et al., 2015; WANNAKAN et al., 2023) Moreover, EDS elemental mapping of 5% Nb:$BiVO_4$ powder, Figure B1(a,f) shows the presence of niobium at the surface of the material.

The powder samples were, then, deposited onto clean FTO substrates using the screen-printing method. Scanning Electron Microscopy (SEM) images of the screen-printed photoanodes Figure 21a,b, show that the $BiVO_4$-based films are formed by homogeneous agglomeration of μm sized rods. Cross-section SEM images, Figure 20a, were taken to measure the thickness of the films. EDS mapping, Figure 20b-d, shows the area of covered by the 5% Nb:$BiVO_4$ film highlighted. The measured average thickness was 1.9 ± 0.2 μm.

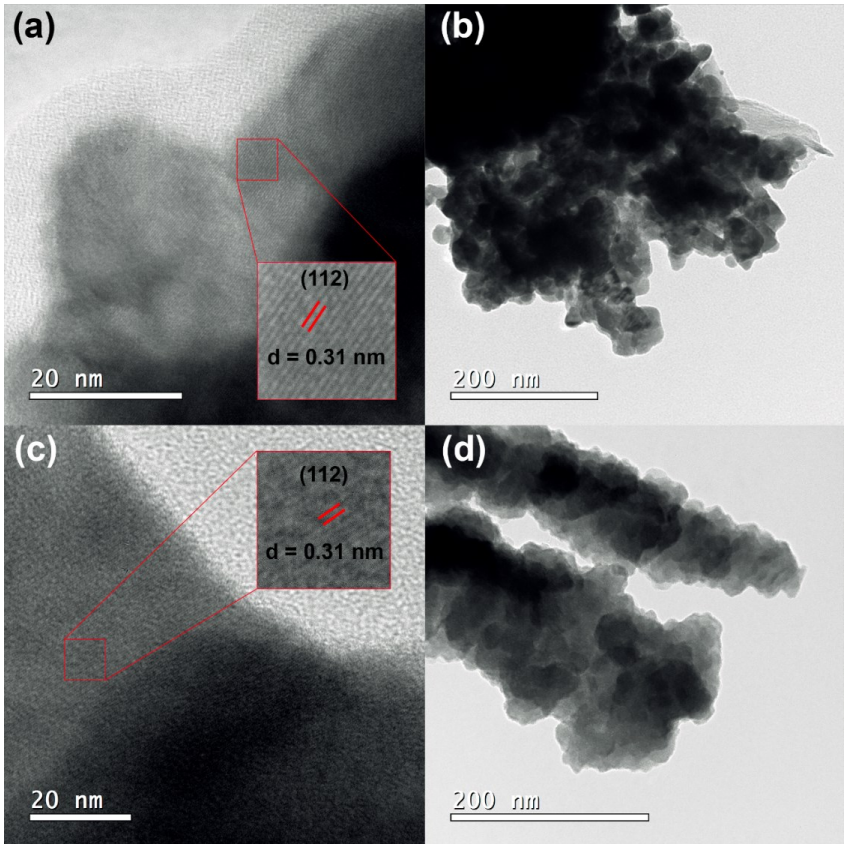

Figure 19. HRTEM images of (a,b) $BiVO_4$ and (c,d) 5% Nb:$BiVO_4$ at different magnification levels.

Diffuse reflectance measurements, Figure 21c, indicate that Nb^{5+} doping did not induce any drastic changes in the optical properties of $BiVO_4$. The strong absorption band up to 500 nm accounts for the intense yellow color of the photoanodes, Figure 21c (insert). All synthesized samples displayed a optical band gap energy of 2.45 ± 0.05 eV, Figure 21d, consistent with other $BiVO_4$ samples obtained through hydrothermal synthesis (OBREGÓN; CABALLERO; COLÓN, 2012; LOPES et al., 2016; CHEN, S.-H.; JIANG; LIN, 2020).

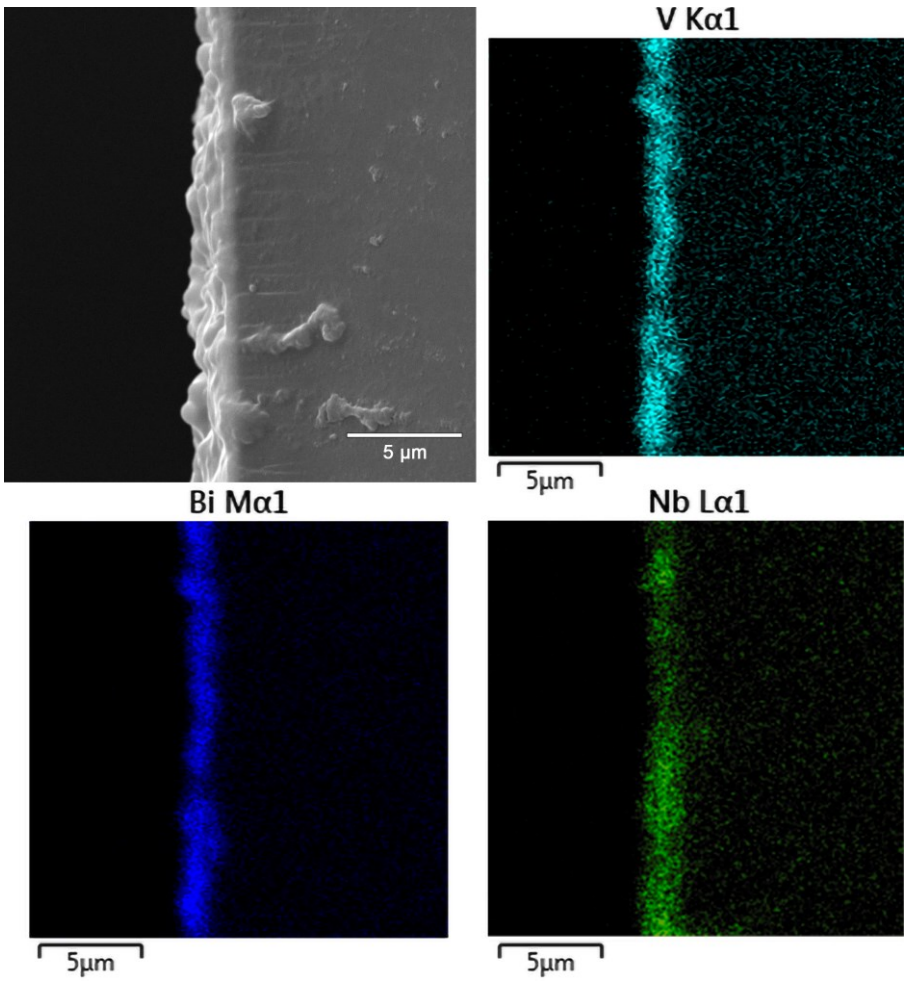

Figure 20. (a) Cross section SEM image of a 5% Nb:$BiVO_4$ film; EDS elemental mapping of (b) V, (c) Bi and (d) Nb.

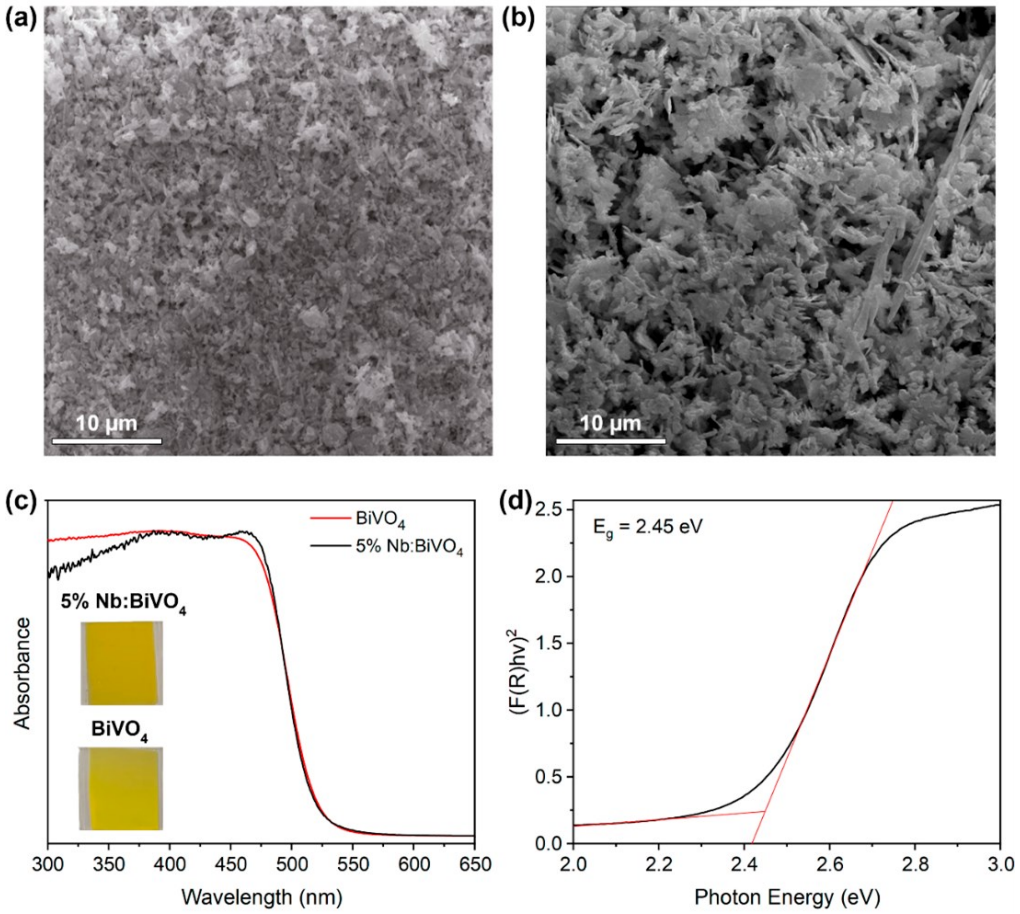

Figure 21. SEM images of thin films of (a) $BiVO_4$ and (b) 5% Nb:$BiVO_4$; (c) diffuse reflectance spectra of $BiVO_4$ and 5% Nb:$BiVO_4$ films and (d) Tauc plot of $BiVO_4$.

Electrochemical Impedance Spectroscopy (EIS) was employed to gain insights into the charge transport process in the obtained photoanodes. The EIS data, Figure B2, show that both pristine $BiVO_4$ and Nb-doped samples exhibit similar behavior under dark conditions, as expected, since the crystalline properties were not significantly affected by Nb^{5+} doping. However, under illuminated conditions, Figure 22a, the 5% Nb:$BiVO_4$ sample demonstrated significantly lower total impedance, when compared to the 1% Nb:$BiVO_4$ and the undoped sample, with both displaying a more capacitive response, characterized by higher phase angles when compared to the 5% Nb:$BiVO_4$, Figure 22b.

The EIS data was fitted using a simplified Randle's circuit as a model, Figure 22a (insert), in which R_s is the resistance of the electrolyte, C_{dl} is the capacitance of the double-layer and R_{ct} is the charge transfer resistance. The fitting data parameters, Table B2 , indicates no relevant changes in the electrochemical properties between $BiVO_4$ and 1% Nb:$BiVO_4$, however, the 5% Nb:$BiVO_4$ films showed a much lower

charge transfer resistance of 634 Ω under simulated sunlight, when compared to the 1290 Ω obtained by the pristine $BiVO_4$ film at the same conditions. This behavior was further investigated using Mott-Schottky plots, Figure 22c,d, which show that the 5% Nb:$BiVO_4$ films exhibit a charge carrier density of -8.15*10^{19} cm^{-3}, twofold higher than that compared to the pristine sample of -4.40*10^{19} cm^{-3}. On the other hand, the flat-band potential (V_{fb}) was not significantly affected by Nb^{5+} doping, with both samples displaying similar V_{fb} values ranging from -0.012 ($BiVO_4$) to 0.069 V vs RHE (5% Nb:$BiVO_4$), consistent with the literature (PARK et al., 2011; DRISYA et al., 2020; KALANUR; SEO, 2022). Thus, Nb^{5+} doping greatly improved charge transport, resulting in an increased charge carrier density across the photoanode surface, however, without significantly shift either the conduction band or the bandgap energy of $BiVO_4$.

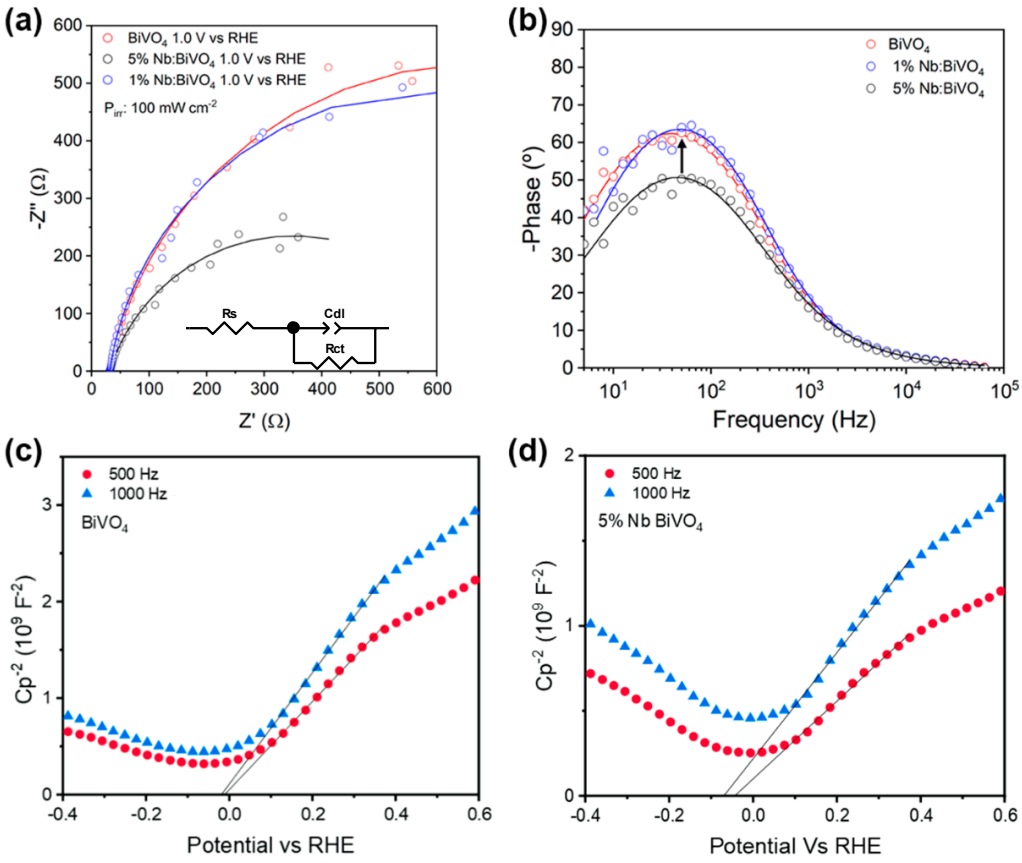

Figure 22. (a) EIS Nyquist plots of $BiVO_4$, 1% Nb:$BiVO_4$ and 5% Nb:$BiVO_4$ in 0.1 M K_2SO_4 at different potentials and 100 mW cm^{-2} illumination. (b) Bode plots under the same conditions. Mott-Schottky plots of (c) $BiVO_4$ and (d) 5% Nb:$BiVO_4$ under simulated sunlight (AM 1.5G 100 mW cm^{-2}).

EPR spin trapping experiments with DMPO (0.1 M) in distilled water suspensions (pH~6), containing 5%Nb:$BiVO_4$ powder under magnetic stirring show the formation of radical adducts under white light illumination. Figure 23a,b display the EPR spectra of DMPO spin adducts as a function of time in pure water and mixed water/glycerol (10%) suspensions. The radical adducts were identified by spectral simulation of the spectra using the Easyspin@ routine in Matlab, Figure 23c. The two DMPO adducts were identified as DMPO-•OH and DMPO-•R. The EPR spectrum of DMPO-•OH adduct is characterized by a hyperfine interaction between the electron spin S = ½ and the nuclear spin I = 1 (from ^{14}N) and the nuclear spin I = ½ (from ^{1}H) leading to $a_N = a_{H\beta}$ = 1.49 mT, resulting in the well-known four-line spectrum with intensity ratios of 1:2:2:1 (BUETTNER, 1987). The EPR spectrum of DMPO-•R adduct is described by a six-line spectrum with equal intensities and hyperfine parameters of a_N = 1.57 mT and $a_{H\beta}$ = 2.29 mT.. This latter DMPO adduct is less specific, but it is probably of organic nature attributed to a carbon-centered radical adduct of DMPO ($a_{H\beta} > a_N$) and references therein, different to the DMPO-•OH adduct, which is oxygen-centered ($a_N > a_{H\beta}$). In mixed water/glycerol (10%) suspension, DMPO formed two different spin adducts, while only one spin adduct was observed in pure water. These results indicate that the organic radical is produced from glycerol, while hydroxyl radicals from water. The concentration of the organic radicals depends on the ratio of water/glycerol mixture. Higher glycerol ratio increased the related EPR DMPO-•R adduct concentration (not shown).

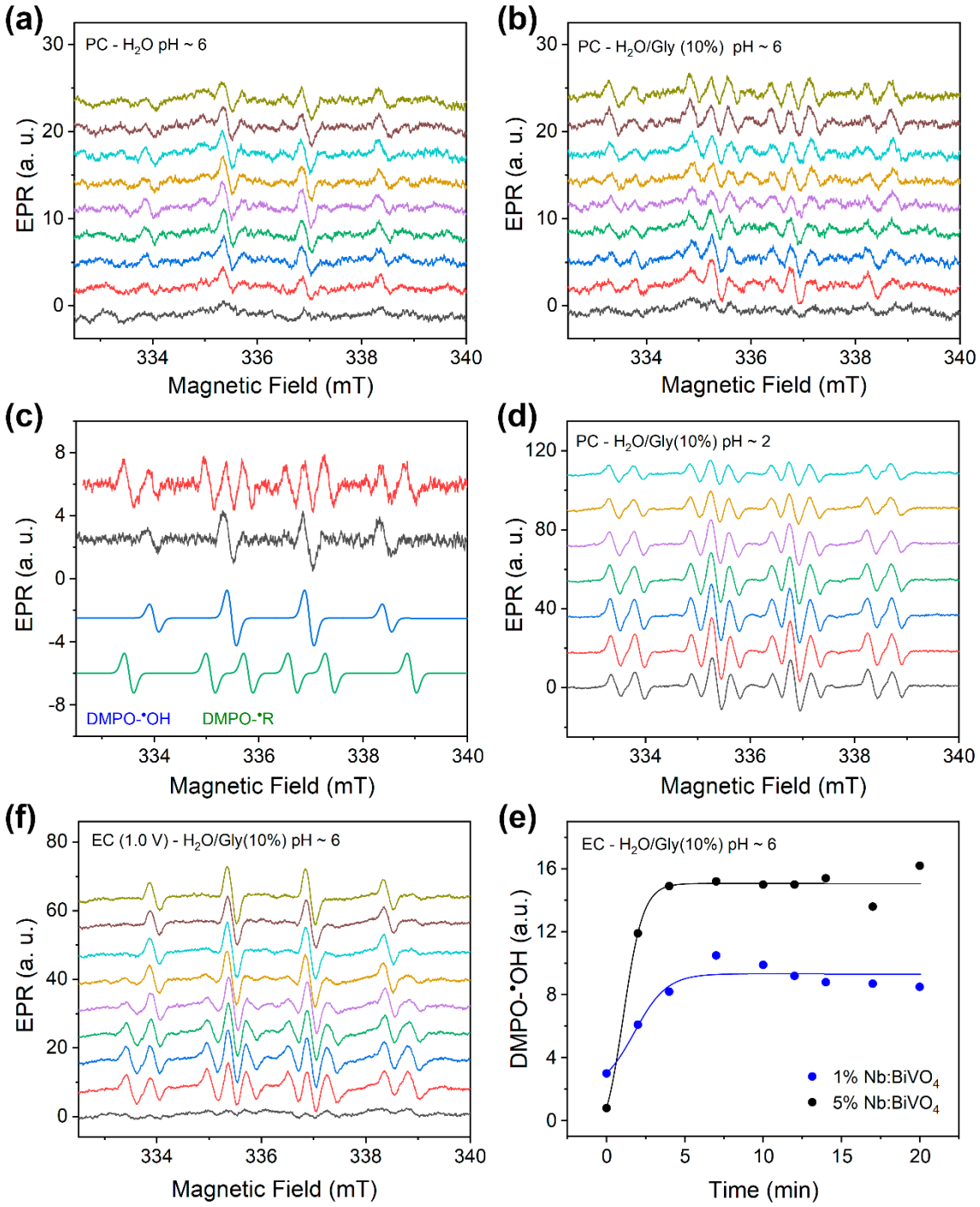

Figure 23. Formation of DMPO spin adducts during spin trapping experiments for 5% Nb:$BiVO_4$ photocatalyst powder under white light (0 – 20 min) for (a) distilled H_2O and (b) H_2O containing 10% of analytical glycerol at pH ~ 6; EPR spectra calculations using Easyspin® identifying DMPO-•OH and DMPO-•R spin adducts; (d) same as in (b) but at pH ~ 2; (e) same as in (b) but using a $BiVO_4$: Nb(5%) photoanode coupled with Pt cathode with applied bias of about 1.0 V; and (f) DMPO-•OH spin adduct concentration as a function of time using different Nb doped $BiVO_4$ photoanodes.

Acidic pHs also favors the formation of these organic radicals. The reaction kinetics are strongly influenced by the pH of the solution. When doing the same spin trapping experiments at pH ~ 2, the same DMPO spin adducts were observed as for pH ~ 6, however with increased concentrations, Figure 23d, similar result reported elsewhere [13]. On the other hand, in mixed water/ glycerol (10%) suspensions at pH ~ 2, we noticed also some formation of spin adducts in the dark (not shown).

When doing the spin trapping experiments with the 5% Nb:$BiVO_4$ photoanode coupled to Pt cathode under a bias of about ~1.0 V vs RHE in the presence of DMPO (0.2 M) in mixed water/glycerol (10%) solution and K_2SO_4 electrolyte (0.1 M) at pH ~ 6 the EPR results, Figure 23e, reveal the formation of the same spin adducts observed before, however, with higher intensities, indicating an accelerated kinetics of the reactions and higher yield for the formation of $^{\bullet}OH$ radicals. Comparing different $BiVO_4$ photoanodes, Figure 23f, the higher Nb^{5+} doped sample (5 %) showed higher efficiency (~ 35 %) in the formation of DMPO-$^{\bullet}OH$ adducts under white light illumination than the undoped $BiVO_4$ or 1% Nb:$BiVO_4$ ones. These results indicate a significantly enhanced ability to generate organic radicals and hydroxyl radicals, which aligns with the EIS results, as the 5% Nb:$BiVO_4$ photoanode also exhibited a higher charge carrier density compared to pristine $BiVO_4$. Moreover, radical formation is largely dependent on the applied bias and illumination, correlating with the much lower charge transfer resistance due to surface defects (oxygen vacancies and/or Nb^{4+} ions) as observed for 5% Nb:$BiVO_4$ films under illumination.

Our findings with DMPO EPR spin trapping align well with the reaction mechanism proposed before (BUETTNER, 1987). Dong Liu et al. utilized a nanoporous $BiVO_4$ photoanode for the photoelectrochemical oxidation of glycerol and discovered that glycerol strongly adsorbs onto the $BiVO_4$ surface. In the initial step of reaction, the adsorbed glycerol molecules are converted into glycerol radicals through direct hole oxidation. These radicals then react with water from the electrolyte, followed by a dehydration step leading to different subproducts of glycerol. In our experiments using DMPO EPR spin trapping, we also observed the generation of organic radicals, although their exact nature remains unknown. Additionally, we detected hydroxyl radicals (see Figure 19. 6 a,b), which may play an important role in guiding the complex photoreforming reaction mechanisms of glycerol towards different subproducts.

The pristine and Nb-doped $BiVO_4$ films were applied as photoanodes in photoelectrochemical cells for photoelectroreforming of crude glycerol and flegmass, Figure B3. For reference, experiments with purified glycerol (glycerin) were also carried out. The glycerol residue was collected at a soybean biodiesel plant and its composition consists of glycerin, with several contaminants such as water, ethanol, methanol and many solid impurities. Flegmass residue is an aqueous byproduct from sugarcane ethanol distillation, consisting of a mixture of various organic compounds, which include ethanol, organic acids and fusel alcohols, such as isobutanol, isoamyl alcohol, and propanol. Although the organic content of the employed sample was relatively high (chemical oxygen demand of 3000 mg mL^{-1}), the concentration of each organic species is small. Ethanol was identified as the main constituent of flegmass, albeit in concentrations below 5% m/m, along with traces of isoamyl alcohol. Flegmass composition is highly dependent on the species of sugarcane used, the fermentation conditions and the following processing steps.

Light-chopped linear sweep voltammograms (LSVs), Figure 24, shows all tested photoanodes with a similar photoresponse profile, consisting of a sharp increase in photocurrent upon light exposure and a prompt decrease when the light is switched off. The LSVs with glycerin (Figure 24a) show that the 5% Nb:$BiVO_4$ photoanode achieved the highest photocurrent, approximately 70% higher than that of the pristine $BiVO_4$ sample, which in turn produced similar photocurrents than the 1% Nb:$BiVO_4$ photoanodes. When crude glycerol was used, Figure 24b, the same trend was observed, although the overall photocurrent was 20% lower. Finally, with flegmass, Figure 24c, the 5% Nb:$BiVO_4$ photoanodes yielded the same level of photocurrent as with pure glycerin, showing nearly 100% increase compared to the other photoanodes. Under all tested conditions, the 5% Nb:$BiVO_4$ films consistently outperformed the others, while the 1% Nb:$BiVO_4$ and pristine $BiVO_4$ films produced similar results, suggesting that lower Nb^{5+} doping levels did not significantly impact $BiVO_4$ performance.

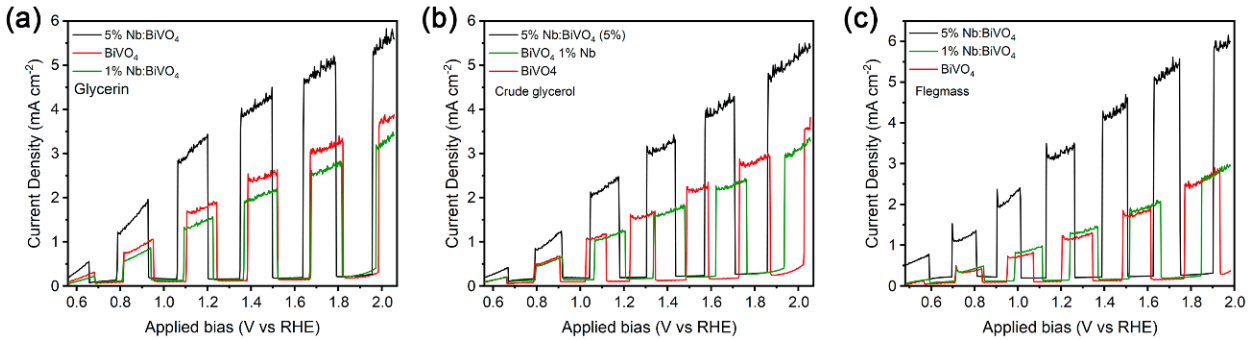

Figure 24. Light-chopped linear sweep voltammetries of pristine $BiVO_4$, 1% and 5% Nb:$BiVO_4$ films in (a) glycerin 10% v/v in K_2SO_4 0.1M, (b) crude glycerol 10% v/v in K_2SO_4 0.1M and (c) raw flegmass with added 0.1 M K_2SO_4.

Long-term photoreforming of crude glycerol was conducted using pristine $BiVO_4$ and 5% Nb:$BiVO_4$ films, as the latter exhibits the best-performing among the Nb-doped photoanodes. The 5% Nb:$BiVO_4$ yielded a higher oxidative photocurrent, Figure 25a, converting 91.4% of glycerol, compared to 73.3% for pristine $BiVO_4$, after 6 hours of irradiation (A.M. 1.5 100 mW cm^{-2}). The H_2 evolution rate was also significantly higher for 5% Nb:$BiVO_4$, reaching 4.2 μmol H_2 cm^{-2} h^{-1} versus 2.3 μmol H_2 cm^{-2} h^{-1} with $BiVO_4$, Figure 25b. The Faradaic efficiency for H_2 evolution was 96% for 5% Nb:$BiVO_4$ and 98% for $BiVO_4$, indicating that crude glycerol photoreforming is viable for sustained green H_2 production. Regarding oxidation products, formic acid was the main product for both pure glycerin and raw glycerol, with a C-based selectivity of 88.9% for 5% Nb:$BiVO_4$ and 71.1% for $BiVO_4$. Other minor products, including oxalic acid (2%), acetic acid (5%), and dihydroxyacetone (< 1%), were also detected. The superior performance observed for the 5% Nb:$BiVO_4$ photoanodes can be explained by the increased charge carrier density, decreased charge transfer resistance at the $BiVO_4$/electrolyte interface and the higher presence of reactive surface states due to the Nb^{5+} doping.

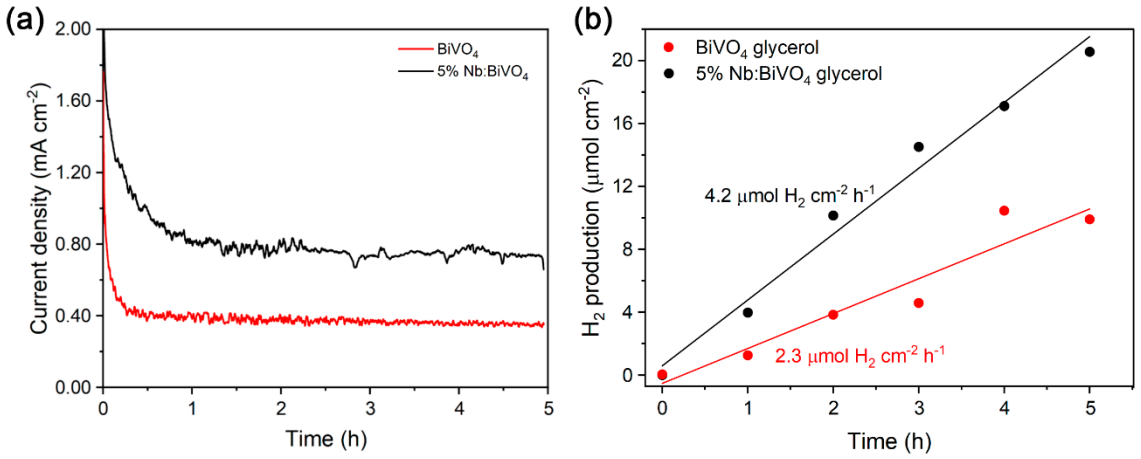

Figure 25. (a) Chronoamperometry graphs of $BiVO_4$ and 5% Nb:$BiVO_4$ in crude glycerol 10% /v in K_2SO_4 0.1M under, 1.0 V vs RHE and 100 mW cm^2 AM1.5G illumination. (b) H_2 evolution from an average of 3 chronoamperometry experiments for $BiVO_4$ and 5% Nb:$BiVO_4$ photoanodes.

A similar behavior was observed when flegmass was used as a sacrificial agent in long-term photoreforming experiments. The current density was consistently higher for 5% Nb:BiVO4, Figure 26a, which also resulted in a higher H_2 evolution rate of 2.4 μmol H_2 cm^{-2} h^{-1}, compared to 0.42 μmol H_2 cm^{-2} h^{-1} achieved with the pristine $BiVO_4$ photoanode, Figure 26b. As flegmass is a more complex matrix than crude glycerol, the quantification and identification of liquid oxidation products proved challenging. Acetic acid was the primary oxidation product for both samples, and the performance was evaluated based on Chemical Oxygen Demand (COD) removal for both materials, Figure 27. Once again, 5% Nb:$BiVO_4$ exhibited superior COD removal of up to 51%, compared to 24% for $BiVO_4$ after 12 h irradiation, Fig 10. These results are promising, especially given that flegmass was used as received, without dilution or pre-treatment, an important consideration for enabling practical applications.

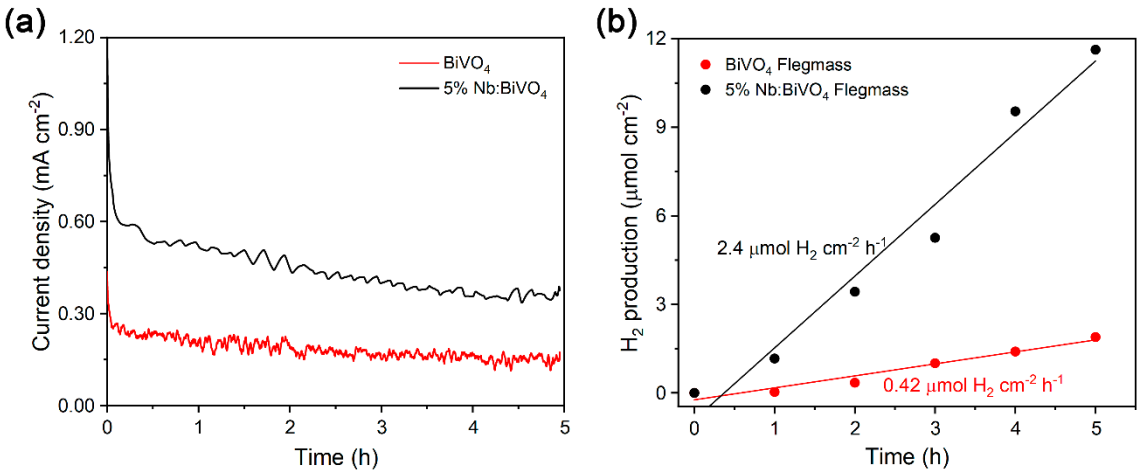

Figure 26. (a) Chronoamperometry graphs of $BiVO_4$ and 5% Nb:$BiVO_4$ in raw flegmass with added K_2SO_4 0.1 M, under 1.0 V vs RHE and 100 mW cm^2 AM1.5G illumination. (b) H_2 evolution from an average of 3 chronoamperometry experiments for $BiVO_4$ and 5% Nb:$BiVO_4$ photoanodes.

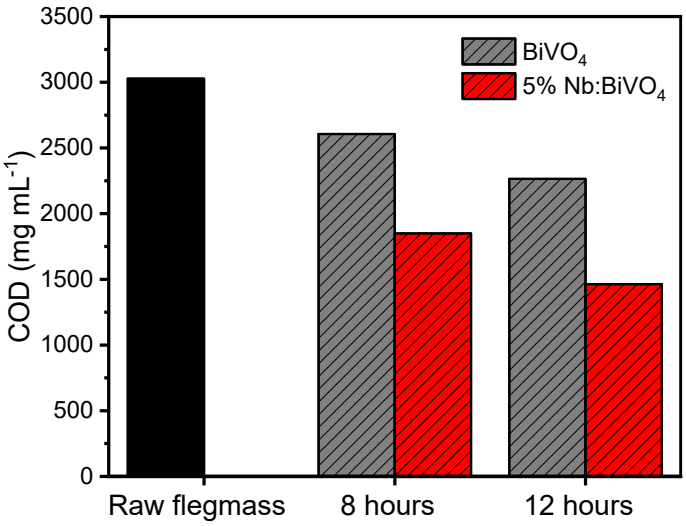

Figure 27. COD removal from flegmass after photoreforming experiments with different durations.

Other researchers have explored similar strategies to enhance the biomass photoelectroreforming capabilities of $BiVO_4$. Some representative results are shown in Table 5. Bora and co-workers reported Mo-doped $BiVO_4$ photoanodes with improved current density in the presence of glycerol (BORA et al., 2022). This enhancement was attributed to the formation of a capacitance layer and a reduction in charge transfer resistance on the photoelectrode, described as a photocharging phenomenon. However, no direct comparison was made with pristine $BiVO_4$

photoanodes. Similarly, Tateno et al. investigated the effect of Ta-doping on $BiVO_4$ photoanodes for the photoelectrochemical oxidation of glycerol (TATENO et al., 2022). They observed a significant increase in photocurrent of over 60% compared to undoped $BiVO_4$, along with enhanced photoanode stability in acidic electrolytes. Notably, Ta doping did not significantly alter the band positions or structural properties of $BiVO_4$, similarly to what we have observed for Nb-doped samples. However, Nb doping resulted in a superior increase of 80% in photocurrent evidencing its effectiveness in improving $BiVO_4$-based photoanodes.

Table 5. Photocurrent density of metal-doped $BiVO_4$ photoanodes compared to this work, under glycerol photoreforming conditions with AM 1.5 G, 100 mW cm^{-2} illumination, and 1.0 V vs RHE.

Photoanode	**Undoped $BiVO_4$ photocurrent density[a]**	**Metal-doped $BiVO_4$ photocurrent density[a]**	**Experimental remarks**	**Ref.**
W:$BiVO_4$	NA	3.1 mA cm^{-2}	0.5 M potassium borate buffer with 0.1 M glycerol	(WU, Y.-H. et al., 2021)
Mo:$BiVO_4$	NA	4.6 mA cm^{-2}	Glycerol 20% v/v with 0.1 M phosphate buffer. After photocharging effect	(BORA et al., 2022)
Ta:$BiVO_4$	1.6 mA cm^{-2}	2.6 mA cm^{-2}	Glycerol 1.0 M with H_2SO_4 25 mM	(TATENO et al., 2022)
Nb:$BiVO_4$	1.2 mA cm^{-2}	2.2 mA cm^{-2}	Glycerol 10% v/v with 0.1 M K_2SO_4	This work
Nb:$BiVO_4$	0.8 mA cm^{-2}	2.4 mA cm^{-2}	Flegmass with added 0.1 M K_2SO_4	This work

a: Estimated based on reported LSV curves (± 0.1 mA cm^{-2}).

In summary, Nb doping at 1% and below did not significantly affect the properties of $BiVO_4$. However, when the Nb content was increased to 5 wt.%, charge transfer across the photoanode bulk and surface was enhanced, as evidenced by the higher charge carrier density and significantly lower charge transfer resistance of the 5% Nb:$BiVO_4$ photoanode compared to pristine $BiVO_4$, which was attributed to the

introduction of Nb^{5+} in the lattice and surface defects (oxygen vacancies and/or Nb^{4+} species). This improvement was reflected in the photoreforming results, where 5% Nb:$BiVO_4$ demonstrated more than twice the photocurrent and hydrogen evolution from both glycerol and flegmass photoreforming, compared to pristine $BiVO_4$. The excellent performance is followed by improved stability under irradiation and in the presence of real biomass-derived residues, which is a proof of concept for possible large-scale application of photoelectroreforming.

3.4. Conclusions

Niobium-doped $BiVO_4$ was synthesized via a facile hydrothermal method, varying the niobium doping content. Nb^{5+} occupied V^{5+} sites mainly at the surface, yielding oxygen vacancies, which are beneficial to the photoelectrochemical performance. The materials were then screen-printed into thin films and tested for the photoelectroreforming of real industrial biomass-derived wastes: crude glycerol and raw flegmass. The $BiVO_4$ sample doped with 5% Nb content demonstrated superior performance, converting 91.4% of glycerol with 88.9% selectivity toward formic acid formation after 5 hours of simulated sunlight illumination, achieving a low-carbon H_2 production rate of 4.2 μmol H_2 cm^{-2} h^{-1}, 84% higher than that of unmodified monoclinic $BiVO_4$. 5% Nb:$BiVO_4$ photoanodes also exhibit better performance for flegmass photoelectroreforming, showing a sixfold increase in H_2 production and twice the COD removal efficiency compared to pristine $BiVO_4$. The improved performance of 5% Nb:BiVO4 was attributed to increased charge density, decreased charge transfer resistance at photoanode/electrolyte interface and surface defect states caused by the Nb^{5+} doping. The present work brings a sustainable approach for green H_2 production using real industrial waste streams as platform, an important step towards a cleaner society.

4. Covalent Organic Frameworks (COFs) for enhanced photocatalytic hydrogen evolution over Pt co-catalyst

Covalent Organic Frameworks (COFs) are an emerging class of crystalline, porous materials constructed from light elements (typically C, H, B, N, and O) linked through strong covalent bonds. Their modular and tunable design allows for precise control over structural, chemical, and optoelectronic properties, making them highly attractive for applications in catalysis, energy storage, gas separation, and photocatalysis. Recently, COFs has drawn attention as a new class of organic photocatalysts for the photocatalytic hydrogen evolution reaction (HER). While the influence of COF structural and optoelectronic properties on HER is well-studied, the role of surface charge in optimizing interfacial interactions with reactants remains underexplored.

The present study explores and demonstrates the effect of different protonation behavior of imine-and amide-linked COFs in acidic conditions on the COF's surface charge and photocatalytic HER. The imine-linked COF was synthesized from benzo[1,2-b:4,5-b′]-dithiophene-2,6-dicarboxaldehyde (BDT) and 4-fold amine functionalized tetraphenylethylene (1,1′,2,2′-tetra-p-aminophenylethylene) (ETTA) building blocks under solvothermal conditions. A post-modification method was applied to induce imine-to-amide linkage conversion. This approach resulted in a crystalline Amide-BDT-ETTA COF, which demonstrated a 300% increase in photocatalytic HER rate compared to its imine form. Zeta potential measurements of the suspensions of the COFs in the presence of ascorbic acid serving as an electron donor reveal a switch from positive to negative surface charge of the COF upon imine-to-amide linkage conversion. The influence of the surface charge on the mechanism of the in situ Pt-photodeposition and subsequent proton reduction will be discussed among the observed changes in hydrophilicity, and optoelectronic properties.

4.1. Specific Objectives

The specific objectives for the work showed this chapter were:

- Synthetize COFs using benzo[1,2-b:4,5-b′]-dithiophene-2,6-dicarboxaldehyde (BDT) and 4-fold amine functionalized tetraphenylethylene (1,1′,2,2′-tetra-p-aminophenylethylene) (ETTA) building blocks
- Convert imine to amide linkages with high yields in the BDT-ETTA COF

- Compare the performance of both amide and imine COFs for photocatalytic hydrogen evolution over *in situ* photoreduced Pt^0 co-catalyst sites
- Study the effect of different protonation behavior of imine-and amide-linked COFs in acidic conditions on the COF's surface charge, Pt particle growth and photocatalytic hydrogen evolution

4.2. Methodology

Imine-BDT-ETTA COF was prepared by suspending BDT (benzo[1,2-b:4,5- b′]dithiophene-2,6-dicarboxaldehyde, 74 mg, 0.30 mmol) and ETTA (1,1,2,2-tetra(p-aminophenyl)ethylene, 58.6 mg, 0.15 mmol) in a solvent mixture of benzyl alcohol and mesitylene (v/v 9:1, 5 mL) in a 25 mL Schott-Duran vial, under argon atmosphere. Acetic acid (6 M, 500 µL) was added to the vessel, and the mixture was placed in a preheated oven at 120 °C for 3 days. The resulting orange precipitate was vacuum filtered, Soxhlet-extracted with dry THF, and dried under reduced pressure, yielding 70 mg of the final material (53% yield).

Conversion of BDT-ETTA from imine to amide linkages, resulting in Amide-BDT-ETTA COF, was adapted from the literature (WALLER et al., 2016). 10 mg of Imine-BDT-ETTA was dispersed in 10 ml of dioxane and the mixture was ultrasonicated for 30 min to obtain a uniform dispersion. The mixture was then centrifuged to separate the solid and liquid phases, and the excess dioxane was removed to obtain a final volume of 1 ml. 2-methyl-2-butene (1274 µL, 12.0 mmol, 480 equiv), aqueous sodium chlorite solution (200 µL, 3.3 M, 0.66 mmol, 26.4 equiv), and glacial acetic acid (68.8 µL, 1.2 mmol, 48 equiv) was added in sequence to a suspension of Imine-BDT-ETTA (10 mg, 0.025 mmol by imine) in dioxane (1 mL). The biphasic suspension was let stand without stirring at room temperature in the dark for 48 h, after which an additional portion of sodium chlorite solution (200 µL, 3.3 M, 0.66 mmol, 26.4 equiv) was added. Thereafter, Amide-BDT-ETTA was isolated by filtration and washed with water (10 mL), then 10% sodium thiosulfate (10 mL), then water (10 mL) and finally acetone (10 mL). This resulting powder was Soxhlet-extracted with methanol and dry THF in sequence, followed by drying under reduced vacuum at room temperature for 16 h, yielding 4 mg of the final material (40% yield).

Reference-COF-1 was prepared by dispersing 10 mg of Imine-BDT-ETTA in 10 ml of dioxane and the mixture was ultrasonicated for 30 min to obtain a uniform dispersion. The mixture was then centrifuged to separate the solid and liquid phases, and the excess dioxane was removed to obtain a final volume of 1 ml. To a final suspension of Imine-BDT-ETTA (10 mg, 0.025 mmol by imine) in dioxane (1 mL) was added 2-methyl-2-butene (1274 µL, 12.0 mmol, 480 equiv), and glacial acetic acid (68.8 µL, 1.2 mmol, 48 equiv) in sequence. The biphasic suspension was let stand without stirring at room temperature in the dark for 48 h, after which Reference-COF-1 was isolated by filtration and washed with water (10 mL), then 10% sodium thiosulfate (10 mL), then water (10 mL) and finally acetone (10 mL). The resulting material was Soxhlet-extracted with methanol and dry THF in sequence, followed by drying under reduced vacuum at room temperature for 16 h.

Reference-COF-2 was prepared by dispersing 10 mg of Imine-BDT-ETTA in 10 ml of dioxane and the mixture was ultrasonicated for 30 min to obtain a uniform dispersion. The mixture was then centrifuged to separate the solid and liquid phases, and the excess dioxane was removed to obtain a final volume of 1 ml. To a final suspension of Imine-BDT-ETTA (10 mg, 0.025 mmol by imine) in dioxane (1 mL) was added 2-methyl-2-butene (1274 µL, 12.0 mmol, 480 equiv), aqueous sodium chlorite solution (40 µL, 3.3 M, 0.66 mmol, 26.4 equiv), and glacial acetic acid (68.8 µL, 1.2 mmol, 48 equiv) in sequence. The biphasic suspension was let stand without stirring at room temperature in the dark for 48 h, after which Reference-COF-2 was isolated by filtration and washed with water (10 mL), then 10% sodium thiosulfate (10 mL), then water (10 mL) and finally acetone (10 mL). The resulting material was Soxhlet-extracted with methanol and dry THF in sequence, followed by drying under reduced vacuum at room temperature for 16 h.

Reference-COF-3 was prepared by dispersing 10 mg of Imine-BDT-ETTA in 10 ml of dioxane and the mixture was ultrasonicated for 30 min to obtain a uniform dispersion. The mixture was then centrifuged to separate the solid and liquid phases, and the excess dioxane was removed to obtain a final volume of 1 ml. To a final suspension of Imine-BDT-ETTA (10 mg, 0.025 mmol by imine) in dioxane (1 mL) was added 2-methyl-2-butene (1274 µL, 12.0 mmol, 480 equiv), and aqueous sodium chlorite solution (200 µL, 3.3 M, 0.66 mmol, 26.4 equiv in sequence. The biphasic suspension was let stand without stirring at room temperature in the dark for 48 h, after which Reference-COF-3 was isolated by filtration and washed with water (10 mL),

then 10% sodium thiosulfate (10 mL), then water (10 mL) and finally acetone (10 mL). The resulting material was Soxhlet-extracted with methanol and dry THF in sequence, followed by drying under reduced vacuum at room temperature for 16 h.

Nitrogen sorption isotherms were recorded on a Quantachrome Autosorb 1 at 77 K within a pressure range from P/P_0 = 0.001 to 0.98. Prior to the measurement of the sorption isotherms, the samples were heated for 24 h at 120 °C under turbo-pumped vacuum. For the evaluation of the surface area the BET model was applied between 0.05 and 0.28 P/P_0. Pore size distributions were calculated using the QSDFT equilibrium model with a carbon kernel for cylindrical pores. Solid state ^{13}C NMR analysis. The solid state ^{13}C cross-polarization magic angle spinning (CP/MAS) spectra were obtained on a Bruker Avance III-500 solid state NMR spectrometer with a 4 mm double resonance MAS probe and at a MAS rate of 10.0 kHz with a contact time of 2-5 ms and a pulse delay of 4 s. Powder X-ray diffraction measurements were performed on a Bruker D8 Discover diffractometer using Ni-filtered Cu Kα radiation and a position sensitive LynxEye detector in Bragg-Brentano geometry.

The structure models of the COFs were constructed on the basis of the previously reported Imine-BDT-ETTA COF structure (SICK et al., 2018) using the Accelrys Materials Studio software package. For each COF *P6* symmetry was applied. The structure models were optimized using the Forcite module with the Dreiding force-field. Structure refinements using the Pawley method were carried out as implemented in the Reflex module of the Materials Studio software. Thompson-Cox-Hastings peak profiles were used, and peak asymmetry was corrected using the Berar-Baldinozzi method.

Infrared (IR) spectra were recorded on a Perkin Elmer Spectrum BX II FT-IR system and a Thermo Scientific Nicolet™ 6700 FT-IR spectrometer in transmission mode. IR data are reported in wavenumbers (cm^{-1}). Scanning electron microscopy (SEM) images. SEM images were recorded with an FEI Helios NanoLab G3 UC scanning electron microscope equipped with a field emission gun operated at 3 kV. Prior to the measurements, the samples were sputtered with carbon. Transmission electron microscopy (TEM) images. TEM images were recorded with an FEI Titan Themis 60 - 300 equipped with a field emission gun operated at 300 kV. X-ray photoelectron spectroscopy (XPS) measurement. The XPS measurements were performed with a VSW TA10 X-ray source providing non-monochromatized Al Kα radiation ($h\nu$ = 1486.6 eV) set at 15 mA and 12 kV and a VSW HA100

hemispherical analyzer. The spectra were recorded with a pass energy of 22 eV and a dwell time of 0.1 s per measurement point. The samples were prepared by drop-casting a dispersion of the respective COF powder in acetonitrile on a silicon wafer. After drying the samples by 60 ºC for 24 h they were transferred to the UHV chamber. The obtained spectra were fitted in Igor Pro 6.0.2.4 using a convolution of Doniach-Ŝunjić and Gaussian functions after a linear background subtraction.

For each photocatalytic assay, 5 mg of the as-prepared COFs were dispersed in 50 mL of ascorbic acid (H_2A) aqueous solution with concentration varying from 2 to 10 mM. Following, a proper amount of platinum precursor (H_2PtCl_6) was added to the suspension in order to obtain 1.0 wt% of platinum loading. The suspension was sonicated for 30 minutes. A custom-made jacketed borosilicate reactor was used to conduct the photocatalytic reactions, which was kept at 20 ºC through a circulating bath. The reactor was illuminated by a Newport 300 W arc Xe lamp, using a 420 nm LP filter. The irradiation intensity was adjusted to 100 mW cm^{-2} using a Newport 1916-C powermeter equipped with an 818-UV/DB optical detector.

During the H_2 evolution experiments, aliquots of 500 µL were sampled from the headspace of the reactor, using a gas-tight syringe, and then injected in a PerkinElmer Clarus 580 gas chromatograph equipped with a thermal conductivity detector (GC-TCD). A molecular sieve coupled with a Porapak N column was used to separate the gas products. Argon was used as carrier gas at 10 mL min^{-1} and the TCD filament was kept at 250 ºC. The produced H_2 was quantified using a calibration curve, which was obtained by sampling known concentrations of analytical standard H_2 under the same experimental conditions as the photocatalytic assays.

The photonic efficiency of a photocatalytic system is determined by the ratio between the number of reacted molecules and the number of incident photons. It is expressed as follows:

$$\xi = \frac{v_{H2}}{I_0} \times 100\%$$

Where v_{H2} represents the H_2 evolution rate (mol s^{-1}) and I_0 is the photon flux at 450 nm (einstein s^{-1}), the wavelength at which both samples exhibit maximum absorption.

COF working electrodes were prepared using an ink made by mixing 5 mg of COF and 3 mg of carbon black in 50 uL of Nafion (~5 % in a mixture of lower aliphatic alcohols and water) and 450 uL of dimethylformamide. The mixture was then

sonicated for 30 minutes. Subsequently, the prepared ink was drop-cast onto the surface of clean FTO glass. The obtained films were dried under vacuum and then used as anodes for the electrochemical experiments. The electrochemical setup was made of a single chamber electrochemical cell, filled with 0.1 M NBu_4PF_6 in acetonitrile, using a Pt wire as counter electrode and Ag as pseudo-reference standardized to the ferrocene/ferrocenium couple. The CV measurements were carried out on an Autolab PGSTAT204 potentiostat/galvanostat at 0.1 V s^{-1} scan speed. The pH dependent absolute potential for the HER was calculated as follows:

$E_{Abs,\ pH}$ = -4.5 eV + 0.059 · pH

The band edges of the studied COFs were calculated considering that the absolute energy of the Fc/Fc^+ redox couple is -5.14 eV relative to the vacuum level, as described elsewhere (SICK et al., 2018).

Zeta potential measurements were recorded using a Malvern Zetasizer instrument at room temperature using 10 mm path length cuvettes by determining the electrophoretic mobility and then applying the Henry equation. The electrophoretic mobility was obtained by performing an electrophoresis experiment on the sample and measuring the velocity of the particles using Laser Doppler Velocimetry (LDV).

Henry equation:

$$\zeta = \frac{3\eta U_e}{2\varepsilon f(\kappa a)}$$

ζ: zeta potential, calculated from electrophoretic mobility (mV),

η: viscosity of the medium (in this study 0.8872 mPa s),

U_e: electrophoretic mobility, measured directly in a given sample in each round of experiment ($m^2\ V^{-1}\ s^{-1}$),

ε: dielectric constant (in this study 78.5),

f(*κa*): Henry's function. According to the Smoluchowski approximation, which is typically used for aqueous samples, *f*(*κa*) = 1.5.

The samples for the measurement were prepared as follows. 1 mg of the COF was dispersed in 20 ml water following by adding the appropriate amount of H_2A to achieve 2 to 10 mM in the final suspensions. Measurements were performed in three independent rounds, with each round consisting of 50 measurement cycles.

4.3. Results and Discussion

Imine-BDT-ETTA COF was synthesized according to the previously reported procedure using an acceptor-type ETTA building block and a donor-type BDT linker (ROTTER et al., 2019) The obtained Imine-BDT-ETTA was subsequently post-modified to convert imine to amide linkages using Pinick oxidation reaction (MOHAMED; YAMADA; TOMIOKA, 2009) where sodium chlorite is used as an oxidizing agent, 2-methyl-2-butene as a free radical scavenger, and acetic acid as a buffer during the oxidation process, Figure 28a. The powder X-ray diffraction pattern shown in for Imine-BDT-ETTA COF in Figure 28b and in Figure 28b for Amide-BDT-ETTA confirm successful synthesis and post-modification of the COF revealing high crystallinity through the presence of a pronounced and sharp 100 reflection along with well-defined higher-order reflections. The structures of Imine-BDT-ETTA and Amide-BDT-ETTA were simulated using force-field methods (RAPPE et al., 1992) comprising a dual-pore Kagome structure in symmetry (Space Group No. 168) (see Figure C1, Figure C2, Table C1, Table C2) with the unit cell parameters being $a = b = 4.64$ nm, $c = 0.446$ nm (*Rwp* = 4.6 %, *Rp* = 3.7 %) and $a = b = 4.78$ nm, $c = 0.448$ nm (*Rwp* = 5.7 %, *Rp* = 3.8 %), respectively. The increase of *a*, *b* and *c* parameters for amide-linked COF in comparison to those for the imine counterpart can be attributed to the bond length change resulting from the conversion of the C=N double bond (0.129 nm from structural simulations) to the C-N single bond (0.135 nm from structural simulations). For comparison, the structure of Amide-BDT-ETTA was also simulated assuming 50 % conversion (see Table C3). The simulated and experimental XRD patterns were consistent (*Rwp* = 7.8 %, *Rp* = 5.2 %), demonstrating that regardless of conversion degree to amide bonds, there are no significant changes in the structure of the COF.

Nitrogen physisorption isotherms were used to monitor the changes in porosity of the COF after the linkage conversion. Like the imine counterpart (Figure C3a) Amide-BDT-ETTA exhibits a sorption isotherm of type IV with two steep nitrogen uptake steps (Figure C3b). The Brunauer–Emmett–Teller (BET) surface area of Amide-BDT-ETTA decreased to 688 $m^2 g^{-1}$ in comparison to Imine-BDT-ETTA being 1679 $m^2 g^{-1}$. Previous studies have reported a decrease in the surface area as a result of post-synthetic modification (WALLER et al., 2016; HAN et al., 2018; ZHOU, Z.-B. et al., 2022). However, the linkage conversion of the Imine-BDT-ETTA did not induce

substantial changes in the pore sizes. Using equilibrium QSDFT method with carbon kernel for cylindrical pores, pore sizes for Imine-BDT-ETTA were calculated to be 1.79 nm and 3.68 nm (vs. 1.72 nm and 3.58 nm based on structural simulations (Figure C1) aligning well with previous reports (WALLER et al., 2016). Pore sizes for Amide-BDT-ETTA were found to be 1.79 nm and 3.55 nm (1.72 nm and 3.58 nm from structural simulations Figure C2).

The morphological characteristics of both COFs were further investigated *via* SEM (Figure C4). SEM images suggest that Imine-BDT-ETTA features a spherical morphology constructed from particles organized in a rose-shaped agglomerates. Notably, Amide-BDT-ETTA shows a more mixed morphology, featuring rod-like agglomerates alongside remaining rose-shaped particles. The chemical conversion of the imine-COF involves a series of processes, including ultrasonication, treatment with different solvents (dioxane, 2-methyl-2-butene), utilization of the inorganic oxidant $NaClO_2$ and exposure to glacial acetic acid which serves as a buffer. To identify the origin of the morphological changes, the following control experiments were conducted: Reference-COF-1 was obtained in the absence of $NaClO_2$, Reference-COF-2 with fivefold reduction in $NaClO_2$ concentration and Reference-COF-3 in absence of acetic acid, while keeping other ingredients consistent with the original conversion procedure (see the Supporting Information). All three reference samples retained crystallinity after all treatment steps, respectively (Figure C5a). As expected, Fourier transform infrared (FT-IR) analysis reveals that for the linkage conversion the oxidant is required (Figure C5b). The rod-shaped particles were observed in all three reference samples (Figure C6), thus indicating that the formation of such structures is not related to the amidation process itself but rather the result of the ultrasonication and the treatment with organic solvents.

^{13}C cross-polarization magic angle spinning (CPMAS) analysis allowed us to determine the local chemical changes of the COF after linkage conversion (Figure 28d). In the ^{13}C NMR spectrum of Amide-BDT-ETTA, a distinctive peak at 161 ppm appeared, which is not present in the NMR spectrum of Imine-BDT-ETTA prior the oxidation. This new signal arises from the formation of amide carbonyl C=O moieties (WALLER et al., 2016). Additionally, a residual signal attributed to C=N bonds at 151 ppm remains detectable in Amide-BDT-ETTA. This observation implies partial oxidation and suggests that the final structural configuration of Amide-BDT-ETTA includes both newly introduced carbonyl C=O functionalities and unreacted imine C=N

bonds from its imine precursor COF. We note that harsher conditions, such as prolonged reaction times and increased amount of oxidative agent to induce a full conversion from imine to amide linkages, resulted in a non-crystalline sample. As demonstrated in previous studies, exposure so strong oxidizing agents can disrupt the crystalline structure by breaking imine bonds (WANG, J.-R. et al., 2024).

FT-IR spectroscopy was applied to further explore the chemical changes induced through linkage conversion, Figure 28e. Imine-BDT-ETTA exhibits a prominent band at 1611 cm^{-1} corresponding to the stretching vibrations of the C=N functional group (WALLER et al., 2018; ZHANG, Y. et al., 2023). Observed vibration peaks in the FT-IR spectra of Imine-BDT-ETTA are in a good agreement with the previously published results (ROTTER et al., 2019) (FEIJOO; PALIUŠYTĖ; SCHNEIDER, 2024). The emergence of a new band at 1315 cm^{-1} in the Amide-BDT-ETTA spectrum reveals the formation of the C–N–C moiety, indicative of the amide linkage (NGUYEN, H. L.; GROPP; YAGHI, 2020). Another pronounced band at 1515 cm^{-1} can be attributed to the in-plane N–H bending vibrations of the secondary amide group (Instrumentation for Fluorescence Spectroscopy, 2006; FOGGIA et al., 2012). As previously substantiated by ^{13}C solid-state NMR analysis, the presence of imine bonds is evident in the FT-IR spectrum of Amide-BDT-ETTA as well. Typically, the stretching vibrations of imine and amide bonds are observed in the spectral range of 1600~1690 cm^{-1} (WALLER et al., 2016; MAGALHÃES et al., 2017; WALLER et al., 2018; KRISHNARAJ et al., 2019; GENDY et al., 2022; KRISHNARAJ et al., 2022; ZHANG, Y. et al., 2023; XUE et al., 2024). However, within the spectral range of Amide-BDT-ETTA, there are multiple overlapping signals, which require more complex analysis. For a deeper analysis of the vibrations associated with the newly formed bonds in the polymeric structure, the FT-IR spectrum of Imine-BDT-ETTA was subtracted from the spectrum of the Amide-BDT-ETTA (Figure C7). In the resulting FT-IR difference spectrum the C=O stretching vibration of the amide bond is evident at 1645 cm^{-1} (Instrumentation for Fluorescence Spectroscopy, 2006; DI FOGGIA et al., 2011; WALLER et al., 2016).

X-ray photoelectron spectroscopy (XPS) analysis was conducted to examine the changes in the oxidation states of the elements present in both COFs (Figure C8). Survey spectra evidence the absence of any impurity and only peaks related to C, S, O and N atoms were identified. High resolution data for each peak were acquired for both COFs and compared to those for the BDT linker (Figure C9). Looking first at C1s

for Imine-BDT-ETTA (Figure C9a), one can observe a major peak at 284.6 eV attributed to carbon atoms in COF structure itself along with a small peak at higher binding energy, 289.5 eV, which can be attributed to unreacted aldehyde groups on the COF surface. For the Amide BDT-ETTA COF, a new feature at 288.1 eV can be identified and attributed to the carbonyl (C=O) moiety, Figure C9b (NAGAKURA, 2006; WANG, W. et al., 2023).

In the S 2p region, the presence of two distinct sulfur environments can be identified for both COFs, each characterized by specific binding energy values of the S $2p_3/_2$ photoelectron peak at 164.2 eV and 169.0 eV (Figure C9d,e). These peaks correspond to "neutral" sulfur species (S–S, S–C) and oxidized sulfur species (S=O), respectively. Amide-BDT-ETTA contains 20 % sulfur in an oxidation state of +VI while Imine-BDT-ETTA contains about 15 % of oxidized sulfur species. Additionally, the presence of oxidized sulfur species (15 %) is also presenting in BDT linker which was utilized for initial synthesis of Imine-BDT-ETTA COF. This data evidence that the COF amidization does induce some additional sulfur oxidation in the COF structure, although relatively small to really induce electronic or structural changes.

The main peak in the O 1s spectra of both COFs (Figure C9g,h) is assigned to surface-adsorbed oxygen species (ZHOU, Z.-B. et al., 2022). For the Amide-BDT-ETTA COF, this peak appears at 533.6 eV, shifted in relation to that for Imine-BDT-ETTA (532.5 eV), evidencing the different surface properties. Moreover, for the Amide-BDT-ETTA a second feature with lower binding energy is observed at 531.0 eV, which agree well with previous reported data for C=O bonds resulted from the amidization reaction (GIEROBA et al., 2020).

In the N 1s region, distinct differences are observed between the two COFs. For Imine-BDT-ETTA COF (Figure C9j), the spectrum can be deconvoluted into two components at binding energies of 398.7 and 402.8 eV, corresponding to imine groups (—C═N—C—) and unreacted amino groups (—C—NH_2) from the ETTA building block, respectively (ZHOU, Z.-B. et al., 2022) (WANG, W. et al., 2023). The comparison between the N 1s spectra of Imine-BDT-ETTA (Figure C9j) and Amide-BDT-ETTA (Figure C9k) reveals a shift toward higher binding energy after the amidization process (from 398.7 to 399.2 eV, Figure C9i). This shift confirms the efficient conversion, consistent with previously reported binding energy changes associated with imine-to-amide transformation.

However, the N 1s peak does not allow for direct quantification of imine-to-amide conversion yield. Complementary evidence from ^{13}C–NMR and FTIR confirms the presence of residual imine groups in Amide-BDT-ETTA COF. To reliably estimate the conversion yield, we have taken the ratio between the corresponding area for the peaks attributed to the amide C═O (C1s at 288.1 eV and O1s at 531.0 eV) and the N1s in the survey spectra, which should be ideally 1:1. The calculated C═O/N ratio was 0.9, suggesting an approximate conversion yield of 90%.

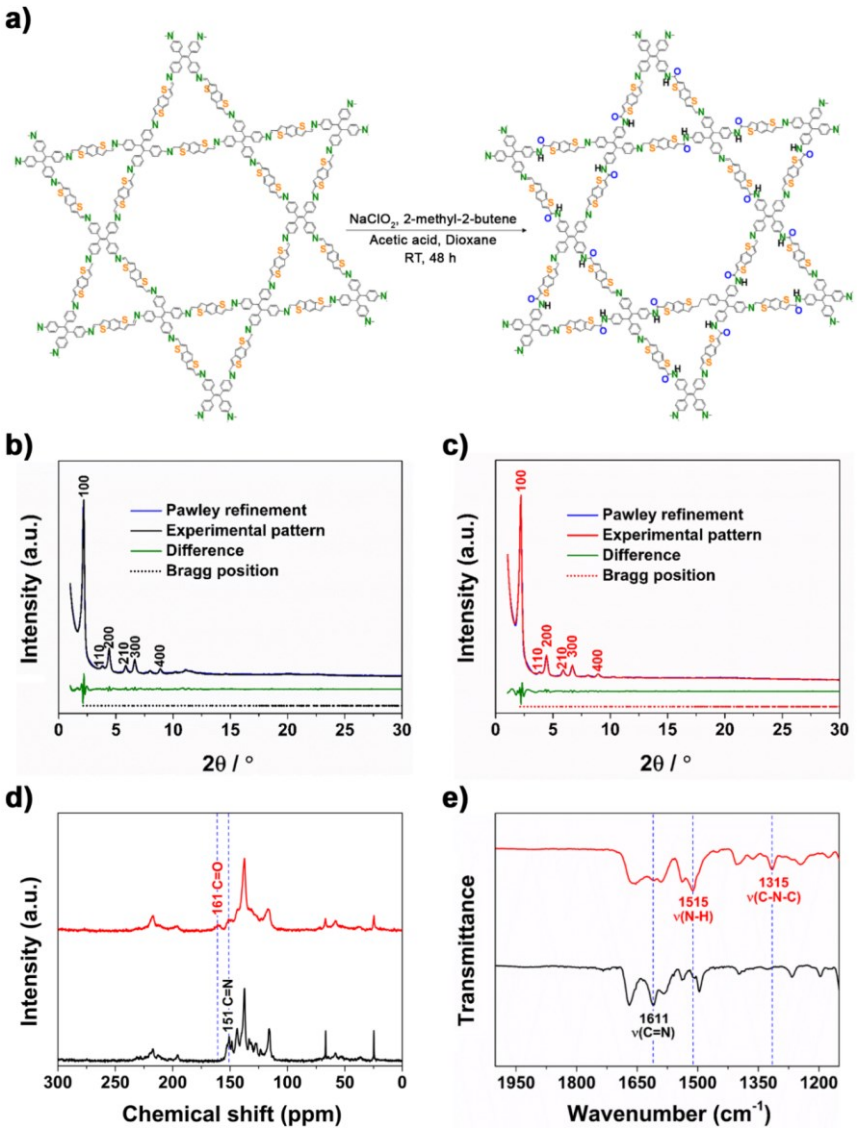

Figure 28. (a) Schematic representation of Imine-BDT-ETTA to Amide-BDT-ETTA conversion. Experimental and Pawley refined PXRD patterns of b) Imine-BDT-ETTA and c) Amide-BDT-ETTA. d) 13C NMR spectra and e) FT-IR spectra of Imine-BDT-ETTA (black) and Amide-BDT-ETTA(red).

The as-prepared imine and amide COFs were tested for the photocatalytic hydrogen evolution. The photocatalytic tests were performed in the presence of 1.0 wt% (Pt/COF) H_2PtCl_6 precursor and ascorbic acid (H_2A) acting as sacrificial electron donor (Equations 5-8) upon illumination with visible light ($\lambda > 420$ nm, 100 mW cm^{-2}). After excitation of the COFs, photogenerated electrons (e^-) and holes (h^+) are formed (Equation 5). The holes can oxidize H_2A to dehydroascorbic acid, A, either directly by two-electron transfer or by one-electron oxidation *via* formation of ascorbyl radical, $HA^{\bullet}$, as an intermediate Equation 6 and Equation 7) thus suppressing the undesired recombination. Simultaneously, the photogenerated electrons can reduce $2H^+$ to H_2 on surface of *in-situ* formed Pt particles Equation 8.

$$COF \xrightarrow{h\nu} e^- + h^+ \qquad \text{(Equation 5)}$$

$$H_2A + h^+ \rightarrow HA^{\bullet} + H^+ \qquad \text{(Equation 6)}$$

$$HA^{\bullet} + h^+ \rightarrow A + H^+ \qquad \text{(Equation 7)}$$

$$2H^+ + 2e^- \rightarrow H_2 \qquad \text{(Equation 8)}$$

Figure 29a shows the hydrogen evolution obtained with Imine- and Amide-BDT-ETTA COFs in the experiments lasting 13 hours. From the linear increase of H_2 production with time, the HER rates for Imine-BDT-ETTA and Amide-BDT-ETTA were quantified to be 0.22 mmol g^{-1} h^{-1} and 0.95 mmol g^{-1} h^{-1}, respectively. These results reveal a pronounced promotion of hydrogen evolution through the linkage conversion. Both COFs were also tested in the absence of light and in the absence of Pt, but no hydrogen evolution was detected. The irradiation of the Pt^0 precursor in the presence of ascorbic acid also does not lead to H_2 evolution. Long-term photocatalytic experiments were performed in which hydrogen evolution was monitored over three cycles of 13 h for 39 h in total (Figure 29b). Both COFs were able to continuously sustain an average HER rate of 0.22 mmol g^{-1} h^{-1} for Imine-BDT-ETTA and of 0.95 mmol g^{-1} h^{-1} for Amide-BDT-ETTA. In subsequent three cycles of 3 hours each and in the presence of 2 mM H_2A, even higher evolution rates for both COF were detected, with the Amide-COF showing an average HER rate of 1.7 mmol g^{-1} h^{-1} while Imine-BDT-ETTA delivered 0.40 mmol g^{-1} h^{-1} (Figure C10). All experiments were performed in triplicate at least.

The HER rate was measured in the presence of different H_2A concentrations using Amide-BDT-ETTA as the photocatalyst to investigate the origin of the increased

HER rate observed at lower H_2A concentration. The increase in H_2A concentration from 2 mM to 6 mM resulted in a gradual increase of HER rate up to 2.6 mmol g^{-1} h^{-1} (Figure C11a). Further increase in the H_2A concentration from 8 mM to 10 mM led to a drop in the HER rate. A similar dependence of H_2 evolution on the concentration of the sacrificial electron donor has been already reported and assigned to a Langmuir-type catalytic behavior (ZHENG et al., 2009; HAMID; DILLERT; BAHNEMANN, 2018; ŠETKA et al., 2019). At low H_2A concentrations, the HER rate is limited by the mass transfer of the H_2A to the Pt/COF surface. At high H_2A concentrations, the coupling of the surface-adsorbed $H^{\bullet}$ radicals on the Pt surface to form H_2 gas might be hindered through competing acid adsorption. It has been reported that H_2A adsorbs at the Pt surface, occupying hydrogen adsorption sites(MOZIA; HECIAK; MORAWSKI, 2011). Moreover, H_2A oxidation is very sensitive to the pH of the reaction media and is favored at higher pH values (ROIG; RIVERA; KENNEDY, 1995; SALKIĆ, 2016). Photocatalytic tests were also performed in the presence of triethanolamine (TEOA) with Amide-BDT-ETTA to investigate the influence of the sacrificial donor on the photocatalytic performance (Figure C11b). Here, the HER rates were significantly lower reaching only 0.63 mmol g^{-1} h^{-1} for Imine-BDT-ETTA and 0.39 mmol g^{-1} h^{-1} for Amide-BDT-ETTA. Usually, the difference in H_2 production when using H_2A or TEOA as electron donors is explained by changes in the pH of the suspensions, which can influence the adsorption and desorption dynamics and equilibria of reactants and products at the photocatalyst surface(XIE et al., 2019; WANG, Y. et al., 2022; ZHANG, J. et al., 2022). Additionally, the presence of TEOA leads to higher pH values of the reaction medium (pH = 10.75) thus reducing the availability of free H^+ which in turn decreases the availability of protons (DU et al., 2009; PELLEGRIN; ODOBEL, 2017).

To explore the origin of the enhanced H_2 evolution with Amide-BDT-ETTA in comparison to Imine-BDT-ETTA, the optoelectronic features of both COFs were examined using cyclic voltammetry (CV), UV-vis absorption spectroscopy (UV-vis), and photoluminescence spectroscopy (PL). CV measurements allowed to quantify the energetic positions of the HOMO levels from half wave potentials for both COFs (Figure C12). Herein, the experiments were conducted using the Fc/Fc^+ redox couple as reference in 0.1 M NBu_4PF_6 acetonitrile solutions as described elsewhere (SICK et al., 2018). The HOMO levels for Imine-BDT-ETTA and Amide-BDT-ETTA are positioned at -4.94 eV (0.44 V vs. SHE) and at -5.31 eV (0.81 V vs. SHE), respectively.

For a photocatalyst to facilitate photo-oxidation *via* photogenerated holes, the HOMO or valence band energy must be more positive (higher potential) than the redox potential of the target oxidation reaction. The more positive HOMO potential of Amide-BDT-ETTA compared to its imine counterpart reveals that it is a stronger photooxidizing agent, enhancing its effectiveness in driving photocatalytic oxidation (DANCE, 2006; KUMAR; SEVILLA, 2018).

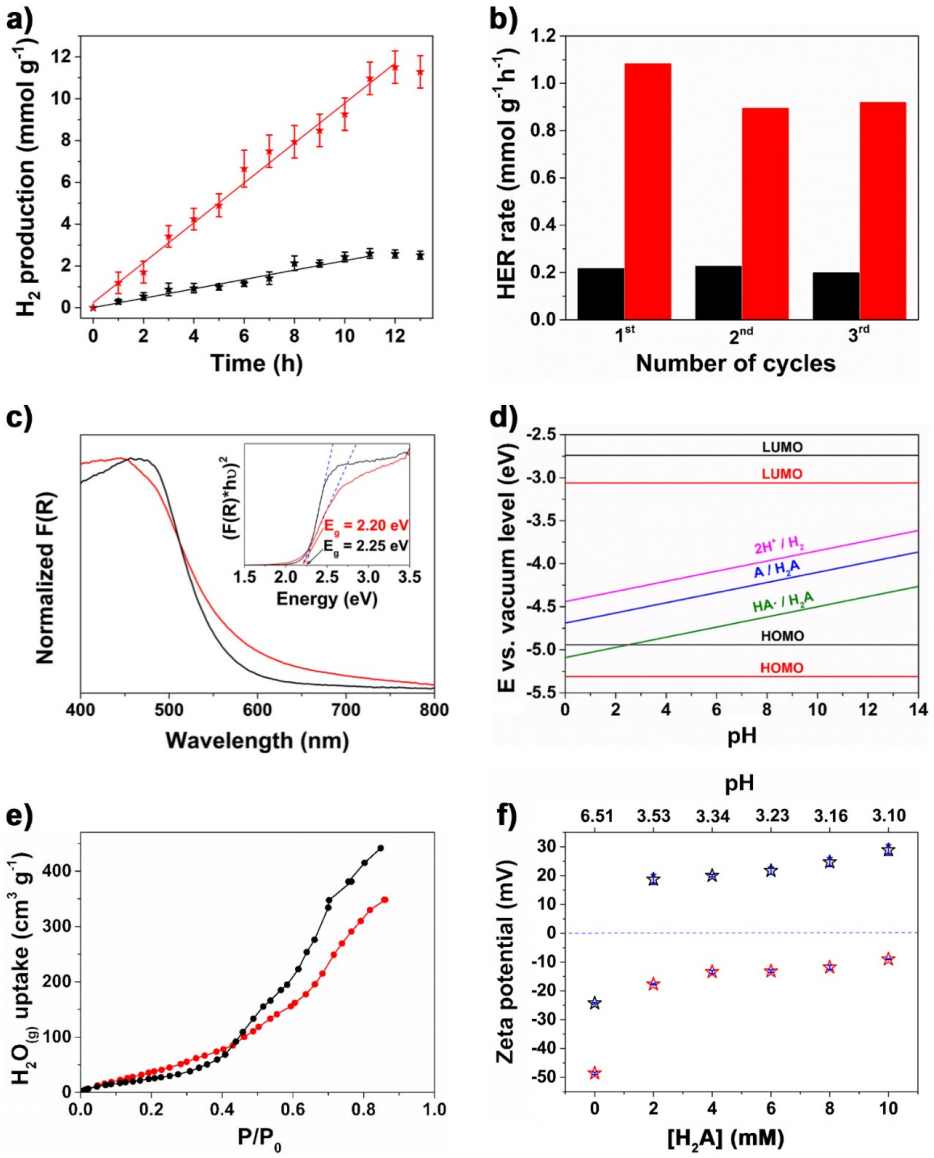

Figure 29. (a) Time course of H_2 evolution and (b) hydrogen evolution rates for three cycles, each 13 h obtained with Imine-BDT-ETTA (black) and Amide-BDT-ETTA (red) including the error bars. Solid lines in (a) represent the linear fitting to extract evolution rates. Conditions of photocatalytic tests: λ > 420 nm, 100 mW cm^{-2}, 0.1 g/l COF suspension containing 10 mM H_2A and 1.0 wt% (Pt/COF) H_2PtCl_6 precursor. (c) F(R)

and Tauc plots (inset) as well as (d) determined energy levels of Imine-BDT-ETTA (black) and of Amide-BDT-ETTA COF (red) including the redox potentials of the studied photocatalytic reaction. (e) Volumetric water vapor adsorption isotherms of Imine-BDT-ETTA (black) and Amide-BDT-ETTA (red). (f) Zeta potential of Imine-BDT-ETTA (black) and Amide-BDT-ETTA (red) as a function of pH, adjusted using varying concentrations of H_2A (0, 2, 4, 6, 8, and 10 mM) including the error bars (blue).

The optical properties of the COFs were evaluated by UV-vis measurement applying the Kubelka-Munk conversion for solid materials (Figure 29c). In contrast to Imine-BDT-ETTA, Amide-BDT-ETTA exhibits a strong visible-light absorption in the spectral region above 510 nm. These findings are consistent with prior studies.(ZHU et al., 2024). Assuming direct optical transitions for both polymers, the optical band gap energies were calculated employing Tauc plots, thereby revealing values of 2.25 eV for Imine-BDT-ETTA and 2.20 eV for Amide-BDT-ETTA (TAUC; GRIGOROVICI; VANCU, 1966; TAUC, 1968; MAKUŁA; PACIA; MACYK, 2018). The stronger optical absorption of the amide-linked COF above 510 nm might originate from the presence of defect states which could reduce the Schottky barrier thus facilitating electron transfer to the Pt and enhancing the proton reduction (GHOSH, R.; PAESANI, 2021). A Schottky barrier at the semiconducting polymer/metal interface has been reported to result from the large band offset between the electron affinity of the polymer *vs.* the work function of the metal (RIKKEN et al., 1994). Schottky barriers should impede the electron injection into the metal, however, the presence of surface states in the polymer can dramatically reduce the barrier, thus allowing fast electron injection and enhancing the photocatalytic performance (KHANCHAITIT et al., 2013; WANG, Y. et al., 2021).

The LUMO energy levels for both COFs were calculated from the HOMO energy levels obtained by the CV measurements and the optical bandgap energies. As evident from Figure 29d, the imine to amide linkage conversion has caused a shift in HOMO and LUMO energies to more negative potentials. Xiang *et al.* reported similar changes upon amidation and attributed the behavior to a more pronounced negative charge accumulation in amide COF as a result of the stronger electron-withdrawing properties of amide linkages (WANG, W. et al., 2023). PL spectra of the COFs were recorded by exciting the materials at 375 nm. Imine-BDT-ETTA and Amide-BDT-ETTA

exhibit strong emission bands centered at 617 nm and 608 nm, respectively (Figure C13). The blue-shift for the latter can be explained by the weakened conjugation arising from oxidation of the imine bonds (MEIER et al., 2017) (KELLER et al., 2019).

The band energy levels for both COFs compared to the redox potentials of the studied photocatalytic reactions is exhibited in Figure 29d. It reveals the low thermodynamic driving force for the Imine-BDT-ETTA to induce the one-electron oxidation of H_2A in the pH range of photocatalytic experiments (from 3.10 to 3.53 as shown in Table C4). On the other hand, Amide-BDT-ETTA can efficiently initiate one and two-electron oxidation of the H_2A, thus enabling more efficient electron accumulation required for the targeted H_2 evolution. Additionally, both COFs are thermodynamically suitable to promote the hydrogen evolution reaction, $2H^+/H_2$ (Equation 8). Here, the potential variation of the HOMO and LUMO levels of the COFs as function of the pH was neglected based on prior studies (SICK et al., 2018). Moreover, the difference in the thermodynamic driving force for proton reduction between Imine- and Amide-BDT-ETTA (see Figure 29d) is less relevant as no H_2 was generated in the absence of Pt. This evidences that the proton reduction proceeds *via* electron transfer at the metal surface.

Among the thermodynamic driving force for the photocatalytic reaction the interactions at the interface between reactants/products and the photocatalyst is essential. In the photocatalytic hydrogen evolution reaction in aqueous media, the hydrophilic character of the COF might influence the efficiency of the process. Herein, volumetric water sorption experiments were conducted for both COFs. Figure 29e shows that at lower relative pressures ($P/P_0 < 0.45$) Amide-BDT-ETTA has a greater water vapor sorption in comparison to Imine-BDT-ETTA, thus evincing its higher affinity for adsorbate (DE LUCA et al., 2001; BURTCH et al., 2013; KORMAN et al., 2020) and stronger hydrophilic character. This is most likely arises from the presence of the carbonyl groups of the amide. The total water vapor uptake for Amide-BDT-ETTA was 348 $cm^3\,g^{-1}$ while for Imine-BDT-ETTA a value of 443 $cm^3\,g^{-1}$ was found. For an adequate comparison, the previously determined BET surface area has to be considered (Figure C3). Accordingly, the water vapor uptake normalized to the BET surface for Amide-BDT-ETTA is higher (0.51 $cm^3\ m^{-2}$) in comparison to Imine-BDT-ETTA (0.26 $cm^3\ m^{-2}$). Hence, the inherent hydrophilic characteristics and increased polarity arising from the presence of C=O bonds and higher concentration of oxidized sulfur in Amide-BDT-ETTA contribute to the elevated HER rate and

supports the formation of stable suspensions in aqueous media in contrast to Imine-BDT-ETTA, Figure C14 (MA et al., 2021).

The observed HER rate dependence on the H_2A concentration for Imine-BDT-ETTA (see Figure C10a) and Amide-BDT-ETTA (see Figure C10b) underscores the effect of the COF structure on the hole-driven H_2A oxidation, aiming at promotion of H_2 evolution. The efficiency of the H_2A oxidation depends on the thermodynamic driving force (discussed above) and its adsorption at the COF surface. In the studied pH region, H_2A is present in a protonated form and it can interact with both COFs only through weak H-bonding formed either with the imine linkage or the C=O bond of amide linkage. Consequently, no adsorption of H_2A onto the surface of either COF was detected in the dark (see Figure C15). However, Amide-BDT-ETTA has a greater tendency to form stronger H-bonds with water molecules, thereby potentially aiding in the eventual reduction of protons (MARINHO et al., 2022a).

The interfacial interactions between the COF and the H_2PtCl_6 precursor present mainly as $[PtCl_6]^{2-}$ are crucial for photocatalytic H_2 evolution, as they dictate Pt growth and distribution on the COF surface. The coordinating sites for metal complexes in the COF structures have been reported to enable controlled growth of Pt particles (LI, Y. et al., 2022). However, the formation of the coordinative bonds may be slower than the charge transfer to the transition metal complexes as the latter is known to happen on nanoseconds to picoseconds timescale (YANG, W. et al., 2019). Additionally, coordinative binding often requires thermal treatment (WU, Q.-J. et al., 2023). Hence, interactions such as electrostatic attraction and repulsion between charged particles are most likely to govern the *in-situ* photodeposition of Pt.

For studies of the columbic interactions between the COFs and $[PtCl_6]^{2-}$ precursor, the surface charge of both COFs was determined by measuring the zeta potential in water-based suspensions (0.1 g L^{-1}) with different H_2A concentrations (0 to 10 mM). As shown in Figure 29f, both COFs have negative surface charge in the absence of H_2A. Imine-BDT-ETTA ([H_2A] = 0 mM) shows a zeta potential of -24.4 ± 0.3 mV, while the zeta potential value for Amide-BDT-ETTA is -48.6 ± 0.5 mV. The Amide-BDT-ETTA exhibits more negative zeta potential (below -30 mV), indicating improved stability in aqueous suspensions compared to its imine counterpart (SHUKLA et al., 2018). The addition of H_2A shifted the zeta potential of Imine-BDT-ETTA to positive values. As shown in previous studies (BOCIAN; DZIUBAKIEWICZ; BUSZEWSKI, 2015; SERRANO-LOTINA et al., 2023), such shift

can be caused by the protonation of functional groups. Imine bonds are known to act as weak bases and are capable of being protonated (YANG, J. et al., 2021). In order to calculate the ratio between protonated and non-protonated forms of the COFs, the Henderson-Hasselbalch equation for weak bases was used (Equation 9) (MIONI; MIONI, 2015)(RADIĆ; PRKIĆ, 2012).

$$\mathrm{pOH} = \mathrm{pK_b} + \log\frac{[\mathrm{AH^+}]}{[\mathrm{A}]} \qquad \text{(Equation 9)}$$

(pK_b: base dissociation constant; [A]: concentration of the base; [AH^+]: concentration of conjugate acid)

Here pK_b values for imine bonds range between 8 to 10, and their conjugate acids (protonated imines) have pK_a (acid dissociation constant) values between 4 and 6 (because pK_b + pK_a = 14),(TREPTOW, 1986) suggesting that protonation of imine linkages occurs at pH levels below 6 (RICE, 2014; LONG et al., 2017). During photocatalytic tests in the presence of H_2A an acidic environment is achieved (pH = 3.10 - 3.53) *i.e.* Imine-BDT-ETTA-COF is predominantly present in protonated form ([A] < [AH^+]). The positive shift of the zeta potential was also observed for Amide-BDT-ETTA, however, it remained in the negative range. The positive shift can be attributed to the protonation of unreacted imine bonds while amide bonds remain non-protonated due to their lower basicity (pK_b values ranging between 13 and 16 while pK_a for conjugate acids (protonated amides) varies between -2 to 1) (RAMAN; MORTLAND, 1969; AYYANGAR; SRINIVASAN, 1984; LOTINA-HENNSEN et al., 1987). This aligns well with well-known fact that more acidic functional groups typically exhibit more negative zeta potential than the more basic functional groups (POSCHMANN; LILLERUD; STOCK, 2023). The protonation of amide linkages occurs in the presence of strong acids at pH values below 1. In the experimental conditions employed for the photocatalytic tests, the amide linkages are in the non-protonated form ([A] > [AH^+]) causing negative zeta potential and negatively charged COF particles. These results suggest the electrostatic attraction of negatively charged Pt-precursor $[PtCl_6]^{2-}$ with positively charged Imine-BDT-ETTA and electrostatic repulsion with negatively charged Amide-BDT-ETTA. Further analysis requires post-characterization of both COFs.

The consistent and stable rates of hydrogen production observed during the illumination lasting 48 hours reveal fair photochemical stability of both COFs.

Accordingly, structural characterization of both COFs was conducted after 13 and 56 hours of illumination in the presence of 10 mM H_2A and 1 wt% Pt loading. The PXRD patterns presented in Figure 30a,b reveals that after 13 and after 56 hours illumination, both COFs exhibit retention of crystalline structure.

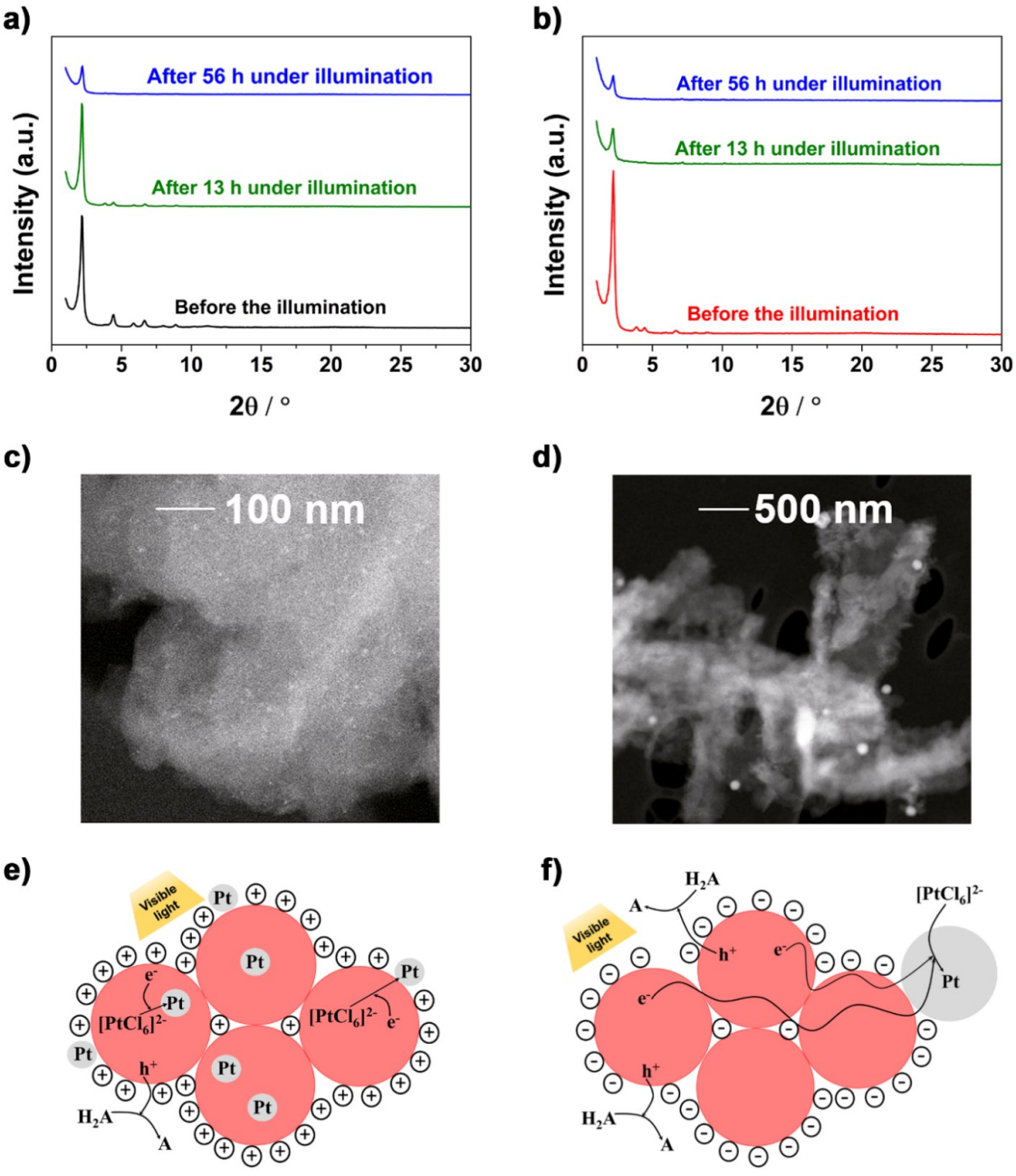

Figure 30. PXRD patterns of (a) Imine-BDT-ETTA and (b) Amide-BDT-ETTA before and after 13 h and 56 h of photocatalytic test. STEM-HAADF images showing distribution of Pt particles in the polymeric structure of (c) Imine-BDT-ETTA and (d) Amide-BDT-ETTA after 13 h of photocatalytic test. Conditions of photocatalytic test: λ

> 420 nm, 100 mW cm^{-2}, 1 g/l COF suspension containing 10 mM H_2A and 1.0 wt% (Pt/COF) H_2PtCl_6 precursor. Schematic representation of interparticle electron transport along agglomerates of (e) Imine-BDT-ETTA and (f) Amide-BDT-ETTA towards the Pt particles (red: COF domains, grey: Pt particles).

To gain insights into structural distribution of Pt particles, scanning transmission electron microscopy (STEM) analysis was performed for both COFs after the 13 hours photocatalytic test. Figure 30c and Figure C16a,b evidences a random distribution of small Pt clusters dispersed within the matrix of Imine-BDT-ETTA. Statistics on Pt size distribution, Figure C17a, evidence an average size of 3.9 nm with a full width at half maximum (FWHM) of 3.6 nm. In contrast, Amide-BDT-ETTA (Figure 30d and Figure C16c,d) displays large Pt particles with more dispersed size distribution. As shown in Figure 17b, the Pt particles in the Amide COF lies within two distinct size ranges. A broad one comprised by particles with average size of 90 nm and a FWHM of 35 nm and a second narrower distribution with average size of 12 nm with a FWHM of 4 nm. From the statical analysis, it is clear that 90% of the Pt particles on the Amide-BDT-ETTA exhibits a bigger size than those on Imine-BDT-ETTA. These results suggest that Pt^0 growth mechanism depends on the linkage of the COF which influences the interactions between COF and Pt precursor.

The attractive interaction between positively charged Imine-BDT-ETTA with the negatively charged Pt-precursor $[PtCl_6]^{2-}$ should promote the high Pt nucleation rate at numerous sites and resulting in homogeneous distribution of small (1-2 nm) Pt particles in the framework (Figure 30e). In contrast, Amide-BDT-ETTA is negatively charged in the acidic environment, leading to repulsion between the COF and the $[PtCl_6]^{2-}$ anions, which is proposed to cause the formation of larger Pt particles. Hereby, the interparticle electron transport along the BDT-ETTA agglomerates to pre- formed metal particles enables the formation of larger particles (Figure 30f).

These results reveal the ability of the COF to serve as an antenna for electron transport. The influence of the surface charge on the formation of Pt particles and in the photocatalytic performance is corroborated by the results in the presence of TEOA as sacrificial agent. In this condition, the medium pH is alkaline and both COFs remain negatively charged. As a result the H_2 evolution rate is decreased when compared to those obtained in the presence of ascorbic acid and the Imine-BDT-COF exhibits better performance than the Amide COF. Thus, the linkage conversion allowed for

tuning of the surface charges of the COF through different protonation behavior of the imine and amide linkage, which had a direct impact on the growth of the Pt particles on the COF surface. Hence, an additional tool for controlling the photocatalytic process was demonstrated.

The influence of the Pt particle size on the hydrogen evolution reaction remains a topic of ongoing debate in the literature (CHEN, S.; KUCERNAK, 2003; CHENG et al., 2016; VAMVASAKIS; LIU; ARMATAS, 2016; NAKIBLI et al., 2018). In general, the overall photocatalytic performance is governed by a sequence of key steps (omitting here the role of the sacrificial donor): i) light absorption, charge separation, and charge transport within the (COF) photocatalyst to the metal co-catalyst, ii) interfacial electron transfer between the photocatalyst and the metal co-catalyst, and iii) proton reduction to form hydrogen atoms on the metal surface, followed by H_2 formation and desorption. While the first step is primarily determined by the intrinsic electronic properties of the (COF) photocatalyst, the second and third steps are influenced by the nature and distribution of the metal particles, particularly their size and interfacial characteristics, including electronic coupling to the COF. The efficiency of charge separation and interfacial electron transfer can indeed be modulated by the Pt particle size, which plays a critical role in facilitating or hindering these processes (NAKIBLI et al., 2018; LIU, Y. et al., 2022). However, the Volmer step—the initial formation of adsorbed hydrogen atoms ($H^{\bullet}$) on the Pt surface—is the rate-limiting step in catalytic hydrogen evolution. Bard and co-workers demonstrated that the kinetics of this step are accelerated as Pt particle size increases on Bi and Pb substrates (ZHOU, M.; BAO; BARD, 2019). Considering these findings, we propose that the larger Pt particles formed on Amide-BDT-ETTA may enhance H_2 production due to improved kinetics of the Volmer step. However, we emphasize that systematic studies on the relationship between Pt particle size, charge separation efficiency, interfacial electron transfer, and hydrogen formation kinetics in COF-based systems are still lacking and warrant further investigation.

4.4. Conclusions

This study demonstrates how the structural, optoelectronic, and interfacial properties of the BDT-ETTA COF are modulated through linkage conversion from imine to amide and their resulting influence on photocatalytic performance. Retaining

its crystallinity upon amidization, the amide-linked COF exhibits a shift in energy levels toward more positive potentials (E vs SCE), enhancing its oxidizing power. This stronger oxidation capability facilitates more efficient hole scavenging, thereby promoting proton reduction while suppressing charge carrier recombination. Additionally, the increased hydrophilicity of Amide-BDT-ETTA, attributed to the presence of C═O bonds, leads to an improved HER rate and enhances the stability of its suspensions in aqueous media compared to Imine-BDT-ETTA. Notably, our findings reveal, for the first time, that surface charge modulation, driven by the distinct protonation behavior of imine and amide linkages, plays a critical role in photocatalytic performance. This interfacial modification strategy effectively switches the surface charge of COFs and alters the in situ Pt-photodeposition mechanism. Specifically, the negatively charged Amide-BDT-ETTA promotes proton adsorption and facilitates the formation of large Pt particles (up to 100 nm), which are highly effective for proton reduction. By highlighting the impact of interfacial properties on reaction mechanisms and photocatalytic hydrogen evolution, this study expands the functional versatility of COFs in photocatalysis. We anticipate that this approach can be further applied to a wide range of photocatalytic reactions and diverse linkage motifs, offering new pathways for designing advanced COF-based photocatalysts.

5. Novel materials for photocatalytic H_2 evolution under visible light

As previously discussed in Chapter 3 of this thesis, Bi_2WO_6 offers several advantages for photoreforming reactions, including physicochemical stability and suitable band edge positions. However, its photocatalytic performance is limited by its absorption being restricted to the UV region and by the low photocurrent densities generated under simulated sunlight, which hinders practical applications. Engineering oxygen vacancies was shown to be an effective strategy to extend the photoresponse of Bi_2WO_6 into the visible spectrum. Another promising approach widely reported in the literature is doping. Nickel was selected as a dopant due to its favorable combination of cost-effectiveness, catalytic activity, and ability to tailor the electronic structure of wide-bandgap semiconductors (ROCHA et al., 2013; ISMAEL, 2023; WU, F. et al., 2024). Unlike platinum, which is widely used as a benchmark co-catalyst for hydrogen evolution but is scarce and expensive, nickel is earth-abundant and economically viable for large-scale applications. Incorporation of Ni^{2+} not only contributes to band gap narrowing by introducing mid-gap states but also surface Ni-based species can act as active catalytic sites for the hydrogen evolution reaction, supporting the adsorption and reduction of protons (MACHADO; AVACA, 1994), thus eliminating the need of a co-catalyst.

In addition to Bi_2WO_6, Nb_2O_5 is a material of great interest within our research group due to its favorable surface chemistry and the ease with which its morphological and structural properties can be tuned via hydrothermal treatment. In previous work, we demonstrated that hydrothermal treatment of optical-grade Nb_2O_5 at pH 8 yields a material with optimized surface and structural properties for photocatalytic hydrogen production.

Finally, by integrating both of the aforementioned strategies, titanium niobium oxynitride (NbTiON) was also investigated as a promising candidate for visible-light-driven hydrogen evolution. By co-doping TiO_2 with niobium and nitrogen, it is possible to obtain a material that combines the desirable surface and structural properties of TiO_2 with a significantly reduced band gap, thereby enhancing its light harvesting capability across a broader spectral range.

5.1. Specific Objectives

The specific objectives for the work showed this chapter were:

- Obtain visible-light-active materials by doping Bi_2WO_6 and Nb_2O_5 with Ni^{2+}/Ni^{3+} through hydrothermal synthesis
- Synthesize titanium oxynitride doped with niobium through an alternative route, using urea as nitrogen source
- Characterize the structure of the resulting materials
- Test the obtained materials for the photoreforming of biomass-derived waste streams under visible light and simulated sunlight conditions

5.2. Methodology

Nickel doped Bi_2WO_6 was obtained by dissolving 2 mmol $Bi(NO_3)_3.5\ H_2O$ (Aldrich) in 50 mL of HNO_3 (1.0 mol L^{-1}) under constant stirring and 1 mmol $Na_2WO_4.2\ H_2O$ in 20 mL deionized water. The tungstate solution was added dropwise into the Bi(III) solution, and the resulting mixture stirred constantly for 20 min. Then, 0.25 mmol of $Ni(NO_3)_2.6H_2O$ was dissolved in 1 mol L^{-1} NH_4OH solution, resulting in a bluish solution due to the formation of $[Ni(NH_3)_6]^{2+}$ complex. Then, the nickel solution was added dropwise to the tungstate solution, under vigorous stirring. The pH of the resultant solution was adjusted to 10 by adding NH_4OH, to keep nickel coordinated with ammonia. The mixture was transferred to an autoclave, kept at 200 ºC for 4 hours (160~180 psi).

Nickel doped Nb_2O_5 was prepared by adding dropwise the forementioned $[Ni(NH_3)_6]^{2+}$ solution in a suspension containing 1 g of optical grade Nb_2O_5 (CBMM) in 50 mL of deionized water, under vigorous stirring. The pH of the resulting suspension was 8. In a previous study, pH = 8 was found to be the best condition for Nb_2O_5 hydrothermal treatment, yielding the material with the best structural and morphological properties for Hydrogen evolution (NUNES, P. H. H., 2022), so the pH was kept at 8. The mixture was transferred to an autoclave and kept at 200 ºC for 24 hours (160~170 psi).

In both cases, the obtained powders were washed with deionized water, ethanol and dried at 80 ºC.

The oxynitride was prepared according with previous reported methodology (BRANCHO et al., 2017). In a typical synthesis, 0.175 mmol of $NbCl_5$ were dissolved using the minimum volume of anhydrous ethanol, followed by the addition of 3.5 mmol of titanium isopropoxide (TTIP) . After homogenization, 4.5 mmol of urea were added to the mixture, which was kept under vigorous magnetic stirring until it became a glassy film. The solid film was transferred to a ceramic crucible and then calcinated at 750 ºC in N_2 atmosphere for 3 hours with a 5 ºC min^{-1} heating and cooling profile. The resulting material, niobium titanium nitride, a fine black powder, went through a second calcination step in air atmosphere, 500 ºC for 30 minutes (10 ºC min^{-1}), resulting in a partially oxidized nitride, namely titanium niobium oxynitride.

The photocatalytic assays were conducted using a jacketed borosilicate 80 mL reactor, filled with 50 mL of a suspension containing 25 mg of photocatalyst in 10% v/v of meOH, glycerol or vinasse. For the flegmass photoreforming experiments 25 mg of photocatalyst were suspended in raw flegmass. The reactor was illuminated by a 300W arc Xe lamp and the suspension was kept at 20 ºC by circulating cooling water.

X-ray diffraction analysis (XRD) was executed utilizing an XRD600 powder diffractometer (Shimadzu) functioning at 40 kV and 30 mA with Cu Kα radiation as the excitation source. Raman spectroscopy was carried out on a LabRAM HR Evolution spectrometer (Horiba). X-ray photoelectron spectroscopy (XPS) measurements were conducted using a Thermo Scientific model K-Alpha spectrometer, which is equipped with an Al Kα X-ray source. All spectra underwent calibration against the C 1s peak, considering a standard binding energy of 284.6 eV. The morphologies of the films were assessed through Scanning Electron Microscopy (SEM) employing a TESCAN Vega3 microscope. Diffuse Reflectance Spectra (DRS) were collected using a UV 2600 spectrophotometer (Shimadzu) that is equipped with an integrating sphere. The transmittance values were converted to absorption equivalent values using the Kulbelka-munk function (PATTERSON; SHELDEN; STOCKTON, 1977; YANG, L.; KRUSE, 2004).

5.3. Results and Discussion

Figure 31 illustrates the experimental band edge positions for the base materials studied in this thesis. It can be seen that, although Bi_2WO_6, Nb_2O_5 and TiO_2 possess conduction band positions that are thermodynamically favorable for driving

hydrogen evolution, their wide band gaps still compromise practical applications. The influence of Ni^{2+}, Nb^{5+} and N^{3-} doping on the band positions of the materials can be predicted based on the known electronic configurations of these systems. In such metal oxide semiconductors, the valence band is primarily composed by oxygen 2p orbitals, while the conduction band is derived mainly from the cation d orbitals (AHMED, MANAN; XINXIN, 2016; SAKAR et al., 2020). Accordingly, Ni^{2+} doping is expected to shift the conduction band edges of Bi_2WO_6 and Nb_2O_5 toward lower potentials. In the case of oxynitrides, a more pronounced shift is expected in the valence band toward less positive potentials, owing to the contribution of N 2p orbitals introduced by nitrogen which is assumed to be the main factor causing the band gap reduction. This explains how the photoactivity of the materials can be shifted to the visible region after the modifications.

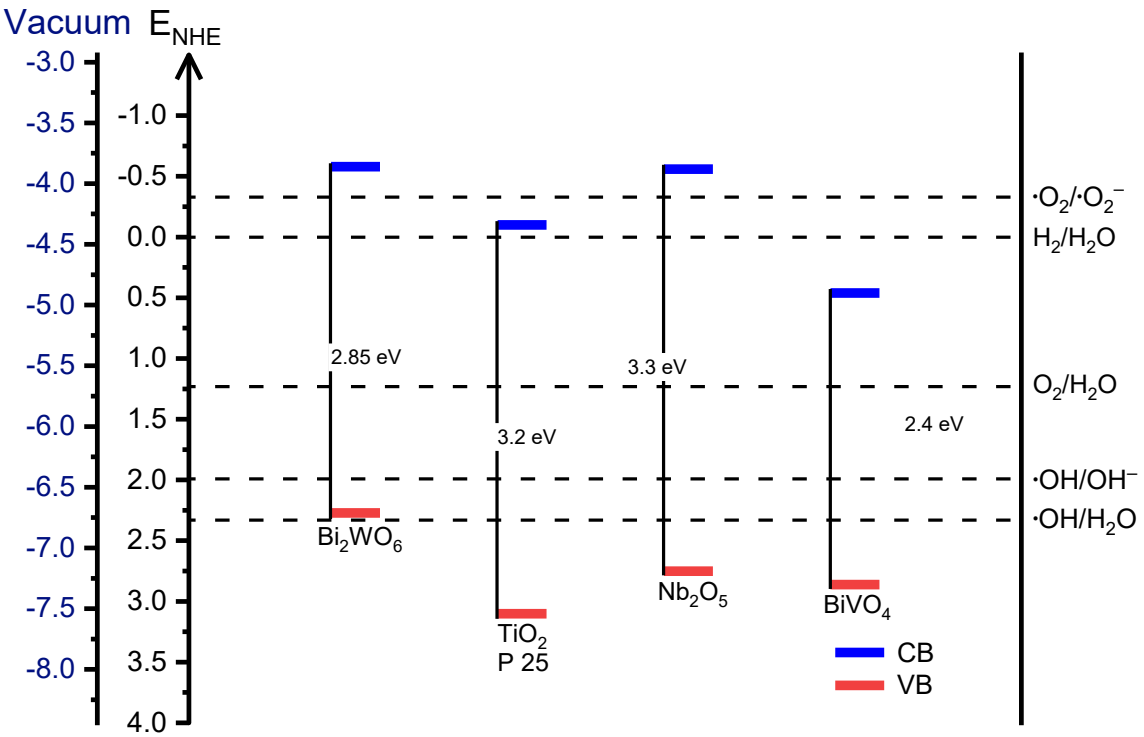

Figure 31. Energy diagram indicating the valence band and conduction band positions for the unmodified semiconductor materials studied in this work.

Both the Nb_2O_5 and Bi_2WO_6 were modified with Ni^{2+} (1% wt/wt.) via hydrothermal treatment, resulting in fine greenish powders. The diffraction patterns of the Bi_2WO_6-based samples were indexed to the orthorhombic phase of Bi_2WO_6 (ICCD 39-0256) without any visible impurities (Figure 32a). No additional peaks were

observed in the diffraction pattern of the nickel-modified sample, only a shift toward higher 2θ angles, indicating that Ni^{2+} ions were incorporated into the crystal lattice of Bi_2WO_6, thereby doping the material. In the case of Nb_2O_5-based samples, the diffraction patterns display a multiphase profile with a mixture of orthorhombic and monoclinic phases; however, the presence of other phases was evident and could not be conclusively assigned using the databases available during this study Figure 32c. No additional peaks were observed in the 1%Ni:Nb_2O_5 sample, but slight changes in the relative intensities were observed in relation to the pristine oxide, possibly due to the hydrothermal treatment.

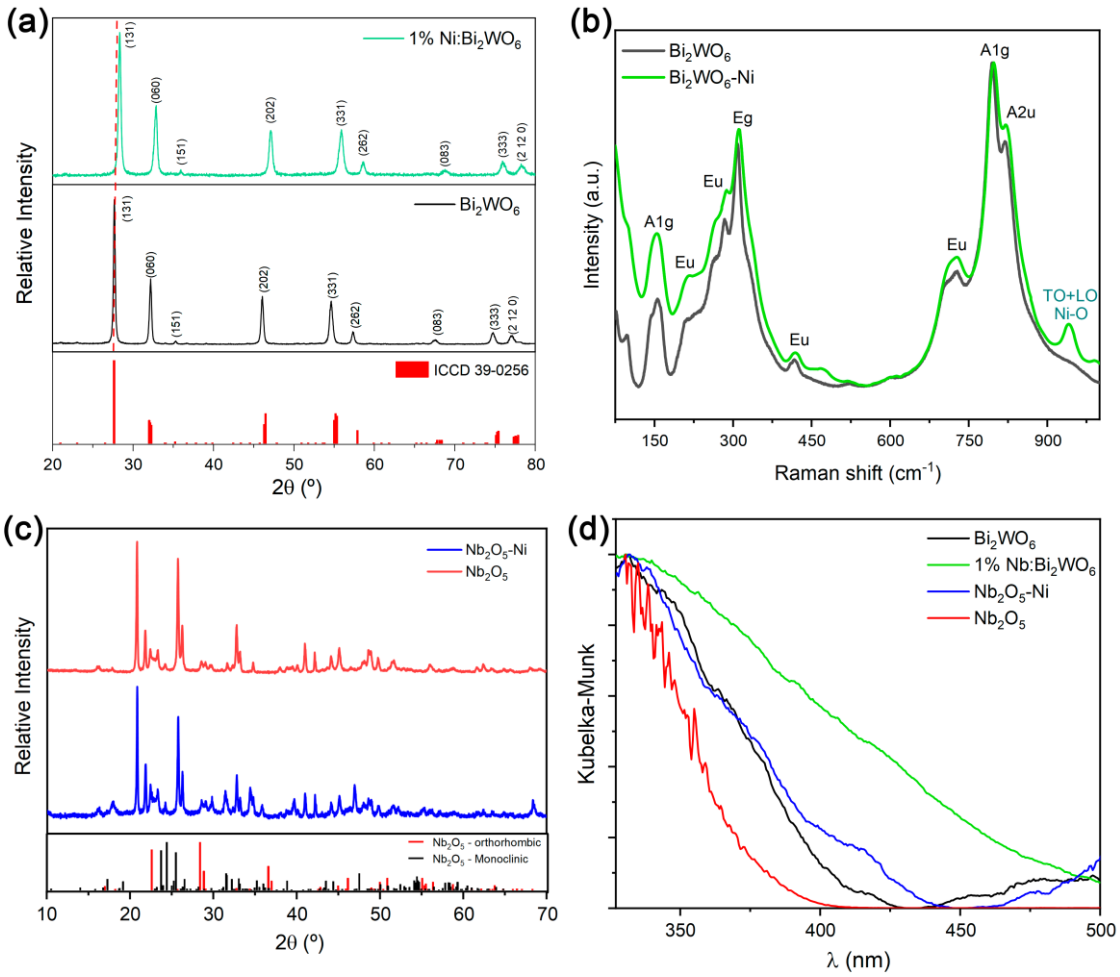

Figure 32. (a) XRD patterns and (b) Raman spectra of Bi_2WO_6 and 1% Ni:Bi_2WO_6; (c) DRX patterns of Nb_2O_5 and 1% Ni:Nb_2O_5; (d) UV-Vis spectra of the powder samples.

The Raman spectrum of the 1% Ni:Bi_2WO_6 sample is also characteristic of orthorhombic Bi_2WO_6 (Figure 32b). The vibrational modes in the 146–165 cm^{-1} range are attributed to translational modes of Bi^{3+} ions. The peaks at 213, 287, 419, and

724 cm^{-1} are associated with vibrations of the WO_6 octahedra. The most intense peak at 310 cm^{-1} arises from apical oxygen stretching (Eg) within the WO_6 octahedra. At 795 and 820 cm^{-1}, symmetric (A_1g) and asymmetric (A_2u) stretching modes are observed in WO_6. Finally, the only additional peak observed in the 1%Ni:Bi_2WO_6 sample, at 940 cm^{-1}, is assigned to the transverse and longitudinal stretching of the Ni–O bond, indicating that nickel modification affected the material's surface.

The ionic radius of Ni^{2+} and Ni^{3+} (69 and 56 pm, octahedral coordination) are significantly smaller than that of Bi^{3+} (103 pm) (SHANNON, 1976), which implies that direct substitution of Bi^{3+} sites by $Ni^{2+/3+}$ would generate considerable lattice strain and require the formation of compensatory defects, such as oxygen vacancies, to maintain charge balance. The observed shift of the diffraction peaks toward higher 2θ angles supports a reduction of lattice parameters, consistent with structural defects. However, the high mismatch in both ionic size and charge also suggests that a substantial fraction of the Ni^{2+} ions are likely accommodated in interstitial positions or adsorbed onto the surface as Ni–O or Ni–OH species. This interpretation is corroborated by the presence of an additional Raman band at ~940 cm^{-1}, attributed to Ni–O vibrations, and the XPS signals characteristic of Ni–OH surface groups, as further discussed below. Replacement of W^{6+} is less likely due to the large mismatch between the charge of the cations.

In the case of Nb_2O_5, the comparison of ionic radii suggests that $Ni^{2+/3+}$ incorporation into is structurally favorable. The ionic radius of Ni^{2+} (69 pm) and Ni^{3+} (56 pm) is very similar to that of Nb^{5+} (64 pm) in octahedral coordination (SHANNON, 1976), indicating that substitutional doping is unlikely to induce significant lattice distortion. However, the substantial difference in ionic charge means that compensatory defects such as oxygen vacancies or mixed-valance states (Nb^{5+} and $Nb^{4+)}$ would be required to maintain charge neutrality.

The DRS spectra of the Ni-modified samples exhibited a shift towards the visible region when compared to their pristine counterparts. 1% Ni:Nb_2O_5 exhibited an absorption tail extending up to 450 nm, while 1% Ni:Bi_2WO_6 showed absorption extending up to 500 nm (Figure 32d), evidencing that in both cases, the absorption was shifted into the visible range. SEM images of the powder samples, Figure 33, revealed that the 1% Ni:Bi_2WO_6 sample presented a morphology of well-organized thin micrometer-scale sheets, while the pristine Bi_2WO_6 exhibits nanosized scale

sheets. In contrast, the 1% Ni:Nb_2O_5 sample showed aggregates of irregular nanometric spheres deposited on larger plates, consistent with its multiphasic composition, similarly the pristine Nb_2O_5 is formed by an irregular agglomerate of inhomogeneous structures.

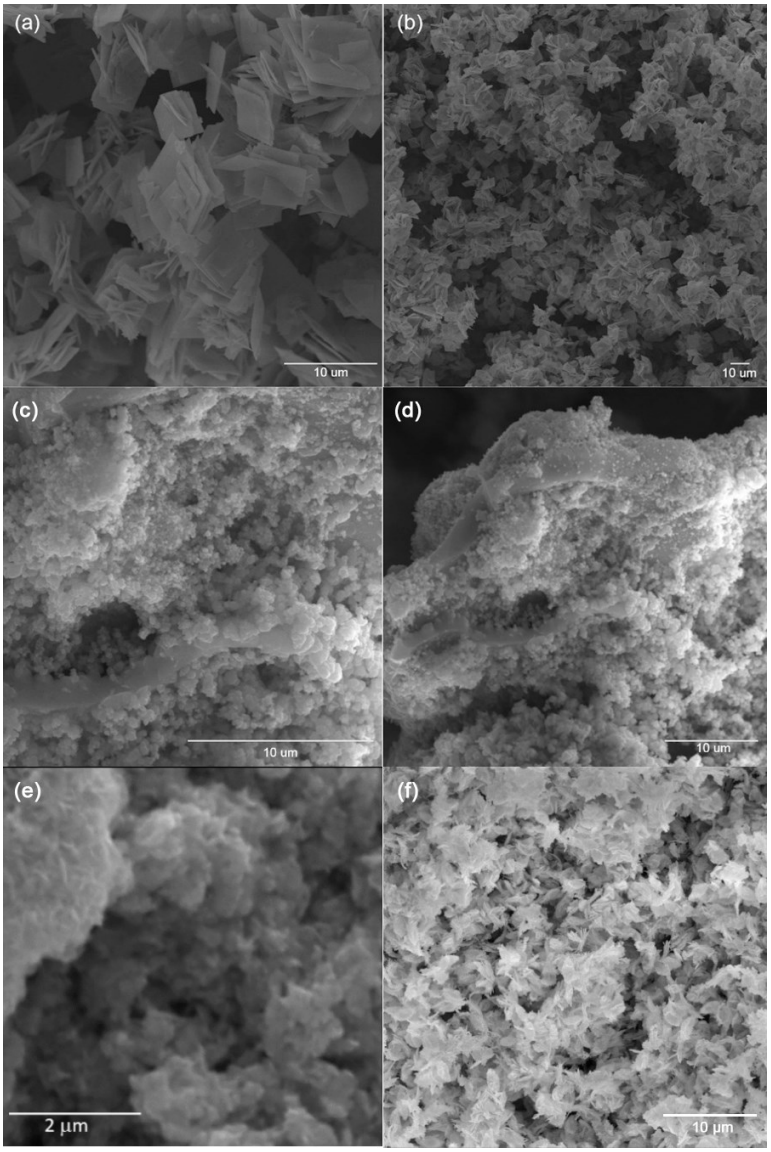

Figure 33. SEM images of (a, b) 1% Ni:Bi_2WO_6 and (c, d) 1% Ni:Nb_2O_5 samples at different magnification levels, (e) Pristine Bi_2WO_6 and (e) pristine Nb_2O_5.

The composition of the samples was investigated through XPS, Figure 34. No significant contamination was identified in the survey spectra of the materials studied, Figure 34a. Additionally, in the high-resolution spectra the Ni 2p doublet, a typical profile of Ni–OH bonds with significant contribution from Ni^{3+}, probably due to the

highly oxidizing hydrothermal synthetic media (JIANG et al., 2015), was observed confirming the incorporation of Ni^{2+} and Ni^{3+} species in both samples, Figure 34b. The nickel content in the samples was quantified by atomic absorption measurements, revealing approximately 0.050 ± 0.01 wt.% nickel in 1% Ni:Nb_2O_5 and 0.040 ± 0.01 wt.% in 1% Ni:Bi_2WO_6, indicating that only half of the total Ni^{2+} content employed in the hydrothermal synthesis was incorporated into the crystalline lattice of the doped materials.

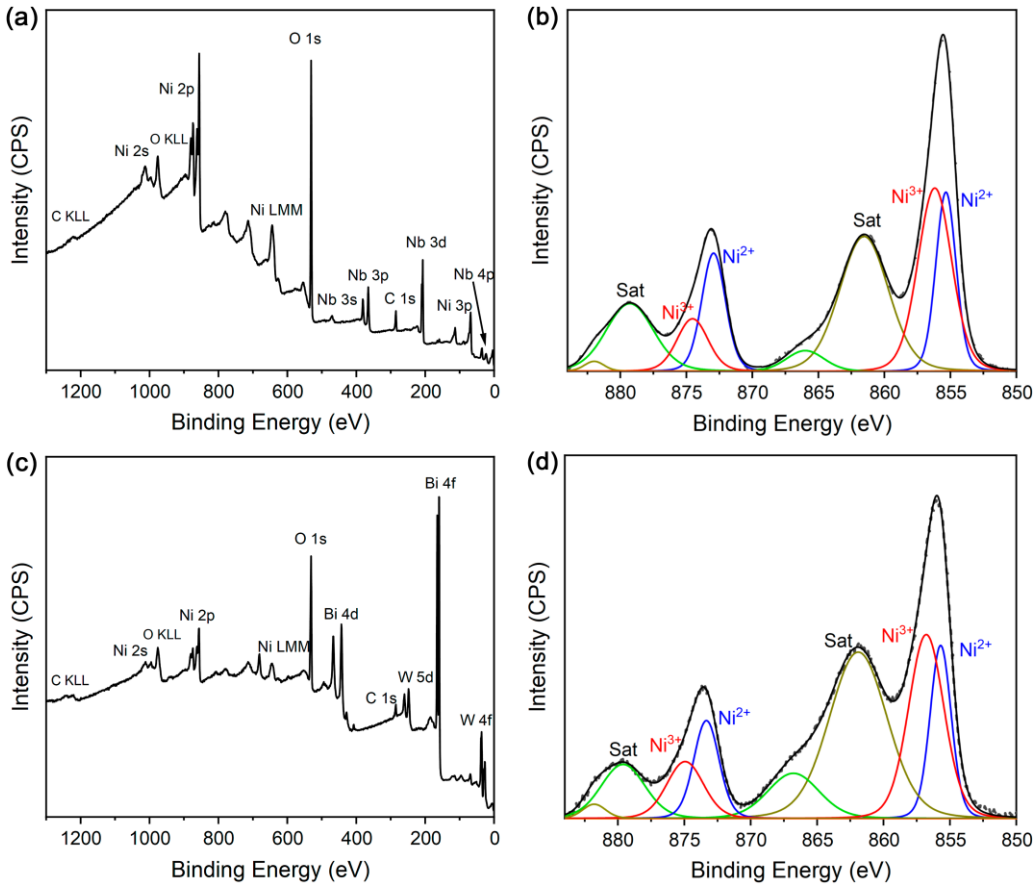

Figure 34. XPS spectra of the nickel-modified samples. (a) Survey spectrum of 1% Ni:Nb_2O_5; (b) Ni 2p HR spectrum of 1% Ni:Nb_2O_5; (c) Survey spectrum of 1% Ni:Bi_2WO_6 and (d) Ni 2p HR spectrum of 1% Ni:Bi_2WO_6.

The photocatalytic performance was evaluated in terms of conversion efficiency and H_2 production in glycerol photoreforming experiments. The materials were suspended in aqueous solutions containing 10% v/v analytical grade glycerin or crude glycerol, and the resulting suspension was irradiated with visible light (λ > 400 nm, 100 mW cm^{-2}), Figure 35a. The unmodified Bi_2WO_6 and Nb_2O_5 samples exhibited no

photoactivity under any of the tested conditions, as these materials lack activity in the visible spectrum. However, for both modified materials, H_2 production was comparable when either raw glycerol or analytical-grade glycerol was used. The 1% Ni:Bi_2WO_6 photocatalyst maintained an H_2 production rate of 1.82 ± 0.1 mmol g^{-1} h^{-1}, while 1%Ni:Nb_2O_5 reached 0.25 ± 0.05 mmol g^{-1} h^{-1} over 5 hours of reaction. Nevertheless, 1% NI:Nb_2O_5 was more efficient in converting crude glycerol, achieving 36% conversion compared to 26% for 1% Nb:Bi_2WO_6.

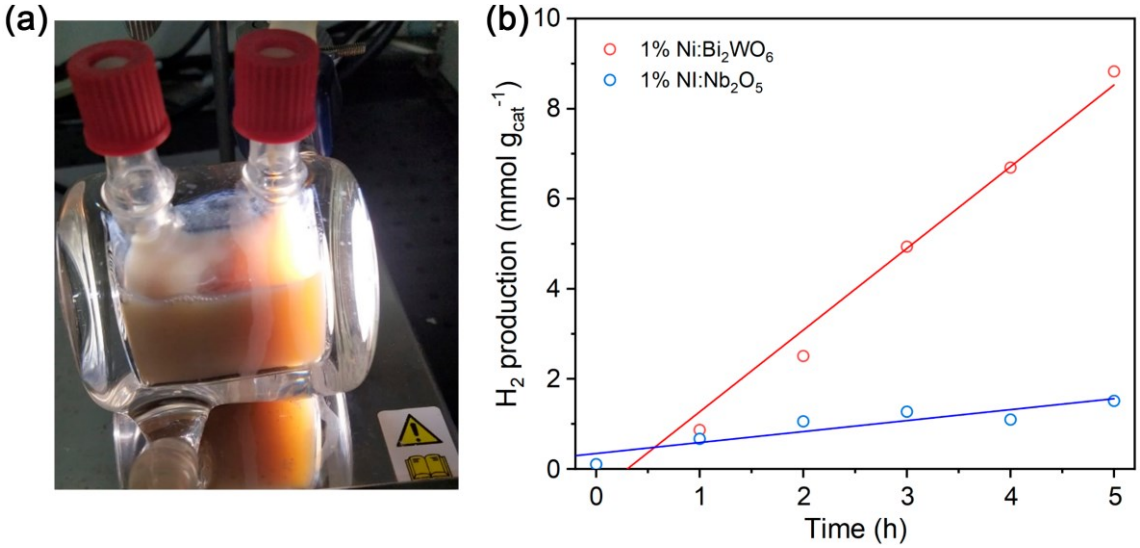

Figure 35. (a) Reactor used in the crude glycerol photoreforming experiments and (b) hydrogen evolution from crude glycerol (10% v/v) photoreforming using nickel-modified materials ($\lambda > 400$ nm, 100 mW cm^{-2})

Additionally, vinasse from sugarcane refineries was employed as a sacrificial reagent in the photoreforming experiments. Vinasse is the main liquid residue generated during sugar and bioethanol production. It has a complex composition and is characterized by a high Chemical Oxygen Demand (COD), strong odor and high turbidity. Therefore, the photocatalysts were also evaluated for their capacity to remove COD from raw vinasse. The vinasse was diluted to 10% v/v to allow light penetration into the suspension. Two illumination conditions were assessed: simulated solar irradiation (Air Mass 1.5G) and visible light ($\lambda > 400$ nm), both at 100 mW cm^{-2}. None of the materials produced H_2 from vinasse photodegradation. Under visible light, 1% Ni:Bi_2WO_6 removed 60% of the initial COD after 5 hours of photocatalytic testing, while 1% Ni :Nb_2O_5 removed only 19%, Figure 36. This difference in performance in

attributed to the broader absorption spectra of 1% Ni:Bi_2WO_6. However, when simulated sunlight was employed, both photocatalysts performed similarly, reducing the initial COD by 20%. Control experiments were also performed by illuminating vinasse without a photocatalyst, whereas no changes on COD were observed. These results are promising and suggest that vinasse can act as an electron donor photoinduced reactions.

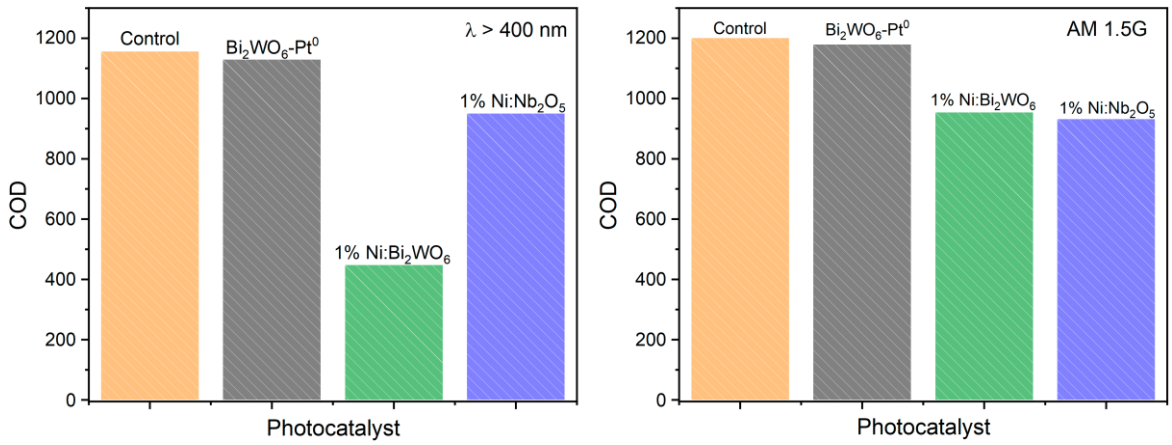

Figure 36. COD removal of vinasse (10% v/v in water) after 5 hours of illumination under (a) visible light (λ > 400 nm, 100 mW cm^{-2}) and (b) simulated sunlight (AM 1.5G, 100 mW cm^{-2}).

Another material that was investigated was titanium and niobium oxynitride. Oxynitrides are a category of materials that have also drawn significant attention recently (AHMED, MANAN; XINXIN, 2016; JIANG, S.; LIU; XU, 2021). These materials exhibit properties of both oxides and nitrides derived from their precursor metals, making them promising candidates in the field of photocatalysis. Additionally, the incorporation of nitrogen into the crystalline structure of oxynitrides reduces their band gap energy, thereby shifting their absorption into the visible spectrum. A secondary metal is often introduced to stabilize the charge imbalance caused by replacing oxygen with nitrogen in the crystal lattice, leading to an increase in cell volume and improved electronic mobility compared to the precursor oxides.

The synthesis of TiO_2-based oxynitride involves two stages. In the first stage, precursors of Ti(IV) and Nb(V) are combined in the presence of excess urea, which acts as a nitrogen source. This mixture is calcined at 750°C in a nitrogen atmosphere

to produce a titanium-niobium nitride. The nitride is then calcined in air, undergoing partial oxidation to form titanium oxynitride doped with niobium and nitrogen (NbTiON).

The diffraction pattern of the material obtained after the first calcination stage in N_2 atmosphere reveals a mix of anatase, rutile, and titanium nitride (TiN), Figure 37. Rietveld refinement shows that approximately 25% of the material is converted to TiN, while 40% corresponds to the anatase phase and the remaining 35% to rutile. Brancho and collaborators (BRANCHO et al., 2017), describe that this phenomenon could be attributed to the formation of oxynitride during the nitride synthesis stage. After the second synthesis stage, Raman spectra show only the anatase and rutile phases, unlike the 100% anatase oxynitride reported by Brancho et al. (BRANCHO et al., 2017). Furthermore, the diffraction pattern of the oxynitride indicates it keeps TiO_2 structure, predominantly composed of the rutile phase with some anatase. Diffuse reflectance analyses demonstrate that the absorption of oxynitride extends up to 500 nm in the visible spectrum, in contrast to TiO_2, whose absorption is confined to the ultraviolet range.

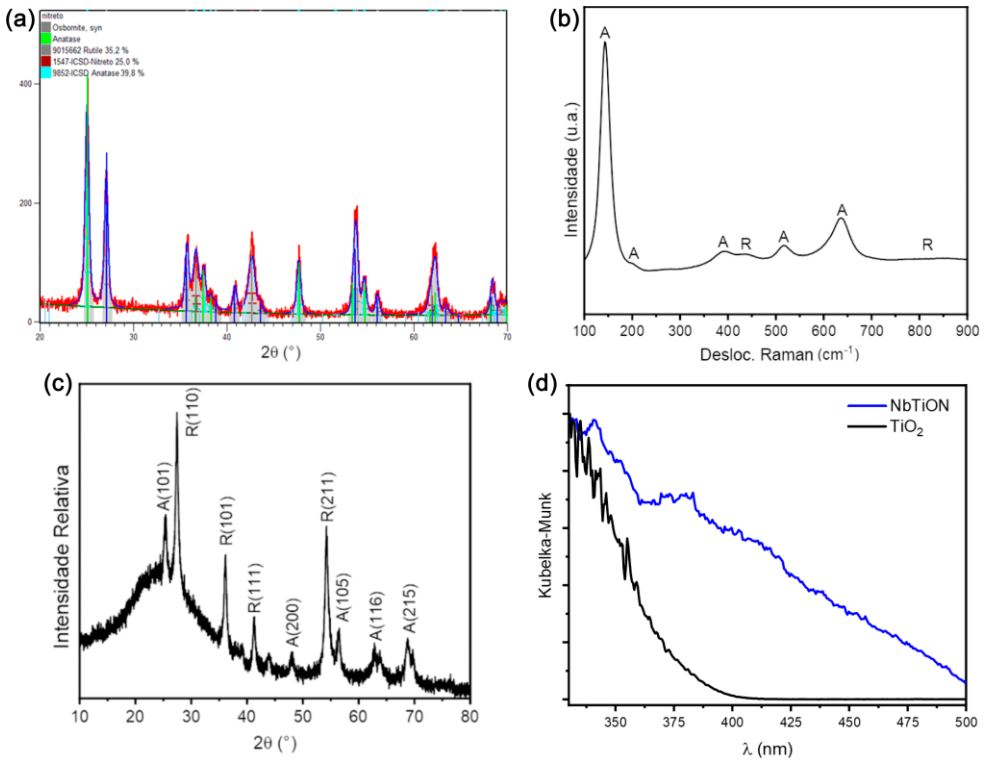

Figure 37. (a) Diffractogram of NbTiON after the first calcination in N_2 atmosphere; (b) Raman and (c) DRX spectra of NbTiON after the last calcination step. (d) UV-Vis spectra of TiO_2 P25 and NbTiON.

The high-resolution XPS spectra of NbTiON confirm that the synthesis was effective in producing the target material as no significant impurities are visible in the survey spectra Figure 38a. After the final calcination step under an air atmosphere, two distinct N 1s peaks are observed, Figure 38b, indicating the partial oxidation of the material. The peak at 403.2 eV corresponds to nitrogen directly bonded to titanium (Ti—N), while the peak at 396.5 eV is associated with nitrogen species bonded to TiO_2 (N—TiO_2) (MACKENZIE; CRAVEN; HATTO, 1999; PIALLAT et al., 2016). Peaks corresponding to Nb(V) species incorporated into the structure are also evident, Figure 38c. Moreover, in the O 1s region, Figure 38d, two peaks are observed in the sample, a phenomenon attributed to the presence of adsorbed water and/or oxygen vacancies in a manner analogous to $BiWO_{(vac)}$. Ti 2p high-resolution XPS spectrum shows features attributed to TiO_2 and TiON which are characteristic of titanium-based oxynitride. Finally, the N1s XPS spectra of the sample collected after the first calcination step in N_2 atmosphere (NbTiN), Figure 38f exhibits a distinct behavior identified a shift towards lower binding energy (397 eV) and by the presence of a significant satellite feature at 400 eV, which are characteristic of nitrogen in TiN (MACKENZIE; CRAVEN; HATTO, 1999; ZUO et al., 2022) corroborating the nitride and, thus, the oxynitride formation.

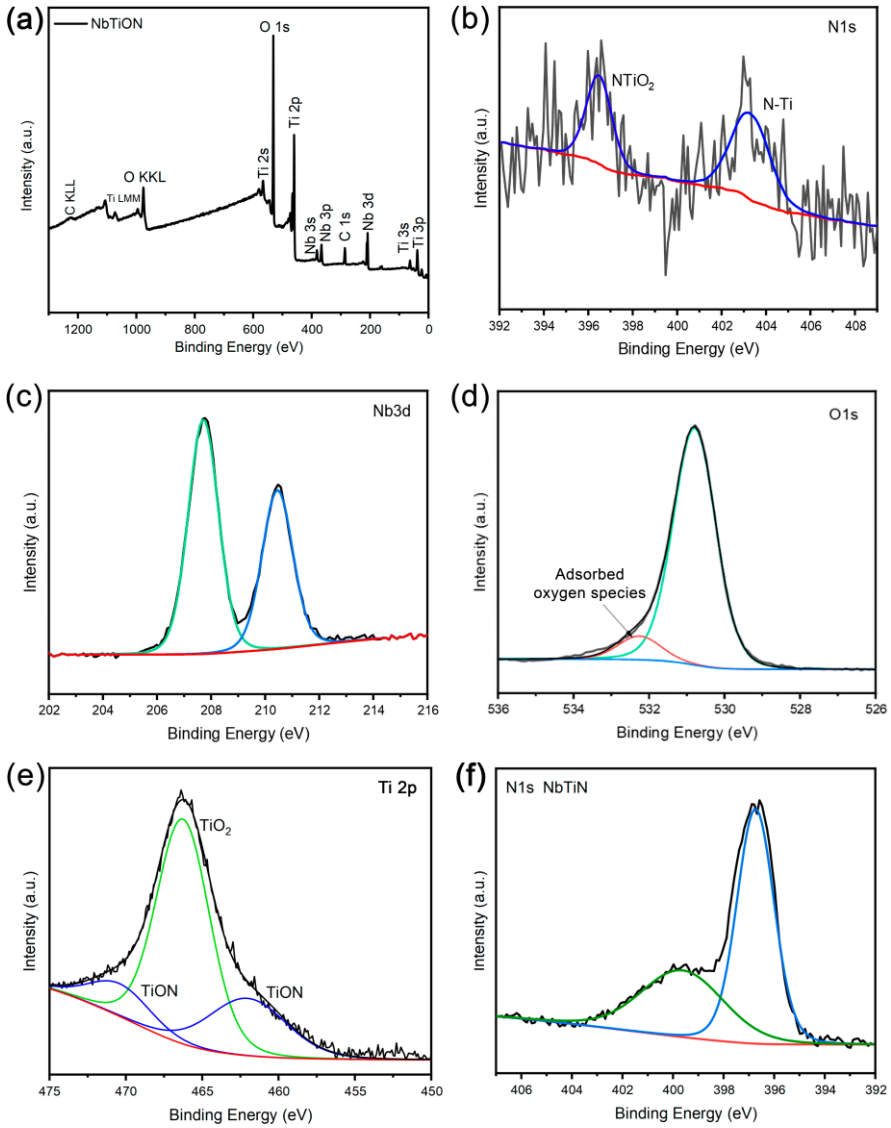

Figure 38. (a) Survey XPS spectra of NbTiON. (b) High-resolution N1s XPS spectrum of NbTiON (c) High-resolution Nb3d XPS spectrum of NbTiON, (d) High-resolution O1s spectrum of NbTiON (e) high resolution spectrum of Ti2p of NbTiON and (f) High-resolution N1s XPS spectrum of NbTiN after the first calcination step in N_2 atmosphere, confirming the formation of the nitride.

While promising results were obtained using vinasse as a sacrificial agent, its application presented significant challenges due to the high turbidity of the solution and the presence of recalcitrant organic components. To overcome these limitations, flegmass, a distillery residue derived from sugarcane processing, was selected as the photoreforming substrate for the experiments involving NbTiON. The main advantage of flegmass is its suitability for direct use, requiring no dilution or additional pre-treatment. A 5% v/v methanol solution was used as a benchmark for hydrogen

evolution, as methanol is known to be an excellent sacrificial electron donor (NUNES, B. N. et al., 2019). Under visible light irradiation (λ > 400 nm, 100 mW cm^{-2}), NbTiON achieved an H_2 evolution rate of 35.0 ± 4.2 μmol g^{-1} h^{-1}, with production continuously increasing over the 10 hours experiment. In contrast, when flegmass was used as the sacrificial agent, the H_2 evolution rate increased fourfold, reaching 140 ± 18 μmol g^{-1} h^{-1} under the same conditions. Control experiments conducted using TiO_2 P25 showed no detectable hydrogen production under visible light, owing to its absorption being restricted to the UV range.

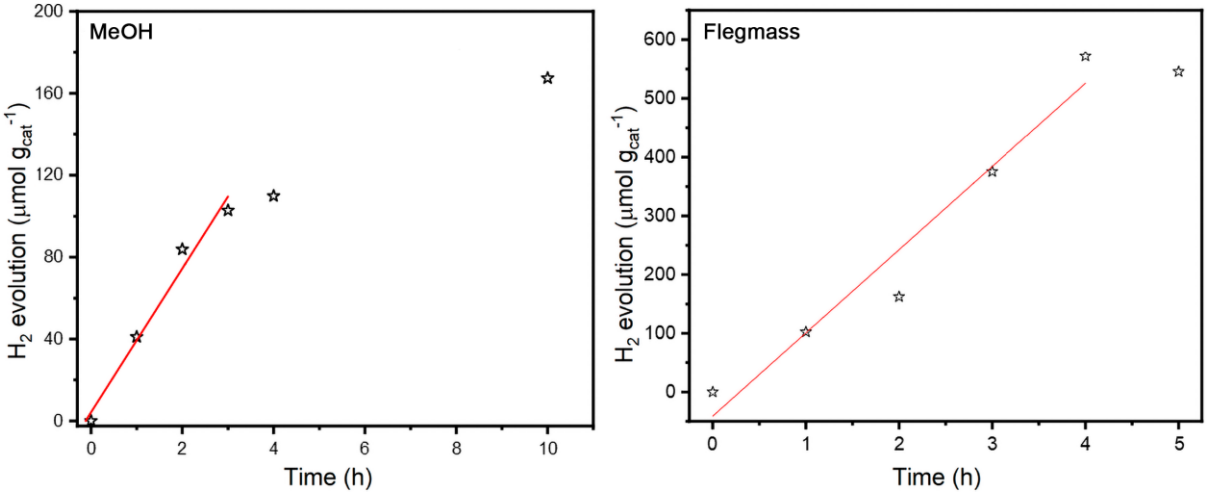

Figure 39. Photocatalytic hydrogen evolution of NbTiON using (a) methanol and (b) flegmass as sacrificial agent. (λ > 400 nm, 100 mW cm^{-2}).

5.4. Conclusions

It was verified that oxynitrides are a promising class of materials for developing visible-light-active photocatalysts. NbTiON achieved a H_2 evolution rate of 140 μmol g^{-1} h^{-1} under visible light (λ > 400 nm, 100 mW cm^{-2}). The NbTiON oxynitride combines the favorable morphological and structural properties of TiO_2 with a narrower band gap and consequently enhanced light harvesting capabilities. This synergistic effect may hold the key to the development of novel photocatalysts enabling scalable biomass photoreforming solutions.

Moreover, Ni doping was successful in shifting the photoactivity of Bi_2WO_6 and Nb_2O_5 to the visible region. The doped materials showed promising results for glycerol photoreforming and vinasse. 1% Ni:Bi_2WO_6 removed 60% of COD of vinasse and achieved a H_2 evolution rate 1.82 ± 0.1 mmol g^{-1} h^{-1} from glycerol photoreforming. Its better performance compared to 1% Ni:Nb_2O_5 was attributed to broader absorption in the visible spectrum.

Although these studies showed that both the Ni-modified materials and the oxynitride are good candidates for biomass photoelectroreforming, immobilizing them as thin films has proven a challenge due to their limited thermal stability. The annealing step is essential to remove organic impurities and enhance the mechanical stability of the films. However, upon calcination, the surface Ni species at the $Ni^{2+/3+}$-doped materials undergo oxidation, generating NiO which poisons the photoanode hindering its performance. Similarly, calcination of NbTiON leads to further oxidation resulting in mixtures of TiO_2 and Nb_2O_5. Therefore, additional studies are needed to develop strategies for fabricating stable photoanodes based on these materials.

6. Bridging the Gap: Toward Practical Light-Driven Low Carbon Hydrogen Production

The pressing global demand for sustainable energy solutions has intensified the search for alternative routes to low-carbon hydrogen production. While photocatalysis and photoelectrochemical reforming represent promising approaches, their large-scale implementation remains limited by challenges such as poor light harvesting, rapid charge carrier recombination, insufficient stability, and the limited use of real-world substrates in testing protocols. This thesis contributes to bridging these gaps by systematically investigating and engineering a range of materials, based on Bi_2WO_6, Nb_2O_5, TiO_2, and novel oxynitride and COF-based systems, for sunlight-driven hydrogen evolution, with particular attention to their performance in complex, industrial biomass-derived waste streams.

Through rational design strategies including oxygen vacancy engineering, metal doping, and the synthesis of oxynitride (NbTiON) and covalent organic frameworks, significant progress was made toward extending the photoresponse of wide band gap semiconductors into the visible region, thus increasing the sunlight harvesting capabilities of these materials. The Ni-doped Bi_2WO_6 and Nb_2O_5-based photocatalysts exhibited notable activity for hydrogen evolution and chemical oxygen demand (COD) removal when tested against crude glycerol and vinasse, confirming their viability in handling real substrates. The $BiWO_{(vac)}$ with engineered oxygen vacancies stood out for its high visible-light absorption when compared to the unmodified Bi_2WO_6 and glycerol photoelectroreforming performance under simulated sunlight conditions. Notably, the COF materials delivered sustained H_2 evolution through ascorbic acid photoreforming during several days of continuous operation, highlighting the robustness of this system.

The photoelectrochemical approach is highlighted due to its increased H_2 evolution kinetics when compared to regular photocatalysis. Moreover, it was shown that the proposed photoelectrochemical systems could reach similar performance when either analytical grade model molecules or real industrial waste streams, such as crude glycerol and flegmass, were employed as substrates. In this context, among all systems studied, Nb-doped $BiVO_4$ emerged as the most efficient and robust photoanode. It demonstrated excellent PEC performance, achieving over 90% glycerol conversion and an 89% selectivity toward formic acid, with a hydrogen evolution rate of 4.2 μmol H_2 cm^{-2} h^{-1} under AM 1.5G irradiation, an 84% increase over undoped $BiVO_4$. Moreover, the 5% Nb:$BiVO_4$ photoanodes yielded the highest photocurrent density among the studied systems. Importantly, the system exhibited

good operational stability during extended operation, making it a leading candidate for practical photoelectroreforming applications.

Therefore, this work reinforces the importance of combining material engineering strategies with realistic testing protocols using actual waste streams as platform for low-carbon hydrogen evolution. It positions Nb-doped $BiVO_4$ photoanodes as a benchmark system for future research on solar-driven biomass valorization and low carbon hydrogen production, while also highlighting the potential of emerging material classes such as oxynitrides and COFs to address the next generation of photo(electro)catalytic challenges.

Building on the promising results obtained in this work, future research will focus on the scaling and practical implementation of the developed photocatalytic and photoelectrochemical systems. Particular attention will be placed on photoelectrochemical approaches, given their superior hydrogen evolution kinetics and potential for system integration. The main challenge ahead lies in bridging the gap between laboratory-scale experiments and industrial applications. To this end, flow-cell configurations capable of operating with real waste streams must be further developed and optimized. Advancing these systems will not only move toward sustainable hydrogen production but also contribute to the valorization of industrial biomass-derived residues, supporting the transition to cleaner and more circular energy technologies.

7. Overall Conclusions

This thesis demonstrates that rational design and engineering of photocatalyst materials can significantly enhance their performance in visible-light-driven photocatalytic and photoelectrochemical hydrogen evolution from biomass-derived real industrial wastes.

Solvothermal synthesis in ethylene glycol successfully produced oxygen-deficient Bi_2WO_6 ($BiWO_{(vac)}$) with improved visible light absorption and charge transport when compared to its counterpart obtained hydrothermally, demonstrating the role of synthetic media in defect generation. The $BiWO_{(vac)}$ photoanodes exhibited improved charge dynamics and conductivity, which resulted in a hydrogen evolution rate of 63 μmol cm^{-2} h^{-1} with a faradaic efficiency of 91%, two times bigger than pristine Bi_2WO_6. Glycerol conversion was found to be 24.5% at pH = 6 with 85% selectivity toward formic acid production.

Doping strategies were successfully employed into known semiconductor oxides through hydrothermal synthesis, $Ni^{2+/3+}$ incorporation into Bi_2WO_6 and Nb_2O_5 were efficient in extending the absorption edge into the visible region and improving the photocatalytic activity of the materials, although photoelectrocatalytic applications are still limited. In the case of $BiVO_4$, the Niobium doping significantly enhanced the photoanode performance, with 5% Nb:$BiVO_4$ exhibiting 80% increase in photocurrent during long-term crude glycerol photoelectroreforming. Moreover, photoelectroreforming of crude glycerol with 5% Nb:$BiVO_4$ after 6 hours of irradiation achieved 91.4% substrate conversion, producing green H_2 at a rate of 4.2 μmol cm^{-2} h^{-1}, much higher than 2.3 μmol cm^{-2} h^{-1} obtained by undoped $BiVO_4$. EPR spin trapping experiments indicated that the main reaction mechanism involves direct hole transfer to adsorbed glycerol on the catalyst surface forming organic radical species. Therefore, 5% Nb:$BiVO_4$ consistently outperformed bare $BiVO_4$ photoanode, highlighting its potential for valorizing low-cost, biomass-derived residues into valuable chemicals and renewable fuels.

NbTiON oxynitride exhibited remarkable visible-light-driven hydrogen evolution when reforming flegmass. The material retained the favorable surface and structural properties of TiO_2 while displaying a shorter band gap and, thus, improved light harvesting capabilities, confirming the potential of oxynitrides as robust photocatalysts for real waste streams.

Covalent Organic Frameworks (COFs) were synthesized as proof-of-concept materials with tailored linkage chemistries, offering promising pathways to engineer porosity, optoelectronic properties, and interfacial interactions for photocatalytic applications. We have demonstrated that demonstrate that converting imine to amide linkages in a thiophene-based COF allows for altering surface charge through different protonation behaviour of the linkages. The amide-linked COF, acts as an antenna that facilitates interdomain electron transport along COF agglomerates, promotes both Pt growth and subsequent proton reduction demonstrating 300 % increase in photocatalytic hydrogen evolution rates compared to its imine form. This work introduces surface charge modulation as a novel tool for controlling photocatalytic processes in COF-based systems expanding the COF functionality in photocatalysis

Overall, this work highlights the importance of combining material innovation with mechanistic understanding to enable scalable, efficient solar-fuel production technologies. The present work brings many sustainable approaches for green H_2 production using highly diversified platforms, representing an important step towards a cleaner society.

8. References

AHMAD, H.; RAUF, A.; AHMAD, A.; ULHAQ, A.; MUHAMMAD, S. First-principles study on the electronic and optical properties of Bi2WO6. **RSC Advances**, v. 11, n. 51, p. 32330-32338, 2021.
https://doi.org/10.1039/D1RA03784F.

AHMAD, M. S.; AB RAHIM, M. H.; ALQAHTANI, T. M.; WITOON, T.; LIM, J.-W.; CHENG, C. K. A review on advances in green treatment of glycerol waste with a focus on electro-oxidation pathway. **Chemosphere**, v. 276, n., p. 130128, 2021.
https://doi.org/10.1016/j.chemosphere.2021.130128.

AHMED, M.; XINXIN, G. A review of metal oxynitrides for photocatalysis. **Inorganic Chemistry Frontiers**, v. 3, n. 5, p. 578-590, 2016.
https://doi.org/10.1039/C5QI00202H.

AHMED, M.; DINCER, I. A review on photoelectrochemical hydrogen production systems: Challenges and future directions. **International Journal of Hydrogen Energy**, v. 44, n. 5, p. 2474-2507, 2019.
https://doi.org/10.1016/j.ijhydene.2018.12.037.

ALFAIFI, B. Y.; TAHIR, A. A.; WIJAYANTHA, K. G. U. Fabrication of Bi2WO6 photoelectrodes with enhanced photoelectrochemical and photocatalytic performance. **Solar Energy Materials and Solar Cells**, v. 195, n., p. 134-141, 2019.
https://doi.org/10.1016/j.solmat.2019.02.031.

AUGUGLIARO, V.; EL NAZER, H. A. H.; LODDO, V.; MELE, A.; PALMISANO, G.; PALMISANO, L.; YURDAKAL, S. Partial photocatalytic oxidation of glycerol in TiO2 water suspensions. **Catalysis Today**, v. 151, n. 1, p. 21-28, 2010.
https://doi.org/10.1016/j.cattod.2010.01.022.

AUGUSTIN, A.; CHUAICHAM, C.; SHANMUGAM, M.; VELLAICHAMY, B.; RAJENDRAN, S.; HOANG, T. K. A.; SASAKI, K.; SEKAR, K. Recent development of organic–inorganic hybrid photocatalysts for biomass conversion into hydrogen production. **Nanoscale Advances**, v. 4, n. 12, p. 2561-2582, 2022.
https://doi.org/10.1039/D2NA00119E.

AYYANGAR, N. R.; SRINIVASAN, K. V. Effect of substituents in the formation of diacetanilides. **Canadian Journal of Chemistry**, v. 62, n. 7, p. 1292-1296, 1984.
https://doi.org/10.1139/v84-215.

BARROSO, M.; PENDLEBURY, S. R.; COWAN, A. J.; DURRANT, J. R. Charge carrier trapping, recombination and transfer in hematite (α-Fe2O3) water splitting photoanodes. **Chemical Science**, v. 4, n. 7, p. 2724-2734, 2013.
https://doi.org/10.1039/C3SC50496D.

BATISTA, L. M. B.; OLIVEIRA, J. L. F.; BEZERRA, F. A.; ARAÚJO, A. M. D. M.; FERNANDES JUNIOR, V. J.; ARAUJO, A. S.; ALVES, A. P. M.; GONDIM, A. D. Synthesis, characterization and evaluation of niobium catalysts in the flash pyrolysis of glycerol. **Solid State Sciences**, v. 97, n., p. 105977, 2019.
https://doi.org/10.1016/j.solidstatesciences.2019.105977.

BEDNARCZYK, K.; STELMACHOWSKI, M.; GMUREK, M. The influence of process parameters on photocatalytic hydrogen production. **Environmental Progress & Sustainable Energy**, v. 38, n. 2, p. 680-687, 2019.
https://doi.org/10.1002/ep.12998.

BHATTACHARJEE, S.; ANDREI, V.; PORNRUNGROJ, C.; RAHAMAN, M.; PICHLER, C. M.; REISNER, E. Reforming of Soluble Biomass and Plastic Derived Waste Using a Bias-Free Cu30Pd70|Perovskite|Pt Photoelectrochemical Device. **Advanced Functional Materials**, v. 32, n. 7, p. 2109313, 2022. https://doi.org/10.1002/adfm.202109313.

BOCIAN, S.; DZIUBAKIEWICZ, E.; BUSZEWSKI, B. Influence of the charge distribution on the stationary phases zeta potential. **Journal of Separation Science**, v. 38, n. 15, p. 2625-2629, 2015. https://doi.org/10.1002/jssc.201500072.

BORA, D. K.; NADJAFI, M.; ARMUTLULU, A.; HOSSEINI, D.; CASTRO-FERNÁNDEZ, P.; TOTH, R. Photoelectrochemical glycerol oxidation on Mo-BiVO4 photoanodes shows high photocharging current density and enhanced H2 evolution. **Energy Advances**, v. 1, n. 10, p. 715-728, 2022. https://doi.org/10.1039/D2YA00077F.

BRANCHO, J. J.; PROCTOR, A. D.; PANUGANTI, S.; BARTLETT, B. M. Urea-glass preparation of titanium niobium nitrides and subsequent oxidation to photoactive titanium niobium oxynitrides. **Dalton Transactions**, v. 46, n. 36, p. 12081-12087, 2017. https://doi.org/10.1039/C7DT03077K.

BUETTNER, G. R. Spin Trapping: ESR parameters of spin adducts 1474 1528V. **Free Radical Biology and Medicine**, v. 3, n. 4, p. 259-303, 1987. https://doi.org/10.1016/S0891-5849(87)80033-3.

BURTCH, N. C.; JASUJA, H.; DUBBELDAM, D.; WALTON, K. S. Molecular-level Insight into Unusual Low Pressure CO2 Affinity in Pillared Metal–Organic Frameworks. **Journal of the American Chemical Society**, v. 135, n. 19, p. 7172-7180, 2013. https://doi.org/10.1021/ja310770c.

BUZZETTI, L.; CRISENZA, G. E. M.; MELCHIORRE, P. Mechanistic Studies in Photocatalysis. **Angewandte Chemie International Edition**, v. 58, n. 12, p. 3730-3747, 2019. https://doi.org/10.1002/anie.201809984.

CAI, X.; WANG, C.; CHEN, Y.; CHENG, Z.; SHU, R.; ZHANG, J.; BU, E.; LIAO, M.; SONG, Q. A novel approach for enhancing hydrogen production from bio-glycerol photoreforming by improving colloidal dispersion stability. **Science of The Total Environment**, v. 627, n., p. 1464-1472, 2018. https://doi.org/10.1016/j.scitotenv.2018.02.009.

CARGNELLO, M.; GASPAROTTO, A.; GOMBAC, V.; MONTINI, T.; BARRECA, D.; FORNASIERO, P. Photocatalytic H2 and Added-Value By-Products – The Role of Metal Oxide Systems in Their Synthesis from Oxygenates. **European Journal of Inorganic Chemistry**, v. 2011, n. 28, p. 4309-4323, 2011. https://doi.org/10.1002/ejic.201100532.

CARMO, M. E. G.; SPIES, L.; SILVA, G. N.; LOPES, O. F.; BEIN, T.; SCHNEIDER, J.; PATROCINIO, A. O. T. From conventional inorganic semiconductors to covalent organic frameworks: advances and opportunities in heterogeneous photocatalytic CO2 reduction. **Journal of Materials Chemistry A**, v. 11, n. 26, p. 13815-13843, 2023. https://doi.org/10.1039/D3TA01470C.

CARRARO, G.; MACCATO, C.; GASPAROTTO, A.; MONTINI, T.; TURNER, S.; LEBEDEV, O. I.; GOMBAC, V.; ADAMI, G.; VAN TENDELOO, G.; BARRECA, D.; FORNASIERO, P. Enhanced Hydrogen Production by Photoreforming of Renewable Oxygenates Through Nanostructured Fe2O3 Polymorphs. **Advanced Functional Materials**, v. 24, n. 3, p. 372-378, 2014.
https://doi.org/10.1002/adfm.201302043.

CHECA, M.; NOGALES-DELGADO, S.; MONTES, V.; ENCINAR, J. M. Recent Advances in Glycerol Catalytic Valorization: A Review. **Catalysts**, v. 10, n. 11, p. 1279, 2020.
https://doi.org/10.3390/catal10111279

CHEN, D.; XIE, Z.; TONG, Y.; HUANG, Y. Review on BiVO4-Based Photoanodes for Photoelectrochemical Water Oxidation: The Main Influencing Factors. **Energy & Fuels**, v. 36, n. 17, p. 9932-9949, 2022.
https://doi.org/10.1021/acs.energyfuels.2c02119.

CHEN, H.; ZHANG, C.; PANG, Y.; SHEN, Q.; YU, Y.; SU, Y.; WANG, J.; ZHANG, F.; YANG, H. Oxygen vacancy regulation in Nb-doped Bi2WO6 for enhanced visible light photocatalytic activity. **RSC Advances**, v. 9, n. 39, p. 22559-22566, 2019.
https://doi.org/10.1039/C9RA02862E.

CHEN, S.-H.; JIANG, Y.-S.; LIN, H.-Y. Easy Synthesis of BiVO4 for Photocatalytic Overall Water Splitting. **ACS Omega**, v. 5, n. 15, p. 8927-8933, 2020.
https://doi.org/10.1021/acsomega.0c00699.

CHEN, S.; KUCERNAK, A. Electrodeposition of Platinum on Nanometer-Sized Carbon Electrodes. **The Journal of Physical Chemistry B**, v. 107, n. 33, p. 8392-8402, 2003.
https://doi.org/10.1021/jp0348934.

CHENG, N.; STAMBULA, S.; WANG, D.; BANIS, M. N.; LIU, J.; RIESE, A.; XIAO, B.; LI, R.; SHAM, T.-K.; LIU, L.-M.; BOTTON, G. A.; SUN, X. Platinum single-atom and cluster catalysis of the hydrogen evolution reaction. **Nature Communications**, v. 7, n. 1, p. 13638, 2016.
https://doi.org/10.1038/ncomms13638.

CHOL, C. G.; DHABHAI, R.; DALAI, A. K.; REANEY, M. Purification of crude glycerol derived from biodiesel production process: Experimental studies and techno-economic analyses. **Fuel Processing Technology**, v. 178, n., p. 78-87, 2018.
https://doi.org/10.1016/j.fuproc.2018.05.023.

COIT M. DUBOSE, D. R., UWE M. OEHLER, EDWARD G. JANZEN. Letter to the editor. **Free Radical Biology and Medicine**, v. 5, n. 1, p. 55-56, 1988.
https://doi.org/10.1016/0891-5849(88)90064-0.

COSTANTINO, F.; KAMAT, P. V. Do Sacrificial Donors Donate H2 in Photocatalysis? **ACS Energy Letters**, v. 7, n. 1, p. 242-246, 2022.
https://doi.org/10.1021/acsenergylett.1c02487.

CÔTÉ, A. P.; BENIN, A. I.; OCKWIG, N. W.; O'KEEFFE, M.; MATZGER, A. J.; YAGHI, O. M. Porous, Crystalline, Covalent Organic Frameworks. **Science**, v. 310, n. 5751, p. 1166-1170, 2005.
https://doi.org/doi:10.1126/science.1120411.

DABODIYA, T. S.; SELVARASU, P.; MURUGAN, A. V. Tetragonal to Monoclinic Crystalline Phases Change of BiVO4 via Microwave-Hydrothermal Reaction: In Correlation with Visible-

Light-Driven Photocatalytic Performance. **Inorganic Chemistry**, v. 58, n. 8, p. 5096-5110, 2019.
https://doi.org/10.1021/acs.inorgchem.9b00193.

DABODIYA, T. S.; GEORGE, T.; MATHEW, F. A.; VADIVEL MURUGAN, A. Ultrastable, High Photoelectrocatalytic Performance of Altervalent Cation-Doped BiVO4 Photoanode and Effect of Interfacial Contact with Nanoporous Carbon for Seawater Splitting Using a 3D-Printed Flow Device. **ACS Applied Energy Materials**, v. 7, n. 6, p. 2309-2328, 2024.
https://doi.org/10.1021/acsaem.3c03068.

DANCE, I. The Correlation of Redox Potential, HOMO Energy, and Oxidation State in Metal Sulfide Clusters and Its Application to Determine the Redox Level of the FeMo-co Active-Site Cluster of Nitrogenase. **Inorganic Chemistry**, v. 45, n. 13, p. 5084-5091, 2006.
https://doi.org/10.1021/ic060438l.

DAS, S.; OHKUBO, T.; KASAI, S.; KOZUKA, Y. Deterministic Influence of Substrate-Induced Oxygen Vacancy Diffusion on Bi2WO6 Thin Film Growth. **Crystal Growth & Design**, v. 21, n. 1, p. 625-630, 2021.
https://doi.org/10.1021/acs.cgd.0c01428.

DASKALAKI, V. M.; KONDARIDES, D. I. Efficient production of hydrogen by photo-induced reforming of glycerol at ambient conditions. **Catalysis Today**, v. 144, n. 1, p. 75-80, 2009.
https://doi.org/10.1016/j.cattod.2008.11.009.

DE LUCA, G.; ARBOUZNIKOV, A.; GOURSOT, A.; PULLUMBI, P. Quantum Chemical Study of Low-pressure Adsorption in Zeolitic Materials. **The Journal of Physical Chemistry B**, v. 105, n. 20, p. 4663-4668, 2001.
https://doi.org/10.1021/jp0033115.

DEAS, R.; PEARCE, S.; GOSS, K.; WANG, Q.; CHEN, W.-T.; WATERHOUSE, G. I. N. Hierarchical Au/TiO2 nanoflower photocatalysts with outstanding performance for alcohol photoreforming under UV irradiation. **Applied Catalysis A: General**, v. 602, n., p. 117706, 2020.
https://doi.org/10.1016/j.apcata.2020.117706.

DITTMER, A.; MENZE, J.; MEI, B.; STRUNK, J.; LUFTMAN, H. S.; GUTKOWSKI, R.; WACHS, I. E.; SCHUHMANN, W.; MUHLER, M. Surface Structure and Photocatalytic Properties of Bi2WO6 Nanoplatelets Modified by Molybdena Islands from Chemical Vapor Deposition. **The Journal of Physical Chemistry C**, v. 120, n. 32, p. 18191-18200, 2016.
https://doi.org/10.1021/acs.jpcc.6b07007.

DODEKATOS, G.; SCHÜNEMANN, S.; TÜYSÜZ, H. Recent Advances in Thermo-, Photo-, and Electrocatalytic Glycerol Oxidation. **ACS Catalysis**, v. 8, n. 7, p. 6301-6333, 2018.
https://doi.org/10.1021/acscatal.8b01317.

DRISYA, K. T.; SOLÍS-LÓPEZ, M.; RÍOS-RAMÍREZ, J. J.; DURÁN-ÁLVAREZ, J. C.; ROUSSEAU, A.; VELUMANI, S.; ASOMOZA, R.; KASSIBA, A.; JANTRANIA, A.; CASTANEDA, H. Electronic and optical competence of TiO2/BiVO4 nanocomposites in the photocatalytic processes. **Scientific Reports**, v. 10, n. 1, p. 13507, 2020.
https://doi.org/10.1038/s41598-020-69032-9.

DU, P.; SCHNEIDER, J.; LUO, G.; BRENNESSEL, W. W.; EISENBERG, R. Visible Light-Driven Hydrogen Production from Aqueous Protons Catalyzed by Molecular Cobaloxime Catalysts. **Inorganic Chemistry**, v. 48, n. 11, p. 4952-4962, 2009.
https://doi.org/10.1021/ic900389z.

ESCAMILLA, J. C.; HIDALGO-CARRILLO, J.; MARTÍN-GÓMEZ, J.; ESTÉVEZ-TOLEDANO, R. C.; MONTES, V.; COSANO, D.; URBANO, F. J.; MARINAS, A. Hydrogen Production through Glycerol Photoreforming on TiO2/Mesoporous Carbon: Influence of the Synthetic Method. **Materials**, v. 13, n. 17, p. 3800, 2020.
https://doi.org/10.3390/ma13173800.

ESSIE, W.; LUO, X.; HE, F.; LIAO, Y.; DUNS, G. J.; QIN, Z. Lignin valorization: A crucial step towards full utilization of biomass, zero waste and circular bioeconomy. **Biocatalysis and Agricultural Biotechnology**, v. 51, n., p. 102777, 2023.
https://doi.org/10.1016/j.bcab.2023.102777.

FANG, G.; LIU, Z.; HAN, C. Enhancing the PEC water splitting performance of BiVO4 co-modifying with NiFeOOH and Co-Pi double layer cocatalysts. **Applied Surface Science**, v. 515, n., p. 146095, 2020.
https://doi.org/10.1016/j.apsusc.2020.146095.

FEIJOO, J.; PALIUŠYTĖ, K.; SCHNEIDER, J. Synthetic control over the energy transfer and charge transfer between carbon dots and covalent organic framework. **Journal of Physics: Energy**, v. 6, n. 2, p. 025018, 2024.
https://doi.org/10.1088/2515-7655/ad3677.

FLÓREZ PARDO, L. M.; LÓPEZ GALÁN, J. E.; LOZANO RAMÍREZ, T. Saccharide Biomass for Biofuels, Biomaterials, and Chemicals. In: Vaz Jr, S. (Ed.). **Biomass and Green Chemistry: Building a Renewable Pathway**. Cham: Springer International Publishing, 2018, p.11-30.
https://doi.org/10.1007/978-3-319-66736-2_2

FOGGIA, M.; TADDEI, P.; TORREGGIANI, A.; DETTIN, M.; TINTI, A. Self-assembling peptides for biomedical applications: IR and Raman spectroscopies for the study of secondary structure. **Proteomics Research Journal**, v. 2, n., p. 231-272, 2012.

GENDY, E. A.; KHODAIR, A. I.; FAHIM, A. M.; OYEKUNLE, D. T.; CHEN, Z. Synthesis, characterization, antibacterial activities, molecular docking, and computational investigation of novel imine-linked covalent organic framework. **Journal of Molecular Liquids**, v. 358, n., p. 119191, 2022.
https://doi.org/10.1016/j.molliq.2022.119191.

GHOSH, R.; PAESANI, F. Unraveling the effect of defects, domain size, and chemical doping on photophysics and charge transport in covalent organic frameworks. **Chemical Science**, v. 12, n. 24, p. 8373-8384, 2021.
https://doi.org/10.1039/D1SC01262B.

GHOSH, S.; NAKADA, A.; SPRINGER, M. A.; KAWAGUCHI, T.; SUZUKI, K.; KAJI, H.; BABURIN, I.; KUC, A.; HEINE, T.; SUZUKI, H.; ABE, R.; SEKI, S. Identification of Prime Factors to Maximize the Photocatalytic Hydrogen Evolution of Covalent Organic Frameworks. **Journal of the American Chemical Society**, v. 142, n. 21, p. 9752-9762, 2020.
https://doi.org/10.1021/jacs.0c02633.

GIEROBA, B.; SROKA-BARTNICKA, A.; KAZIMIERCZAK, P.; KALISZ, G.; LEWALSKA-GRACZYK, A.; VIVCHARENKO, V.; NOWAKOWSKI, R.; PIETA, I. S.; PRZEKORA, A. Spectroscopic studies on the temperature-dependent molecular arrangements in hybrid chitosan/1,3-β-D-glucan polymeric matrices. **International Journal of Biological Macromolecules**, v. 159, n., p. 911-921, 2020.
https://doi.org/10.1016/j.ijbiomac.2020.05.155.

GRIGIONI, I.; STAMPLECOSKIE, K. G.; JARA, D. H.; DOZZI, M. V.; ORIANA, A.; CERULLO, G.; KAMAT, P. V.; SELLI, E. Wavelength-Dependent Ultrafast Charge Carrier Separation in the WO3/BiVO4 Coupled System. **ACS Energy Letters**, v. 2, n. 6, p. 1362-1367, 2017. https://doi.org/10.1021/acsenergylett.7b00216.

GÜNNEMANN, C.; CURTI, M.; GERRIT ECKERT, J.; SCHNEIDER, J.; BAHNEMANN, D. W. Tailoring the Photoelectrochemical Activity of TiO2 Electrodes by Multilayer Screen-Printing. **ChemCatChem**, v. 11, n. 24, p. 6439-6450, 2019. https://doi.org/10.1002/cctc.201901872.

HAMID, S.; DILLERT, R.; BAHNEMANN, D. W. Photocatalytic Reforming of Aqueous Acetic Acid into Molecular Hydrogen and Hydrocarbons over Co-catalyst-Loaded TiO2: Shifting the Product Distribution. **The Journal of Physical Chemistry C**, v. 122, n. 24, p. 12792-12809, 2018. https://doi.org/10.1021/acs.jpcc.8b02691.

HAN, X.; HUANG, J.; YUAN, C.; LIU, Y.; CUI, Y. Chiral 3D Covalent Organic Frameworks for High Performance Liquid Chromatographic Enantioseparation. **Journal of the American Chemical Society**, v. 140, n. 3, p. 892-895, 2018. https://doi.org/10.1021/jacs.7b12110.

HE, S.; MUIZEBELT, I.; HEERES, A.; SCHENK, N. J.; BLEES, R.; HEERES, H. J. Catalytic pyrolysis of crude glycerol over shaped ZSM-5/bentonite catalysts for bio-BTX synthesis. **Applied Catalysis B: Environmental**, v. 235, n., p. 45-55, 2018. https://doi.org/10.1016/j.apcatb.2018.04.047.

HE, Z.; NING, X.; YANG, G.; WANG, H.; CAO, Y.; PENG, F.; YU, H. Selective oxidation of glycerol over supported noble metal catalysts. **Catalysis Today**, v. 365, n., p. 162-171, 2021. https://doi.org/10.1016/j.cattod.2020.04.019.

HEDAYAT, N.; DU, Y.; ILKHANI, H. Review on fabrication techniques for porous electrodes of solid oxide fuel cells by sacrificial template methods. **Renewable and Sustainable Energy Reviews**, v. 77, n., p. 1221-1239, 2017. https://doi.org/10.1016/j.rser.2017.03.095.

HERRMANN, J. M. Heterogeneous photocatalysis: state of the art and present applications In honor of Pr. R.L. Burwell Jr. (1912–2003), Former Head of Ipatieff Laboratories, Northwestern University, Evanston (Ill). **Topics in Catalysis**, v. 34, n. 1, p. 49-65, 2005. https://doi.org/10.1007/s11244-005-3788-2.

HOFFMANN, M. R.; MARTIN, S. T.; CHOI, W.; BAHNEMANN, D. W. Environmental Applications of Semiconductor Photocatalysis. **Chem Rev**, v. 95, n. 1, p. 69-96, 1995. https://doi.org/10.1021/cr00033a004.

HORANYI, G.; RIZMAYER, E. M. RADIOTRACER AND ELECTROCHEMICAL STUDY OF THE ADSORPTION AND ELECTROCATALYTIC OXIDATION OF GLYCEROL AT A PLATINIZED PLATINUM-ELECTRODE. **Acta Chemica Scandinavica, Series B: Organic Chemistry and Biochemistry**, v. 37, n. 5, p. 451-457, 1983. https://doi.org/10.3891/acta.chem.scand.37b-0451.

HOSSAIN, Q. S.; NISHAT, S. S.; SULTANA, M.; MAHI, T. A.; AHMED, S.; KHAN, M. N. I.; DAS, H. N.; BASHAR, M. S.; AKHTAR, U. S.; JAHAN, S.; CHOWDHURY, F.; HOSSAIN, K. S.; IMRAN, S. M. S.; AHMED, I. A combined first principles and experimental approach to Bi2WO6. **RSC Advances**, v. 13, n. 51, p. 36130-36143, 2023.

https://doi.org/10.1039/D3RA06648G.

HU, X.; LU, J.; LIU, Y.; CHEN, L.; ZHANG, X.; WANG, H. Sustainable catalytic oxidation of glycerol: a review. **Environmental Chemistry Letters**, v. 21, n. 5, p. 2825-2861, 2023. https://doi.org/10.1007/s10311-023-01608-z.

HUANG, L.-W.; VO, T.-G.; CHIANG, C.-Y. Converting glycerol aqueous solution to hydrogen energy and dihydroxyacetone by the BiVO4 photoelectrochemical cell. **Electrochimica Acta**, v. 322, n., p. 134725, 2019. https://doi.org/10.1016/j.electacta.2019.134725.

HUO, W. C.; DONG, X. A.; LI, J. Y.; LIU, M.; LIU, X. Y.; ZHANG, Y. X.; DONG, F. Synthesis of Bi2WO6 with gradient oxygen vacancies for highly photocatalytic NO oxidation and mechanism study. **Chemical Engineering Journal**, v. 361, n., p. 129-138, 2019. https://doi.org/10.1016/j.cej.2018.12.071.

IERVOLINO, G.; VAIANO, V.; MURCIA, J. J.; RIZZO, L.; VENTRE, G.; PEPE, G.; CAMPIGLIA, P.; HIDALGO, M. C.; NAVÍO, J. A.; SANNINO, D. Photocatalytic hydrogen production from degradation of glucose over fluorinated and platinized TiO2 catalysts. **Journal of Catalysis**, v. 339, n., p. 47-56, 2016. https://doi.org/10.1016/j.jcat.2016.03.032.

Instrumentation for Fluorescence Spectroscopy. In: Lakowicz, J. R. (Ed.). **Principles of Fluorescence Spectroscopy**. Boston, MA: Springer US, 2006, p.27-61.
ISMAEL, M. One-step ultrasonic-assisted synthesis of Ni-doped g-C3N4 photocatalyst for enhanced photocatalytic hydrogen evolution. **Inorganic Chemistry Communications**, v. 151, n., p. 110607, 2023. https://doi.org/10.1016/j.inoche.2023.110607.

JIANG, S.; LIU, Y.; XU, J. Rare earth oxynitrides: promising visible-light-driven photocatalysts for water splitting. **Materials Advances**, v. 2, n. 4, p. 1190-1203, 2021. https://doi.org/10.1039/D0MA00867B.

JIANG, W.; HUANGFU, T.; YANG, X.; BAO, L.; LIU, Y.; XU, G.; HAN, G. Surfactant-free hydrothermal synthesis of hierarchical flower-like Bi2WO6 mesosphere nanostructures with excellent visible-light photocatalytic activity. **CrystEngComm**, v. 21, n. 41, p. 6293-6300, 2019. https://doi.org/10.1039/C9CE01170F.

JUNG, M.; HART, J. N.; BOENSCH, D.; SCOTT, J.; NG, Y. H.; AMAL, R. Hydrogen evolution via glycerol photoreforming over Cu–Pt nanoalloys on TiO2. **Applied Catalysis A: General**, v. 518, n., p. 221-230, 2016. https://doi.org/10.1016/j.apcata.2015.10.040.

KAHRAMAN, A.; BARZGAR VISHLAGHI, M.; BAYLAM, I.; SENNAROGLU, A.; KAYA, S. Roles of Charge Carriers in the Excited State Dynamics of BiVO4 Photoanodes. **The Journal of Physical Chemistry C**, v. 123, n. 47, p. 28576-28583, 2019. https://doi.org/10.1021/acs.jpcc.9b07391.

KAHYAOGLU, A.; BEDEN, B.; LAMY, C. Oxydation electrocatalitique du glycerol sur electrodes d'or et de platine en milieu aqueux. **Electrochimica Acta**, v. 29, n. 10, p. 1489-1492, 1984. https://doi.org/10.1016/0013-4686(84)87033-4.

KALANUR, S. S.; SEO, H. An experimental and density functional theory studies of Nb-doped BiVO4 photoanodes for enhanced solar water splitting. **Journal of Catalysis**, v. 410, n., p. 144-155, 2022.
https://doi.org/10.1016/j.jcat.2022.04.019.

KARAK, S.; DEY, K.; BANERJEE, R. Maneuvering Applications of Covalent Organic Frameworks via Framework-Morphology Modulation. **Advanced Materials**, v. 34, n. 49, p. 2202751, 2022.
https://doi.org/10.1002/adma.202202751.

KAUSHIK, M.; B, V.; SM, D.; M, G. K. H.; SHETTY, S. K.; C, M. Recent Advances in Efficient Nanostructured Photocatalysts for Hydrogen Fuel Production: A Short Review. **ECS Transactions**, v. 107, n. 1, p. 7563, 2022.
https://doi.org/10.1149/10701.7563ecst.

KE, G.; DUAN, F.; LIU, B.; LIU, X.; WEN, J.; JIA, B.; LIU, X.; HE, H.; ZHOU, Y. Mo or W doping into the surface of BiVO4 film photoanodes through a photoelectrochemical treating approach for efficient solar water oxidation. **Journal of Alloys and Compounds**, v. 934, n., p. 167883, 2023.
https://doi.org/10.1016/j.jallcom.2022.167883.

KELLER, N.; SICK, T.; BACH, N. N.; KOSZALKOWSKI, A.; ROTTER, J. M.; MEDINA, D. D.; BEIN, T. Dibenzochrysene enables tightly controlled docking and stabilizes photoexcited states in dual-pore covalent organic frameworks. **Nanoscale**, v. 11, n. 48, p. 23338-23345, 2019.
https://doi.org/10.1039/C9NR08007D.

KENNEDY, J.; BAHRUJI, H.; BOWKER, M.; DAVIES, P. R.; BOULEGHLIMAT, E.; ISSARAPANACHEEWIN, S. Hydrogen generation by photocatalytic reforming of potential biofuels: Polyols, cyclic alcohols, and saccharides. **Journal of Photochemistry and Photobiology A: Chemistry**, v. 356, n., p. 451-456, 2018.
https://doi.org/10.1016/j.jphotochem.2018.01.031.

KHANCHAITIT, P.; HAN, K.; GADINSKI, M. R.; LI, Q.; WANG, Q. Ferroelectric polymer networks with high energy density and improved discharged efficiency for dielectric energy storage. **Nature Communications**, v. 4, n. 1, p. 2845, 2013.
https://doi.org/10.1038/ncomms3845.

KIM, D.; LIM, W.-G.; KIM, Y.; OH, L. S.; KIM, S.; PARK, J. H.; JO, C.; KIM, H. J.; KANG, J.; LEE, S.; LIM, E. Amorphous antimony oxide as reaction pathway modulator toward electrocatalytic glycerol oxidation for selective dihydroxyacetone production. **Applied Catalysis B: Environmental**, v. 339, n., p. 123104, 2023.
https://doi.org/10.1016/j.apcatb.2023.123104.

KIM, H. J.; KIM, Y.; LEE, D.; KIM, J.-R.; CHAE, H.-J.; JEONG, S.-Y.; KIM, B.-S.; LEE, J.; HUBER, G. W.; BYUN, J.; KIM, S.; HAN, J. Coproducing Value-Added Chemicals and Hydrogen with Electrocatalytic Glycerol Oxidation Technology: Experimental and Techno-Economic Investigations. **ACS Sustainable Chemistry & Engineering**, v. 5, n. 8, p. 6626-6634, 2017.
https://doi.org/10.1021/acssuschemeng.7b00868.

KIM, J. H.; HANSORA, D.; SHARMA, P.; JANG, J.-W.; LEE, J. S. Toward practical solar hydrogen production – an artificial photosynthetic leaf-to-farm challenge. **Chemical Society Reviews**, v. 48, n. 7, p. 1908-1971, 2019.
https://doi.org/10.1039/C8CS00699G.

KIMURA, H.; TSUTO, K.; WAKISAKA, T.; KAZUMI, Y.; INAYA, Y. Selective oxidation of glycerol on a platinum-bismuth catalyst. **Applied Catalysis A: General**, v. 96, n. 2, p. 217-228, 1993.
https://doi.org/10.1016/0926-860X(90)80011-3.

KONDARIDES, D. I.; DASKALAKI, V. M.; PATSOURA, A.; VERYKIOS, X. E. Hydrogen Production by Photo-Induced Reforming of Biomass Components and Derivatives at Ambient Conditions. **Catalysis Letters**, v. 122, n. 1, p. 26-32, 2008.
https://doi.org/10.1007/s10562-007-9330-3.

KONDARIDES, D. I.; PATSOURA, A.; VERYKIOS, X. E. Anaerobic Photocatalytic Oxidation of Carbohydrates in Aqueous Pt/TiO2 Suspensions with Simultaneous Production of Hydrogen. **Journal of Advanced Oxidation Technologies**, v. 13, n. 1, p. 116-123, 2010.
https://doi.org/10.1515/jaots-2010-0115.

KORMAN, K. J.; DECKER, G. E.; DWORZAK, M. R.; DEEGAN, M. M.; ANTONIO, A. M.; TAGGART, G. A.; BLOCH, E. D. Using Low-Pressure Methane Adsorption Isotherms for Higher-Throughput Screening of Methane Storage Materials. **ACS Applied Materials & Interfaces**, v. 12, n. 36, p. 40318-40327, 2020.
https://doi.org/10.1021/acsami.0c11200.

KOZLOVA, E. A.; KURENKOVA, A. Y.; GERASIMOV, E. Y.; GROMOV, N. V.; MEDVEDEVA, T. B.; SARAEV, A. A.; KAICHEV, V. V. Comparative study of photoreforming of glycerol on Pt/TiO2 and CuOx/TiO2 photocatalysts under UV light. **Materials Letters**, v. 283, n., p. 128901, 2021.
https://doi.org/10.1016/j.matlet.2020.128901.

KRISHNARAJ, C.; KACZMAREK, A. M.; JENA, H. S.; LEUS, K.; CHAOUI, N.; SCHMIDT, J.; VAN DEUN, R.; VAN DER VOORT, P. Triggering White-Light Emission in a 2D Imine Covalent Organic Framework Through Lanthanide Augmentation. **ACS Applied Materials & Interfaces**, v. 11, n. 30, p. 27343-27352, 2019.
https://doi.org/10.1021/acsami.9b07779.

KRISHNARAJ, C.; JENA, H. S.; RAWAT, K. S.; SCHMIDT, J.; LEUS, K.; VAN SPEYBROECK, V.; VAN DER VOORT, P. Linker Engineering of 2D Imine Covalent Organic Frameworks for the Heterogeneous Palladium-Catalyzed Suzuki Coupling Reaction. **ACS Applied Materials & Interfaces**, v. 14, n. 45, p. 50923-50931, 2022.
https://doi.org/10.1021/acsami.2c14882.

KUEHNEL, M. F.; REISNER, E. Solar Hydrogen Generation from Lignocellulose. **Angewandte Chemie International Edition**, v. 57, n. 13, p. 3290-3296, 2018.
https://doi.org/10.1002/anie.201710133.

KUMAR, A.; SEVILLA, M. D. SOMO–HOMO Level Inversion in Biologically Important Radicals. **The Journal of Physical Chemistry B**, v. 122, n. 1, p. 98-105, 2018.
https://doi.org/10.1021/acs.jpcb.7b10002.

KWON, Y.; BIRDJA, Y.; SPANOS, I.; RODRIGUEZ, P.; KOPER, M. T. M. Highly Selective Electro-Oxidation of Glycerol to Dihydroxyacetone on Platinum in the Presence of Bismuth. **ACS Catalysis**, v. 2, n. 5, p. 759-764, 2012.
https://doi.org/10.1021/cs200599g.

LI, C.; HOFMEISTER, E.; KRIVTSOV, I.; MITORAJ, D.; ADLER, C.; BERANEK, R.; DIETZEK, B. Photodriven Charge Accumulation and Carrier Dynamics in a Water-Soluble Carbon Nitride Photocatalyst. **ChemSusChem**, v. 14, n. 7, p. 1728-1736, 2021. https://doi.org/10.1002/cssc.202002921.

LI, T.; MO, J. Y.; WEEKES, D. M.; DETTELBACH, K. E.; JANSONIUS, R. P.; SAMMIS, G. M.; BERLINGUETTE, C. P. Photoelectrochemical Decomposition of Lignin Model Compound on a BiVO4 Photoanode. **ChemSusChem**, v. 13, n. 14, p. 3622-3626, 2020. https://doi.org/10.1002/cssc.202001134.

LI, X.; GAO, Q.; ANEESH, J.; XU, H.-S.; CHEN, Z.; TANG, W.; LIU, C.; SHI, X.; ADARSH, K. V.; LU, Y.; LOH, K. P. Molecular Engineering of Bandgaps in Covalent Organic Frameworks. **Chemistry of Materials**, v. 30, n. 16, p. 5743-5749, 2018. https://doi.org/10.1021/acs.chemmater.8b02560.

LI, X.; LI, C.; XU, Y.; LIU, Q.; BAHRI, M.; ZHANG, L.; BROWNING, N. D.; COWAN, A. J.; TANG, J. Efficient hole abstraction for highly selective oxidative coupling of methane by Au-sputtered TiO2 photocatalysts. **Nature Energy**, v. 8, n. 9, p. 1013-1022, 2023. https://doi.org/10.1038/s41560-023-01317-5.

LI, Y.; YANG, L.; HE, H.; SUN, L.; WANG, H.; FANG, X.; ZHAO, Y.; ZHENG, D.; QI, Y.; LI, Z.; DENG, W. In situ photodeposition of platinum clusters on a covalent organic framework for photocatalytic hydrogen production. **Nature Communications**, v. 13, n. 1, p. 1355, 2022. https://doi.org/10.1038/s41467-022-29076-z.

LI, Z.; DENG, T.; MA, S.; ZHANG, Z.; WU, G.; WANG, J.; LI, Q.; XIA, H.; YANG, S.-W.; LIU, X. Three-Component Donor−π–Acceptor Covalent–Organic Frameworks for Boosting Photocatalytic Hydrogen Evolution. **Journal of the American Chemical Society**, v. 145, n. 15, p. 8364-8374, 2023. https://doi.org/10.1021/jacs.2c11893.

LIANG, X.; GAO, T.; CUI, Y.; DONG, Q.; LI, X.; LABIDI, A.; LICHTFOUSE, E.; LI, F.; YU, F.; WANG, C. Photoreforming of poly(ethylene-terephthalate) plastic into valuable chemicals and hydrogen over BiVO4/MoOx: Synergistic promotion of oxidation and reduction processes. **Appl. Catal. B: Environ.**, v. 357, n., p. 124326, 2024. https://doi.org/10.1016/j.apcatb.2024.124326.

LICHTIN, N. N.; DONG, J.; VIJAYAKUMAR, K. M. Photopromoted TiO2-Catalyzed Oxidative Decomposition of Organic Pollutants in Water and in the Vapor Phase. **Water Quality Research Journal**, v. 27, n. 1, p. 203-210, 1992. https://doi.org/10.2166/wqrj.1992.012.

LIU, D.; LIU, J.-C.; CAI, W.; MA, J.; YANG, H. B.; XIAO, H.; LI, J.; XIONG, Y.; HUANG, Y.; LIU, B. Selective photoelectrochemical oxidation of glycerol to high value-added dihydroxyacetone. **Nature Communications**, v. 10, n. 1, p. 1779, 2019. https://doi.org/10.1038/s41467-019-09788-5.

LIU, Y.; YANG, W.; CHEN, Q.; CULLEN, D. A.; XIE, Z.; LIAN, T. Pt Particle Size Affects Both the Charge Separation and Water Reduction Efficiencies of CdS–Pt Nanorod Photocatalysts for Light Driven H2 Generation. **Journal of the American Chemical Society**, v. 144, n. 6, p. 2705-2715, 2022. https://doi.org/10.1021/jacs.1c11745.

LONG, G.-F.; WAN, K.; LIU, M.-Y.; LIANG, Z.-X.; PIAO, J.-H.; TSIAKARAS, P. Active sites and mechanism on nitrogen-doped carbon catalyst for hydrogen evolution reaction. **Journal of Catalysis**, v. 348, n., p. 151-159, 2017. https://doi.org/10.1016/j.jcat.2017.02.021.

LOPES, O. F.; CARVALHO, K. T. G.; NOGUEIRA, A. E.; AVANSI, W.; RIBEIRO, C. Controlled synthesis of BiVO4 photocatalysts: Evidence of the role of heterojunctions in their catalytic performance driven by visible-light. **Applied Catalysis B: Environmental**, v. 188, n., p. 87-97, 2016. https://doi.org/10.1016/j.apcatb.2016.01.065.

LÓPEZ-TENLLADO, F. J.; HIDALGO-CARRILLO, J.; MONTES, V.; MARINAS, A.; URBANO, F. J.; MARINAS, J. M.; ILIEVA, L.; TABAKOVA, T.; REID, F. A comparative study of hydrogen photocatalytic production from glycerol and propan-2-ol on M/TiO2 systems (M=Au, Pt, Pd). **Catalysis Today**, v. 280, n., p. 58-64, 2017. https://doi.org/10.1016/j.cattod.2016.05.009.

LOTINA-HENNSEN, B.; KING, B.; ALBORES, M.; POZAS, R. UNCOUPLING OF PHOTOPHOSPHORYLATION BY NITROGENOUS BASES. NO CORRELATION Ofb UNCOUPLING WITH pKb and PARTITION COEFFICIENT. **Photochemistry and Photobiology**, v. 46, n. 2, p. 287-293, 1987. https://doi.org/10.1111/j.1751-1097.1987.tb04768.x.

LUO, L.; CHEN, W.; XU, S.-M.; YANG, J.; LI, M.; ZHOU, H.; XU, M.; SHAO, M.; KONG, X.; LI, Z.; DUAN, H. Selective Photoelectrocatalytic Glycerol Oxidation to Dihydroxyacetone via Enhanced Middle Hydroxyl Adsorption over a Bi2O3-Incorporated Catalyst. **Journal of the American Chemical Society**, v. 144, n. 17, p. 7720-7730, 2022. https://doi.org/10.1021/jacs.2c00465.

MA, S.; LI, Z.; JIA, J.; ZHANG, Z.; XIA, H.; LI, H.; CHEN, X.; XU, Y.; LIU, X. Amide-linked covalent organic frameworks as efficient heterogeneous photocatalysts in water. **Chinese Journal of Catalysis**, v. 42, n. 11, p. 2010-2019, 2021. https://doi.org/10.1016/S1872-2067(21)63836-6.

MACHADO, S. A. S.; AVACA, L. A. The hydrogen evolution reaction on nickel surfaces stabilized by H-absorption. **Electrochimica Acta**, v. 39, n. 10, p. 1385-1391, 1994. https://doi.org/10.1016/0013-4686(94)E0003-I.

MACKENZIE, M.; CRAVEN, A. J.; HATTO, P. Erosion and deposition during the sputter cleaning of substrates prior to the cathodic arc evaporation of transition metal nitride coatings. **Thin Solid Films**, v. 349, n. 1, p. 176-185, 1999. https://doi.org/10.1016/S0040-6090(99)00219-9.

MADRIZ, L.; TATÁ, J.; CARVAJAL, D.; NÚÑEZ, O.; SCHARIFKER, B. R.; MOSTANY, J.; BORRÁS, C.; CABRERIZO, F. M.; VARGAS, R. Photocatalysis and photoelectrochemical glucose oxidation on Bi2WO6: Conditions for the concomitant H2 production. **Renewable Energy**, v. 152, n., p. 974-983, 2020. https://doi.org/10.1016/j.renene.2020.01.071.

MAGALHÃES, T. M.; GUERRA, R. C.; SAN GIL, R. A. D. S.; VALENTE, A. P.; SIMÃO, R. A.; SOARES, B. G.; MENDES, T. D. C.; PYRRHO, A. D. S.; SOUSA, V. P. D.; RODRIGUES-FURTADO, V. L. PAMAM dendrimer hydrogel film—biocompatible material to an efficient dermal delivery of drugs. **Journal of Nanoparticle Research**, v. 19, n. 8, p. 277, 2017. https://doi.org/10.1007/s11051-017-3965-9.

MAKUŁA, P.; PACIA, M.; MACYK, W. How To Correctly Determine the Band Gap Energy of Modified Semiconductor Photocatalysts Based on UV–Vis Spectra. **The Journal of Physical Chemistry Letters**, v. 9, n. 23, p. 6814-6817, 2018. https://doi.org/10.1021/acs.jpclett.8b02892.

MARINHO, J. Z.; SANTOS, L. M.; MACARIO, L. R.; LONGO, E.; MACHADO, A. E. H.; PATROCINIO, A. O. T.; LIMA, R. C. Rapid Preparation of (BiO)2CO3 Nanosheets by Microwave-Assisted Hydrothermal Method with Promising Photocatalytic Activity Under UV-Vis Light. **Journal of the Brazilian Chemical Society**, v. 26, n., p., 2015. https://doi.org/10.5935/0103-5053.20150002

MARINHO, J. Z.; NASCIMENTO, L. L.; SANTOS, A. L. R.; FARIA, A. M.; MACHADO, A. E. H.; PATROCINIO, A. O. T. On the influence of hydrothermal treatment pH on the performance of Bi2WO6 as photocatalyst in the glycerol photoreforming. **Photochemical & Photobiological Sciences**, v. 21, n., p. 1659–1675, 2022a. https://doi.org/10.1007/s43630-022-00249-5.

MARINHO, J. Z.; NASCIMENTO, L. L.; SANTOS, A. L. R.; FARIA, A. M.; MACHADO, A. E. H.; PATROCINIO, A. O. T. On the influence of hydrothermal treatment pH on the performance of Bi2WO6 as photocatalyst in the glycerol photoreforming. **Photochemical & Photobiological Sciences**, v. 21, n. 9, p. 1659-1675, 2022b. https://doi.org/10.1007/s43630-022-00249-5.

MAURINO, V.; BEDINI, A.; MINELLA, M.; RUBERTELLI, F.; PELIZZETTI, E.; MINERO, C. Glycerol Transformation Through Photocatalysis: A Possible Route to Value Added Chemicals. **Journal of Advanced Oxidation Technologies**, v. 11, n. 2, p. 184-192, 2008. https://doi.org/doi:10.1515/jaots-2008-0201.

MEIER, C. B.; SPRICK, R. S.; MONTI, A.; GUIGLION, P.; LEE, J.-S. M.; ZWIJNENBURG, M. A.; COOPER, A. I. Structure-property relationships for covalent triazine-based frameworks: The effect of spacer length on photocatalytic hydrogen evolution from water. **Polymer**, v. 126, n., p. 283-290, 2017. https://doi.org/10.1016/j.polymer.2017.04.017.

MIONI, R.; MIONI, G. A mathematical model of pH, based on the total stoichiometric concentration of acids, bases and ampholytes dissolved in water. **Scandinavian Journal of Clinical and Laboratory Investigation**, v. 75, n. 6, p. 452-469, 2015. https://doi.org/10.3109/00365513.2015.1042402.

MOHAMED, M. A.; YAMADA, K.-I.; TOMIOKA, K. Accessing the amide functionality by the mild and low-cost oxidation of imine. **Tetrahedron Letters**, v. 50, n. 26, p. 3436-3438, 2009. https://doi.org/10.1016/j.tetlet.2009.02.174.

MOSS, B.; LE, H.; CORBY, S.; MORITA, K.; SELIM, S.; SOTELO-VAZQUEZ, C.; CHEN, Y.; BORTHWICK, A.; WILSON, A.; BLACKMAN, C.; DURRANT, J. R.; WALSH, A.; KAFIZAS, A. Anisotropic Electron Transport Limits Performance of Bi2WO6 Photoanodes. **The Journal of Physical Chemistry C**, v. 124, n. 35, p. 18859-18867, 2020. https://doi.org/10.1021/acs.jpcc.0c03539.

MOZIA, S.; HECIAK, A.; MORAWSKI, A. W. Photocatalytic acetic acid decomposition leading to the production of hydrocarbons and hydrogen on Fe-modified TiO2. **Catalysis Today**, v. 161, n. 1, p. 189-195, 2011. https://doi.org/10.1016/j.cattod.2010.09.020.

MUSSO, M.; VEIGA, S.; DE LEÓN, A.; QUEVEDO, A.; BUSSI, J. Characterization and application of a bismuth titanate Bi2Ti2O7 synthetized through a solvothermal route for glycerol photooxidation and photoreforming. **Materials Letters**, v. 330, n., p. 133346, 2023. https://doi.org/10.1016/j.matlet.2022.133346.

NAGAKURA, S. On the Electronic Structure of the Carbonyl and the Amide Groups. **Bulletin of the Chemical Society of Japan**, v. 25, n. 3, p. 164-168, 2006. https://doi.org/10.1246/bcsj.25.164.

NAKIBLI, Y.; MAZAL, Y.; DUBI, Y.; WÄCHTLER, M.; AMIRAV, L. Size Matters: Cocatalyst Size Effect on Charge Transfer and Photocatalytic Activity. **Nano Letters**, v. 18, n. 1, p. 357-364, 2018. https://doi.org/10.1021/acs.nanolett.7b04210.

NAM, Y.; LI, L.; LEE, J. Y.; PREZHDO, O. V. Strong Influence of Oxygen Vacancy Location on Charge Carrier Losses in Reduced TiO2 Nanoparticles. **The Journal of Physical Chemistry Letters**, v. 10, n. 11, p. 2676-2683, 2019. https://doi.org/10.1021/acs.jpclett.9b00987.

NANDAL, V.; SHOJI, R.; MATSUZAKI, H.; FURUBE, A.; LIN, L.; HISATOMI, T.; KANEKO, M.; YAMASHITA, K.; DOMEN, K.; SEKI, K. Unveiling charge dynamics of visible light absorbing oxysulfide for efficient overall water splitting. **Nature Communications**, v. 12, n. 1, p. 7055, 2021. https://doi.org/10.1038/s41467-021-27199-3.

NASCIMENTO, L. L.; MARINHO, J. Z.; DOS SANTOS, A. L. R.; DE FARIA, A. M.; SOUZA, R. A. C.; WANG, C.; PATROCINIO, A. O. T. Photoelectrochemical reforming of glycerol by Bi2WO6 photoanodes: Role of the electrolyte pH on the H2 evolution efficiency and product selectivity. **Applied Catalysis A: General**, v. 646, n., p. 118867, 2022. https://doi.org/10.1016/j.apcata.2022.118867.

NASCIMENTO, L. L.; CARVALHO SOUZA, R. A.; ZACOUR MARINHO, J.; WANG, C.; PATROCINIO, A. O. T. Light-driven conversion of biomass-derived compounds into green fuels and chemicals. **Journal of Cleaner Production**, v. 449, n., p. 141709, 2024. https://doi.org/10.1016/j.jclepro.2024.141709.

NAVAKOTESWARA RAO, V.; MALU, T. J.; CHERALATHAN, K. K.; SAKAR, M.; PITCHAIMUTHU, S.; RODRÍGUEZ-GONZÁLEZ, V.; MAMATHA KUMARI, M.; SHANKAR, M. V. Light-driven transformation of biomass into chemicals using photocatalysts – Vistas and challenges. **Journal of Environmental Management**, v. 284, n., p. 111983, 2021. https://doi.org/10.1016/j.jenvman.2021.111983.

NAVARRO, R. M.; SÁNCHEZ-SÁNCHEZ, M. C.; ALVAREZ-GALVAN, M. C.; VALLE, F. D.; FIERRO, J. L. G. Hydrogen production from renewable sources: biomass and photocatalytic opportunities. **Energy & Environmental Science**, v. 2, n. 1, p. 35-54, 2009. https://doi.org/10.1039/B808138G.

NGUYEN, C. C.; NGUYEN, D. L. T.; NGUYEN, D. M. T.; NGUYEN, V.-H.; NANDA, S.; VO, D.-V. N.; SHOKOUHIMEHR, M.; DO, H. H.; KIM, S. Y.; VAN LE, Q. Chapter 1 - Nanostructured photocatalysts: Introduction to photocatalytic mechanism and nanomaterials for energy and environmental applications. In: Nguyen, V.-H., Vo, D.-V. N., *et al* (Ed.). **Nanostructured Photocatalysts**: Elsevier, 2021, p.3-33.

NGUYEN, H. L.; GROPP, C.; YAGHI, O. M. Reticulating 1D Ribbons into 2D Covalent Organic Frameworks by Imine and Imide Linkages. **Journal of the American Chemical Society**, v. 142, n. 6, p. 2771-2776, 2020.

https://doi.org/10.1021/jacs.9b13971.

NIE, Y.-C.; YU, F.; WANG, L.-C.; XING, Q.-J.; LIU, X.; PEI, Y.; ZOU, J.-P.; DAI, W.-L.; LI, Y.; SUIB, S. L. Photocatalytic degradation of organic pollutants coupled with simultaneous photocatalytic H2 evolution over graphene quantum dots/Mn-N-TiO2/g-C3N4 composite catalysts: Performance and mechanism. **Applied Catalysis B: Environmental**, v. 227, n., p. 312-321, 2018.
https://doi.org/10.1016/j.apcatb.2018.01.033.

NISHIMURA, N.; RAPHAEL, B.; MAEDA, K.; LE GENDRE, L.; ABE, R.; KUBOTA, J.; DOMEN, K. Effect of TiCl4 treatment on the photoelectrochemical properties of LaTiO2N electrodes for water splitting under visible light. **Thin Solid Films**, v. 518, n. 20, p. 5855-5859, 2010.
https://doi.org/10.1016/j.tsf.2010.05.094.

NUNES, B. N.; HAISCH, C.; EMELINE, A. V.; BAHNEMANN, D. W.; PATROCINIO, A. O. T. Photocatalytic properties of layer-by-layer thin films of hexaniobate nanoscrolls. **Catalysis Today**, v. 326, n., p. 60-67, 2019.
https://doi.org/10.1016/j.cattod.2018.06.029.

NUNES, P. H. H. **Efeito do tratamento hidrotérmico em função do pH no desempenho fotocatalítico de amostras de Nb2O5**. Instituto de Química - IQUFU, Universidade Federal de Uberlândia - UFU, Uberlândia - MG, 2022.

NWOSU, U.; ZHAO, H.; KIBRIA, M.; HU, J. Unlocking Selective Pathways for Glucose Photoreforming by Modulating Reaction Conditions. **ACS Sustainable Chemistry & Engineering**, v. 10, n. 18, p. 5867-5874, 2022.
https://doi.org/10.1021/acssuschemeng.1c08708.

OBREGÓN, S.; CABALLERO, A.; COLÓN, G. Hydrothermal synthesis of BiVO4: Structural and morphological influence on the photocatalytic activity. **Applied Catalysis B: Environmental**, v. 117-118, n., p. 59-66, 2012.
https://doi.org/10.1016/j.apcatb.2011.12.037.

PAI, M. R.; BANERJEE, A. M.; RAWOOL, S. A.; SINGHAL, A.; NAYAK, C.; EHRMAN, S. H.; TRIPATHI, A. K.; BHARADWAJ, S. R. A comprehensive study on sunlight driven photocatalytic hydrogen generation using low cost nanocrystalline Cu-Ti oxides. **Solar Energy Materials and Solar Cells**, v. 154, n., p. 104-120, 2016.
https://doi.org/10.1016/j.solmat.2016.04.036.

PANAGIOTOPOULOU, P.; KARAMEROU, E. E.; KONDARIDES, D. I. Kinetics and mechanism of glycerol photo-oxidation and photo-reforming reactions in aqueous TiO2 and Pt/TiO2 suspensions. **Catalysis Today**, v. 209, n., p. 91-98, 2013.
https://doi.org/10.1016/j.cattod.2012.09.029.

PARK, H. S.; KWEON, K. E.; YE, H.; PAEK, E.; HWANG, G. S.; BARD, A. J. Factors in the Metal Doping of BiVO4 for Improved Photoelectrocatalytic Activity as Studied by Scanning Electrochemical Microscopy and First-Principles Density-Functional Calculation. **The Journal of Physical Chemistry C**, v. 115, n. 36, p. 17870-17879, 2011.
https://doi.org/10.1021/jp204492r.

PATTERSON, E. M.; SHELDEN, C. E.; STOCKTON, B. H. Kubelka-Munk optical properties of a barium sulfate white reflectance standard. **Applied Optics**, v. 16, n. 3, p. 729-732, 1977.
https://doi.org/10.1364/AO.16.000729.

PELLEGRIN, Y.; ODOBEL, F. Sacrificial electron donor reagents for solar fuel production. **Comptes Rendus Chimie**, v. 20, n. 3, p. 283-295, 2017. https://doi.org/10.1016/j.crci.2015.11.026.

PERINI, N.; HESSEL, C.; BOTT-NETO, J. L.; PIRES, C. T. G. V. M. T.; FERNANDEZ, P. S.; SITTA, E. Photoelectrochemical oxidation of glycerol on hematite: thermal effects, in situ FTIR and long-term HPLC product analysis. **Journal of Solid State Electrochemistry**, v. 25, n. 3, p. 1101-1110, 2021. https://doi.org/10.1007/s10008-020-04878-7.

PIALLAT, F.; GASSILLOUD, R.; CAUBET, P.; VALLÉE, C. Investigation of TiN thin film oxidation depending on the substrate temperature at vacuum break. **Journal of Vacuum Science & Technology A**, v. 34, n. 5, p., 2016. https://doi.org/10.1116/1.4960648.

PINGMUANG, K.; NATTESTAD, A.; KANGWANSUPAMONKON, W.; WALLACE, G. G.; PHANICHPHANT, S.; CHEN, J. Phase-controlled microwave synthesis of pure monoclinic BiVO4 nanoparticles for photocatalytic dye degradation. **Applied Materials Today**, v. 1, n. 2, p. 67-73, 2015. https://doi.org/10.1016/j.apmt.2015.09.003.

PLUCINSKI, A.; LYU, Z.; SCHMIDT, B. V. K. J. Polysaccharide nanoparticles: from fabrication to applications. **Journal of Materials Chemistry B**, v. 9, n. 35, p. 7030-7062, 2021. https://doi.org/10.1039/D1TB00628B.

POSCHMANN, M. P. M.; LILLERUD, K. P.; STOCK, N. Acidic Properties of Known and New COOH-Functionalized M(IV) Metal-Organic Frameworks. **Chemistry – A European Journal**, v. 29, n. 48, p. e202301760, 2023. https://doi.org/10.1002/chem.202301760.

QARAAH, F. A.; MAHYOUB, S. A.; HEZAM, A.; ZHANG, W.; XIU, G.; MUNYANEZA, J.; WU, C. Facile synthesis of flower-like hierarchical N-doped Nb2O5/C nanostructures with efficient photocatalytic activity under visible light. **RSC Advances**, v. 10, n. 54, p. 32309-32322, 2020. https://doi.org/10.1039/D0RA02868A.

QI, Y.; ZHANG, J.; KONG, Y.; ZHAO, Y.; CHEN, S.; LI, D.; LIU, W.; CHEN, Y.; XIE, T.; CUI, J.; LI, C.; DOMEN, K.; ZHANG, F. Unraveling of cocatalysts photodeposited selectively on facets of BiVO4 to boost solar water splitting. **Nature Communications**, v. 13, n. 1, p. 484, 2022. https://doi.org/10.1038/s41467-022-28146-6.

RADIĆ, N.; PRKIĆ, A. Historical remarks on the Henderson-Hasselbalch equation: its advantages and limitations and a novel approach for exact pH calculation in buffer region. **Reviews in Analytical Chemistry**, v. 31, n. 2, p. 93-98, 2012. https://doi.org/doi:10.1515/revac-2012-0001.

RAMAN, K. V.; MORTLAND, M. M. Proton Transfer Reactions at Clay Mineral Surfaces. **Soil Science Society of America Journal**, v. 33, n. 2, p. 313-317, 1969. https://doi.org/10.2136/sssaj1969.03615995003300020040x.

RAPPE, A. K.; CASEWIT, C. J.; COLWELL, K. S.; GODDARD, W. A., III; SKIFF, W. M. UFF, a full periodic table force field for molecular mechanics and molecular dynamics simulations. **Journal of the American Chemical Society**, v. 114, n. 25, p. 10024-10035, 1992. https://doi.org/10.1021/ja00051a040.

RAVELLI, D.; DONDI, D.; FAGNONI, M.; ALBINI, A. Photocatalysis. A multi-faceted concept for green chemistry. **Chemical Society Reviews**, v. 38, n. 7, p. 1999-2011, 2009. https://doi.org/10.1039/B714786B.

RIBAO, P.; ALEXANDRA ESTEVES, M.; FERNANDES, V. R.; RIVERO, M. J.; RANGEL, C. M.; ORTIZ, I. Challenges arising from the use of TiO2/rGO/Pt photocatalysts to produce hydrogen from crude glycerol compared to synthetic glycerol. **International Journal of Hydrogen Energy**, v. 44, n. 53, p. 28494-28506, 2019. https://doi.org/10.1016/j.ijhydene.2018.09.148.

RICE, J. E. Remington's Pharmaceutical Sciences, 19th edition. Chapter 4 - Acids and Bases. Philadelphia College of Pharmacy. In: Rice, J. E. (Ed.). **Organic Chemistry Concepts and Applications for Medicinal Chemistry**. Boston: Academic Press, 2014, p.67-84.

RIKKEN, G. L. J. A.; BRAUN, D.; STARING, E. G. J.; DEMANDT, R. Schottky effect at a metal-polymer interface. **Applied Physics Letters**, v. 65, n. 2, p. 219-221, 1994. https://doi.org/10.1063/1.112678.

ROCHA, T. D. S.; NASCIMENTO, E. S.; DA SILVA, A. C.; OLIVEIRA, H. D. S.; GARCIA, E. M.; DE OLIVEIRA, L. C. A.; MONTEIRO, D. S.; RODRIGUEZ, M.; PEREIRA, M. C. Enhanced photocatalytic hydrogen generation from water by Ni(OH)2 loaded on Ni-doped δ-FeOOH nanoparticles obtained by one-step synthesis. **RSC Advances**, v. 3, n. 43, p. 20308-20314, 2013. https://doi.org/10.1039/C3RA43561J.

ROIG, M. G.; RIVERA, Z. S.; KENNEDY, J. F. A model study on rate of degradation of L-ascorbic acid during processing using home-produced juice concentrates. **International Journal of Food Sciences and Nutrition**, v. 46, n. 2, p. 107-115, 1995. https://doi.org/10.3109/09637489509012538.

ROTTER, J. M.; WEINBERGER, S.; KAMPMANN, J.; SICK, T.; SHALOM, M.; BEIN, T.; MEDINA, D. D. Covalent Organic Framework Films through Electrophoretic Deposition—Creating Efficient Morphologies for Catalysis. **Chemistry of Materials**, v. 31, n. 24, p. 10008-10016, 2019. https://doi.org/10.1021/acs.chemmater.9b02286.

RUMAYOR, M.; CORREDOR, J.; RIVERO, M. J.; ORTIZ, I. Prospective life cycle assessment of hydrogen production by waste photoreforming. **Journal of Cleaner Production**, v. 336, n., p. 130430, 2022. https://doi.org/10.1016/j.jclepro.2022.130430.

SACHA, C.; LAIA, F.; ANDREAS, K.; JAMES R, D. **Determining the Role of Oxygen Vacancies in the Photocatalytic Performance of WO3 for Water Oxidation**, 2019

SAKAR, M.; PRAKASH, R. M.; SHINDE, K.; BALAKRISHNA, G. R. Revisiting the materials and mechanism of metal oxynitrides for photocatalysis. **International Journal of Hydrogen Energy**, v. 45, n. 13, p. 7691-7705, 2020. https://doi.org/10.1016/j.ijhydene.2019.04.222.

SALKIĆ, M. Spectrophotometric Determination of L-Ascorbic Acid Based on Its Oxidation by Potassium Peroxodisulfate in the Presence of Cu(II) as Catalyst. **Journal of Analytical Chemistry**, v. 71, n. 2, p. 153-157, 2016. https://doi.org/10.1134/S1061934816020088.

SANWALD, K. E.; BERTO, T. F.; EISENREICH, W.; GUTIÉRREZ, O. Y.; LERCHER, J. A. Catalytic routes and oxidation mechanisms in photoreforming of polyols. **Journal of Catalysis**, v. 344, n., p. 806-816, 2016. https://doi.org/10.1016/j.jcat.2016.08.009.

SEGOVIA-GUZMÁN, M. O.; ROMÁN-AGUIRRE, M.; VERDE-GOMEZ, J. Y.; COLLINS-MARTÍNEZ, V. H.; ZARAGOZA-GALÁN, G.; RAMOS-SÁNCHEZ, V. H. Green Cu2O/TiO2 heterojunction for glycerol photoreforming. **Catalysis Today**, v. 349, n., p. 88-97, 2020. https://doi.org/10.1016/j.cattod.2018.05.031.

SERRANO-LOTINA, A.; PORTELA, R.; BAEZA, P.; ALCOLEA-RODRIGUEZ, V.; VILLARROEL, M.; ÁVILA, P. Zeta potential as a tool for functional materials development. **Catalysis Today**, v. 423, n., p. 113862, 2023. https://doi.org/10.1016/j.cattod.2022.08.004.

ŠETKA, M.; CALAVIA, R.; VOJKŮVKA, L.; LLOBET, E.; DRBOHLAVOVÁ, J.; VALLEJOS, S. Raman and XPS studies of ammonia sensitive polypyrrole nanorods and nanoparticles. **Scientific Reports**, v. 9, n. 1, p. 8465, 2019. https://doi.org/10.1038/s41598-019-44900-1.

SHAHIRAH, M. N. N.; GIMBUN, J.; LAM, S. S.; NG, Y. H.; CHENG, C. K. Synthesis and characterization of a LaNi/α-Al2O3 catalyst and its use in pyrolysis of glycerol to syngas. **Renewable Energy**, v. 132, n., p. 1389-1401, 2019. https://doi.org/10.1016/j.renene.2018.09.033.

SHANNON, R. D. Revised effective ionic radii and systematic studies of interatomic distances in halides and chalcogenides. **Acta Crystallographica Section A**, v. 32, n. 5, p. 751-767, 1976. https://doi.org/10.1107/S0567739476001551.

SHI, T.; WANG, H.; LI, L.; ZHAO, Z.; WANG, C.; ZHANG, X.; XIE, Y. Enhanced photostability in protonated covalent organic frameworks for singlet oxygen generation. **Matter**, v. 5, n. 3, p. 1004-1015, 2022. https://doi.org/10.1016/j.matt.2022.01.003.

SHUKLA, T.; UPMANYU, N.; PRAKASH PANDEY, S.; GOSH, D. Chapter 1 - Lipid nanocarriers. In: Grumezescu, A. M. (Ed.). **Lipid Nanocarriers for Drug Targeting**: William Andrew Publishing, 2018, p.1-47.

SICK, T.; HUFNAGEL, A. G.; KAMPMANN, J.; KONDOFERSKY, I.; CALIK, M.; ROTTER, J. M.; EVANS, A.; DÖBLINGER, M.; HERBERT, S.; PETERS, K.; BÖHM, D.; KNOCHEL, P.; MEDINA, D. D.; FATTAKHOVA-ROHLFING, D.; BEIN, T. Oriented Films of Conjugated 2D Covalent Organic Frameworks as Photocathodes for Water Splitting. **Journal of the American Chemical Society**, v. 140, n. 6, p. 2085-2092, 2018. https://doi.org/10.1021/jacs.7b06081.

SIMÕES, M.; BARANTON, S.; COUTANCEAU, C. Electrochemical Valorisation of Glycerol. **ChemSusChem**, v. 5, n. 11, p. 2106-2124, 2012. https://doi.org/10.1002/cssc.201200335.

SONG, X.; WU, Y.; ZHANG, X.; LI, X.; ZHU, Z.; MA, C.; YAN, Y.; HUO, P.; YANG, G. Boosting charge carriers separation and migration efficiency via fabricating all organic van der Waals heterojunction for efficient photoreduction of CO2. **Chemical Engineering Journal**, v. 408, n., p. 127292, 2021. https://doi.org/10.1016/j.cej.2020.127292.

SPELTINI, A.; STURINI, M.; DONDI, D.; ANNOVAZZI, E.; MARASCHI, F.; CARATTO, V.; PROFUMO, A.; BUTTAFAVA, A. Sunlight-promoted photocatalytic hydrogen gas evolution from water-suspended cellulose: a systematic study. **Photochemical & Photobiological Sciences**, v. 13, n. 10, p. 1410-1419, 2014.
https://doi.org/10.1039/c4pp00128a.

STEGBAUER, L.; SCHWINGHAMMER, K.; LOTSCH, B. V. A hydrazone-based covalent organic framework for photocatalytic hydrogen production. **Chemical Science**, v. 5, n. 7, p. 2789-2793, 2014.
https://doi.org/10.1039/C4SC00016A.

STEGBAUER, L.; ZECH, S.; SAVASCI, G.; BANERJEE, T.; PODJASKI, F.; SCHWINGHAMMER, K.; OCHSENFELD, C.; LOTSCH, B. V. Tailor-Made Photoconductive Pyrene-Based Covalent Organic Frameworks for Visible-Light Driven Hydrogen Generation. **Advanced Energy Materials**, v. 8, n. 24, p. 1703278, 2018.
https://doi.org/10.1002/aenm.201703278.

SUN, Z.; GUO, J.; ZHU, S.; MAO, L.; MA, J.; ZHANG, D. A high-performance Bi2WO6–graphene photocatalyst for visible light-induced H2 and O2 generation. **Nanoscale**, v. 6, n. 4, p. 2186-2193, 2014.
https://doi.org/10.1039/C3NR05249D.

TATENO, H.; CHEN, S.-Y.; MISEKI, Y.; NAKAJIMA, T.; MOCHIZUKI, T.; SAYAMA, K. Photoelectrochemical Oxidation of Glycerol to Dihydroxyacetone Over an Acid-Resistant Ta:BiVO4 Photoanode. **ACS Sustainable Chemistry & Engineering**, v. 10, n. 23, p. 7586-7594, 2022.
https://doi.org/10.1021/acssuschemeng.2c01282.

TAUC, J.; GRIGOROVICI, R.; VANCU, A. Optical Properties and Electronic Structure of Amorphous Germanium. **physica status solidi (b)**, v. 15, n. 2, p. 627-637, 1966.
https://doi.org/10.1002/pssb.19660150224.

TAUC, J. Optical properties and electronic structure of amorphous Ge and Si. **Materials Research Bulletin**, v. 3, n. 1, p. 37-46, 1968.
https://doi.org/10.1016/0025-5408(68)90023-8.

TAYLOR, S.; MEHTA, M.; SAMOKHVALOV, A. Production of Hydrogen by Glycerol Photoreforming Using Binary Nitrogen–Metal-Promoted N-M-TiO2 Photocatalysts. **Chemphyschem**, v. 15, n. 5, p. 942-949, 2014.
https://doi.org/10.1002/cphc.201301140.

TREPTOW, R. S. The conjugate acid base chart. **Journal of Chemical Education**, v. 63, n. 11, p. 938, 1986.
https://doi.org/10.1021/ed063p938.

VAMVASAKIS, I.; LIU, B.; ARMATAS, G. S. Size Effects of Platinum Nanoparticles in the Photocatalytic Hydrogen Production Over 3D Mesoporous Networks of CdS and Pt Nanojunctions. **Advanced Functional Materials**, v. 26, n. 44, p. 8062-8071, 2016.
https://doi.org/10.1002/adfm.201603292.

WALLER, P. J.; LYLE, S. J.; OSBORN POPP, T. M.; DIERCKS, C. S.; REIMER, J. A.; YAGHI, O. M. Chemical Conversion of Linkages in Covalent Organic Frameworks. **Journal of the American Chemical Society**, v. 138, n. 48, p. 15519-15522, 2016.
https://doi.org/10.1021/jacs.6b08377.

WALLER, P. J.; ALFARAJ, Y. S.; DIERCKS, C. S.; JARENWATTANANON, N. N.; YAGHI, O. M. Conversion of Imine to Oxazole and Thiazole Linkages in Covalent Organic Frameworks. **Journal of the American Chemical Society**, v. 140, n. 29, p. 9099-9103, 2018. https://doi.org/10.1021/jacs.8b05830.

WANG, D.; KAO, M.-R.; LI, J.; SUN, P.; MENG, Q.; VYAS, A.; LIANG, P.-H.; WANG, Y.-S.; HSIEH, Y. S. Y. Novel Two-Step Process in Cellulose Depolymerization: Hematite-Mediated Photocatalysis by Lytic Polysaccharide Monooxygenase and Fenton Reaction. **Journal of Agricultural and Food Chemistry**, v. 70, n. 32, p. 9941-9947, 2022. https://doi.org/10.1021/acs.jafc.2c02445.

WANG, J.-R.; SONG, K.; LUAN, T.-X.; CHENG, K.; WANG, Q.; WANG, Y.; YU, W. W.; LI, P.-Z.; ZHAO, Y. Robust links in photoactive covalent organic frameworks enable effective photocatalytic reactions under harsh conditions. **Nature Communications**, v. 15, n. 1, p. 1267, 2024. https://doi.org/10.1038/s41467-024-45457-y.

WANG, T.; FENG, C.; LIU, J.; WANG, D.; HU, H.; HU, J.; CHEN, Z.; XUE, G. Bi2WO6 hollow microspheres with high specific surface area and oxygen vacancies for efficient photocatalysis N2 fixation. **Chemical Engineering Journal**, v. 414, n., p. 128827, 2021. https://doi.org/10.1016/j.cej.2021.128827.

WANG, W.; HUANG, D.; ZHENG, W.; ZHAO, X.; HE, K.; PANG, H.; XIANG, Y. Construction of Amide-Linked Covalent Organic Frameworks by N-Heterocyclic Carbene-Mediated Selective Oxidation for Photocatalytic Dehalogenation. **Chemistry of Materials**, v. 35, n. 17, p. 7154-7163, 2023. https://doi.org/10.1021/acs.chemmater.3c01425.

WANG, X.; ZHENG, X.; HAN, H.; FAN, Y.; ZHANG, S.; MENG, S.; CHEN, S. Photocatalytic hydrogen evolution from biomass (glucose solution) on Au/CdS nanorods with Au3+ self-reduction. **Journal of Solid State Chemistry**, v. 289, n., p. 121495, 2020. https://doi.org/10.1016/j.jssc.2020.121495.

WANG, Y.; VOGEL, A.; SACHS, M.; SPRICK, R. S.; WILBRAHAM, L.; MONIZ, S. J. A.; GODIN, R.; ZWIJNENBURG, M. A.; DURRANT, J. R.; COOPER, A. I.; TANG, J. Current understanding and challenges of solar-driven hydrogen generation using polymeric photocatalysts. **Nature Energy**, v. 4, n. 9, p. 746-760, 2019. https://doi.org/10.1038/s41560-019-0456-5.

WANG, Y.; NASREEN, S.; KAMAL, D.; LI, Z.; WU, C.; HUO, J.; CHEN, L.; RAMPRASAD, R.; CAO, Y. Tuning Surface States of Metal/Polymer Contacts Toward Highly Insulating Polymer-Based Dielectrics. **ACS Applied Materials & Interfaces**, v. 13, n. 38, p. 46142-46150, 2021. https://doi.org/10.1021/acsami.1c12854.

WANG, Y.; WANG, H.; LI, Y.; ZHANG, M.; ZHENG, Y. Designing a 0D/1D S-Scheme Heterojunction of Cadmium Selenide and Polymeric Carbon Nitride for Photocatalytic Water Splitting and Carbon Dioxide Reduction. **Molecules**, v. 27, n. 19, p. 6286, 2022.

WANNAKAN, K.; KHANSAMRIT, K.; SENASU, T.; NANAN, S. Ultrasound-Assisted Synthesis of a ZnO/BiVO4 S-Scheme Heterojunction Photocatalyst for Degradation of the Reactive Red 141 Dye and Oxytetracycline Antibiotic. **ACS Omega**, v. 8, n. 5, p. 4835-4852, 2023. https://doi.org/10.1021/acsomega.2c07020.

WILSON, A. A.; SHALVEY, T. P.; KAFIZAS, A.; MUMTAZ, A.; DURRANT, J. R. Analysis of charge trapping and long lived hole generation in SrTiO3 photoanodes. **Sustainable Energy & Fuels**, v. 7, n. 20, p. 5066-5075, 2023. https://doi.org/10.1039/D3SE00886J.

WU, F.; ZHANG, X.; WANG, L.; LI, G.; HUANG, J.; SONG, A.; MENG, A.; LI, Z. Enhanced Spin-Polarized Electric Field Modulating p-Band Center on Ni-Doped CdS for Boosting Photocatalytic Hydrogen Evolution. **Small**, v. 20, n. 27, p. 2309439, 2024. https://doi.org/10.1002/smll.202309439.

WU, Q.-J.; SI, D.-H.; YE, S.; DONG, Y.-L.; CAO, R.; HUANG, Y.-B. Photocoupled Electroreduction of CO2 over Photosensitizer-Decorated Covalent Organic Frameworks. **Journal of the American Chemical Society**, v. 145, n. 36, p. 19856-19865, 2023. https://doi.org/10.1021/jacs.3c06113.

WU, X.; LUO, N.; XIE, S.; ZHANG, H.; ZHANG, Q.; WANG, F.; WANG, Y. Photocatalytic transformations of lignocellulosic biomass into chemicals. **Chemical Society Reviews**, v. 49, n. 17, p. 6198-6223, 2020. https://doi.org/10.1039/d0cs00314j.

WU, Y.-H.; KUZNETSOV, D. A.; PFLUG, N. C.; FEDOROV, A.; MÜLLER, C. R. Solar-driven valorisation of glycerol on BiVO4 photoanodes: effect of co-catalyst and reaction media on reaction selectivity. **Journal of Materials Chemistry A**, v. 9, n. 10, p. 6252-6260, 2021. https://doi.org/10.1039/D0TA10480A.

XIAO, D.; CHENG, G.; SHE, H.; CHEN, X.; HUANG, J.; WANG, L.; WANG, Q. Enhanced Photoelectrochemical Water Splitting Performance of BiVO4 Photoanode by Integrating Electron-Rich Polyoxometalate into Metal–Organic Framework. **The Journal of Physical Chemistry C**, v. 128, n. 37, p. 15266-15276, 2024. https://doi.org/10.1021/acs.jpcc.4c03542.

XIAO, Y.; WANG, K.; DONG, W.; LI, L. Molecular engineering in tunable crystallinity of 2D covalent organic frameworks for efficient photocatalytic hydrogen evolution. **Polymer**, v. 300, n., p. 126980, 2024. https://doi.org/10.1016/j.polymer.2024.126980.

XIE, A.; PAN, Z.-H.; YU, M.; LUO, G.-G.; SUN, D. Photocatalytic hydrogen production from acidic aqueous solution in BODIPY-cobaloxime-ascorbic acid homogeneous system. **Chinese Chemical Letters**, v. 30, n. 1, p. 225-228, 2019. https://doi.org/10.1016/j.cclet.2018.05.003.

XUE, R.; LIU, Y.-S.; WANG, M.-Y.; GUO, H.; YANG, W.; GUO, J.-X.; YANG, G.-Y. Rational Conversion of Imine Linkages to Amide Linkages in Covalent Organic Frameworks for Photocatalytic Oxidation with Enhanced Photostability. **ChemSusChem**, v. 17, n. 19, p. e202400732, 2024. https://doi.org/10.1002/cssc.202400732.

YANG, J.; ACHARJYA, A.; YE, M.-Y.; RABEAH, J.; LI, S.; KOCHOVSKI, Z.; YOUK, S.; ROESER, J.; GRÜNEBERG, J.; PENSCHKE, C.; SCHWARZE, M.; WANG, T.; LU, Y.; VAN DE KROL, R.; OSCHATZ, M.; SCHOMÄCKER, R.; SAALFRANK, P.; THOMAS, A. Protonated Imine-Linked Covalent Organic Frameworks for Photocatalytic Hydrogen Evolution. **Angewandte Chemie International Edition**, v. 60, n. 36, p. 19797-19803, 2021. https://doi.org/10.1002/anie.202104870.

YANG, L.; KRUSE, B. Revised Kubelka–Munk theory. I. Theory and application. **Journal of the Optical Society of America A**, v. 21, n. 10, p. 1933-1941, 2004. https://doi.org/10.1364/JOSAA.21.001933.

YANG, W.; GODIN, R.; KASAP, H.; MOSS, B.; DONG, Y.; HILLMAN, S. A. J.; STEIER, L.; REISNER, E.; DURRANT, J. R. Electron Accumulation Induces Efficiency Bottleneck for Hydrogen Production in Carbon Nitride Photocatalysts. **Journal of the American Chemical Society**, v. 141, n. 28, p. 11219-11229, 2019. https://doi.org/10.1021/jacs.9b04556.

YANG, X.; LIANG, S.; MIAO, J.; YANG, Y.; ZHANG, S. Gradient-Doped BiVO(4) Dual Photoanodes for Highly Efficient Photoelectrochemical Water Splitting. **Chemphyschem**, v. 26, n. 1, p. e202400692, 2025. https://doi.org/10.1002/cphc.202400692.

YANG, Z.; ZHONG, W.; CHEN, Y.; WANG, C.; MO, S.; ZHANG, J.; SHU, R.; SONG, Q. Improving Glycerol Photoreforming Hydrogen Production Over Ag2O-TiO2 Catalysts by Enhanced Colloidal Dispersion Stability. **Frontiers in Chemistry**, v. 8, n., p., 2020. https://doi.org/10.3389/fchem.2020.00342.

YAO, G.; GUO, Y.; LE, Y.; JIN, B.; HE, R.; ZHONG, H.; JIN, F. Energy Valorization of Food Waste: Rapid Conversion of Typical Polysaccharide Components to Formate. **Industrial & Engineering Chemistry Research**, v. 59, n. 39, p. 17069-17075, 2020. https://doi.org/10.1021/acs.iecr.0c01073.

YU, J.; DAPPOZZE, F.; MARTÍN-GOMEZ, J.; HIDALGO-CARRILLO, J.; MARINAS, A.; VERNOUX, P.; CARAVACA, A.; GUILLARD, C. Glyceraldehyde production by photocatalytic oxidation of glycerol on WO3-based materials. **Applied Catalysis B: Environmental**, v. 299, n., p. 120616, 2021. https://doi.org/10.1016/j.apcatb.2021.120616.

YU, J.; GONZÁLEZ-COBOS, J.; DAPPOZZE, F.; GRIMALDOS-OSORIO, N.; VERNOUX, P.; CARAVACA, A.; GUILLARD, C. First PEM photoelectrolyser for the simultaneous selective glycerol valorization into value-added chemicals and hydrogen generation. **Applied Catalysis B: Environmental**, v. 327, n., p. 122465, 2023. https://doi.org/10.1016/j.apcatb.2023.122465.

ZHANG, C.; ZHU, Y. Synthesis of Square Bi2WO6 Nanoplates as High-Activity Visible-Light-Driven Photocatalysts. **Chemistry of Materials**, v. 17, n. 13, p. 3537-3545, 2005. https://doi.org/10.1021/cm0501517.

ZHANG, G.; LI, X.; LIAO, Q.; LIU, Y.; XI, K.; HUANG, W.; JIA, X. Water-dispersible PEG-curcumin/amine-functionalized covalent organic framework nanocomposites as smart carriers for in vivo drug delivery. **Nature Communications**, v. 9, n. 1, p. 2785, 2018. https://doi.org/10.1038/s41467-018-04910-5.

ZHANG, J.; WANG, J.; TANG, Y.; LIU, K.; ZHANG, B.; MA, G. Insight into the Light-Driven Hydrogen Production over Pure and Rh-Doped Rutile in the Presence of Ascorbic Acid: Impact of Interfacial Chemistry on Photocatalysts. **ACS Applied Materials & Interfaces**, v. 14, n. 30, p. 34656-34664, 2022. https://doi.org/10.1021/acsami.2c06302.

ZHANG, L.; SHI, J.; LIU, M.; JING, D.; GUO, L. Photocatalytic reforming of glucose under visible light over morphology controlled Cu2O: efficient charge separation by crystal facet engineering. **Chemical Communications**, v. 50, n. 2, p. 192-194, 2014.

https://doi.org/10.1039/C3CC46423G.

ZHANG, M.; SUN, R.; LI, Y.; SHI, Q.; XIE, L.; CHEN, J.; XU, X.; SHI, H.; ZHAO, W. High H2 Evolution from Quantum Cu(II) Nanodot-Doped Two-Dimensional Ultrathin TiO2 Nanosheets with Dominant Exposed {001} Facets for Reforming Glycerol with Multiple Electron Transport Pathways. **The Journal of Physical Chemistry C**, v. 120, n. 20, p. 10746-10756, 2016. https://doi.org/10.1021/acs.jpcc.6b01030.

ZHANG, M.; WU, X.; XIE, Y.; HAO, X.; WANG, Q.; ZHAO, Y.; WU, J.; PAN, X. Effect of COF linkage isomerism on photocatalytic hydrogen evolution performance. **Materials Chemistry Frontiers**, v. 7, n. 21, p. 5399-5405, 2023. https://doi.org/10.1039/D3QM00807J.

ZHANG, Y.; ZHANG, N.; TANG, Z.-R.; XU, Y.-J. Identification of Bi2WO6 as a highly selective visible-light photocatalyst toward oxidation of glycerol to dihydroxyacetone in water. **Chemical Science**, v. 4, n. 4, p. 1820-1824, 2013. https://doi.org/10.1039/C3SC50285F.

ZHANG, Y.; CIRIMINNA, R.; PALMISANO, G.; XU, Y.-J.; PAGLIARO, M. Sol-gel entrapped visible light photocatalysts for selective conversions. **RSC Advances**, v. 4, n. 35, p. 18341-18346, 2014. https://doi.org/10.1039/C4RA01031K.

ZHANG, Y.; LIU, S.; ZHANG, Q.; NING, T.; WANG, X.; LU, A. Effect of Nb5+ doping on the microstructure and conductivity of Li1.125Ta0.875Zr0.125SiO5 electrolyte. **Journal of Alloys and Compounds**, v. 902, n., p., 2022. https://doi.org/10.1016/j.jallcom.2022.163760.

ZHANG, Y.; SHI, W.; ZHAO, Y.; ZHANG, C.; ZHI, Y. Linkage Design in Two-Dimensional Covalent Organic Frameworks for High Iodine Uptake. **Macromolecular Rapid Communications**, v. 44, n. 7, p. 2200787, 2023. https://doi.org/10.1002/marc.202200787.

ZHENG, X.-J.; WEI, L.-F.; ZHANG, Z.-H.; JIANG, Q.-J.; WEI, Y.-J.; XIE, B.; WEI, M.-B. Research on photocatalytic H2 production from acetic acid solution by Pt/TiO2 nanoparticles under UV irradiation. **International Journal of Hydrogen Energy**, v. 34, n. 22, p. 9033-9041, 2009. https://doi.org/10.1016/j.ijhydene.2009.09.019.

ZHONG, M.; LI, X.; CHU, X.; GUI, H.; ZUO, S.; YAO, C.; LI, Z.; CHEN, Y. Solar driven catalytic conversion of cellulose biomass into lactic acid over copper reconstructed natural mineral. **Applied Catalysis B: Environmental**, v. 317, n., p. 121718, 2022. https://doi.org/10.1016/j.apcatb.2022.121718.

ZHONG, W.; WANG, C.; ZHAO, H.; PENG, S.; TIAN, Z.; SHU, R.; CHEN, Y. Synergistic effect of photo-thermal catalytic glycerol reforming hydrogen production over 2D Au/TiO2 nanoflakes. **Chemical Engineering Journal**, v. 446, n., p. 137063, 2022. https://doi.org/10.1016/j.cej.2022.137063.

ZHOU, M.; BAO, S.; BARD, A. J. Probing Size and Substrate Effects on the Hydrogen Evolution Reaction by Single Isolated Pt Atoms, Atomic Clusters, and Nanoparticles. **Journal of the American Chemical Society**, v. 141, n. 18, p. 7327-7332, 2019. https://doi.org/10.1021/jacs.8b13366.

ZHOU, Z.-B.; HAN, X.-H.; QI, Q.-Y.; GAN, S.-X.; MA, D.-L.; ZHAO, X. A Facile, Efficient, and General Synthetic Method to Amide-Linked Covalent Organic Frameworks. **Journal of the American Chemical Society**, v. 144, n. 3, p. 1138-1143, 2022. https://doi.org/10.1021/jacs.1c12392.

ZHU, Y.; HUANG, D.; WANG, W.; LIU, G.; DING, C.; XIANG, Y. Sequential Oxidation/Cyclization of Readily Available Imine Linkages to Access Benzoxazole-Linked Covalent Organic Frameworks. **Angewandte Chemie International Edition**, v. 63, n. 11, p. e202319909, 2024. https://doi.org/10.1002/anie.202319909.

ZIYAI, M. R.; MEHRPOOYA, M.; AGHBASHLO, M.; OMID, M.; ALSAGRI, A. S.; TABATABAEI, M. Techno-economic comparison of three biodiesel production scenarios enhanced by glycerol supercritical water reforming process. **Int. J. Hydrogen Energy**, v. 44, n. 33, p. 17845-17862, 2019. https://doi.org/10.1016/j.ijhydene.2019.05.017.

ZUBAIR, M.; LI, G.; WANG, B.; WANG, L.; YU, H. Electrochemical Kinetics and Cycle Stability Improvement with Nb Doping for Lithium-Rich Layered Oxides. **ACS Applied Energy Materials**, v. 2, n. 1, p. 503-512, 2019. https://doi.org/10.1021/acsaem.8b01534.

ZUO, Y.; ZHENG, T.; ZHANG, Y.; SHI, H.; JIANG, L. Facile access to high-efficiency degradation of tetracycline hydrochloride with structural optimization of TiN. **Environmental Science and Pollution Research**, v. 29, n. 24, p. 36854-36864, 2022. https://doi.org/10.1007/s11356-022-18661-w.

9. Appendices

9.1. Appendix A – Supporting information of chapter 2

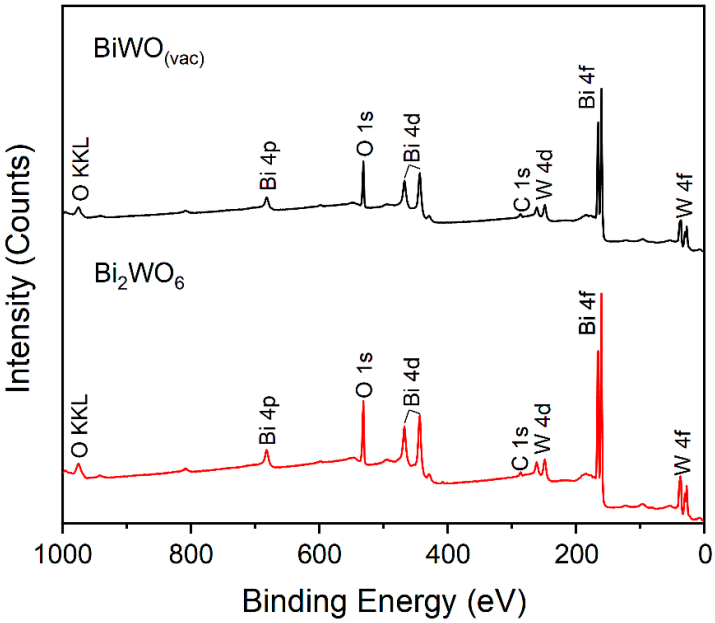

Figure A1. XPS survey spectra of Bi_2WO_6 (red) and $BiWO_{(Vac)}$ (black) powder samples.

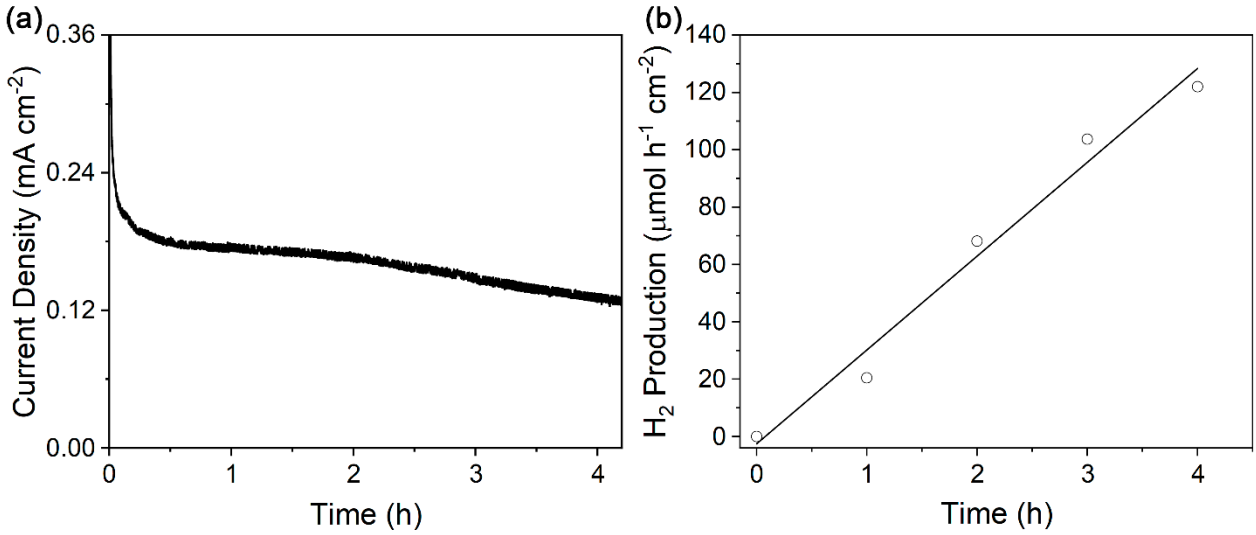

Figure A2. Chronoamperometry of pristine Bi_2WO_6 photoanodes in crude glycerol electrolyte (10% glycerol v/v in K_2SO_4 0.1 M) under 0.8 V vs Ag/AgCl and illumination (AM 1.5G, 100 mW cm^{-2}) and (b) H_2 evolution from the chronoamperometric experiment.

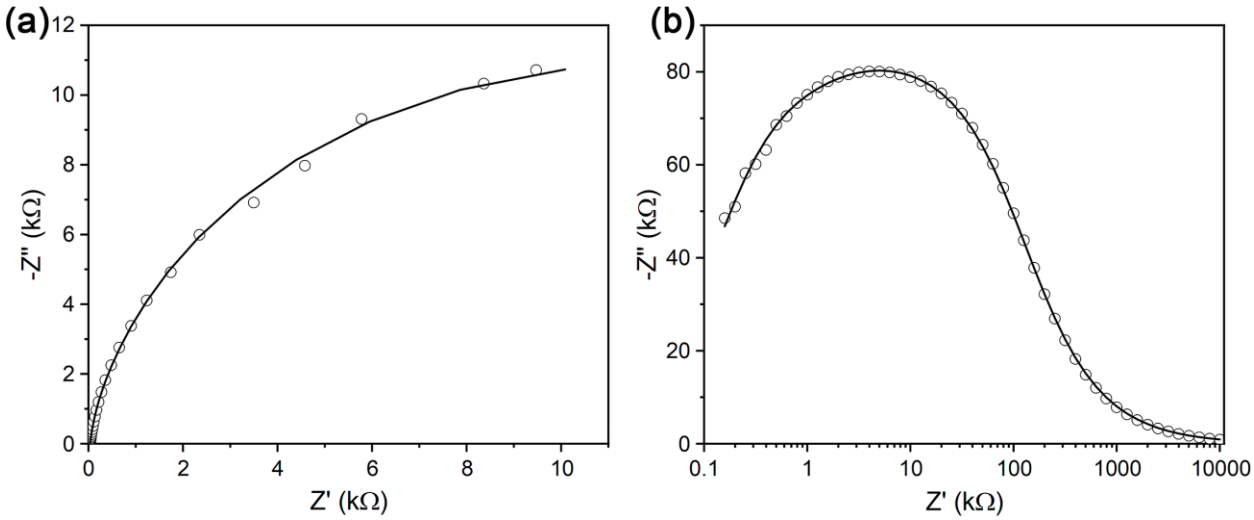

Figure A3. (a) EIS Nyquist and (b) Bode plot of pristine Bi_2WO_6 photoanode taken under illuminated conditions (AM 1.5G, 100 mW cm^{-2}) at 1.0 V vs Ag/AgCl. Fitting parameters: R_{CT} = 23.2 kΩ, R_{TP} = 6.0 kΩ.

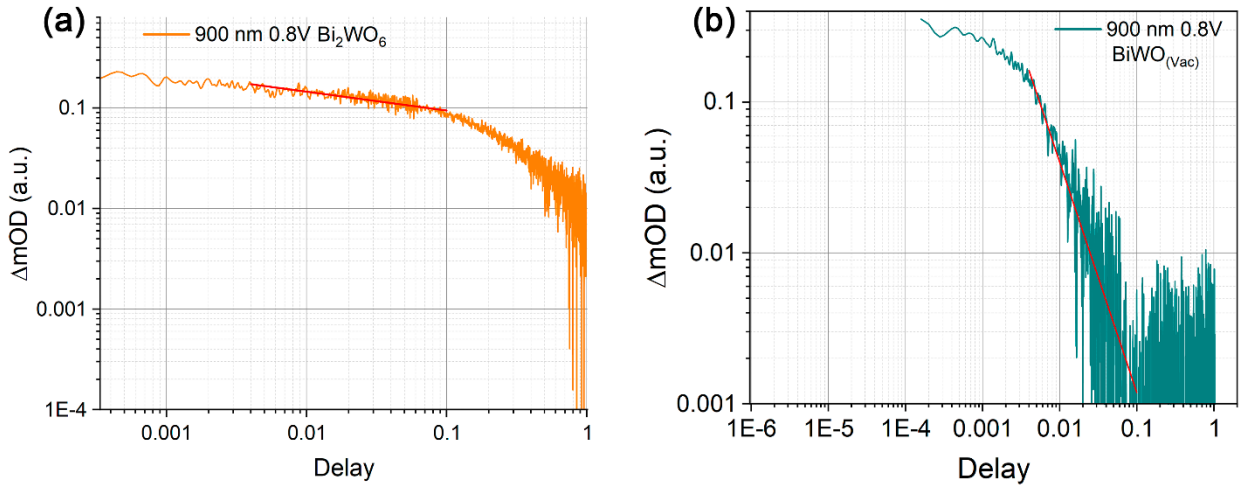

Figure A4. Power law decay fitting of (a) Bi_2WO_6 photoanode and (b) $BiWO_{(vac)}$ probed at 900 nm and under applied bias of 0.8 V vs Ag/AgCl.

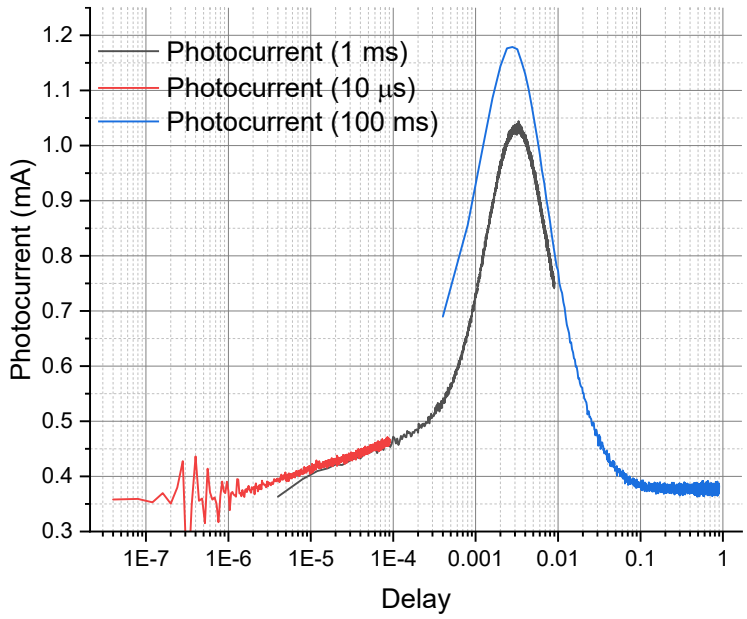

Figure A5. Transient photocurrent trace spectrum of $BiWO_{(vac)}$ photoanodes.

Table A1. EIS data fitting parameters for the $BiWO_{(vac)}$ photoanodes.

Bias (V vs Ag/AgCl)	R_{Tp} (Dark)	R_{CT} (Dark)	R_{TP} (Light)	R_{CT} (Light)
1.0 V	2.9 kΩ	23.5 kΩ	5.7 kΩ	14.0 kΩ
0.8 V	1.8 kΩ	49.6 kΩ	6.2 kΩ	23.7 kΩ
0.6 V	0.2 kΩ	69.9 kΩ	6.1 kΩ	30.0 kΩ
0.4 V	0.5 kΩ	76.2 kΩ	6.0 kΩ	31.6 kΩ
0.2 V	0.4 kΩ	86.4 kΩ	5.3 kΩ	32.8 kΩ

9.2. Appendix B – Supporting information of chapter 3

Table B1. Fitting parameters of the XPS data.

Sample	C (%)	Bi (%)	V (%)	O (%)	Nb (%)	Bi/V
$BiVO_4$	10.46	23.84	13.61	52.09	-	1.75
5% Nb:$BiVO_4$	6.88	20.22	8.73	59.10	5.07	2.32
1% Nb:$BiVO_4$	20.0	23.48	10.98	45.22	0.45	2.175
0.1% Nb:$BiVO_4$	13.6	23.93	12.34	50.13	-	1.94

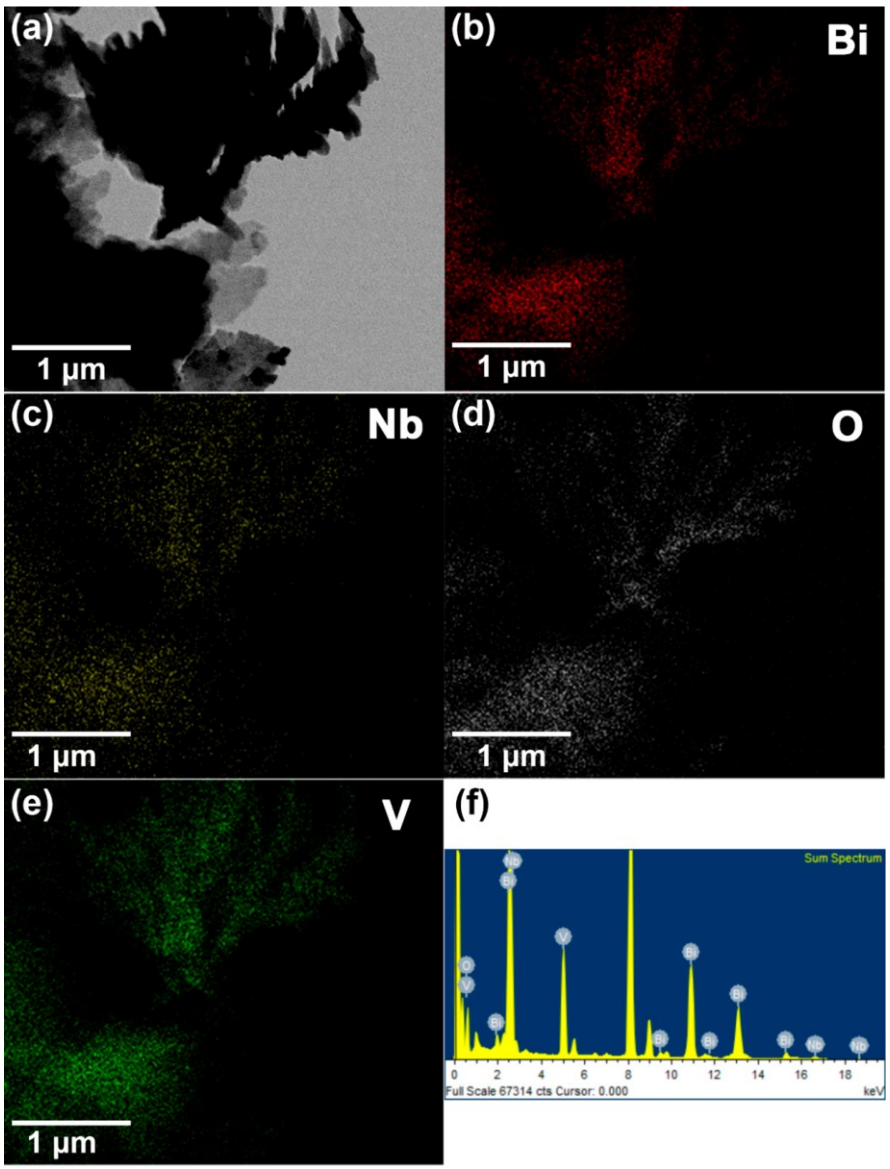

Figure B1. TEM-EDS mapping of 5% Nb:$BiVO_4$ powder(a - e) and (f) EDS sum spectrum.

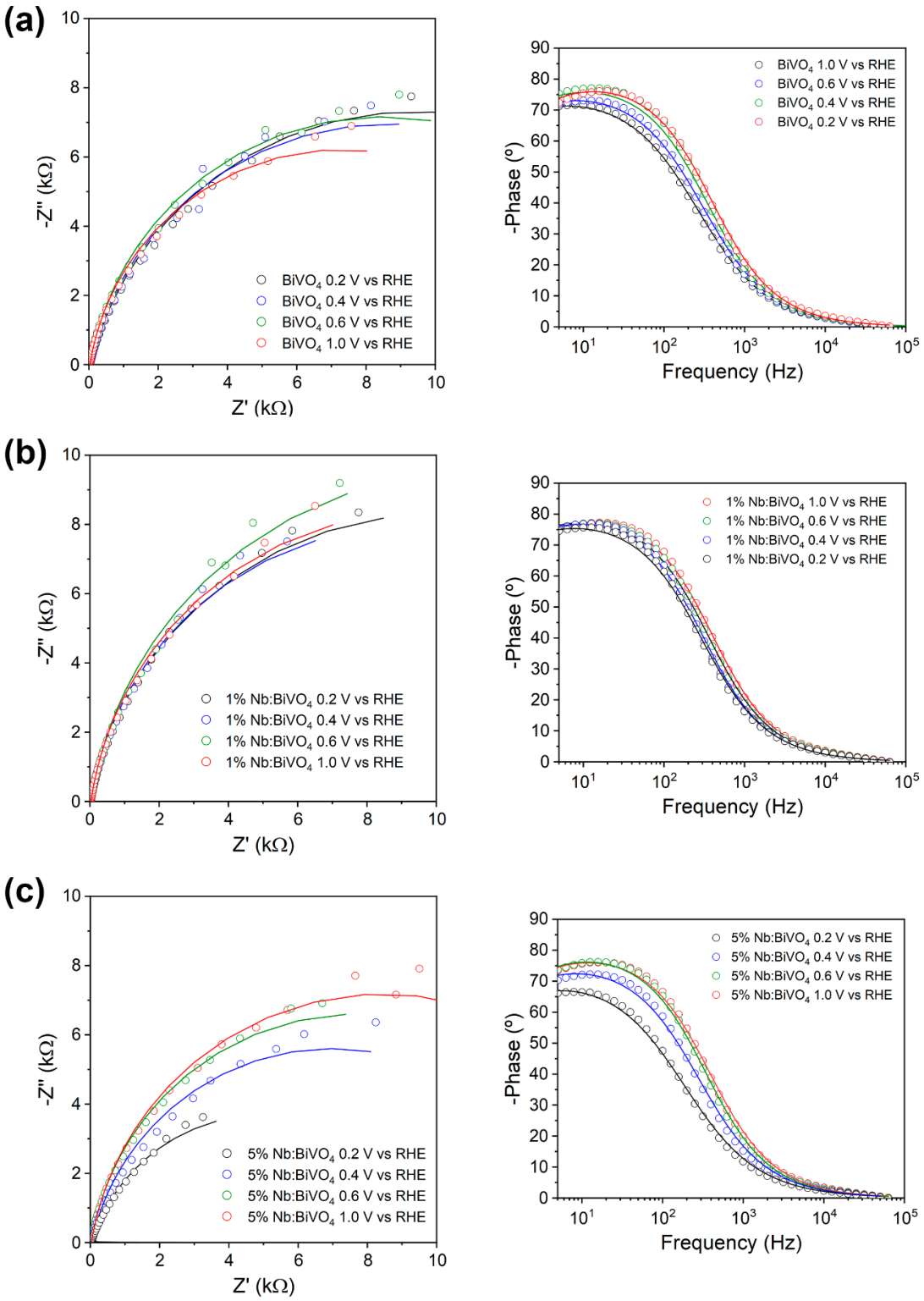

Figure B2. Nyquist and bode EIS plots of (a) $BiVO_4$, (b) 0.1% Nb:$BiVO_4$ and (c) 5% Nb:$BiVO_4$ at different potentials. All measurements were performed in dark with 0.1 M K_2SO_4 electrolyte.

Table B2. EIS data fitting parameters.

Sample	Bias (RHE)	Rs(Ω)	Rct (Ω)	CPE (s^n)	n	χ^2 (10^{-3})
5% Nb:$BiVO_4$ (light)	1.0 V	31.6	634	$7.3x10^{-5}$	0.81	2.7
5% Nb:$BiVO_4$	1.0 V	32.4	16854	$2.8x10^{-5}$	0.90	3.0
$BiVO_4$ (light)	1.0 V	31.8	1290	$3.9x10^{-5}$	0.88	1.1
$BiVO_4$	1.0 V	32.2	14485	$2.7x10^{-5}$	0.90	1.6
$BiVO_4$	0.6 V	32.0	19416	$2.8x10^{-5}$	0.91	1.3
$BiVO_4$	0.4 V	32.0	17224	$4.57x10^{-5}$	0.86	2.4
$BiVO_4$	0.2 V	32.0	18738	$6.1x10^{-5}$	0.85	2.3

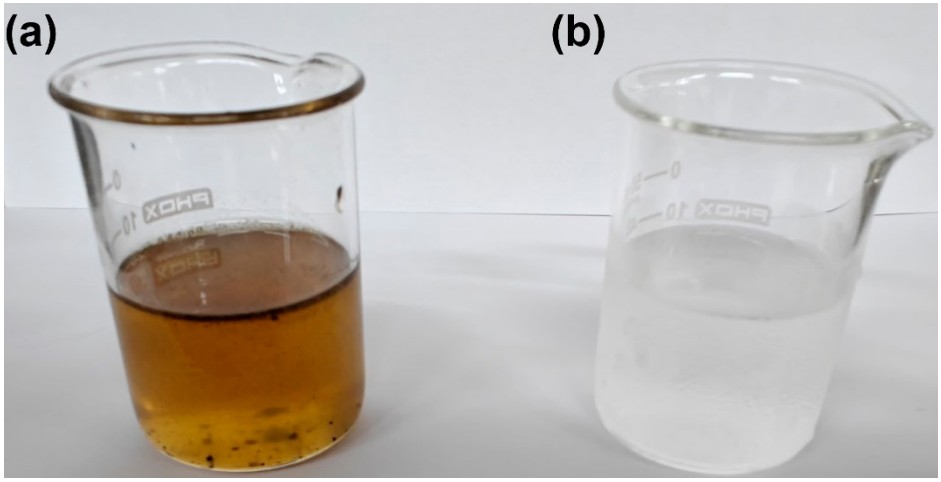

Figure B3. (a) Crude glycerol and (b) flegmass that were used in this study.

9.3. Appendix C – Supporting information of chapter 4

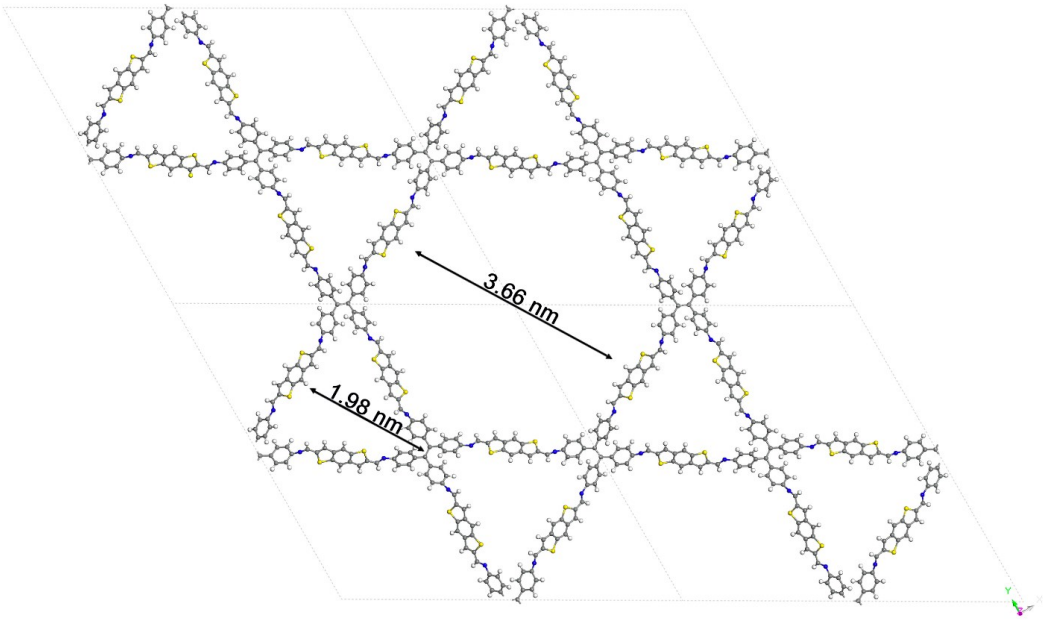

Figure C1. Simulated Kagome structure of Imine-BDT-ETTA.

Structural parameters of Imine-BDT-ETTA:

Unit Cell Parameters (*P6*):

$a = b = 4.641$ nm, $c = 0.447$ nm

$\alpha = \beta = 90$ º, $\gamma = 120$ º

Table C1. Fractional coordinates of Imine-BDT-ETTA.

C1	C	0.48488	148.320	0.27866
C2	C	0.51472	0.54810	0.28876
C3	C	0.54703	0.52009	0.32098
C4	C	0.57525	0.54268	0.15422
C5	C	0.60616	0.54449	0.19731
C6	C	0.60923	0.52384	0.41010
C7	C	0.58184	0.50322	0.58725
C8	C	0.55167	0.50259	0.55024
C9	C	0.46020	0.42402	0.44830
C10	C	0.46340	0.39632	0.52071
C11	C	0.49111	0.39437	0.43094
C12	C	0.51510	0.41916	0.25108

C13	C	0.51285	0.44705	0.17380
N14	N	0.50224	0.62709	0.55696
C15	C	0.49283	0.64461	0.69314
N16	N	0.63889	0.52197	0.45301
C17	C	0.66745	0.53819	0.31775
C18	C	0.49687	0.32253	0.61467
S19	S	0.46352	0.29767	0.34968
C20	C	0.47186	0.26430	0.42403
C21	C	0.49747	0.27299	0.62728
C22	C	0.51131	0.30666	0.73550
C23	C	0.50801	0.25069	0.71007
C24	C	0.49177	0.21909	0.58145
C25	C	0.46596	0.20993	0.37917
C26	C	0.45541	0.23242	0.29525
C27	C	0.45299	0.17604	0.27100
C28	C	0.46890	0.16145	0.39059
S29	S	0.50186	0.18726	0.65424
H30	H	0.43913	0.42443	0.54517
H31	H	0.44527	0.37716	0.66617
H32	H	0.53703	0.41799	0.18828
H33	H	0.53437	0.46629	0.06758
H34	H	0.53125	0.31766	0.89847
H35	H	0.52801	0.25749	0.86879
H36	H	0.43562	0.22572	0.13452
H37	H	0.43324	0.16431	0.10728
H38	H	0.44331	0.11526	0.14900
H39	H	0.52604	0.36730	0.86435
H40	H	0.62692	0.56104	0.05796
H41	H	0.57300	0.55797	0.01601
H42	H	0.58421	0.48774	0.75540
H43	H	0.53060	0.48739	0.68770

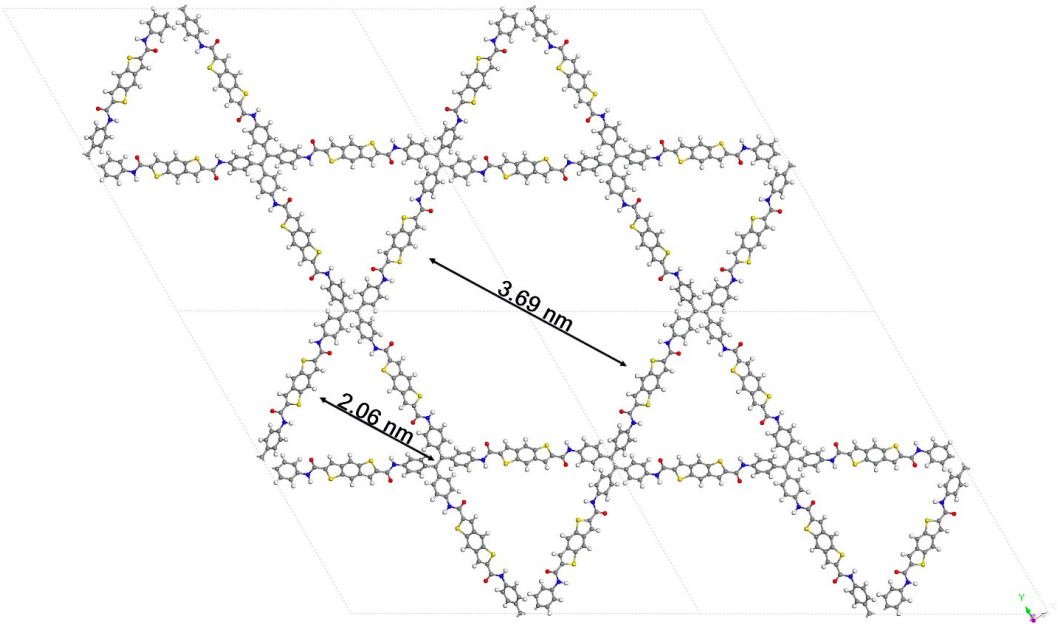

Figure C2. Simulated Kagome structure of Amide-BDT-ETTA.

Structural parameters of fully (100%) amidized Amide-BDT-ETTA

Unit Cell Parameters (*P6*):

$a = b = 4.781$ nm, $c = 0.448$ nm

$\alpha = \beta = 90$ °, $\gamma = 120$ °

Table C2. Fractional coordinates of fully (100%) oxidized Amide-BDT-ETTA.

C1	C	0.48369	148.521	0.33321
C2	C	0.52241	0.54821	0.33528
C3	C	0.54474	0.51214	0.36387
C4	C	0.57274	0.53115	0.18995
C5	C	0.60124	0.52990	0.23550
C6	C	0.60253	0.50973	0.45772
C7	C	0.57461	0.49027	0.62587
C8	C	0.54663	0.49256	0.58555
C9	C	0.44904	0.42667	0.47581
C10	C	0.44250	0.39460	0.49319
C11	C	0.46443	0.38614	0.37885
C12	C	0.49242	0.40972	0.23659

C13	C	0.49889	0.44180	0.21559
N14	N	0.54176	0.64639	0.41138
C15	C	0.51749	0.65345	0.51616
N16	N	0.63138	0.50794	0.51263
C17	C	0.66389	0.53407	0.46122
C18	C	0.47741	0.31317	0.49350
S19	S	0.44395	0.28097	0.27960
C20	C	0.45949	0.25512	0.39199
C21	C	0.48703	0.27049	0.56985
C22	C	0.49700	0.30428	0.62475
C23	C	0.50238	0.25383	0.67696
C24	C	0.48894	0.22113	0.59735
C25	C	0.46130	0.20576	0.42078
C26	C	0.44601	0.22243	0.31316
C27	C	0.45132	0.17203	0.36452
C28	C	0.47111	0.16316	0.49127
S29	S	0.50475	0.19529	0.70394
H30	H	0.43167	0.43159	0.58390
H31	H	0.42081	0.37645	0.60634
H32	H	0.50947	0.40309	0.14583
H33	H	0.52183	0.45829	0.12074
H34	H	0.51780	0.32048	0.75988
H35	H	0.52386	0.26560	0.81602
H36	H	0.42461	0.21069	0.17309
H37	H	0.43047	0.15590	0.22962
H38	H	0.62193	0.54404	0.09179
H39	H	0.57246	0.54692	0.01774
H40	H	0.57499	0.47426	0.79612
H41	H	0.52558	0.47877	0.71954
O42	O	0.13911	0.50733	0.62913
O43	O	0.89245	0.33146	0.39605
H44	H	0.56552	0.66565	0.38945
H45	H	0.62882	0.48690	0.61184

Structural parameters of partially (50%) oxidized Amide-BDT-ETTA

Unit Cell Parameters (P6):

$a = b = 4.749$ nm, $c = 0.447$ nm

$\alpha = \beta = 90$ º, $\gamma = 120$ º

Table C3. Fractional coordinates of partially (50%) oxidized Amide-BDT-ETTA.

C1	C	0.48432	148.461	0.38418
C2	C	0.51927	0.54774	0.38439
C3	C	0.54538	0.51508	0.40932
C4	C	0.57251	0.53551	0.23115
C5	C	0.60187	0.53578	0.26161
C6	C	0.60481	0.51526	0.47096
C7	C	0.57813	0.49539	0.65177
C8	C	0.54930	0.49634	0.62704
C9	C	0.45327	0.42585	0.52296
C10	C	0.44866	0.39449	0.53153
C11	C	0.47148	0.38751	0.41026
C12	C	0.49915	0.41204	0.27012
C13	C	0.50448	0.44361	0.25494
N14	N	0.53394	0.64495	0.43012
C15	C	0.50887	0.65207	0.50951
N16	N	0.63381	0.51315	0.50190
C17	C	0.66179	0.53232	0.37952
C18	C	0.48554	0.31470	0.47330
S19	S	0.45191	0.28421	0.25146
C20	C	0.46618	0.25691	0.35089
C21	C	0.49346	0.27083	0.53285
C22	C	0.50438	0.30459	0.59932
C23	C	0.50760	0.25287	0.63550
C24	C	0.49327	0.22033	0.54624
C25	C	0.46604	0.20650	0.36336
C26	C	0.45191	0.22443	0.26118
C27	C	0.45508	0.17281	0.29547

C28	C	0.47361	0.16255	0.42326
S29	S	0.50726	0.19275	0.64687
H30	H	0.43491	0.42906	0.63342
H31	H	0.42727	0.37546	0.64170
H32	H	0.51695	0.40680	0.17385
H33	H	0.52742	0.46109	0.16548
H34	H	0.52517	0.31964	0.73954
H35	H	0.52878	0.26368	0.77909
H36	H	0.43071	0.21362	0.11768
H37	H	0.43443	0.15785	0.15331
H38	H	0.44718	0.11295	0.24398
H40	H	0.62149	0.55131	0.11336
H41	H	0.57082	0.55106	0.06511
H42	H	0.57985	0.47951	0.81549
H43	H	0.52904	0.48174	0.76732
H44	H	0.55792	0.66413	0.42032
O45	O	0.56058	0.89147	0.58254

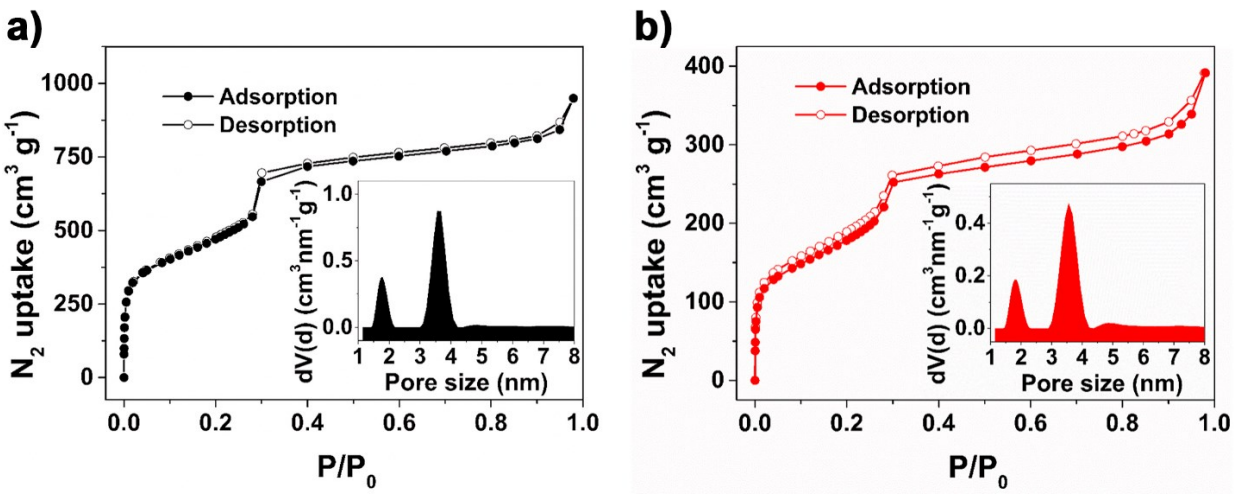

Figure C3. Nitrogen sorption isotherms with resulting pore size distribution of (a) Imine-BDT-ETTA and (b) Amide-BDT-ETTA.

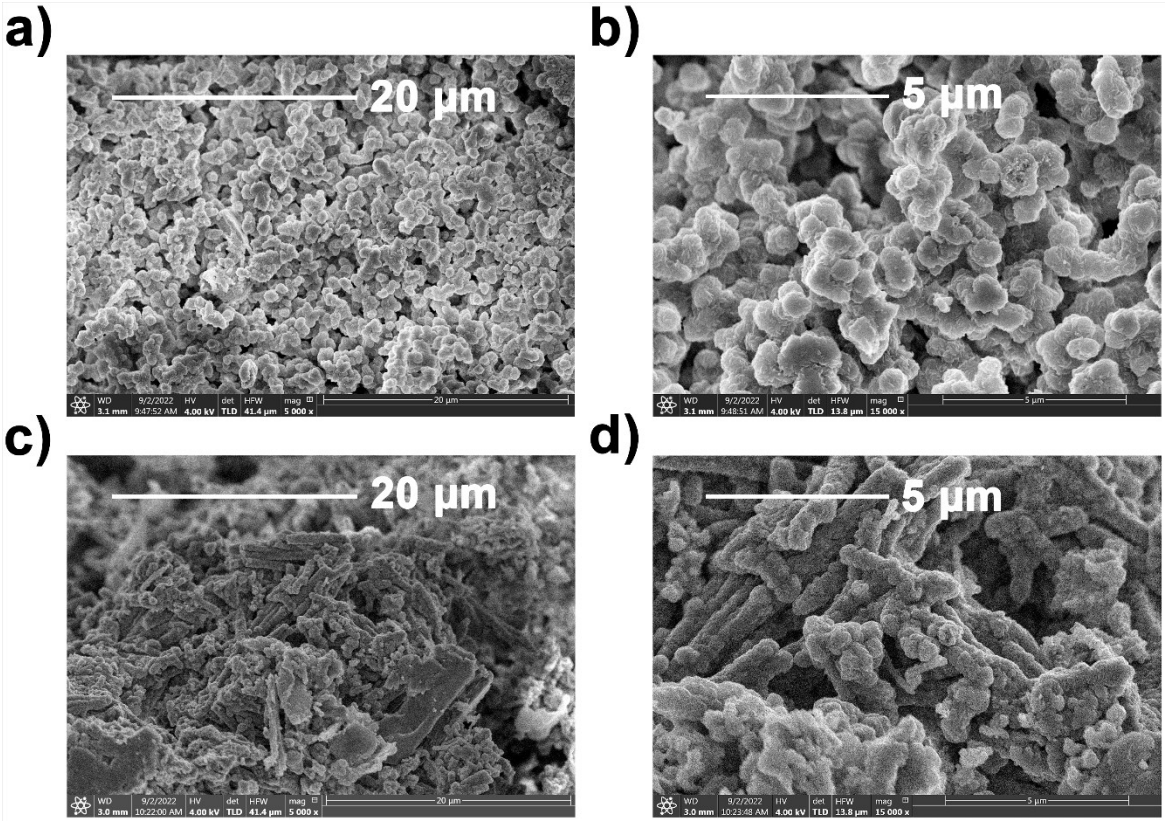

Figure C4. SEM images of (a,b) Imine-BDT-ETTA and (c,d) Amide-BDT-ETTA.

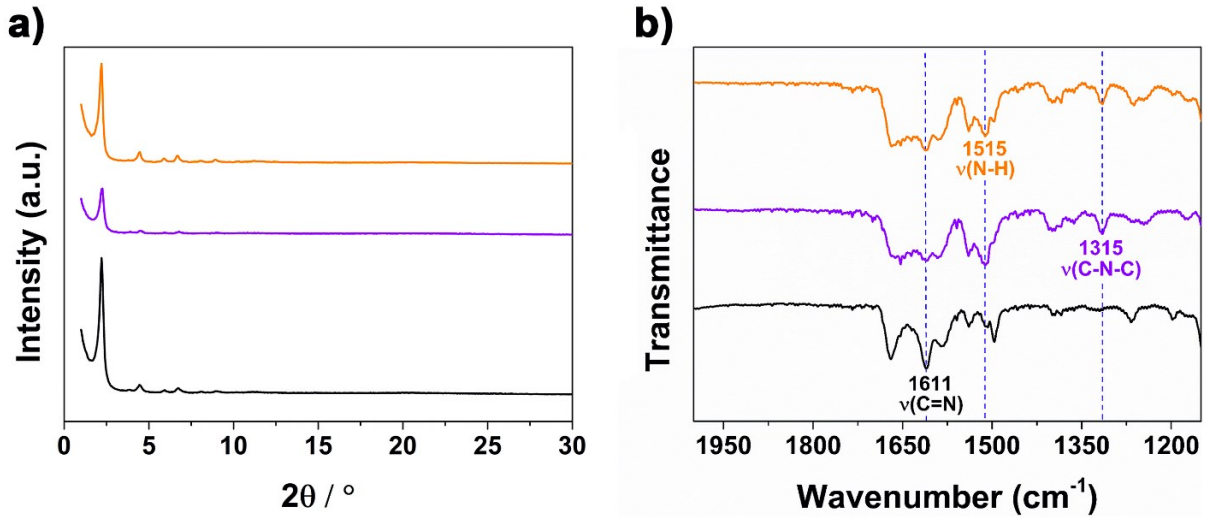

Figure C5. (a) PXRD pattern and (b) FT-IR spectra of three reference samples: Reference-COF-1 (black), Reference-COF-2 (purple) and Reference-COF-3 (orange).

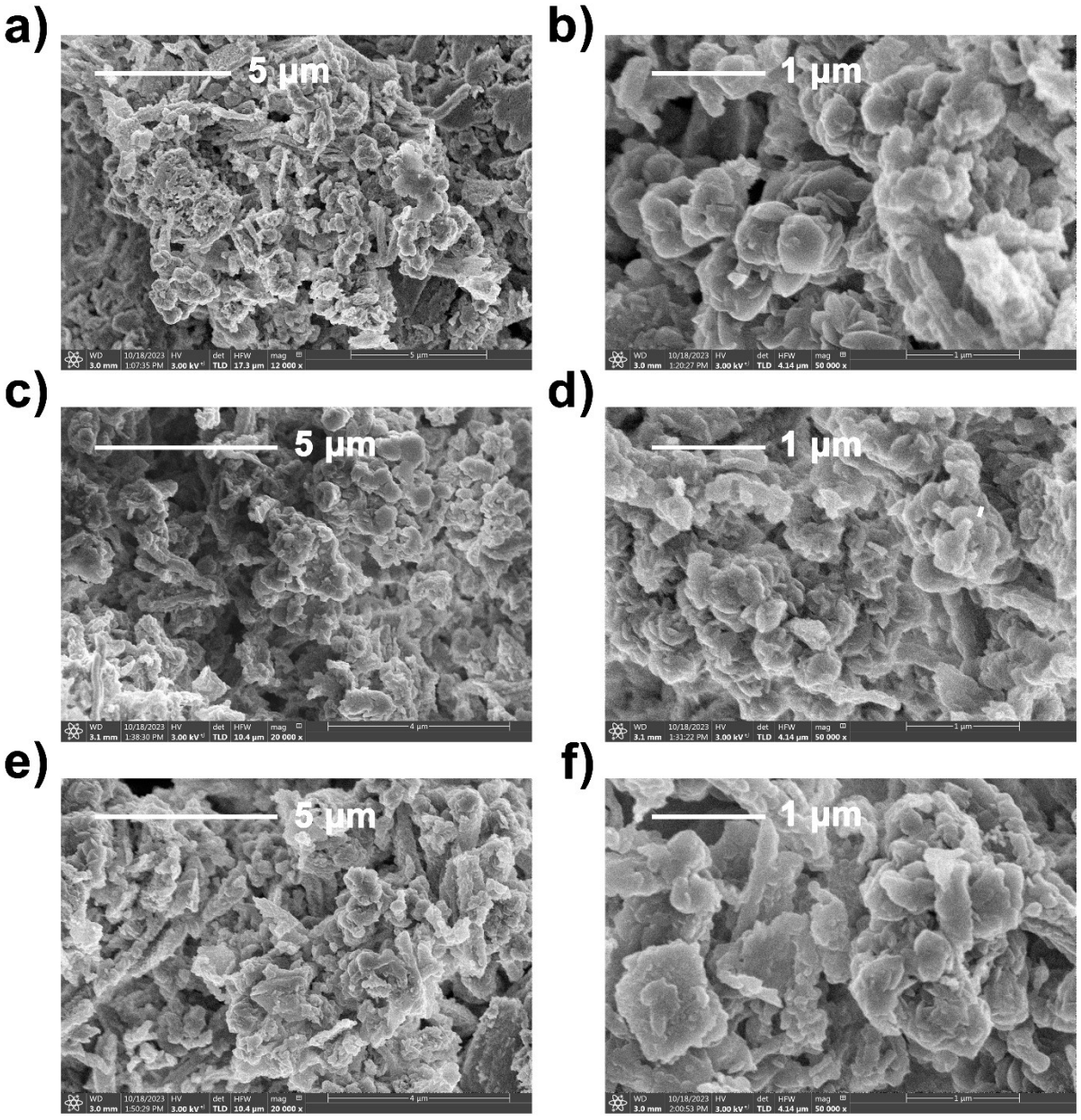

Figure C6. SEM images of three reference samples: (a,b) Reference-COF-1, (c,d) Reference-COF-2 and (e,f) Reference-COF-3.

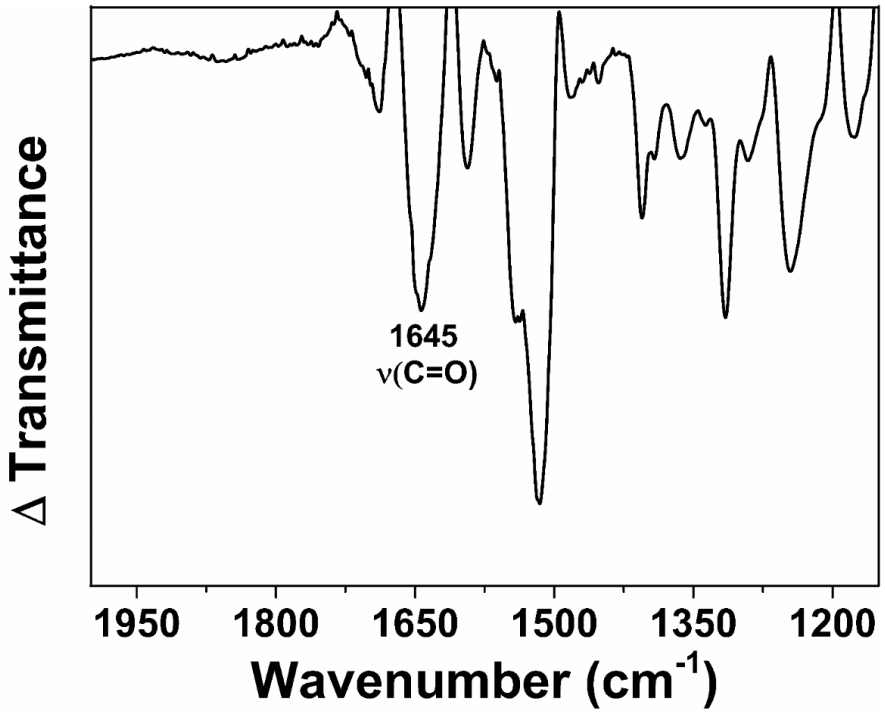

Figure C7. FT-IR difference spectrum obtained through the subtraction of the Imine-BDT-ETTA spectrum from Amide-BDT-ETTA spectrum.

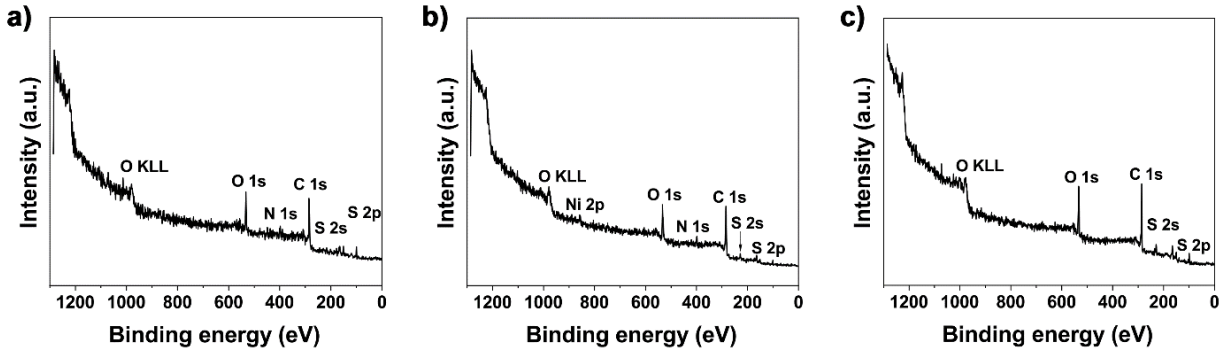

Figure C8. Full XPS spectrum of (a) Imine-BDT-ETTA COF, (b) Amide-BDT-ETTA COF and (c) BDT linker. O KLL Auger lines correspond to oxygen Auger transitions with an initial K-shell vacancy and a final double L-shell vacancy. Their kinetic energies remain independent of the ionizing radiation. Ni peak originates from the screws or the sample holder.

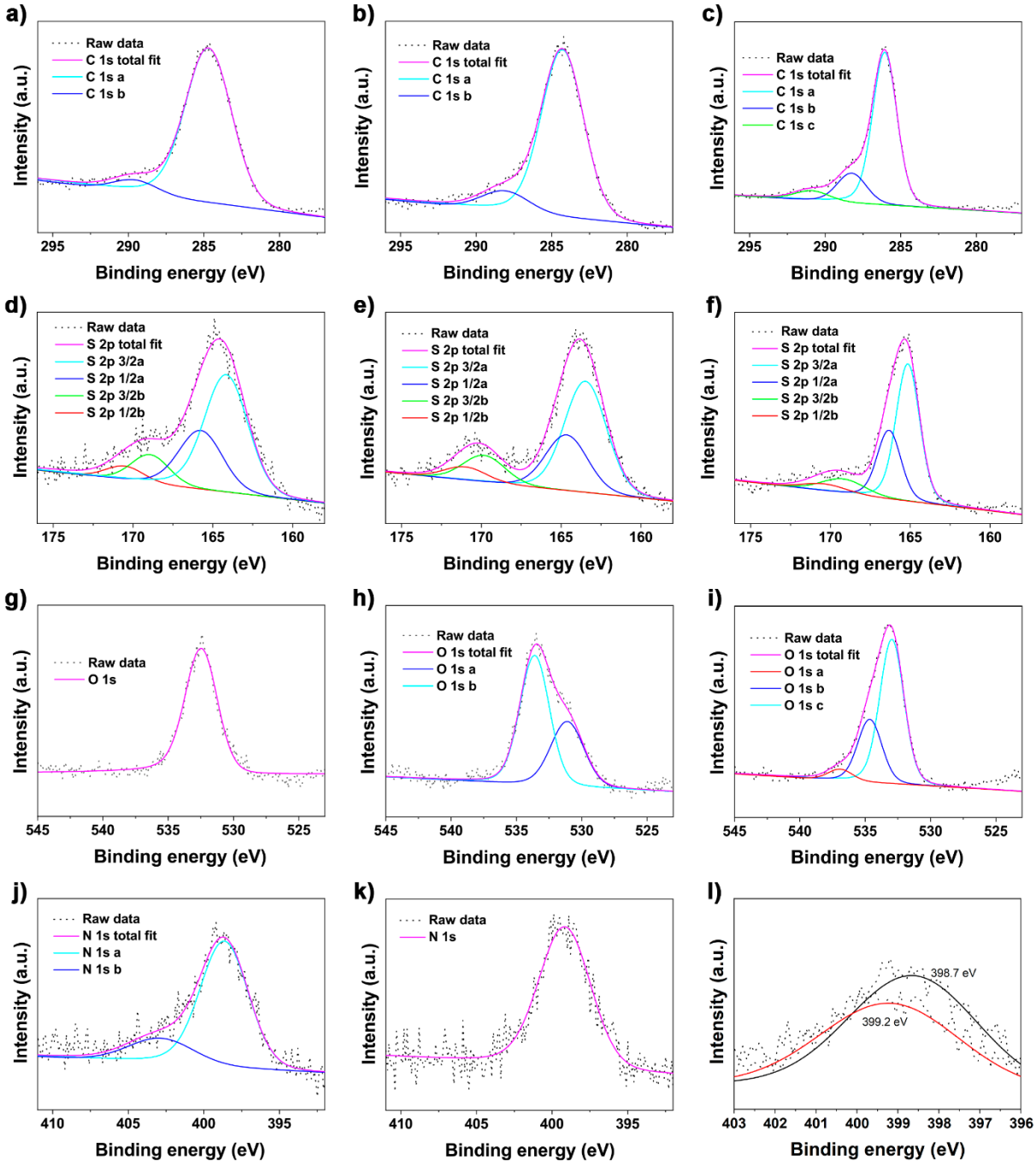

Figure C9. Carbon 1s XPS spectra of (a) Imine-BDT-ETTA, (b) Amide-BDT-ETTA and (c) BDT linker. Two carbon environments for both COFs: 284.7 eV and 289.5 eV for Imine-BDT-ETTA, and 284.3 eV and 288.1 eV for Amide-BDT-ETTA. The carbon signals 284.7 eV and 284.3 eV correspond to overlapping C=C, C–N, and C=N bonds. The higher binding energy peaks indicate oxidized carbon species from surface oxidation. The 288.1 eV peak in Amide-BDT-ETTA suggests a carbonyl (C=O) moiety, while the 289.5 eV peak in Imine-BDT-ETTA likely originates from unreacted aldehyde groups, indicating lower electron density in Imine-BDT-ETTA. S 2p XPS spectra of (d)

Imine-BDT-ETTA, (e) Amide-BDT-ETTA and (f) BDT linker. Oxygen 1s XPS spectra of (g) Imine-BDT-ETTA COF, (h) Amide-BDT-ETTA COF and (i) BDT linker. Oxygen species between 532 eV and 536 eV correspond to carbonyl groups, amide bonds and sulfonyl groups. Nitrogen 1s XPS spectra of (j) Imine-BDT-ETTA and (k) Amide-BDT-ETTA. For Imine-BDT-ETTA revealed two nitrogen species at 398.6 eV (C=N and C–N bonds) and 402.8 eV (ammonium salts). The presence of 402.8 eV signal exclusively in Imine-BDT-ETTA suggests the presence of unreacted amino groups remaining after COF formation. For Amide-BDT-ETTA, one nitrogen species was observed at 399.0 eV, which implies in the existence of the C=N and C–N bonds. (l) The comparison between the N 1s spectra of Imine-BDT-ETTA (black) and Amide-BDT-ETTA (red) reveals a shift toward higher binding energy after the amidization process (from 398.7 to 399.2 eV), confirming the efficient conversion of imine to amide.

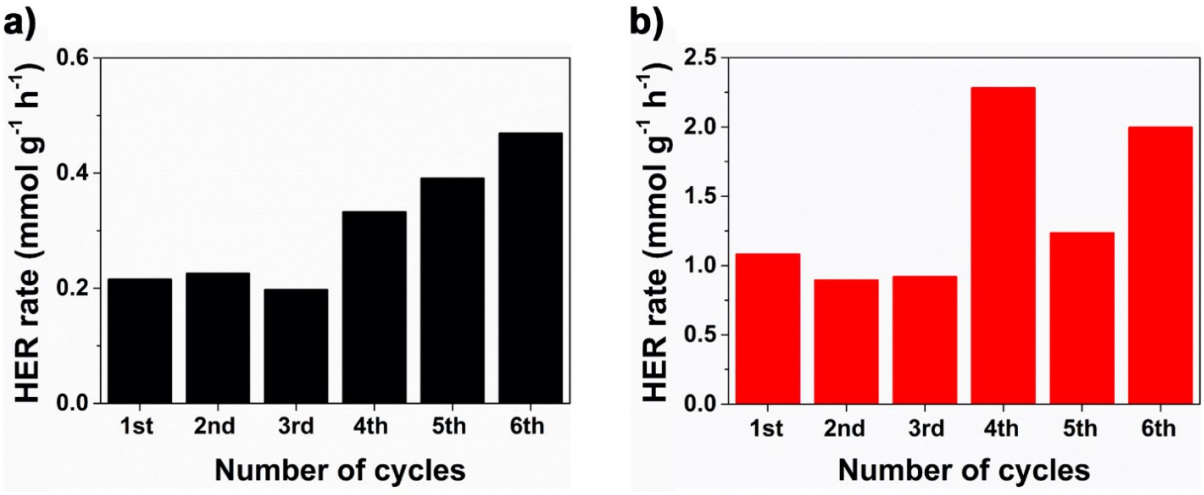

Figure C10. HER rates using 10 mM H_2A (1st-3rd cycles) and 2 mM H_2A (4th-6th cycles) for (a) Imine-BDT-ETTA and (b) Amide-BDT-ETTA. Conditions of photocatalytic tests: $\lambda > 420$ nm, 100 mW cm^{-2}, 1 g/L COF suspension in H_2A, 1.0 wt% (Pt/COF) using H_2PtCl_6 precursor.

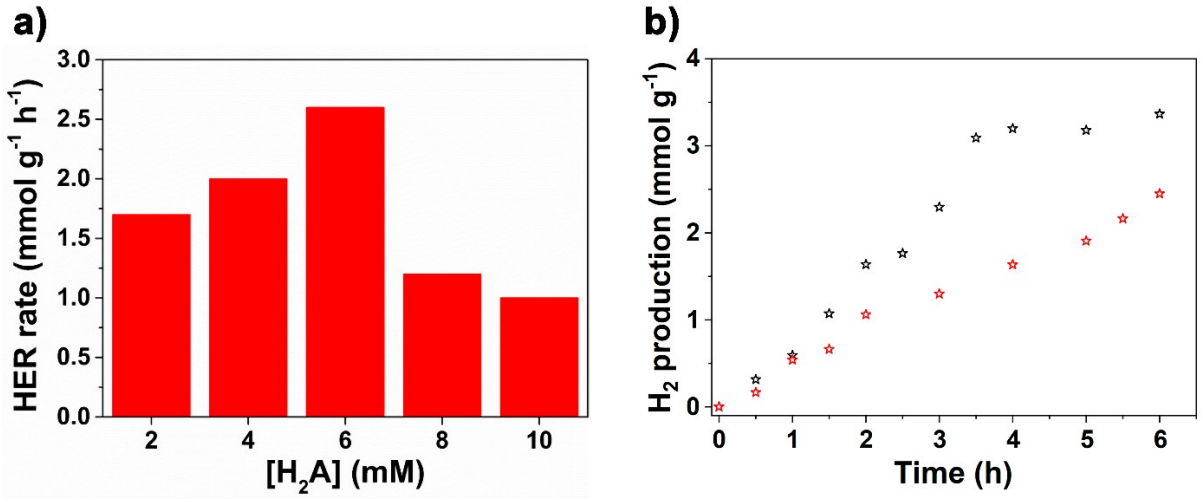

Figure C11. (a) HER rates depending on the concentration of H_2A for the Amide-BDT-ETTA. (b) H_2 evolution using 0.75 M TEOA suspension for the Imine-BDT-ETTA (black) and Amide-BDT-ETTA (red). Conditions of photocatalytic tests: λ > 420 nm, 100 mW cm^{-2}, 1 g/L COF suspension, 1.0 wt% (Pt/COF) using H_2PtCl_6 precursor

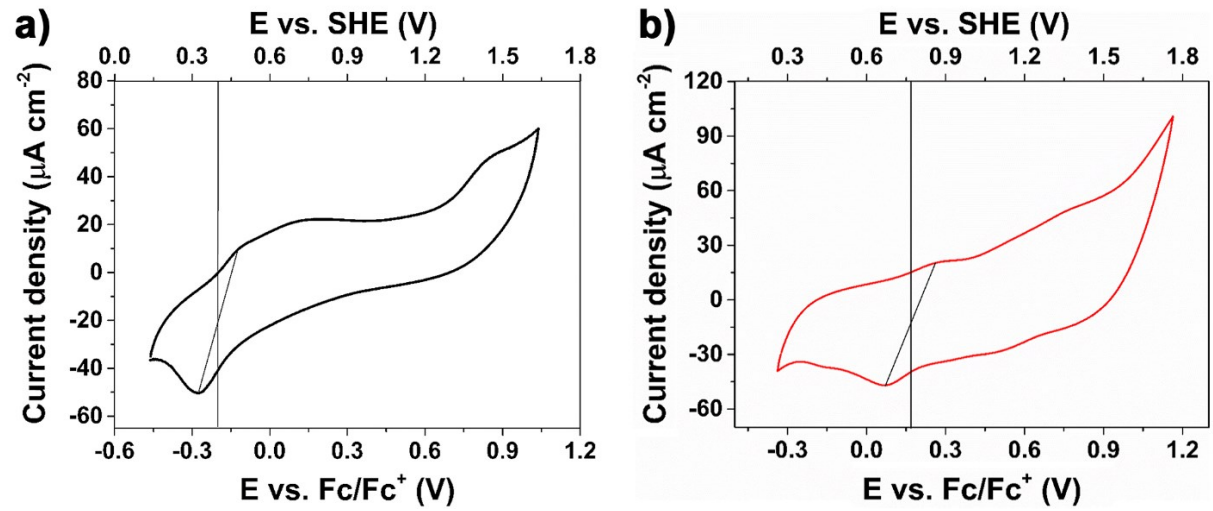

Figure C12. CV plot of (a) Imine-BDT-ETTA and of (b) Amide-BDT-ETTA recorded in 0.1 M NBu4PF6 in acetonitrile.

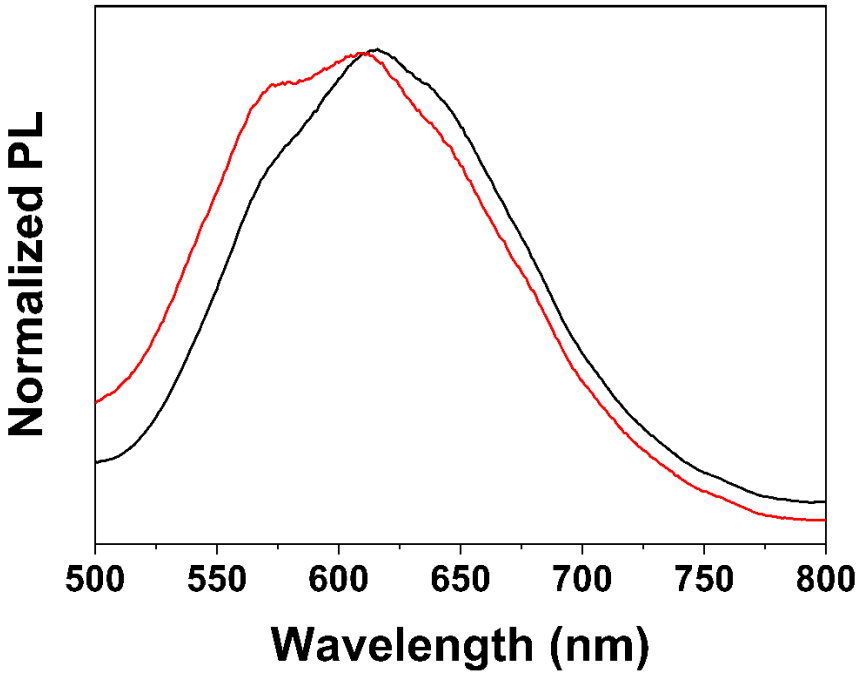

Figure C13. PL spectra for Imine-BDT-ETTA (black) and Amide-BDT-ETTA (red).

Table C4. pH Values measured at different concentrations of H_2A.

Concentration of H_2A (mM)	pH value
0	6.51
2	3.53
4	3.34
6	3.23
8	3.16
10	3.10

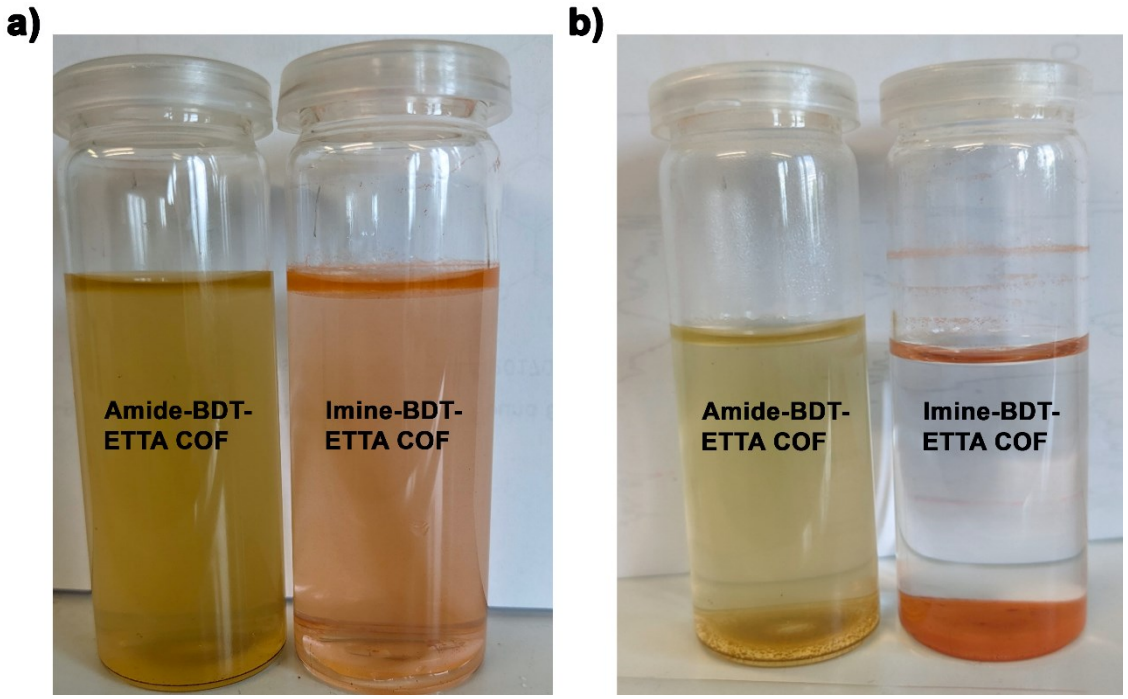

Figure C14. Suspensions in water of Amide-BDT-ETTA and Imine-BDT-ETTA (a) after the ultrasonication and (b) one hour after the ultrasonication.

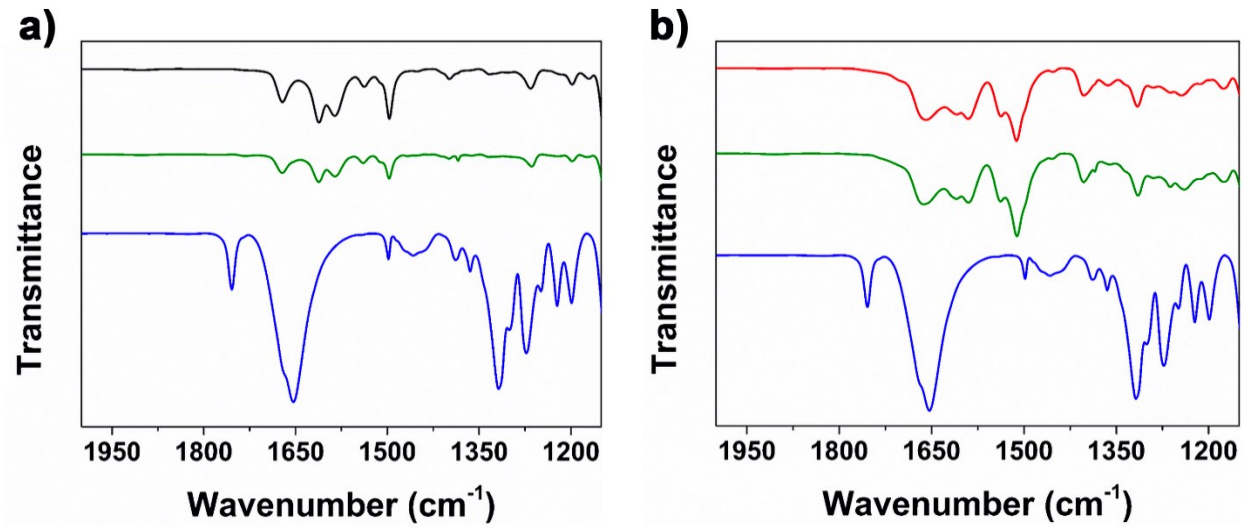

Figure C15. FT-IR spectra of (a) Imine-BDT-ETTA (black), Imine-BDT-ETTA treated with H_2A (green) and H_2A (blue) and (b) Amide-BDT-ETTA (red), Amide-BDT-ETTA treated with H_2A (green) and H_2A (blue).

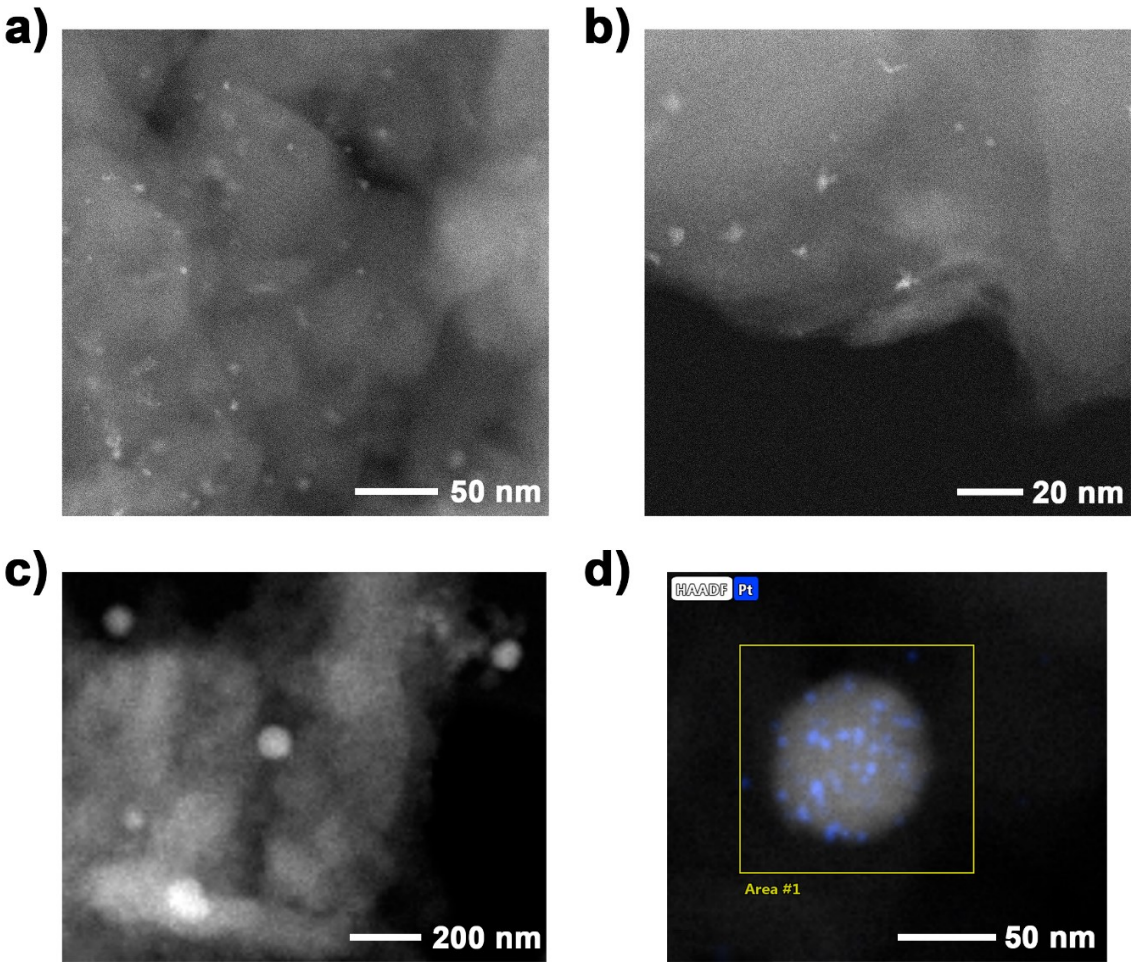

Figure C16. Images of Pt particles within (a,b) Imine-BDT-ETTA-COF and (c,d) Amide-BDT-ETTA structure obtained after 13 h illumination. Conditions of illumination: λ > 420 nm, 100 mW cm^{-2}, 1 g/L COF suspension containing 10 mM H_2A, 1.0 wt% (Pt/COF) using H_2PtCl_6 precursor.

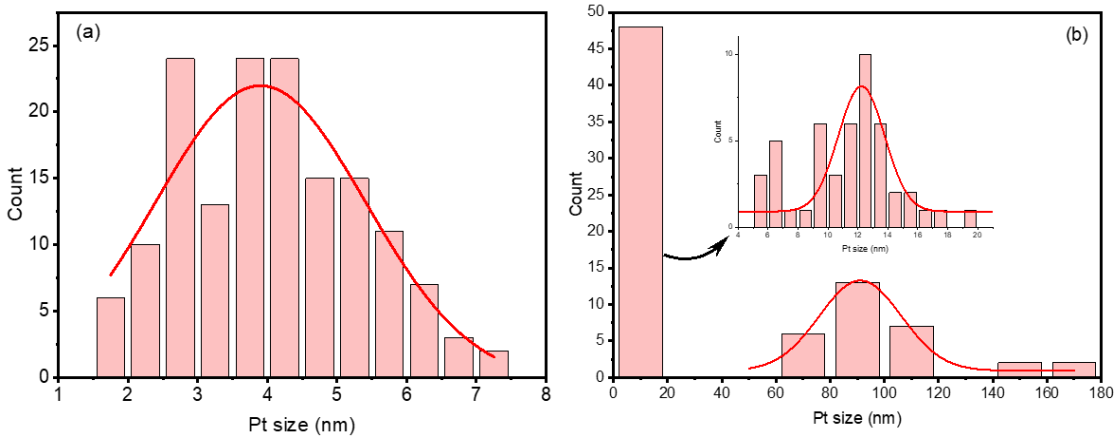

Figure C17. Pt size distribution in the Imine-BDT-ETTA-COF (a) and in the Amide-BDT-ETTA-COF (b) following 13 h of irradiation in the presence of 10 mM H_2A.

CURRICULUM VITAE

LUCAS LEÃO NASCIMENTO

lucasleaolln@gmail.com

Uberlândia – MG / Brazil

Education

B.Sc. **(2018)** Industrial Chemistry, Universidade Federal de Uberlândia, 2016.

M.Sc. **(2021)** Chemistry, Universidade Federal de Uberlândia under the supervision of Professor Antônio Otávio de Toledo Patrocinio. Dissertation title: "Foto(eletro)reforma do glicerol empregando filmes de Bi_2WO_6 como fotoanodos seletivos"

International Research Internship

November **2023** to July **2024** – University of Liverpool - Stephenson Institute for Renewable Energy (SIRE). Under the supervision of Prof. Dr. Alexander J. Cowan. (CAPES: 88887.892434/2023-00)

April 2025 to **June** 2025 - Ludwig-Maximilians-Universität München (LMU) – Department of Physical Chemistry - Bein Research Group. Under the supervision of Prof. Dr. Thomas Bein and Dr. Jenny Schneider. Internship funded by the Alexander von Humboldt-Stiftung.

Articles Submitted for Publication

NASCIMENTO, L. L.; SOUZA, R. A; NUNES, P. H.; COSTA, J.; RICARDO, I.; MARSON, E.; KRAMBROCK, K.; PATROCINIO O. T. P. Photoreforming of industrial waste streams using Nb-doped BiVO4 photoanodes for sustainable hydrogen production. **RSC Sustainability**, *under revision*, **2025**.

Publications – Journal Articles

1. PALIUŠYTĖ, K.; **NASCIMENTO, L. L.**; ILLNER, H.; WIEDMAIER, M.; GUNTERMANN, R.; DÖBLINGER, M.; BEIN, T.; PATROCINIO, A. O. T.; SCHNEIDER, J. Surface Charge Modulation in Covalent Organic Frameworks for Controlled Pt-Photodeposition and Enhanced Photocatalytic Hydrogen Evolution. **Small**, p. 2500870, **2025**. https://doi.org/10.1002/smll.202500870

2. **NASCIMENTO, L. L.**; CARVALHO SOUZA, R. A.; ZACOUR MARINHO, J.; WANG, C.; PATROCINIO, A. O. T. Light-driven conversion of biomass-derived compounds into green fuels and chemicals. **Journal of Cleaner Production**, v. 449, n., p. 141709, **2024**. https://doi.org/10.1016/j.jclepro.2024.141709

3. ROSA, R. H.; SILVA, R. S.; **NASCIMENTO, L. L.**; OKURA, M. H.; PATROCINIO, A. O. T.; ROSSIGNOLO, J. A. Photocatalytic and Antimicrobial Activity of TiO_2 Films Deposited on Fiber-Cement Surfaces**. Catalysts**, v. 13, n. 5, p. 861, **2023**. https://doi.org/10.3390/catal13050861

4. DOS SANTOS, W. S.; CARMO, É. J.; **NASCIMENTO, L. L.**; PATROCÍNIO, A. O. T.; GUO, R.; BHALLA, A. S.; GUERRA, J. D. S. Enhanced electron lifetime in bismuth-vanadium-oxide based bifunctional hybrid photoactive heterostructures. **Journal of Physics and Chemistry of Solids**, v. 180, p. 111438, **2023**. https://doi.org/10.1016/j.jpcs.2023.111438

5. COSTA, I. G. F.; RIBEIRO, S. R. F. L.; **NASCIMENTO, L. L.**; PATROCINIO, A. O. T.; CARDOSO, V. L.; BATISTA, F. R. X.; REIS, M. H. M. Well-dispersed titanium dioxide and silver nanoparticles on external and internal surfaces of asymmetric alumina hollow fibers for enhanced chromium (VI) photoreductions. **Environmental Science and Pollution Research**, 30., n. 22, p. 62508, **2023**. https://doi.org/10.1007/s11356-023-26528-x

6. **NASCIMENTO, L. L.**; MARINHO, J. Z.; DOS SANTOS, A. L. R.; DE FARIA, A. M.; SOUZA, R. A. C.; WANG, C.; PATROCINIO, A. O. T. Photoelectrochemical reforming of glycerol by Bi2WO6 photoanodes: Role of the electrolyte pH on the H2 evolution efficiency and product selectivity. **Applied Catalysis A: General**, v. 646, p. 118867, **2022**. https://doi.org/10.1016/j.apcata.2022.118867

7. MARINHO, J. Z.; **NASCIMENTO, L. L.**; SANTOS, A. L. R.; FARIA, A. M.; MACHADO, A. E. H.; PATROCINIO, A. O. T. On the influence of hydrothermal treatment pH on the performance of Bi2WO6 as photocatalyst in the glycerol photoreforming. **Photochemical & Photobiological Sciences**, v. 21, n., p. 1659–1675, **2022**. https://doi.org/10.1007/s43630-022-00249-5

8. DOS SANTOS, W. S.; CARMO, E. J.; **NASCIMENTO, L. L.**; PATROCÍNIO, A. O. T.; GUERRA, J. D. S. Influence of the chemical nature of the deposition solution on the formation of heterostructural BVO films. **Journal of Physics: Conference Series**, v. 2298, n. 1, p. 012014, **2022**. https://dx.doi.org/10.1088/1742-6596/2298/1/012014

9. ZAMBIAZI, P. J.; APARECIDO, G. D. O.; VASCONCELOS DE BARROS FERRAZ, T.; SKINNER, W. S. J.; YOSHIMURA, R. G.; MOREIRA, D. E. B.; GERMSCHEIDT, R. L.; **NASCIMENTO, L. L.**; PATROCINIO, A. O.; FORMIGA, A. L. B.; BONACIN, J. A. Electrocatalytic Water Oxidation Reaction Promoted by Cobalt-Prussian Blue and its Thermal Decomposition Product Under Mild Conditions. Dalton Transactions, v. 49, n. 45 p. 16368, **2020**. http://dx.doi.org/10.1039/D0DT02220A

10. **NASCIMENTO, L. L**.; BRUSSASCO, J. G.; GARCIA, I. A.; PAULA, L. F.; POLO, A. S.; PATROCINIO, A. O. T. Aluminum oxides as alternative building blocks for efficient layer-by-layer blocking layers in dye-sensitized solar cells. **Journal of Physics: Condensed Matter**, v. 33, n. 5, p. 055002, **2020**. http://dx.doi.org/10.1088/1361-648X/abc30e

11. DOS SANTOS, W. S.; CARMO, É. J.; MENDEZ-GONZÁLEZ, Y.**;** **NASCIMENTO, L. L**.; PATROCÍNIO, A. O. T.; GUO, R.; BHALLA, A. S.; M'PEKO, J.-C.; GUERRA, J. D. S. Innovative multifunctional hybrid photoelectrode design based on a ternary heterojunction with super-enhanced efficiency for artificial photosynthesis. **Scientific Reports**, v. 10, n. 1, p. 10669, **2020**. https://doi.org/10.1038/s41598-020-67768-y

12. SALOMÃO, P. E. A.; GOMES, D. S.; FERREIRA, E. J. C.; MOURA, F.; **NASCIMENTO, L. L.**; PATROCÍNIO, A. O. T.; PEREIRA, M. C. Photoelectrochemical hydrogen production from water splitting using heterostructured nanowire arrays of Bi2O3/BiAl oxides as a photocathode. **Solar Energy Materials and Solar Cells**, v. 194, n., p. 276-284, **2019**. https://doi.org/10.1016/j.solmat.2018.12.037

13. OLIVEIRA, A. T.; RODRIGUEZ, M.; ANDRADE, T. S.; DE SOUZA, H. E. A.; ARDISSON, J. D.; OLIVEIRA, H. S.; OLIVEIRA, L. C. A.; LORENÇON, E.; SILVA, A. C.; **NASCIMENTO, L. L.**; PATROCÍNIO, A. O. T.; PEREIRA, M. C. High Water Oxidation Performance of W-Doped BiVO4 Photoanodes Coupled to V2O5 Rods as a Photoabsorber and Hole Carrier. **Solar RRL**, v. 2, n. 8, p. 1800089, **2018**. https://doi.org/10.1002/solr.201800089

14. DOS SANTOS, W. S.; RODRIGUEZ, M.; AFONSO, A. S.; MESQUITA, J. P.; **NASCIMENTO, L. L.**; PATROCÍNIO, A. O. T.; SILVA, A. C.; OLIVEIRA, L. C. A.; FABRIS, J. D.; PEREIRA, M. C. A hole inversion layer at the BiVO4/Bi4V2O11 interface produces a high tunable photovoltage for water

splitting. **Scientific Reports**, v. 6, n. 1, p. 31406, **2016**. https://doi.org/10.1038/srep31406

Publications – Extension

1. OLIVEIRA, MARCUS VINICIUS SILVA; **NASCIMENTO, LUCAS LEÃO**; SILVA, SAMUEL CARLOS; REZENDE, THAÍS KARINE DE LIMA; BORGES, PEDRO HENRIQUE DE SOUZA; KIKUTI, ELAINE. Prosa científica: o uso de plataformas digitais como ferramentas entre estudantes e o mercado de atuação. OPEN SCIENCE RESEARCH XII. 1ed.: Editora Científica Digital, **2023**, v. 12, p. 1014-1024. https://doi.org/10.37885/230713752

Book Chapters

1. PAULO H. H. NUNES, **LUCAS LEÃO NASCIMENTO**, RAFAEL A. C. SOUZA, ANTONIO O. T. PATROCÍNIO. SÍNTESE HIDROTÉRMICA DE ÓXIDOS SEMICONDUTORES NANOESTRUTURADOS: UM MINI-REVIEW. OPEN SCIENCE RESEARCH XII. 1ed.: Editora Científica Digital, **2023**, v.12, p 1076-1087. https://doi.org/10.37885/230713909

Abstracts in scientific meetings

1. **LUCAS L. NASCIMENTO**, RAFAEL A. SOUZA, PAULO H. NUNES, ANTONIO O. T. PATROCINIO, ALEXANDER J. COWAN. Biomass photoreforming mediated by Ni(II) modified Bi2WO6 and Nb2O5 photocatalysts. 1st UK solar chemicals symposium, **2024**.

2. **LUCAS L. NASCIMENTO**, RAFAEL SOUZA 1 E ANTONIO O. T. PATROCINIO. Bi_2WO_6 modificado com Ni^{2+} ou Cu^{2+} aplicado na fotodegradação de vinhaça sob luz visível. 35º Congresso Latino-Americano de Química (CLAQ 2022), **2022**.

3. **LUCAS LEÃO NASCIMENTO**, RAFAEL A. C. SOUZA, PAULO H. H. NUNES E ANTONIO O. T. PATROCÍNIO. Preparação de Bi2WO6 e Nb2O5 para degradação de vinhaça sob irradiação visível. XXXIV ERSBQ-MG, **2022**.

4. **NASCIMENTO, L. L**.; PATROCINIO, A. O. T. ; MARINHO, J. Z. . Development of Bi2WO6 photoanodes for selective glycerol valorization to formic acid. XIX Brazilian Materials Research Society Meeting (XIX B-MRS), **2021**.

5. MARINHO, J. Z. ; **NASCIMENTO, L. L.** ; MACHADO, A. E. H. ; PATROCINIO, A. O. T. . Promising photoelectrochemical activity of Bi2WO6 and TiO2 photoanodes for glycerol valorization. IX Encontro da Escola Brasileira de Química Verde, **2019**.

6. **NASCIMENTO, L. L**.; MARINHO, J. Z. ; PATROCINIO, A. O. T. . Atividade fotoeletrocatalítica de fotoanodos de TiO2 e Bi2WO6 para conversão de energia solar e oxidação do glicerol. XVIII Brazil MRS Meeting, **2019**.

Oral presentation in scientific meetings

1. **LUCAS L. NASCIMENTO**, RAFAEL A. SOUZA, PAULO H. NUNES, ANTONIO O. T. PATROCINIO. Photoreforming of real biomass-derived industrial waste streams promoted by Nb-doped BiVO4 photoanodes. International Workshop on Photoactive Materials for Sustainable Energy Conversion

2. **LUCAS LEÃO NASCIMENTO**, RAFAEL A. C. SOUZA, PAULO H. H. NUNES, ANTONIO O. T. PATROCÍNIO. Preparação de Bi2WO6 e Nb2O5 para degradação de vinhaça sob irradiação visível. XXXIV ERSBQ-MG, **2022**.

3. **NASCIMENTO, L. L**.; PATROCINIO, A. O. T. ; MARINHO, J. Z. . Development of Bi2WO6 photoanodes for selective glycerol valorization to formic acid. XIX Brazilian Materials Research Society Meeting (XIX B-MRS), **2021**.

Scientific divulgation

1. NASCIMENTO, L. L. Vivências dos discentes do PPGQUI no exterior. XI Workshop de Pós-graduação em Química, Uberlândia, **2024**.

Extension project

1. Voluntary participation in the organizing team of the extension project “Prosa Científica: A Química inserida na sociedade”, promoted by the Institute of Chemistry of the Federal University of Uberlândia and coordinated by Prof. Dr. Elaine Kikuti, from January to December **2023**.

Patent deposit

Célula Fotoeletroquímica Para Promoção de Reações de foto(Eletro)Reforma de Derivados de Biomassa. Patente de Invenção (PI). Número do Processo: BR 10 2024 008925 1

Organization of scientific events

1. International Workshop on Photoactive Materials for Sustainable Energy Conversion. Universidade Federal de Uberlândia, Uberlândia - MG, Brazil from March 19 to 21, **2025**.

Awards and recognitions

IOP Trusted Reviewer, IOP Publishing, **2022**.

Bernhard Gross Award, Sociedade Brasileiras de Pesquisa em Materiais – SBPMAT, **2021**.

ACS Energy Letters and Energy & Fuels Prize, ACS Publications, **2021**.

Honorary Mention, Escola Brasileira de Química Verde, **2019**.